Dissertation zur Erlangung des Doktorgrades

der Fakultät für Chemie und Pharmazie

der Ludwig-Maximilians-Universität München

Thin Films Based on $Cs_2AgBiBr_6$ as Absorber Materials in Lead-Free Perovskite Solar Cells

Maximilian Thomas Sirtl

aus

München, Deutschland

2021

Erklärung

Diese Dissertation wurde im Sinne von § 7 der Promotionsordnung vom 28. November 2011 von Herrn Prof. Dr. Thomas Bein betreut

Eidesstattliche Versicherung

Diese Dissertation wurde eigenständig und ohne unerlaubte Hilfe bearbeitet

München, den 18.10.2021

_____

Maximilian Sirtl

Dissertation eingereicht am:	21. Oktober 2021
Erstgutachter:	Prof. Dr. Thomas Bein
Zweitgutachter:	Prof. Dr. Achim Hartschuh
Mündliche Prüfung am:	16. November 2021

Acknowledgement

First, I would like to thank my supervisor, Prof. Dr. Thomas Bein. I am very grateful to be part of your research group! Thanks to your guidance, I was able to accomplish all the challenges during my PhD time and projects, gaining a lot of self-confidence in scientific discussions. Thank you, Thomas, for always supporting me and pushing me forward, to give talks at important conferences and meetings. Special thanks for all your contributions to my publications and for proof-reading this thesis.

Wolfgang, although only for 1 year, I am really happy you joined our group! Working with you was a real pleasure and I think that our papers prove the fruitful collaboration we had. Thank you so much for working with me, leading me towards a new horizon in research and showing me how to sell stories online fast. Who knew that our “let’s measure subgap EQE and rate dependent *J/V* and look what happens”-paper (a.k.a. “Bottlenecks”) would eventually become the foundation of my whole thesis.

I would also like to thank my many collaboration partners, inside and outside the LMU.

Thank you Prof. Müller Buschbaum, Lennart Reb and Sebastian Grott! Besides the nice collaboration on grazing incident measurements, being on conferences with you was always a blast. Thank you, Sebastian for making the SolTech PhD symposia always a memorable event.

My special thanks to Prof. Vladimir Dyakonov, Dr Kristofer Tvingstedt, Philipp Rieder, Patrick Dörflinger and especially Melina Armer for your optoelectronic measurements that led to a lot of fruitful discussions and eventually to a large number of publications together! Thank you, Melina, for always giving maximum effort and speed with my measurements, providing me with results almost immediately after receiving my samples! Sorry again for pushing you into the ice-water called SPP-Meeting Potsdam 😉

I would like to thank Corinna Heidt for all the administrative help and the occasional Friday-afternoon smoke 😉. Also many thanks to Steffen Schmidt for all the SEM measurements and nice discussions about my EDX results. My thanks go also to our technician, Tina, who ensures that our lab work can run smoothly.

Thank you, AK Bein, for the awesome working atmosphere during my whole PhD! It really was a pleasure to start as an F-intern and eventually go all the way up to the PhD with all of

you, giving me tons of nice memories and moments (and confusing me with a very famous musician), especially during the many BBQs and conferences.

Sabrina, it was always a pleasure to meet first thing in the morning for a coffee and discuss the latest hockey results and why you're not allowed to wear a frock from the 'Rotter Stier'. To the office 3.027 (the 'Biergarten', Roman, Laura, Andi and Rik), I think I spent more time in your office than in mine. Thanks for all the fun chats and after-work beers, always giving a good laugh and a fun time. Thank you, Marcella for teaming up with me crying about the PV community and the oh-so mean reproducibility of our experiments! Thanks for always stepping up when I needed help and showing me the EQE setup for the 1000th time. Thanks to my long-time office mate Pati, not only for choosing memes for our office-door but also for accompanying me at the far end of our Dolomites-hike 😉. Anderson, thank you for always helping me with glove-box responsibilities and all the office pranks we played at each other! Thank you Waschtl and Zolli for not only an unforgettable first conference, but also being helpful when I was stuck with my experiments ('da hilft eigentlich nur noch ein Bier!').

My special thanks to the PV lab! Somehow, I managed to start during a complete generation shift so I worked with a big number of people. Thank you, Nadja, Meltem, Pablo, Hongi and Michiel for introducing me into the world of perovskites and solar cells and teaching me on how to properly work in a PV lab and how essential the right music is to do so. My special thanks to you, Michiel, for giving me so many interesting projects and for mentoring me during my internships, as well as Master Thesis and the start of my PhD, forcing me to give a talk at an international conference just after I started my PhD! Doing my F-internship with you was the start to this crazy and wonderful time 😊

Thank you, Andi, Rik, Flo and Schorsch for joining the perovskite lab and making this place so much fun to work at! All these friendly mockings (Sirtl-batch, Sirtl-Subgroup, etc), real fruitful discussions and occasional suppers made it a pleasure to work here. Thank you for always being open minded, respectful and trustworthy! I could always rely on you and you were always the first to help when something was up. Thanks to you, I was not only able to widen my scientific horizon, but also my musical.

Special thanks to Andi, always taking the Monday and Tuesday morning shift during the first Corona Lock-Down with me and for all the music sessions (and lectures) leading to a serious 'Between the Buried and Me' and 'Mother's Cake' obsession.

Thank you, Rik for all the fun lab-work, being my first master student and for showing me how to not treat DMSO vials inside the glovebox 😉. I will never forget the 2-day long glovebox clean-up thanks to which our names are now written in the back =D.

At this point I want to thank all my students I was happy to supervise during my time here: Sophia Wandelt, Rik Hooijer, Sebastian Klenk and Patrick Ganswindt. Thank you all for all your effort and work, helping me a lot during my research and helping me to constantly develop my solar cells and projects. You all taught me a lot about mentoring and how it is possible to be more nervous at the talks of other people than on my own ones. Especially Rik and Sebi, you went all the way from F-student to PhD student with me and I am very thankful for that.

I also would like to thank my friends Luca, Max ('Schrotti'), Lukas and David for always being there for me. We went through a lot together and without you and your support I wouldn't have gone so far. Thank you, Wurzy for going the whole 10 years (actually it was more =D) at this campus with me, from bending glass in the pre-university course up to blowing stuff up on purpose or trying to squeeze 0.x % PCE out of solar cells.

Many thanks to my family and especially my mother for always supporting me and asking the real important questions no PhD student wants to hear ('when will you be finished?'). Thank you for always being there when needed.

My biggest gratitude goes to my fiancée Johanna! Thank you for always being with me and telling me not to do organic chemistry ('is that you who stinks?') and for always having an ear for me. Thank you for all the talk-rehearsals you had to listen to and for sharing the excitement when I came up with yet another idea and crazy theory on my results. With you I can pass every challenge and I am really grateful to have you in my life.

Table of Contents

List of Abbreviations

1D	One-dimensional
2D	Two-dimensional
3D	Three-dimensional
AE2T	5,5‘-diylbis(amino-ethyl)-[2,2‘-bithiophene]
AM1-5G	Air mass 1.5 global
AMER	North, Central and South America
APAC	Asia Pacific
b2b	band-to-band (recombination)
BSE	Back scattered electrons
CB	Conduction band
CBM	Conduction band minimum
CdTe	Cadmium telluride
CIGS	Copper indium gallium diselenide
CPCM	Conductor-like polarizable continuum model
c-TiO2	Compact titanium dioxide
CTL	Charge transport layer
CV	Cyclic voltammetry
DCM	Dichloromethane
DFT	Density Functional Theory
DMSO	Dimethyl sulfoxide
DSC	Differential Scanning Calometry
DSSC	Dye Sensitized Solar Cells

EDOT-Amide-TPA	N,N‘-bis(4-(bis(4-methoxyphenyl)amino)phenyl)-2,3-dihydrothieno[3,4-b][1,4]dioxine-5,7-dicarboxamide
EDOT-MPH	5,7-bis((E)-(2,2-bis(4-methoxyphenyl)hydrazineylidene)methyl)-2,3-dihydrothieno[3,4-b][1,4]dioxine
EDOT-OMeTPA	4,4'-(((1E,1'E)-(2,3-dihydrothieno[3,4-b][1,4]dioxine-5,7-diyl)bis(methaneylylidene))bis(azaneylylidene))bis(N,N-bis(4-methoxyphenyl)aniline)
EDX	Energy dispersive X-ray spectroscopy
Eg	Bandgap energy
EL	Electroluminescence
ELQE	Electroluminescence quantum efficiency
EQE	External quantum efficiency
Erf	Error function
ETL	Electron transport layer
FA	Formamidinium
FAMACs	Formamidinium methylammonium cesium
FF	Fill factor
FPEA	Fluorophenethylammonium
FTO	Fluorine-doped tin oxide
FWHM	Full-width at half maximum
GIWAXS	Grazing incidence wide angle X-ray scattering
GW	Gigawatt
HOMO	Highest occupied molecular orbital
HTL	Hole transporting layer
HTM	Hole transporting material

I/V	Current/Voltage
IPA	Isopropyl alcohol
IPCE	Incident photon to current efficiency
IQE	Internal quantum efficiency
IR	Infrared
ITO	Indium-doped tin oxide
J/V	Current density/Voltage
J_{int}	Integrated Photocurrent
J_{MPP}	Current Density at the Maximum Power Point
J_{SC}	Short Circuit Current Density
KE	Kinetic Energy
LiTFSI	Lithium bis(trifluoromethanesulfonyl)imide
log	logarithmic
LUMO	Lowest Unoccupied Molecular Orbital
MA	Methylammonium
$MAPbI_3$ (MAPI)	Methylammonium Lead Iodide
MEA	Middle East and Africa
MHz	Megahertz
MPP	Maximum Power Point
mp-TiO2	mesoporous Titania
NMR	Nuclear Magnetic Resonance
OPV	Organic Photovoltaics
P3HT	Poly(3-hexylthiophen-2,5-diyl)
PCE	Power Conversion efficiency

PEA(Br)	Phenethyl Ammonium (Bromide)
PES	Photoelectron Spectroscopy
P_{in}	Incident Power
PL	Photoluminescence
PLQY	Photoluminescence Quantum Yield
P_{MPP}	Power at Maximum Power Point
PTAA	Poly-[bis-(4-phenyl)-2,4,5-trimethylphenyl)-amine]
PV	Photovoltaic
(P)XRD	(Powder) X-Ray Diffraction
R.H.	Relative Humidity
rpm	rounds per minute
R_S	Series Resistance
R_{SH}	Shunt Resistance
RT	Room Temperature
SC	Spincoating
SEM	Scanning Electron Microscopy
SI	Supporting Information
Spiro-OMeTAD	2,2',7,7'-Tetrakis-9,9'-spirobifluorene
SRH	Shockley-Read-Hall
TCO	Transparent Conductive Oxide
TCSPC	Time-correlated Single Photon Counting
TGA	Thermo-Gravimetric Analysis
TRMC	Time-resolved Microwave Conductivity
TRPL	Time-resolved Photoluminescence

TWy	Terawatt year
UPS	Ultraviolet Photoelectron Spectroscopy
UV	Ultraviolet
UV-Vis	Ultraviolet to Visible Spectrosopy
V950	9-ethyl-3-{*N*,*N*-bis[(4-methoxyphenyl)vinyl]amino}-9H-carbazole
VB	Valence Band
VBM	Valence Band Maximum
V_{MPP}	Voltage at Maximum Power Point
V_{OC}	Open Circuit Voltage
XPS	X-ray Photoelectron Spectroscopy

Abstract

Lead-based halide perovskites have recently attracted enormous attention as, owing to their outstanding optoelectronic properties and simple synthesis procedures, solar cells comprising these materials have achieved power conversion efficiencies of up to 25 % within only a decade. However, these materials suffer from some significant issues such as a rather low stability towards light, air and humidity, as well as the severe toxicity of lead itself. Hence, a growing research focus has been directed at possible alternatives, using no lead atoms and gaining stability. Some of the most promising alternative candidates are the double perovskites, which have the composition $A_2B^IB^{III}X_6$ and basically double up the regular perovskite structure, substituting two divalent lead cations by one monovalent and one trivalent metal cation.

In this thesis, we first investigated the bottlenecks of the prototypical double perovskite $Cs_2AgBiBr_6$ when implemented in full solar cells. We used *J/V*-scans with different scan rates to determine the ionic behavior of the material and revealed a strong dependence of the material's behavior on the scan rate of the measurement. We moreover reveal a change in field direction within the solar cells, detectable by voltage dependent external quantum efficiency (EQE) measurements, where a rapid drop of the signal was observed, followed by a strong increase, where the maximum did not follow the shape of the absorption-spectrum anymore. We linked this to an inversion of the electrical field, caused by a poor selectivity of the contact materials, leading to an enhanced forward photocurrent. Using electroluminescence (EL) measurements, we determined the amount of non-radiative V_{OC} losses within the solar cell to explain the generally low V_{OC}.

Following this, we investigated the influence of the stoichiometry of the material's precursors in the stock solution prior to the thin film synthesis. By working simultaneously with an AgBr excess and a $BiBr_3$ deficiency, we observed a strong enhancement in the thin films' orientation, as well as crystallinity, using grazing incidence wide angle X-Ray scattering (GIWAXS). While this is known to enhance the optoelectronic properties of lead-based perovskites, we observed similar effects, mainly an increased charge carrier lifetime, as well as an improved charge carrier mobility, determined with time resolved photoluminescence (TRPL) and time resolved microwave conductivity (TRMC). This ultimately led to an enhanced solar cell performance, going from 0.97 % up to 1.11 %, while the dominant recombination regime did not change.

In the third part of the thesis, we investigated the influence of longer organic cation spacers such as phenethyl ammonium bromide (PEABr) in order to form a 2D/3D hybrid interface. We show, that applying an ultra-thin layer does not significantly change the properties of the pristine films, but that it does have a significant impact when employed in complete solar cells. While the recombination behavior of the pristine films does not change, solar cells comprising the 2D/3D hybrid thin films show significant improvement compared to the 3D reference. This was linked to a change in the recombination behavior, as well as an improvement of the contact-selectivity. Again, voltage dependent EQE was applied and the results show no field inversion for the hybrid thin films. This was linked to an improvement of the energy level alignment at the perovskite/hole-transport material (HTM) interface as shown using photoelectron spectroscopy (PES).

Lastly, we investigated a new HTM for lead-based perovskites. Here, we investigated the hydrazone-based low-cost material EDOT-MPH. We applied this new HTM on lead-based perovskites and achieved efficiencies comparable to cells with the popular (but costly) Spiro-OMeTAD. While the conductivity of the new material is within the same order of magnitude of well-established materials, EDOT-MPH exhibits comparable and highly reproducible performance in solar cells, at only a fraction of synthesis cost. We show that by using hydrazone-based functionality groups, the environmental impact of the HTM can be significantly reduced.

1 Introduction

1.1 The Global Energy-Landscape

The need for alternative, sustainable ways to produce energy has been rising continuously during the last decades and the reasons for that are manifold. First of all, the continuous increase of the average lifespan of humans itself leads to a vast increase of the population on earth and therefore increases the need for more energy in general, especially due to the industrial rise of developing countries.[1] Moreover, the traditional energy supplies consist mainly of fossil fuels that are non-abundant and will probably deplete within the next few decades. The combustion of fossil fuels, moreover, results in the release of CO_2 which is also known as a 'green-house gas' and speeds up the global warming.[2,3] The reason for the global warming effect of CO_2 can be found in the molecular structure which allows the molecule to be IR active. After sun irradiation heats up the earth's surface, this energy is again emitted in form of IR irradiation back towards space. However, the higher the CO_2 concentration in the air, the more of this irradiation is absorbed by those molecules, which start to vibrate and reemit the energy towards the surface. This allows for only a fraction of IR radiation to exit into space and leads to a reheating of the earth's surface.[3]

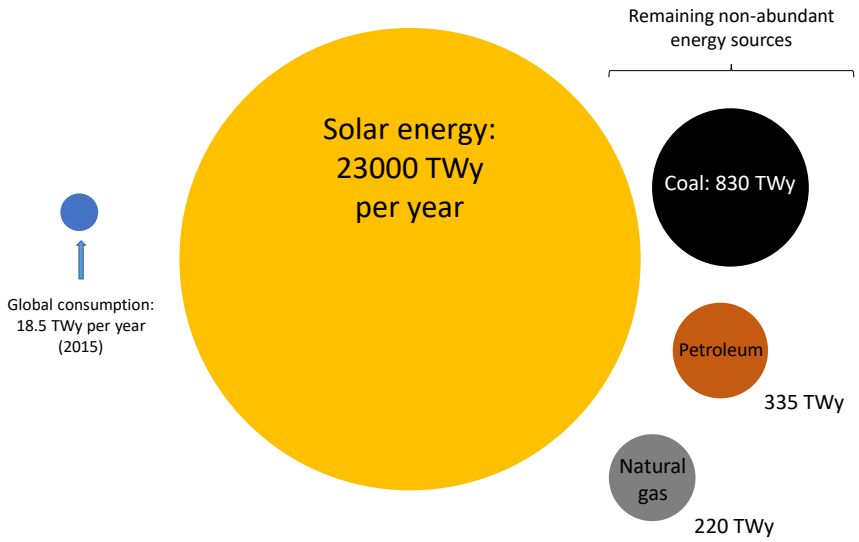

Figure 1.1: Schematic illustration of the abundance of the solar energy compared to global energy consumption and the known non-abundant energy sources coal, petroleum and natural gas in 2015.[4,5] The size of the spheres correlates approximately with the amount of energy shown in the diagram.[4,5]

Therefore, the future of energy production can directly be linked to the future of the development of so-called green energy sources such as wind, water or solar energy. Due to its large abundance, the solar irradiation is a great energy source, delivering about 23,000 terawatt years (TWy) reaching the earth's surface, while the global energy consumption in 2015 was 18.5 TWy (Figure 1.1). This means that the energy that reaches the earth's surface during 6 h solar irradiation would be sufficient to cover the world's energy demand for a whole year.

Photovoltaics (PV) represents the technology to directly convert solar energy in form of light into electricity. This technology is on a strong rise within the renewable energy techniques as the production cost of PV modules has decreased drastically over the years and the markets for PV demands were expanded massively. Especially the market expansion led to a drastic price drop since it caused a constant development of production techniques and upscaling of the PV production capacities by companies.[6] This trend can be seen in the capacity evolution of the total installed solar photovoltaics between the years 2000 and 2019 (~0 up to 633.7 GW), as well as the projected overall capacity for the year 2024 (Figure 1.2).[7]

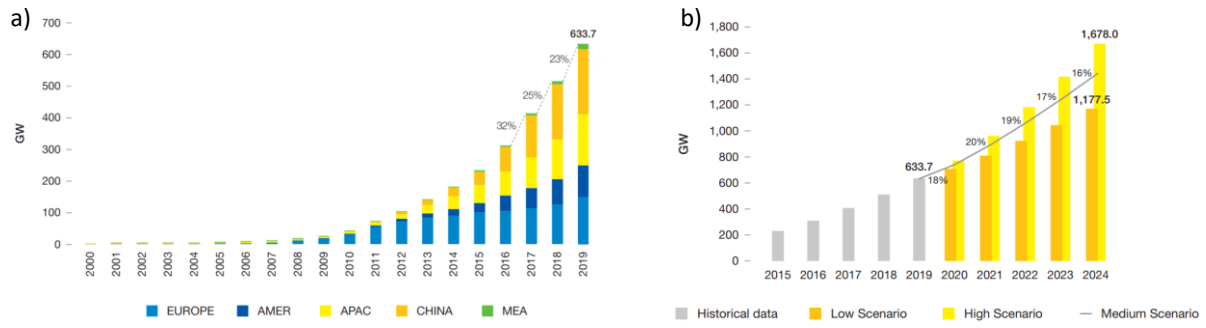

Figure 1.2: Capacity diagrams of photovoltaic installations. A) Capacity evolution over time sorted by regions: Europe (light blue); North, Central, and South America (AMER, dark blue); Asian Pacific States without China (APAC, yellow), China (orange); Middle East and Africa (MEA, green). B) Projected development of the global PV capacity with past years shown with grey scale bars, the minimum expectations shown with orange scale bars, maximum expectations shown with yellow scale bars and the medium expectations shown with a black line.[7]

1.2 Solar Cell Basics

To function in a solar cell, the absorber material needs to fulfil certain requirements. The most important precondition is that the material is a semiconductor. A semiconductor is defined as a material in which the conduction band (CB) and the valence band (VB) are separated by an energy gap of a defined energy. In the ground state, the valence band of the semiconductor is

completely filled, while the conduction band is completely empty, hence the semiconductor is not conductive. This state of non-conductivity can be disrupted by several processes. One possibility is called doping, where an impurity is inserted into the semiconducting material, either by adding an electron into the CB (n-doping) or a positively charged counterpart, an electron hole, into the VB (p-doping).[3,8]

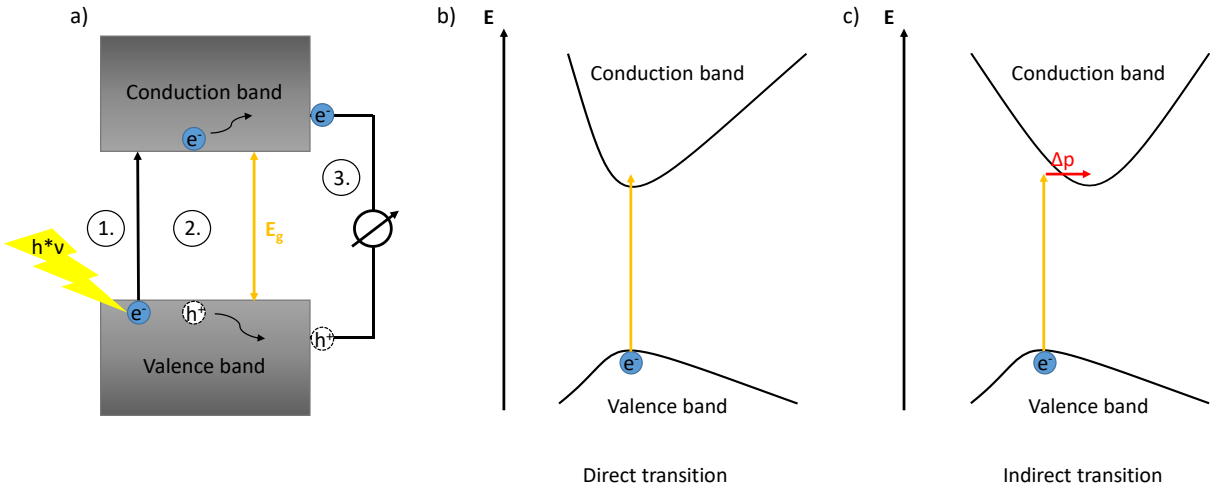

Figure 1.3: Schematic representation of the excitation process in a semiconductor and the principle of a direct bandgap and an indirect bandgap. a) Shows the process of electron excitation: 1. The electron is excited from the valence band into the conduction band by an external energy source, e.g., light. This process leaves behind a positively charged electron hole. 2. The electron and hole can move freely within their bands and are, in the case of a solar cell, in the third step extracted from the semiconductor via an external circuit. b) Shows the principle of an electron transition in a direct semiconductor and c) shows the same in an indirect semiconductor, where an additional momentum change of the electron is required to reach the conduction band minimum.

Another method is the excitation of an electron from the valence band into the conduction band, a process with which an electron hole is formed in the valence band (Figure 1.3 a). Unlike for insulators, the bandgap energy of a typical semiconductor in solar cells is small enough for an external energy source such as visible light to excite an electron. The energy required for the excitation process is dependent on the nature as well as the energy of the bandgap. The nature of the bandgap is determined by the position of the valence band maximum (VBM) relative to the position of the conduction band minimum (CBM). If the two extrema are located directly opposite to each other (in momentum space), the nature of the bandgap is direct and the electron can be excited solely by the incident light (Figure 1.3 b). If the two extrema are shifted to each other, an indirect bandgap is formed and the electron requires an additional momentum change

to be excited into the conduction band (Figure 1.3 c). Hence, the probability of an excitation is smaller for an indirect bandgap compared to the direct bandgap.[3,8] Once the electron is excited, both electron and electron hole can move freely within the CB and VB and can be extracted by an external circuit (Figure 1.3 a).

If we now bring an n-doped semiconductor in contact with a p-doped semiconductor, we build a p-n-junction, which is the simplest way to construct a solar cell. After contacting the two materials, the excess electrons from the n-doped region move towards the p-doped region, while the excess holes move along the opposite direction to bring the electrochemical potential of the junction into equilibrium. At the contact area, both charge carriers recombine and create a charge-free area, also called the depletion area. Due to the movement of the free charge carriers, fixed ion cores are left behind, whose potential difference builds up the so-called built-in potential, keeping the residual holes in the p-region and the residual electrons in the n-region in place. If now a positive external bias is applied, the charge carriers may get sufficient energy to cross the depletion region and therefore current flow is achieved.[8,9] The p-n junction is also referred to as a diode, which is the reason why ideal solar cells can be described using a simple diode model (Figure 1.4 a).

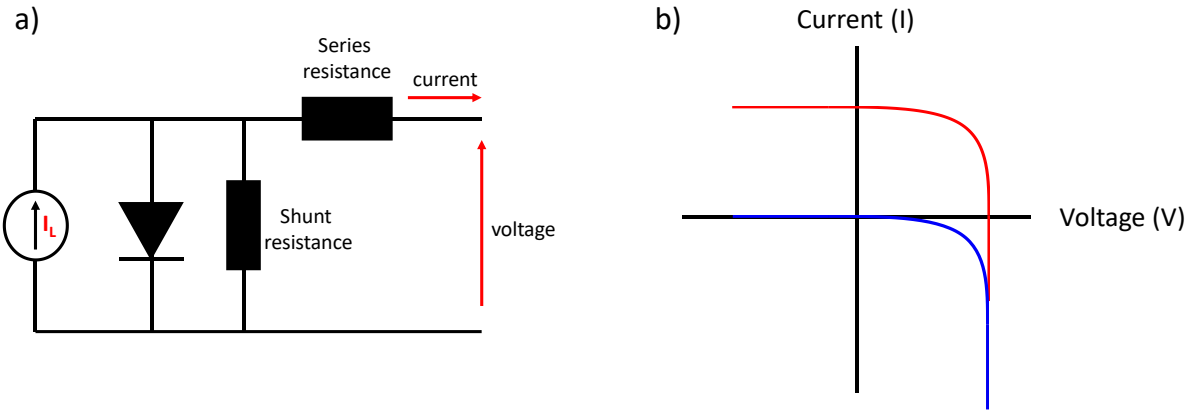

Figure 1.4: Schematic representation of a) the diode model of a solar cell and b) the *I/V* characteristics of such a diode in the dark (blue line) and under light illumination (red line).

If the junction is operated without light, the current flow will increase under forward bias conditions, while in reverse bias, the current flow will be small as shown in the corresponding current-voltage (*I/V*) curve in blue in Figure 1.4 b). The equation for the ideal diode applies:

$$I = I_0 \left(e^{\frac{qV}{kT}} - 1 \right) \tag{1.1}$$

Where I is the net current flowing through the diode, I_0 is the dark current, q is the electron charge, V is the applied voltage across the diode, k is Boltzmann's constant and T the absolute temperature in K.

If the junction is now illuminated, additional current is flowing and the current-voltage curve shows a large positive value along the I axis (red line in Figure 1.4 b). The diode equation transforms into the following:

$$I = I_L - I_0 \left(e^{\frac{qV}{kt}} - 1 \right) \tag{1.2}$$

Where I_L is the light-induced current.

However, in a real solar cell, resistances caused by interfaces or external contacts have to be taken into account, as can be seen in the diode model in Figure 1.4 a). The series resistance, for instance, reduces the overall current flow within the diode, while the shunt resistance influences the overall voltage of the diode as shown by equation (1.3):

$$I = I_L - I_0 \left(e^{\frac{q(V+IR_S)}{nkt}} \right) - \frac{V + IR_s}{R_{SH}} \tag{1.3}$$

Where R_{SH} is the shunt resistance and R_S is the series resistance.

The exact impact of those parameters on the solar cell performance will be further discussed in chapter 2.10.

So far, the photovoltaic market is dominated by silicon solar cells, since the power conversion efficiency (PCE) is already rather high in large-scale solar modules, the material is quite stable, and because of the great abundance of the precursor material SiO_2.[10,11] However, Si has an indirect bandgap, which requires rather thick layers to induce sufficient absorption, leading to the need for more material and demanding production methods to achieve the required high purity to reach sufficient charge carrier mobility. As a result, the production of Si-based solar cells is rather complicated and energy consuming, leading to time- and energy intensive processes.[11]

Therefore, several alternatives have been explored and developed in the past. As an example, thin film solar cells using cadmium telluride (CdTe) or copper indium gallium diselenide (CIGS) can compete with Si solar cells regarding the PCE while reducing the layer thickness by a factor of 10, however, they require the use of either rare (Te) or toxic (Cd, Se) metals and high vacuum and/or high temperature production.[12,13] Other approaches use dyes on large

bandgap semiconductors (DSSC) or large organic molecules (OPV) as absorber materials that address the requirement of low-cost materials and low-cost production methods. These materials can be solution processed and solar cells can be fabricated at low temperatures. This offers the possibility to produce solar cells on flexible substrates, even using a printer, making the production interesting for applications in windows and facades of buildings.[14,15] Yet, these kinds of solar cells are still somewhat limited in device performance and suffer from degradation, issues that however are of great interest in research and are on a fast way to be improved.[16–18]

In the last decade, a new class of solar cells entered the group of thin film photovoltaics: perovskite solar cells (PSCs). This type of solar cells has attracted great interest since their introduction in 2009, as they improved their lab-scale efficiency from 3.8 % to above 25 % in 2020, an increase for which Si-based solar cells needed about 50 years of development.[19,20] Being solution processable at low temperature, this kind of material holds big promises for low-cost, light weight and high performance, thus having the potential to revolutionize the photovoltaics market.[19–22]

1.3 Perovskite Solar Cells

Perovskites are chemical compounds with the formula ABX_3 that crystallize in a cubic closed packed structure in which the *B* cations build up the unit cells and are octahedrally surrounded by the *X* anions und thus have the coordination number 6. The large *A* cation has the coordination number 12 and sits in the voids generated by the BX_6-octahedra (Figure 1.5).[23]

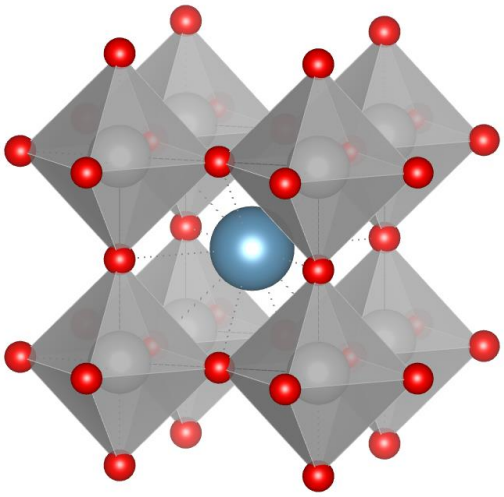

Figure 1.5: Schematic representation of the crystal structure of a perovskite: The A-cation is represented by the blue sphere, while the B cation is represented by the grey spheres. The X anions are shown as red spheres and build the octahedra surrounding each B cation.

All atomic sites can be occupied by a large variety of atoms whose ionic radii are in the optimal range to stabilize the structure. The stability of ABX_3 perovskite structures can be calculated using a tolerance factor t that was introduced by Goldschmidt:[24]

$$t = \frac{R_A + R_B}{\sqrt{2 * (R_B + R_X)}} \tag{1.4}$$

With R_A, R_B and R_X being the ionic radii of the respective ions.

For an ideal cubic perovskite structure, the tolerance factor equals 1. In general, perovskite structures are considered to be stable for a value of the tolerance factor of $0.81 < t < 1.11$.[25,26] However, it is well known for many compounds to form the desired structures only at elevated temperatures, although the tolerance factor is within the stable values. Methylammonium lead iodide for instance crystallizes in a tetragonal structure at room temperature and only forms and stabilizes its cubic phase upon heating.

1.3.1 Lead-Based Perovskites

For solar cell applications, perovskites with small organic cations such as methylammonium occupying the *A*-site, *B* = Lead (Pb) and *X* = Halogen atoms proved to be the most promising candidates. They form organic-inorganic hybrid perovskites and reach efficiencies of above 20 %. Especially methylammonium lead iodide ($MAPbI_3$) first described in 1978 can be seen as the archetype of halide perovskite solar cells, as this material exhibits excellent optoelectronic and charge carrier properties such as long charge carrier diffusion length and

lifetime, as well as a narrow direct bandgap and a high absorption coefficient.[27–30] Moreover, the properties of this materials can be easily tuned. By changing the composition of the *A*-ion with different organic or inorganic ions such as formamidinium (FA) or cesium (Cs), the stability and efficiency of the solar cells can be easily tuned,[25] while the bandgap energy of the resulting material is easily changed by variation of the halide anion *X* where the bandgap energy is reduced by going from chlorine to iodine.[31]

To function as a solar cell, the perovskite material needs to be brought into certain device-architectures. There are several possibilities, however all are based on the principle of sandwiching the active layer between two charge transport layers (hole-transport material, HTM and electron transport layer, ETL) and two electrodes to form a heterojunction as shown in Figure 1.6.[25]

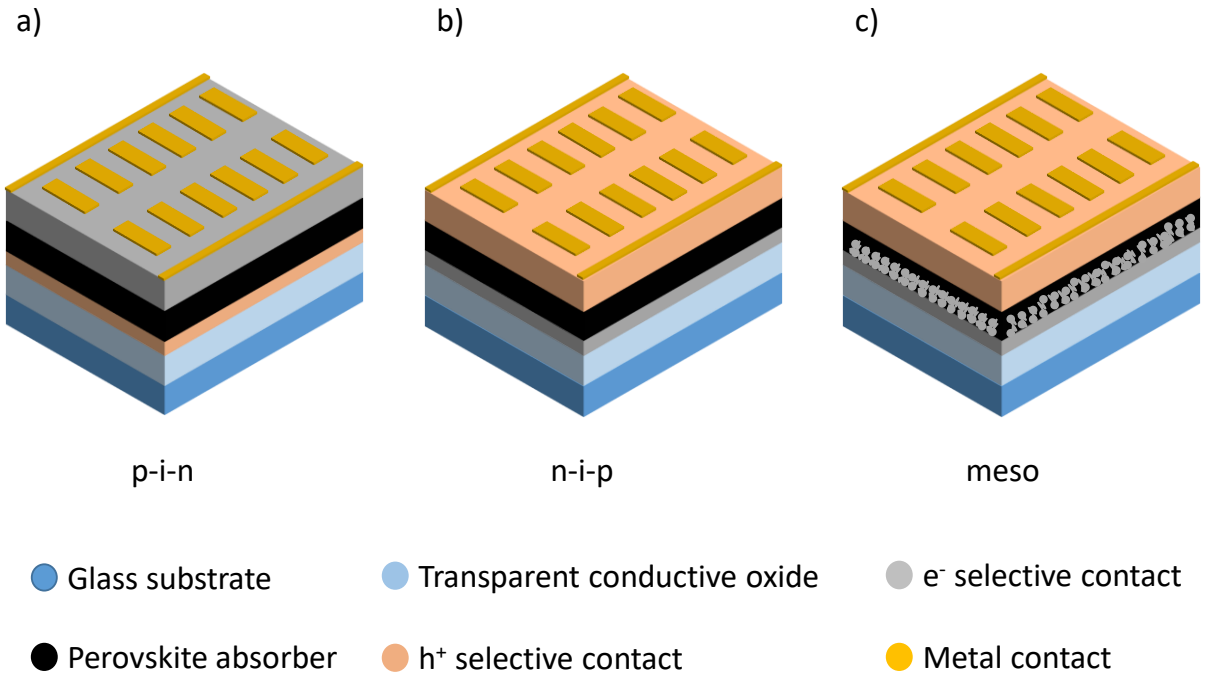

Figure 1.6: Schematic representation of different solar cell architectures. a) n-i-p junction, b) p-i-n junction and c) mesoporous structure.

For every architecture, the basic principle is the same: On top of a glass sheet, we have a transparent conductive oxide (TCO) as an electrode (usually indium doped tin oxide, ITO or fluorine doped tin oxide, FTO), followed by a charge transport layer (CTL) which is covered by the active layer. On top of the active layer, the second CTL is deposited, followed by the back electrode which is a metal (usually Gold, Silver or Aluminum). The architectures differ by the order of the CTLs starting from the glass substrate. A p-i-n junction is formed, if the

device architecture is glass/TCO/HTM/perovskite/ETL (Figure 1.6 a). An n-i-p junction is formed, if the architecture is glass/TCO/ETL/perovskite/HTM (Figure 1.6 b).[25,32] Another variation of the n-i-p junction is the mesoporous solar cell in which the ETL is a combination of a planar and mesoporous material (such as TiO_2), an architecture that yielded the most efficient perovskite solar cells in the beginning of lead halide perovskite research (Figure 1.6 c).[25,33,34]

To choose the right architecture for the respective perovskite, the energy levels of the different layers within the solar cell have to be taken into account.

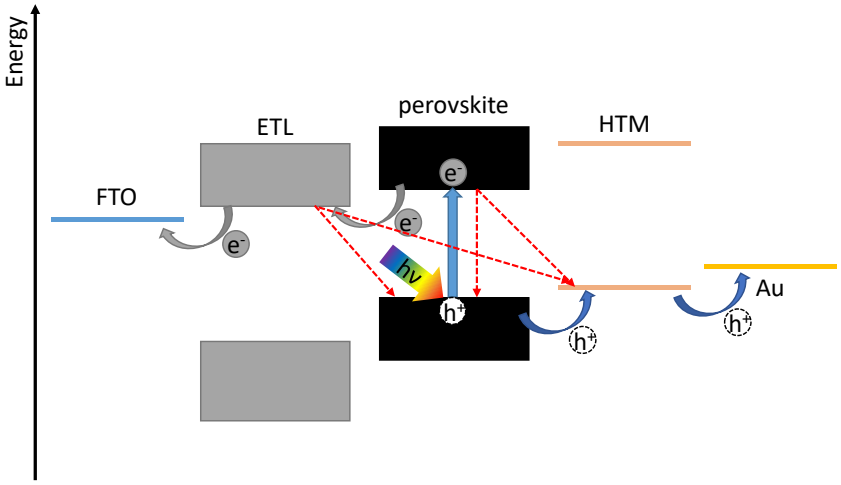

Figure 1.7: Schematic representation of an energy level diagram in a solar cell with the n-i-p architecture. Upon excitation, an electron is brought into the conduction band while an electron hole stays in the valence band. To prevent recombination (red arrows), the CTLs transport the charge carriers to the designated electrode using an energy cascade.

Figure 1.7 shows a schematic energy level diagram of a standard perovskite solar cell with methylammonium lead iodide as the active layer. Upon solar irradiation, an electron is excited from the valence band of the perovskite into the conduction band, leaving behind a positively charged electron hole for form an exciton. Depending on the binding energy between the electron and hole (exciton binding energy), the exciton dissociates into free charge carrier within picoseconds. To prevent the two free charge carriers from direct recombination, both need to be extracted at the respective electrodes (electron at the FTO electrode, electron hole at the Au electrode). To achieve efficient charge extraction, the respective charge carrier transporters are employed in the system to form an energy cascade that forces the charge carriers towards the designated contacts.[3,8]

By application of an ETL whose conduction band minimum (CBM) lays between the CBM of the perovskite and the FTO contact, the electron is efficiently conducted towards the respective electrode. By choosing an HTL with the energy of the valence band maximum (VBM) between the VBM of the perovskite and the energy of the back electrode, efficient hole-extraction is ensured. Note that typically organic HTMs are employed. Hence, we do not have a typical valence band but often more localized molecular orbitals. Therefore, the energy of the highest occupied molecular orbital (HOMO) of the HTM is used for the energy level alignment. Apart from transporting charges, the CTLs also block the countercharge in order to prevent unwanted recombination as indicated with the red dotted arrows in Figure 1.7. This is achieved by the valence band maximum of the ETL to block holes and the lowest unoccupied molecular orbital (LUMO) of the HTM to block the electrons. In the standard architecture, also used in this work, the ETL is TiO_2, while for the HTM either the small molecule Spiro-OMeTAD or the polymer P3HT is used.[35,36]

To reduce unwanted recombination, several figures of merit are important regarding the material. First, the charge carrier diffusion length needs to be considered. This figure gives the average distance a charge carrier can travel until it recombines.[8,25,29] The layer thickness of the absorber material needs to be smaller compared to this value to make sure, that most of the charge carriers can be extracted. The diffusion length depends on another important figure of merit, the charge carrier lifetime. This value gives the average time, the free charge carrier can exist until it recombines with a counter charge. With larger diffusion length and higher charge carrier lifetime, unwanted recombination (indicated by the dashed lines in Figure 1.7) is less likely and the charge carrier density remains high. The charge carrier density over time can be expressed by the following equation:[3,8]

$$\frac{dn}{dt} = -k_1 * n - k_2 * n^2 - k_3 * n^3 \qquad (1.5)$$

Where k_1 is the rate constant for monomolecular (trap assisted) recombination, k_2 is the rate constant for bimolecular (band-to-band) recombination and k_3 is the rate constant for recombination of higher order, e.g. Auger recombination.

1.3.2 Stability and Toxicity of Lead-Based Perovskites

Although being a serious competitor to Si based solar cells, lead-based perovskite solar cells suffer from drawbacks that have so far impeded industrial applications of this technology. Apart

from using severely toxic lead compounds, lead-based perovskite solar cells proved to be rather unstable against ambient conditions such as UV-irradiation, air and humidity.[37–41]

The mechanisms behind the cell degradation are manifold and can be induced by several factors, both intrinsically by the material itself and extrinsically, induced by the different layers within the solar cell. For one, the charge transport layers can have a major influence on the stability of the solar cells. Mesoporous TiO_2, for instance, is known to absorb UV light and can start degradation reactions within the lead-perovskite layer.[42] Another serious extrinsic degradation factor is the HTM, as these materials are known to form a glassy phase under thermal stress. Moreover, most HTMs require addition of dopant salts that are either hygroscopic or open a pathway for ion diffusion from the back electrode to the perovskite layer (Figure 1.8 a).[43–45] Hence, much research focuses on the development of both the ETL and HTMs, the latter being discussed later in this work.[21,45,46]

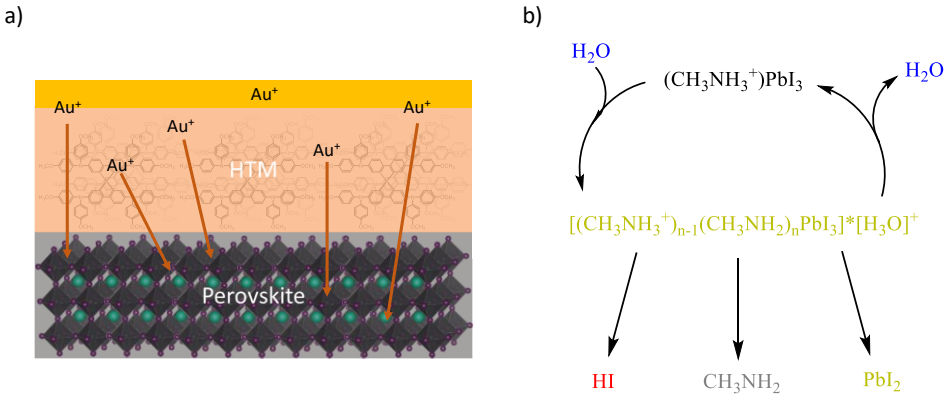

Figure 1.8: Schematic representation of possible degradation pathways: a) ion migration from the back electrode via the HTM toward the perovskite layer, b) degradation products by hydration of $MAPbI_3$.[47]

While the extrinsic stability can be tuned by intelligent design of the transport layers and the overall cell structure, the intrinsic stability can be changed by tuning the composition of the perovskite. Especially moisture is a major problem for lead-based perovskites since water molecules react with the perovskite to form HI, methyl amine and lead iodide, an effect that is accelerated by heat and illumination (Figure 1.8 b).[40,41,47] In addition to the humidity issue, UV light can break Pb-I bonds upon absorption, while the organic ammonium cations can become more reactive upon heating.[39,48,49]

It has been shown that tuning the composition of the *A*-site cation induces an increased stability of the resulting perovskite. Here, the introduction of formamidinium and/or cesium as a blend to MA increased the overall stability.[50–52] The reason can be found in the size of the cations,

stabilizing the black perovskite phase and suppressing the formation of the unwanted yellow perovskite phase. Moreover, it was found that the addition of Cs^+ to perovskites comprising FA^+ and MA^+ cations leads to the formation of larger crystallites within the thin films and reduces the trap density, as well as the charge recombination rates.[53,54]

Another approach, especially dealing with the issue of the low stability towards humidity, is the incorporation of large organic cations such as phenethylammonium (PEA^+) or fluorophenethyl ammonium (FEA^+) cations instead of Cs/FA/MA. This leads to a reduction of the dimensionality of the perovskite structure from 3D to 2D to form the so-called Ruddlesden-Popper phases, which results in a strong increase of the stability of the structure towards humidity (Figure 1.9). Moreover, large cations tend to be less reactive compared to their small counterparts and help reducing the stability issues originating from that side.[55–59]

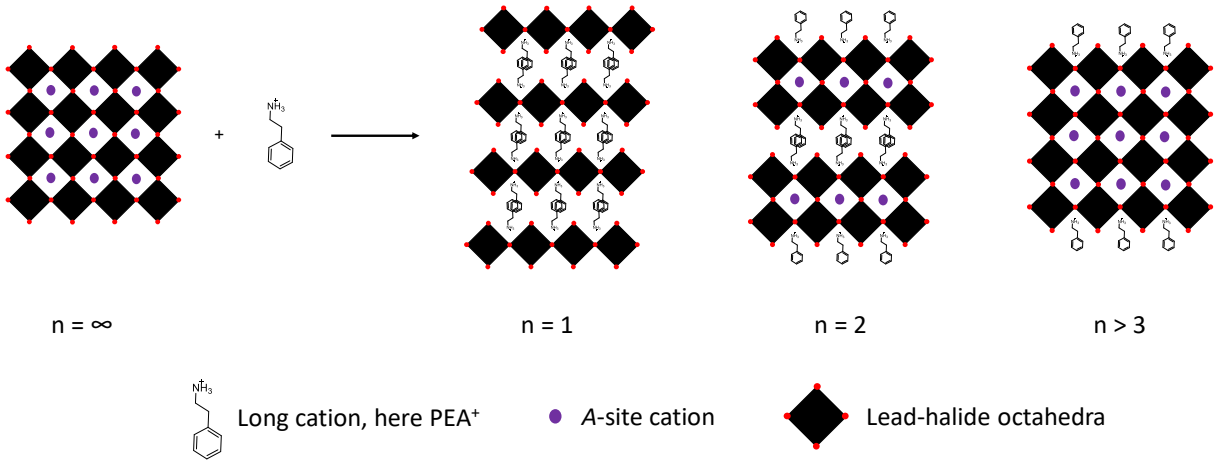

Figure 1.9: Schematic representation of the formation reaction of 2D perovskite with n = 1; n = 2 and n > 3. The black rhombi represent the lead-octahedra while the purple circles represent the A-site cation. The chemical structure shows a large cation, as example, the phenethylammonium cation (PEA^+) was chosen.

However, by reducing the dimension of the perovskite structure, not only the stability is enhanced, but also the bandgap of the resulting material is increased as well as the exciton binding energy, while the overall charge carrier dynamics are hampered due to the insulating barrier inserted with the large organic cation, thus leading to a severely reduced PV performance.[55,59,60] For lead-based perovskites, a large variety of different organic cations was used so far in this context, providing the possibility to tune the distance between the octahedral layers. An important figure of merit is the n-value, which gives the number of octahedral layers that are connected to each other. For an n-value of 1, no octahedral layer is connected to another

one but isolated by an organic layer and a pure 2D perovskite is formed (Figure 1.9). For n values >3, a 'quasi-2D' perovskite is formed (Figure 1.9), while for n = ∞, a 3D perovskite results.[55,59,60]

While the rather low PCE in 2D perovskite solar cells compared to their 3D counterparts suggests a large trade-off between stability and power output, recent research showed that a combination of both principles does not only increase the stability of the resulting solar cells, but also showed the potential to increase the overall efficiency of the perovskite solar cells by forming 2D/3D bilayer perovskite solar cells, in the following called 2D/3D hybrid perovskites. Here, a thin layer of a 2D perovskite is formed on top of the surface of the 3D perovskite to form a capping layer to combine the outstanding optoelectronic properties of the 3D perovskite with the stabilizing effect of the 2D perovskite. One factor boosting the performance compared to the pure 3D perovskite is a passivating effect of the 2D layer, hence leading to a reduction of the trap density on the surface and therefore less unwanted recombination. To achieve a hybrid perovskite film, the 3D films were either immersed in a solution of the long cation, or the same solution was deposited on top of the 3D layer, initializing the 2D-perovskite formation.[56,61–63]

1.3.3 Lead-Free Double Perovskites

While the stability issues of lead-based perovskites can in principle be overcome by either encapsulation of the devices or tuning of the composition of the *A*-site cation, the toxicity can only be reduced by substitution of the lead atoms. The first approach to do so was the substitution with elements of the same group while retaining basically the same perovskite structure. Due to the beneficial optoelectronic properties of Sn-based perovskites, solar cells comprising this material soon reached efficiencies of up to 13 %.[64] However, Sn^{2+} ions are rather unstable towards air as they readily oxidize to Sn^{4+}, which leads to a fast degradation of the solar cells employing this material. Hence, again complicated encapsulation is necessary for these solar cells to ensure sufficient device stability.[65–67]

Another approach was to substitute two lead ions with the total charge of +4 within the perovskite lattice with a monovalent metal cation and a trivalent cation to expand the perovskite structure and form a double perovskite with the chemical formula $A_2M^{I+}M^{III+}X_6$ (Figure 1.10). In the general double perovskite structure, the lead atoms are substituted by alternating monovalent and trivalent cations as shown in Figure 1.10 with Ag^+ and Bi^{3+}. These two

substitutes are both octahedrally surrounded by the halide anions while the *A*-site cation (here Cs^+) is located in the resulting voids and retains the coordination number 12.

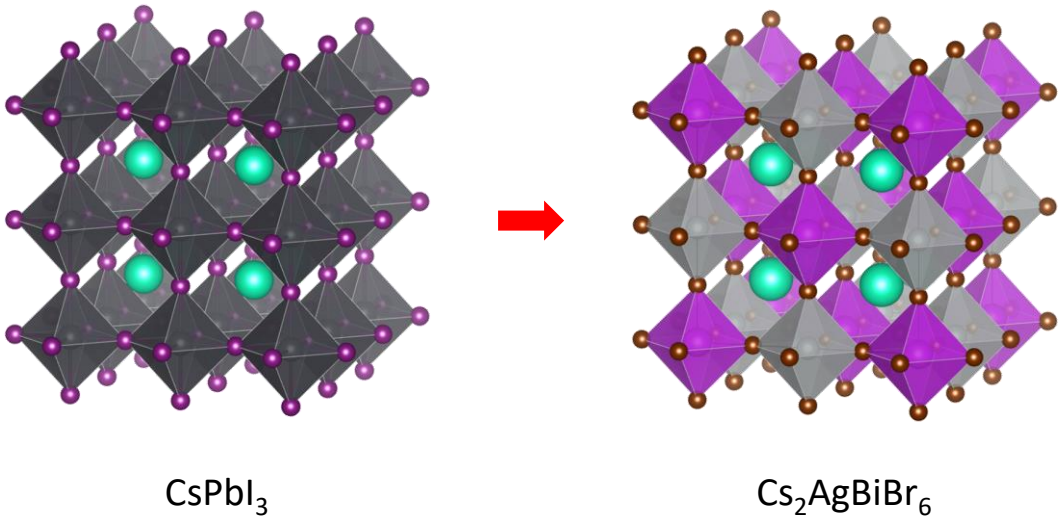

Figure 1.10: Comparison of a 2x2x2 crystal super-cell of the $CsPbI_3$ perovskite and the corresponding structure of the $Cs_2AgBiBr_6$ double perovskite. The black octahedra are the lead-octahedra, built up by purple iodine atoms. The purple octahedra are with Bi^{3+} acting as center atom and the grey octahedra with Ag^+ acting as center atom. The brown spheres are bromine atoms while the turquoise spheres are cesium atoms.

Several different compounds have been synthesized already, including Bi^{3+} or Sb^{3+} as trivalent cations and Ag^+, In^+, Cu^+ or Au^+ as monovalent cations.[68–73] Among all these combinations, $Cs_2AgBiBr_6$ (first synthesized by McClure et al.[74]) appears to be one of the promising candidates to compete with lead-based halide perovskites. This material proved to be thermodynamically stable[75–77] and shows promising optoelectronic properties such as a rather high charge carrier lifetime ranging from >200 ns in a thin film to 500 ns in a single crystal.[78–80] Moreover, this material fulfils the requirement of low toxicity and shows significant stability towards humidity and air. Theoretical calculations show rather small effective masses for holes and electrons which should translate into good charge carrier dynamics.[75–77] The material is solution processable and can hence be synthesized rather easily, factors that have enabled solar cell production in various ways to exceed a PCE of 3 % within only a few years.[79,81–83]

However, $Cs_2AgBiBr_6$ also suffers from several drawbacks, hampering a fast development of high-performance solar cells. Hence, a lot of research interest has emerged to identify the bottlenecks of this material, to be able to overcome them, and to boost the efficiency of $Cs_2AgBiBr_6$ solar cells.

The material has a rather large and indirect bandgap between 1.9 eV and 2.3 eV which implies that single-junction cells cannot be expected to provide maximum PCE as predicted by the Shockley-Queisser limit.[79,84–88] The potential performance is further compromised by a rather low electron diffusion length, accompanied by a high trap density and a large exciton binding energy.[86,89,90] Moreover, self-trapping events of charge carriers have been observed,[91] that have been also described as the ultrafast localization of a band-like polaron or the formation of color-centers and have been attributed to a large electron-phonon coupling.[92,93]

While tracking down these bottlenecks may provide possible pathways to further improve the thin film quality of $Cs_2AgBiBr_6$ solar cells and may eventually lead to an improvement of the overall efficiency, the large bandgap and therefore the expected small photocurrent remain issues to be addressed.

While tunability of the large bandgap is desired, it can only be influenced by significant efforts such as high pressure or low temperature where the compound also undergoes a phase-transition,[94,95] or *via* doping and/or alloying.[96–98] Changing the bandgap *via* halide-exchange has not been realized so far, as three-dimensional Cs_2AgBiI_6 is thermodynamically unstable owing to both Goldschmidt's tolerance factor and the high stability of the competing ternary $Cs_3Bi_2I_9$ phase.[99]

However, in order to stabilize the iodine phase of the Bi based double perovskite, the incorporation of a long cation was investigated to form a low-dimensional material, similar to lead-based materials as described in Section 1.3.1. While Connor et al. first introduced low-dimensional double perovskites in 2018, using standard large cations such as butylammonium bromide to investigate the influence on the bandgap to switch from indirect to direct,[100] Jana et al. used a large oligothiophene as spacer cation to stabilize, with $[AE2T]_2AgBiI_8$, the first Ag-Bi double perovskite with iodine, which expresses a direct bandgap with a reduced energy of 2.0 eV.[101] Several other studies were published afterwards, realizing the stabilization of the iodine compound, however struggling to form thin films with good morphology and promising charge carrier dynamics.[102–104]

All the above-mentioned properties and synthetic possibilities make the Ag-Bi double perovskite one of the more promising candidates to compete with lead-based perovskites in the long run. Even though the solar cell efficiency will not reach the same heights as their lead-based relatives, the Ag-Bi double perovskite is very attractive for investigations due to the unique behavior regarding absorption, emission and charge carrier properties. Even if the

theoretical efficiency maximum of around 8 %[105] might not be reached, this material system gives the great opportunity to gain insights in the very unique photophysics (e.g. relation between absorption and emission) and materials' physics, as well as the chemical challenges of device engineering of unknown materials with non-optimal chemical properties in terms of solubility and processing. These challenges help to develop improvement strategies for future systems such as the promising material Cu_2AgBiI_6, where so far only the material but no thin films or devices were reported.[106]

If not for solar cells, the optoelectronic properties of $Cs_2AgBiBr_6$ do qualify this material for a number of different applications. Especially the high stability and the large number of heavy elements makes it interesting for detector applications, hence several reports were published investigating $Cs_2AgBiBr_6$ amongst others as an X-ray photon absorber material.[107–109]

1.4 Hole-Transporting Materials

As already mentioned, much research effort has been dedicated to the development of new hole-transporting materials. The reasons are manifold, especially since intelligent design of the HTM layer can create possibilities to simultaneously enhance the efficiency and stability of the resulting solar cells.[21,110–113]

1.4.1 State-of-the-Art Materials

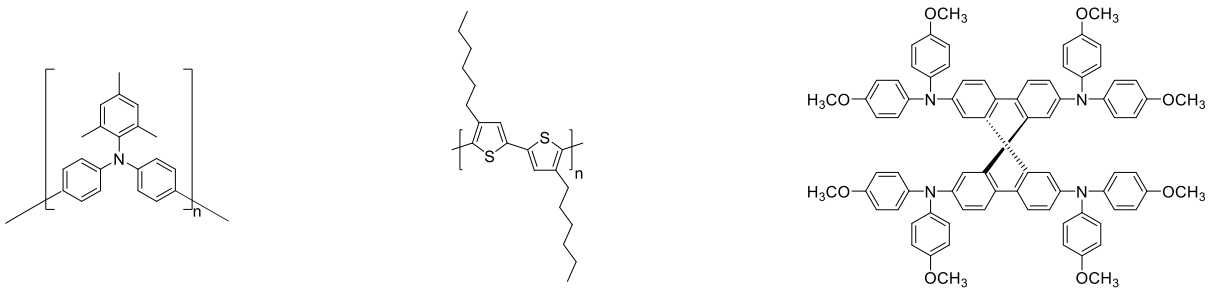

PTAA P3HT Spiro-OMeTAD

Figure 1.11: State-of-the-art HTMs that are most commonly used in perovskite solar cells: poly-[bis-(4-phenyl)-2,4,5-trimethylphenyl)-amin] (PTAA), poly(3-hexylthiophen-2,5-diyl) (P3HT) and 2,2',7,7'-tetrakis-9,9'-spirobifluorene (Spiro-OMeTAD).

Figure 1.11 shows the chemical structure of the current state-of-the-art HTMs poly-[bis-(4-phenyl)-2,4,5-trimethylphenyl)-amin] (PTAA), poly(3-hexylthiophen-2,5-diyl) (P3HT) and 2,2',7,7'-tetrakis-9,9'-spirobifluorene (Spiro-OMeTAD). The materials prove to achieve very

high efficiencies when employed in perovskite solar cells, both lead-based and lead-free as described in sections 1.3.1 and 1.3.3. Especially Spiro-OMeTAD is used for prototype solar cells because of its well-studied properties and performance.

To function as an HTM, several requirements need to be fulfilled. As discussed in Section 1.3.1, the HOMO energy level of the material has to lie between the VBM of the perovskite and the back electrode. Also, the LUMO needs to be high enough to efficiently block electrons. The HTM should provide sufficient conductivity, as well as hole-mobility and the bandgap of the material should be large enough to avoid parasitic absorption losses within the solar cell. Additionally, the material should be soluble in common organic solvents and feature a high thermal and ambient stability.[45] The HTMs shown in Figure 1.11 fulfil several of these requirements, foremost the energy level alignment. However, they also suffer from several drawbacks such as a rather low conductivity that has to be increased by the addition of some additives, mostly lithium bis(trifluoromethanesulfonyl)imide (LiTFSI), which is known to be rather hygroscopic and may induce hydration of the solar cell, as well as ion migration.[35,36,45] Another issue that arises, is the rather poor film formation of the HTMs described above and a relatively small bandgap that might cause parasitic light absorption of photons reflected from the back electrode.

The largest drawback of these HTMs, however, is the extremely high cost at which these molecules and polymers are synthesized. In case of Spiro-OMeTAD, the synthesis is rather complicated and requires several purification steps including column chromatography and chlorinated solvents. Especially the use of the chlorinated solvents is viewed as unsuitable regarding the environmental impact.[21,35,36]

1.4.2 Alternative Materials

To address the issues discussed, much effort has been put into the design and development of new and low-cost HTMs that may increase the stability as well as the performance of the resulting solar cells.[45] In the last couple of years, several promising small molecules and inorganic HTMs have been published, several originating from our laboratories and shown in Figure 1.12.

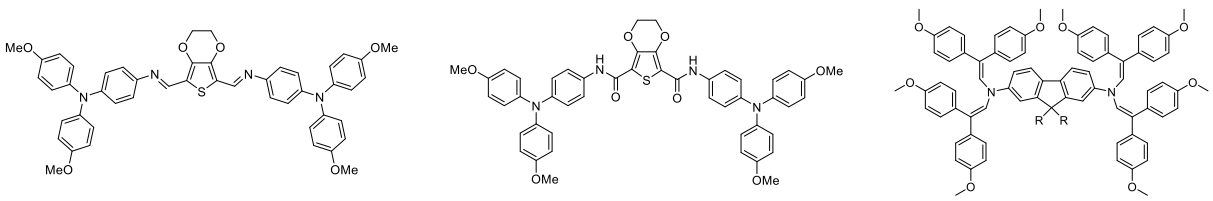

Figure 1.12: Chemical structure of low-cost HTM alternatives: Azomethine-based HTMs with the example of EDOT-OMeTPA, amide-based HTMs with the example of EDOT-Amide-TPA, both published by this group[35,36] and fluorene-based HTMs.[113]

The simplest way to reduce the cost factor in the synthesis of organic HTMs is the reduction of synthesis steps, as well as the synthesis itself. Especially condensation chemistry opened a pathway for low-cost synthesis of organic small molecules as it was done for EDOT-Amide-TPA and azomethine- or fluorene-based HTMs (Figure 1.12).[36,110,112,113] This technology further avoids excessive purification efforts by only using recrystallization processes or sublimation, and the HTMs synthesized this way show the great potential to not only compete but to possibly outperform the state-of-the-art materials.

In the search for alternative HTMs, additional requirements were addressed. Hence, not only the efficiency or cost-factor have been focused on, but also the molecular design is of great importance. By choosing different functional groups, organic HTMs show the potential to protect the active layer from external influences such as hydration and additionally can passivate surface trap states of the same. Moreover, a lot of effort was put into the development of dopant-free HTMs in order to rule out a possible acceleration of perovskite degradation due to the hydrophilicity of common HTM additives.[114–116]

1.5 Outline of the Thesis

In this work, the double perovskite $Cs_2AgBiBr_6$ was investigated as an alternative to lead-based perovskites for photovoltaic applications.

In Chapter 3, we investigated the performance-limiting factors of complete solar cells comprising this material as absorber in order to attack these issues and push the efficiency of $Cs_2AgBiBr_6$-solar cells closer toward the theoretical limit. The chapter describes the link between radiative V_{OC} losses within the cells and the ionic behavior of the solar cells which was determined by the measurement of electroluminescence (EL) and the external quantum efficiency (EQE).

In Chapter 4, we describe the influence of the precursor stoichiometry on the optoelectronic and structural properties of $Cs_2AgBiBr_6$ thin films. To understand the structural changes, we used grazing incident wide angle X-ray scattering (GIWAXS) measurements to show a change in crystallite orientation within the thin films. We moreover show a change in the optoelectronic properties of the thin film using photoluminescence (PL) measurements both time-resolved (TRPL) and in steady state mode.

In Chapter 5, we investigated the synthesis of 2D/3D hybrid double perovskites by using phenethyl ammonium bromide (PEABr) as a spacer cation in thin films. We first synthesized the pure 2D compound $(PEA)_4AgBiBr_4$ and afterwards developed a reproducible synthesis protocol for 2D/3D hybrid perovskite thin films to investigate the impact of the 2D layer on the performance of double perovskite solar cells, showing for the first time a working device using this architecture with improved optoelectronic properties, as well as power-conversion efficiency.

Chapter 6 describes the effect of different hole-transporting materials (HTM) on the efficiency of the perovskite solar cells, as well as the origin of the improvement of the solar cells. To investigate the changes in the efficiency, as well as the stability of the resulting solar cells, we used impedance spectroscopy (EIS), XPS and HRTEM measurements. We optimized the deposition of the HTM EDOT-Amide-TPA and revealed a large impact of the HTM on the solar cell efficiency.

1.6 References

[1] International Energy Agency, *World Energy Outlook 2020* **2021**.

[2] M. Höök, X. Tang, *Energy Policy* **2013**, *52*, 797.

[3] P. Würfel, U. Würfel, *Physics of solar cells: From basic principles to advanced concepts*, Wiley-VCH, Weinheim **2010**.

[4] R. Perez, M. Perez **2009**.

[5] R. Perez, M. Perez **2015**.

[6] A. Jäger-Waldau, *JRC EU Science Hub PV Status Report 2019* **2019**.

[7] SolarPower Europe, *Global Market Outlook 2020-2024*.

[8] W. Tress, *Organic solar cells: Theory, experiment, and device simulation*, Springer Science and Business Media, New York **2014**.

[9] D. S. Ginley, D. Cahen, *Fundamentals of materials for energy and environmental sustainability*, Cambridge Univ. Press, New York **2012**.

[10] L. Wu, Z. Yang, Y. Cheng, Z. Lu, P. Zhang, M. Zhao, R. Gong, X. Yuan, Y. Zheng, J. Duan, *Optics express* **2013**, *21*, 5239.

[11] M. Gratzel, *Nature* **2001**, *414*, 338.

[12] Nakamura M., Yamaguchi K., Kimoto Y., Yasaki Y., Kato T., Sugimoto H., *IEEE Journal of Photovoltaics* **2019**, https://www.solar-frontier.com/eng/news/2019/0117_press.html.

[13] F. Solar, *Press release, https://investor. firstsolar. com/news/press-release-details/2014/First-Solar-Builds-the-Highest-Efficiency-Thin-Film-PV-Cell-on-Record/default. aspx* **2014**.

[14] C. N. Hoth, P. Schilinsky, S. A. Choulis, C. J. Brabec, *Nano letters* **2008**, *8*, 2806.

[15] F. C. Krebs, *Solar Energy Materials and Solar Cells* **2009**, *93*, 394.

[16] A. Distler, C. J. Brabec, H.-J. Egelhaaf, *Prog Photovolt Res Appl* **2021**, *29*, 24.

[17] X. Du, T. Heumueller, W. Gruber, A. Classen, T. Unruh, N. Li, C. J. Brabec, *Joule* **2019**, *3*, 215.

[18] X. Xu, J. Xiao, G. Zhang, L. Wei, X. Jiao, H.-L. Yip, Y. Cao, *Science Bulletin* **2020**, *65*, 208.

[19] A. Kojima, K. Teshima, Y. Shirai, T. Miyasaka, *Journal of the American Chemical Society* **2009**, *131*, 6050.

[20] M. Jeong, I. W. Choi, E. M. Go, Y. Cho, M. Kim, B. Lee, S. Jeong, Y. Jo, H. W. Choi, J. Lee, J.-H. Bae, S. K. Kwak, D. S. Kim, C. Yang, *Science (New York, N.Y.)* **2020**, *369*, 1615.

[21] M. L. Petrus, J. Schlipf, C. Li, T. P. Gujar, N. Giesbrecht, P. Müller-Buschbaum, M. Thelakkat, T. Bein, S. Hüttner, P. Docampo, *Adv. Energy Mater.* **2017**, *7*, 1700264.

[22] M. Green, E. Dunlop, J. Hohl-Ebinger, M. Yoshita, N. Kopidakis, X. Hao, *Prog. Photovolt. Res. Appl.* **2021**, *29*, 3.

[23] U. Müller, *Anorganische Strukturchemie*, Vieweg + Teubner, Wiesbaden **2009**.

[24] V. M. Goldschmidt, *Naturwissenschaften* **1926**, *14*, 477.

[25] J.-P. Correa-Baena, M. Saliba, T. Buonassisi, M. Grätzel, A. Abate, W. Tress, A. Hagfeldt, *Science (New York, N.Y.)* **2017**, *358*, 739.

[26] T. Jesper Jacobsson, J.-P. Correa-Baena, M. Pazoki, M. Saliba, K. Schenk, M. Grätzel, A. Hagfeldt, *Energy Environ. Sci.* **2016**, *9*, 1706.

[27] S. de Wolf, J. Holovsky, S.-J. Moon, P. Löper, B. Niesen, M. Ledinsky, F.-J. Haug, J.-H. Yum, C. Ballif, *The journal of physical chemistry letters* **2014**, *5*, 1035.

[28] S. Sun, T. Salim, N. Mathews, M. Duchamp, C. Boothroyd, G. Xing, T. C. Sum, Y. M. Lam, *Energy Environ. Sci.* **2014**, *7*, 399.

[29] S. D. Stranks, G. E. Eperon, G. Grancini, C. Menelaou, M. J. P. Alcocer, T. Leijtens, L. M. Herz, A. Petrozza, H. J. Snaith, *Science (New York, N.Y.)* **2013**, *342*, 341.

[30] F. Deschler, M. Price, S. Pathak, L. E. Klintberg, D.-D. Jarausch, R. Higler, S. Hüttner, T. Leijtens, S. D. Stranks, H. J. Snaith, M. Atatüre, R. T. Phillips, R. H. Friend, *The journal of physical chemistry letters* **2014**, *5*, 1421.

[31] Y. Tong, E. Bladt, M. F. Aygüler, A. Manzi, K. Z. Milowska, V. A. Hintermayr, P. Docampo, S. Bals, A. S. Urban, L. Polavarapu, J. Feldmann, *Angewandte Chemie (International ed. in English)* **2016**, *55*, 13887.

[32] N. J. Jeon, J. H. Noh, Y. C. Kim, W. S. Yang, S. Ryu, S. I. Seok, *Nature materials* **2014**, *13*, 897.

[33] J.-P. Correa-Baena, A. Abate, M. Saliba, W. Tress, T. Jesper Jacobsson, M. Grätzel, A. Hagfeldt, *Energy Environ. Sci.* **2017**, *10*, 710.

[34] M. Saliba, J.-P. Correa-Baena, M. Grätzel, A. Hagfeldt, A. Abate, *Angewandte Chemie (International ed. in English)* **2018**, *57*, 2554.

[35] M. L. Petrus, K. Schutt, M. T. Sirtl, E. M. Hutter, A. C. Closs, J. M. Ball, J. C. Bijleveld, A. Petrozza, T. Bein, T. J. Dingemans, T. J. Savenije, H. Snaith, P. Docampo, *Adv. Energy Mater.* **2018**, *8*, 1801605.

[36] M. L. Petrus, A. Music, A. C. Closs, J. C. Bijleveld, M. T. Sirtl, Y. Hu, T. J. Dingemans, T. Bein, P. Docampo, *J. Mater. Chem. A* **2017**, *5*, 25200.

[37] A. Binek, M. L. Petrus, N. Huber, H. Bristow, Y. Hu, T. Bein, P. Docampo, *ACS applied materials & interfaces* **2016**, *8*, 12881.

[38] A. M. A. Leguy, Y. Hu, M. Campoy-Quiles, M. I. Alonso, O. J. Weber, P. Azarhoosh, M. van Schilfgaarde, M. T. Weller, T. Bein, J. Nelson, P. Docampo, P. R. F. Barnes, *Chem. Mater.* **2015**, *27*, 3397.

[39] M. L. Petrus, Y. Hu, D. Moia, P. Calado, A. M. A. Leguy, P. R. F. Barnes, P. Docampo, *ChemSusChem* **2016**, *9*, 2699.

[40] J. Yang, B. D. Siempelkamp, D. Liu, T. L. Kelly, *ACS nano* **2015**, *9*, 1955.

[41] R. J. Sutton, G. E. Eperon, L. Miranda, E. S. Parrott, B. A. Kamino, J. B. Patel, M. T. Hörantner, M. B. Johnston, A. A. Haghighirad, D. T. Moore, H. J. Snaith, *Adv. Energy Mater.* **2016**, *6*, 1502458.

[42] S.-W. Lee, S. Kim, S. Bae, K. Cho, T. Chung, L. E. Mundt, S. Lee, S. Park, H. Park, M. C. Schubert, S. W. Glunz, Y. Ko, Y. Jun, Y. Kang, H.-S. Lee, D. Kim, *Scientific reports* **2016**, *6*, 38150.

[43] S. Cacovich, L. Ciná, F. Matteocci, G. Divitini, P. A. Midgley, A. Di Carlo, C. Ducati, *Nanoscale* **2017**, *9*, 4700.

[44] K. Domanski, J.-P. Correa-Baena, N. Mine, M. K. Nazeeruddin, A. Abate, M. Saliba, W. Tress, A. Hagfeldt, M. Grätzel, *ACS nano* **2016**, *10*, 6306.

[45] X. Yin, Z. Song, Z. Li, W. Tang, *Energy Environ. Sci.* **2020**, *13*, 4057.

[46] K. Valadi, S. Gharibi, R. Taheri-Ledari, S. Akin, A. Maleki, A. E. Shalan, *Environ Chem Lett* **2021**, *19*, 2185.

[47] J. M. Frost, K. T. Butler, F. Brivio, C. H. Hendon, M. van Schilfgaarde, A. Walsh, *Nano letters* **2014**, *14*, 2584.

[48] Y. Li, X. Xu, C. Wang, B. Ecker, J. Yang, J. Huang, Y. Gao, *J. Phys. Chem. C* **2017**, *121*, 3904.

[49] S. Wang, Y. Jiang, E. J. Juarez-Perez, L. K. Ono, Y. Qi, *Nat Energy* **2017**, *2*.

[50] A. Binek, F. C. Hanusch, P. Docampo, T. Bein, *The journal of physical chemistry letters* **2015**, *6*, 1249.

[51] N. Pellet, P. Gao, G. Gregori, T.-Y. Yang, M. K. Nazeeruddin, J. Maier, M. Grätzel, *Angewandte Chemie (International ed. in English)* **2014**, *53*, 3151.

[52] O. J. Weber, B. Charles, M. T. Weller, *J. Mater. Chem. A* **2016**, *4*, 15375.

[53] Y. Hu, E. M. Hutter, P. Rieder, I. Grill, J. Hanisch, M. F. Aygüler, A. G. Hufnagel, M. Handloser, T. Bein, A. Hartschuh, K. Tvingstedt, V. Dyakonov, A. Baumann, T. J. Savenije, M. L. Petrus, P. Docampo, *Adv. Energy Mater.* **2018**, *8*, 1703057.

[54] C. Yi, J. Luo, S. Meloni, A. Boziki, N. Ashari-Astani, C. Grätzel, S. M. Zakeeruddin, U. Röthlisberger, M. Grätzel, *Energy Environ. Sci.* **2016**, *9*, 656.

[55] P. Liu, N. Han, W. Wang, R. Ran, W. Zhou, Z. Shao, *Advanced materials (Deerfield Beach, Fla.)* **2021**, *33*, e2002582.

[56] J. Schlipf, Y. Hu, S. Pratap, L. Bießmann, N. Hohn, L. Porcar, T. Bein, P. Docampo, P. Müller-Buschbaum, *ACS Appl. Energy Mater.* **2019**, *2*, 1011.

[57] K. Zheng, Y. Chen, Y. Sun, J. Chen, P. Chábera, R. Schaller, M. J. Al-Marri, S. E. Canton, Z. Liang, T. Pullerits, *J. Mater. Chem. A* **2018**, *6*, 6244.

[58] M. Li, W.-W. Zuo, Y.-G. Yang, M. H. Aldamasy, Q. Wang, S. H. T. Cruz, S.-L. Feng, M. Saliba, Z.-K. Wang, A. Abate, *ACS Energy Lett.* **2020**, *5*, 1923.

[59] Y. Chen, Y. Sun, J. Peng, J. Tang, K. Zheng, Z. Liang, *Advanced materials (Deerfield Beach, Fla.)* **2018**, *30*.

[60] A. Krishna, S. Gottis, M. K. Nazeeruddin, F. Sauvage, *Adv. Funct. Mater.* **2019**, *29*, 1806482.

[61] Z. Wang, Q. Lin, F. P. Chmiel, N. Sakai, L. M. Herz, H. J. Snaith, *Nat Energy* **2017**, *2*.

[62] Y. Hu, J. Schlipf, M. Wussler, M. L. Petrus, W. Jaegermann, T. Bein, P. Müller-Buschbaum, P. Docampo, *ACS Nano* **2016**, *10*, 5999.

[63] Y. Liu, S. Akin, L. Pan, R. Uchida, N. Arora, J. V. Milić, A. Hinderhofer, F. Schreiber, A. R. Uhl, S. M. Zakeeruddin, A. Hagfeldt, M. I. Dar, M. Grätzel, *Sci. Adv.* **2019**, *5*, eaaw2543.

[64] K. Nishimura, M. A. Kamarudin, D. Hirotani, K. Hamada, Q. Shen, S. Iikubo, T. Minemoto, K. Yoshino, S. Hayase, *Nano Energy* **2020**, *74*, 104858.

[65] E. W.-G. Diau, E. Jokar, M. Rameez, *ACS Energy Lett.* **2019**, *4*, 1930.

[66] Q. Tai, X. Guo, G. Tang, P. You, T.-W. Ng, D. Shen, J. Cao, C.-K. Liu, N. Wang, Y. Zhu, C.-S. Lee, F. Yan, *Angewandte Chemie (International ed. in English)* **2019**, *58*, 806.

[67] Z. Yang, M. Zhong, Y. Liang, L. Yang, X. Liu, Q. Li, J. Zhang, D. Xu, *Adv. Funct. Mater.* **2019**, *29*, 1903621.

[68] Z. Xiao, K.-Z. Du, W. Meng, J. Wang, D. B. Mitzi, Y. Yan, *Journal of the American Chemical Society* **2017**, *139*, 6054.

[69] F. Wei, Z. Deng, S. Sun, F. Zhang, D. M. Evans, G. Kieslich, S. Tominaka, M. A. Carpenter, J. Zhang, P. D. Bristowe, A. K. Cheetham, *Chem. Mater.* **2017**, *29*, 1089.

[70] G. Volonakis, A. A. Haghighirad, H. J. Snaith, F. Giustino, *J. Phys. Chem. Lett.* **2017**, *8*, 3917.

[71] G. Volonakis, A. A. Haghighirad, R. L. Milot, W. H. Sio, M. R. Filip, B. Wenger, M. B. Johnston, L. M. Herz, H. J. Snaith, F. Giustino, *The journal of physical chemistry letters* **2017**, *8*, 772.

[72] Z. Li, S. R. Kavanagh, M. Napari, R. G. Palgrave, M. Abdi-Jalebi, Z. Andaji-Garmaroudi, D. W. Davies, M. Laitinen, J. Julin, M. A. Isaacs, R. H. Friend, D. O. Scanlon, A. Walsh, R. L. Z. Hoye, *J. Mater. Chem. A* **2020**, *8*, 21780.

[73] N. Glück, T. Bein, *Energy Environ. Sci.* **2020**, *13*, 4691.

[74] E. T. McClure, M. R. Ball, W. Windl, P. M. Woodward, *Chem. Mater.* **2016**, *28*, 1348.

[75] Z. Xiao, W. Meng, J. Wang, Y. Yan, *ChemSusChem* **2016**, *9*, 2628.

[76] M. R. Filip, X. Liu, A. Miglio, G. Hautier, F. Giustino, *J. Phys. Chem. C* **2018**, *122*, 158.

[77] M. R. Filip, S. Hillman, A. A. Haghighirad, H. J. Snaith, F. Giustino, *J. Phys. Chem. Lett.* **2016**, *7*, 2579.

[78] A. H. Slavney, T. Hu, A. M. Lindenberg, H. I. Karunadasa, *J. Am. Chem. Soc.* **2016**, *138*, 2138.

[79] E. Greul, M. L. Petrus, A. Binek, P. Docampo, T. Bein, *J. Mater. Chem. A* **2017**, *5*, 19972.

[80] R. L. Z. Hoye, L. Eyre, F. Wei, F. Brivio, A. Sadhanala, S. Sun, W. Li, K. H. L. Zhang, J. L. MacManus-Driscoll, P. D. Bristowe, R. H. Friend, A. K. Cheetham, F. Deschler, *Adv. Mater. Interfaces* **2018**, *5*, 1800464.

[81] W. Gao, C. Ran, J. Xi, B. Jiao, W. Zhang, M. Wu, X. Hou, Z. Wu, *Chemphyschem* **2018**, *19*, 1696.

[82] F. Igbari, R. Wang, Z.-K. Wang, X.-J. Ma, Q. Wang, K.-L. Wang, Y. Zhang, L.-S. Liao, Y. Yang, *Nano Lett.* **2019**, *19*, 2066.

[83] B. Wang, N. Li, L. Yang, C. Dall'Agnese, A. K. Jena, S.-I. Sasaki, T. Miyasaka, H. Tamiaki, X.-F. Wang, *J. Am. Chem. Soc.* **2021**, *143*, 2207.

[84] E. T. McClure, M. R. Ball, W. Windl, P. M. Woodward, *Chem. Mater.* **2016**, *28*, 1348.

[85] R. L. Z. Hoye, L. Eyre, F. Wei, F. Brivio, A. Sadhanala, S. Sun, W. Li, K. H. L. Zhang, J. L. MacManus-Driscoll, P. D. Bristowe, R. H. Friend, A. K. Cheetham, F. Deschler, *Adv. Mater. Interfaces* **2018**, *5*, 1800464.

[86] G. Longo, S. Mahesh, L. R. V. Buizza, A. D. Wright, A. J. Ramadan, M. Abdi-Jalebi, P. K. Nayak, L. M. Herz, H. J. Snaith, *ACS Energy Lett.* **2020**, *5*, 2200.

[87] W. Shockley, H. J. Queisser, *Journal of Applied Physics* **1961**, *32*, 510.

[88] S. Rühle, *Solar Energy* **2016**, *130*, 139.

[89] Y. Yin, W. Tian, J. Leng, J. Bian, S. Jin, *The journal of physical chemistry letters* **2020**, *11*, 6956.

[90] R. Kentsch, M. Scholz, J. Horn, D. Schlettwein, K. Oum, T. Lenzer, *J. Phys. Chem. C* **2018**, *122*, 25940.

[91] A. D. Wright, L. R. V. Buizza, K. J. Savill, G. Longo, H. J. Snaith, M. B. Johnston, L. M. Herz, *The journal of physical chemistry letters* **2021**, *12*, 3352.

[92] D. Bartesaghi, A. H. Slavney, M. C. Gélvez-Rueda, B. A. Connor, F. C. Grozema, H. I. Karunadasa, T. J. Savenije, *J. Phys. Chem. C* **2018**, *122*, 4809.

[93] S. J. Zelewski, J. M. Urban, A. Surrente, D. K. Maude, A. Kuc, L. Schade, R. D. Johnson, M. Dollmann, P. K. Nayak, H. J. Snaith, P. Radaelli, R. Kudrawiec, R. J. Nicholas, P. Plochocka, M. Baranowski, *J. Mater. Chem. C* **2019**, *7*, 8350.

[94] C. Lv, X. Yang, Z. Shi, L. Wang, L. Sui, Q. Li, J. Qin, K. Liu, Z. Zhang, X. Li, Q. Lou, D. Yang, J. Zang, R. Liu, B. Liu, C.-X. Shan, *J. Phys. Chem. C* **2020**, *124*, 1732.

[95] L. Schade, A. D. Wright, R. D. Johnson, M. Dollmann, B. Wenger, P. K. Nayak, D. Prabhakaran, L. M. Herz, R. Nicholas, H. J. Snaith, P. G. Radaelli, *ACS Energy Lett.* **2019**, *4*, 299.

[96] Z. Li, S. R. Kavanagh, M. Napari, R. G. Palgrave, M. Abdi-Jalebi, Z. Andaji-Garmaroudi, D. W. Davies, M. Laitinen, J. Julin, M. A. Isaacs, R. H. Friend, D. O. Scanlon, A. Walsh, R. L. Z. Hoye, *J. Mater. Chem. A* **2020**, *8*, 21780.

[97] E. M. Hutter, M. C. Gélvez-Rueda, D. Bartesaghi, F. C. Grozema, T. J. Savenije, *ACS omega* **2018**, *3*, 11655.

[98] N. Pai, J. Lu, M. Wang, A. S. R. Chesman, A. Seeber, P. V. Cherepanov, D. C. Senevirathna, T. R. Gengenbach, N. V. Medhekar, P. C. Andrews, U. Bach, A. N. Simonov, *J. Mater. Chem. A* **2020**, *8*, 2008.

[99] P. Vishnoi, R. Seshadri, A. K. Cheetham, *J. Phys. Chem. C* **2021**, *125*, 11756.

[100] B. A. Connor, L. Leppert, M. D. Smith, J. B. Neaton, H. I. Karunadasa, *Journal of the American Chemical Society* **2018**, *140*, 5235.

[101] M. K. Jana, S. M. Janke, D. J. Dirkes, S. Dovletgeldi, C. Liu, X. Qin, K. Gundogdu, W. You, V. Blum, D. B. Mitzi, *Journal of the American Chemical Society* **2019**, *141*, 7955.

[102] Y. Li, T. Yang, Z. Xu, X. Liu, X. Huang, S. Han, Y. Liu, M. Li, J. Luo, Z. Sun, *Angew. Chem.* **2020**, *132*, 3457.

[103] F. Schmitz, J. Horn, N. Dengo, A. E. Sedykh, J. Becker, E. Maiworm, P. Bélteky, Á. Kukovecz, S. Gross, F. Lamberti, K. Müller-Buschbaum, D. Schlettwein, D. Meggiolaro, M. Righetto, T. Gatti, *Chem. Mater.* **2021**, *33*, 4688.

[104] Z. Xu, X. Liu, Y. Li, X. Liu, T. Yang, C. Ji, S. Han, Y. Xu, J. Luo, Z. Sun, *Angewandte Chemie (International ed. in English)* **2019**, *58*, 15757.

[105] C. N. Savory, A. Walsh, D. O. Scanlon, *ACS Energy Lett. 1, 949 (2016)*.

[106] H. C. Sansom, G. Longo, A. D. Wright, L. R. V. Buizza, S. Mahesh, B. Wenger, M. Zanella, M. Abdi-Jalebi, M. J. Pitcher, M. S. Dyer, T. D. Manning, R. H. Friend, L. M. Herz, H. J. Snaith, J. B. Claridge, M. J. Rosseinsky, *Journal of the American Chemical Society* **2021**, *143*, 3983.

[107] W. Pan, H. Wu, J. Luo, Z. Deng, C. Ge, C. Chen, X. Jiang, W.-J. Yin, G. Niu, L. Zhu, L. Yin, Y. Zhou, Q. Xie, X. Ke, M. Sui, J. Tang, *Nature Photon* **2017**, *11*, 726.

[108] J. A. Steele, W. Pan, C. Martin, M. Keshavarz, E. Debroye, H. Yuan, S. Banerjee, E. Fron, D. Jonckheere, C. W. Kim, W. Baekelant, G. Niu, J. Tang, J. Vanacken, M. van der Auweraer, J. Hofkens, M. B. J. Roeffaers, *Advanced materials (Deerfield Beach, Fla.)* **2018**, *30*, e1804450.

[109] W. Yuan, G. Niu, Y. Xian, H. Wu, H. Wang, H. Yin, P. Liu, W. Li, J. Fan, *Adv. Funct. Mater.* **2019**, *29*, 1900234.

[110] M. L. Petrus, K. Schutt, M. T. Sirtl, E. M. Hutter, A. C. Closs, J. M. Ball, J. C. Bijleveld, A. Petrozza, T. Bein, T. J. Dingemans, T. J. Savenije, H. Snaith, P. Docampo, *Adv. Energy Mater.* **2018**, *8*, 1801605.

[111] N. Arora, M. I. Dar, A. Hinderhofer, N. Pellet, F. Schreiber, S. M. Zakeeruddin, M. Grätzel, *Science (New York, N.Y.)* **2017**, *358*, 768.

[112] M. Daskeviciene, S. Paek, Z. Wang, T. Malinauskas, G. Jokubauskaite, K. Rakstys, K. T. Cho, A. Magomedov, V. Jankauskas, S. Ahmad, H. J. Snaith, V. Getautis, M. K. Nazeeruddin, *Nano Energy* **2017**, *32*, 551.

[113] S. Daskeviciute, C. Momblona, K. Rakstys, A. A. Sutanto, M. Daskeviciene, V. Jankauskas, A. Gruodis, G. Bubniene, V. Getautis, M. K. Nazeeruddin, *J. Mater. Chem. A* **2021**, *9*, 301.

[114] T. Niu, W. Zhu, Y. Zhang, Q. Xue, X. Jiao, Z. Wang, Y.-M. Xie, P. Li, R. Chen, F. Huang, Y. Li, H.-L. Yip, Y. Cao, *Joule* **2021**, *5*, 249.

[115] S. Oh, N. Khan, S.-M. Jin, H. Tran, N. Yoon, C. E. Song, H. K. Lee, W. S. Shin, J.-C. Lee, S.-J. Moon, E. Lee, S. K. Lee, *Nano Energy* **2020**, *72*, 104708.

[116] F. Zhang, Z. Yao, Y. Guo, Y. Li, J. Bergstrand, C. J. Brett, B. Cai, A. Hajian, Y. Guo, X. Yang, J. M. Gardner, J. Widengren, S. V. Roth, L. Kloo, L. Sun, *Journal of the American Chemical Society* **2019**, *141*, 19700.

2 Characterization Techniques

2.1 X-Ray Diffraction (XRD)

X-ray diffraction (XRD) is a common technique to investigate the structural properties of a crystalline material. It can be used to determine the exact structure of a single crystalline material, as well as to calculate the interatomic distance within the crystal lattice, the atomic radii and can give information about the crystallinity and the size of the crystallites in thin films. The interatomic resolution of the structural analysis is caused by the wavelength of X-rays which typically lies in the range of a few Angstroms (10^{-10} m) and therefore lies within the interatomic distances that occur in a single crystal and fulfils the physical premise for interaction with the material.

X-rays are generally created when high-speed electrons, accelerated with several kV at the cathode, collide with a metallic anode, where they slow down and rapidly lose their kinetic energy. Depending on the pattern of slow-down and therefore the emitted energy, continuous X-ray irradiation with various wavelengths is generated (‘Bremsstrahlung’). The maximum energy of the emitted photon is determined by the acceleration voltage that is applied between the anode and the cathode.[1]

Electromagnetic waves can interact with matter in a manifold of various possibilities, dependent on their wavelength. The interaction of the X-ray is based on a scattering-process, where incident X-ray photons are elastically scattered by the electron (clouds) of the atoms within the periodic crystal lattice in the crystalline sample, hence constructive or destructive interference can occur, depending on the path difference between the two scattered waves. This principle is shown in Figure 2.1, where the pathway of two different X-rays 1 and 2 is shown before and after interaction with the atoms A and B.

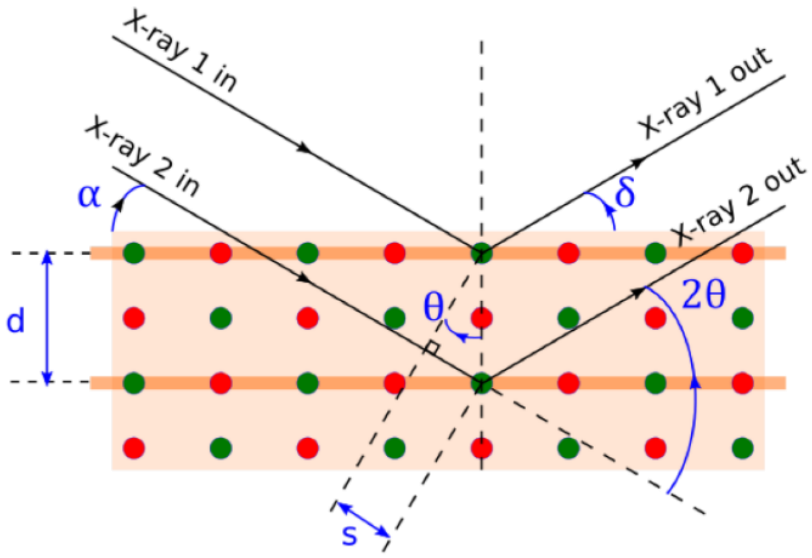

Figure 2.1: Schematic representation of process of X-rays diffracted at a periodic crystal lattice. The red and green dots represent the atoms of the lattice, α is the incident and δ exit angle. θ is the Bragg angle, d is the distance between the reflecting crystal planes and s is the half value of the path difference between X-ray 1 and X-ray 2.[2]

If two scattered X-rays are in phase, the path difference of the two beams is an integer multiple of the wavelength of the X-ray and constructive interference occurs as given by Bragg's law of diffraction (Equation (2.1)):

$$n*\lambda = 2d*\sin\theta \tag{2.1}$$

Where n is the diffraction order, λ is the X-ray wavelength, d is the distance between the two lattice planes and θ is the Bragg angle.

If the above Bragg condition is fulfilled, the atoms in the periodic crystal lattice with the interplanar spacing d will diffract the X-ray photons with the angle 2θ, dependent on the electron density of the atom. As a result, a diffraction peak is observed on the detector at a specific angle. The relative intensities of the resulting peaks are characteristic for every atom, and they depend on the atomic positions in the lattice.

The XRD pattern can be obtained from measurements both in the reflection (Bragg Brentano geometry) and the transmission mode (Debye Scherrer geometry). Additional information about the crystallite size and the crystallite orientation can also be extracted from XRD data.

In the Debye-Scherrer geometry, a spinning powder-sample is placed between the fixed X-ray source and the movable detector. Here, only the detector scans different angles with respect to

the sample and records the intensity of the scattered X-ray photons. In contrast to the Bragg-Brentano geometry, the Debye Scherrer geometry allows for the detection of all possible crystal planes due to the multiple orientation of the powder and the spinning of the sample, as well as the scanning of the detector. This geometry is also used to determine the structure of single crystals.[3]

While the position of the XRD-reflections give information about the structure of the investigated material, the broadening of the peaks correlates with the crystallite size of the sample and can be estimated using the Scherrer equation (2.2):[1]

$$D = \frac{K * \lambda}{B_{1/2} * cos\theta} \tag{2.2}$$

Where D is the mean diameter of the crystallite domain, K is the shape factor, a dimensionless factor close to unity (~0.9), λ is the wavelength of the X-ray irradiation, $B_{1/2}$ is the line broadening at half the maximum intensity in radians and θ is the Bragg angle.

2.2 Grazing Incidence Wide Angle X-Ray Scattering (GIWAXS)

Grazing incidence wide angle X-ray scattering is a well-established method to obtain information about the crystal phase and orientation of the thin film with respect to the substrate surface normal. The geometry is very similar to the one used for XRD measurements, yet, the incidence angle of the X-rays is kept constant at very low angles <1 °, which ensures a relatively long footprint and thus a rather large sample volume to be probed (Figure 2.2). The detector is very close to the sample to have access to large angles.

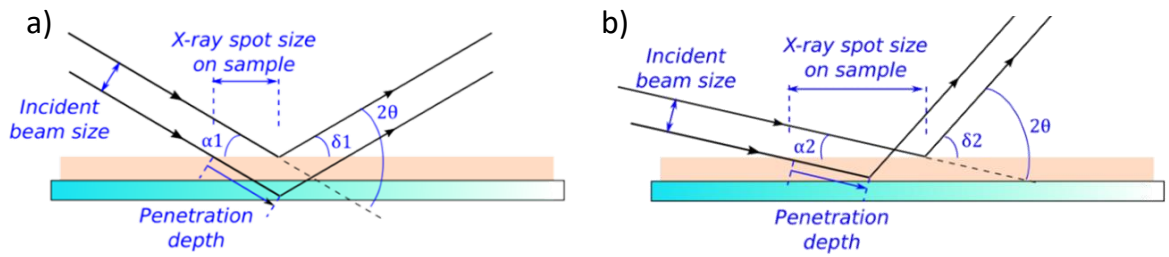

Figure 2.2: Pathway of incident X-rays through a thin film with respect to the incident angle. a) larger incident angle α_1, comparable to standard X-ray diffraction measurements that results in a large penetration depth and a small spot size of the X-rays and a small exit angle δ_1. b) low incident angle α_2

that results in a smaller penetration depth and large X-ray spot size on the sample, as well as a large exit angle δ_2.[2]

By the combination of the measurement with a 2D detector, much more information is obtained from the patterns compared to regular XRD measurements that use either a point detector or a 1D-detector (Figure 2.3). The dimensionality of the detector offers the possibility to analyze both the crystallinity and the orientation of the samples by using the azimuthal angle χ to the normal component q_z of the scattering vector, leading to partial rings in case of increasing orientation or even dots in case of single crystals or perfectly aligned thin films. In contrast, random crystallite orientation (perfect polycrystallinity) leads to the formation of Debye-Scherrer rings with homogeneous intensity distribution.[4]

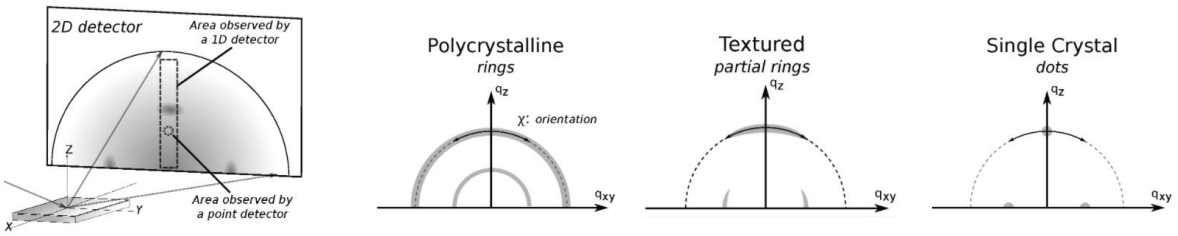

Figure 2.3: Schematic illustration of the detector geometry used for GIWAXS measurements, as well as the possible intensity distribution observable in the detector image, depending on the crystallinity and orientation of the investigated material.[2]

A cut along the azimuthal angle χ provides direct information about the orientation and crystallinity of the sample. A cut at $\chi = 0°$ corresponds to an XRD pattern recorded with Bragg-Brentano geometry with a 1D detector. Here, q_z is directly related to 2θ and information is given about the out-of-plane direction in the thin film. If the cut is made along $\chi = 90°$, information is given about the in-plane direction of the thin film.

2.3 Scanning Electron Microscopy (SEM)

Scanning electron microscopy (SEM) is a widely used method to gain insights in the micro- or nanomorphology of thin films. Modern microscopes provide insight into layer thickness, crystallite size of the thin film or surface topography with resolution down to about 1 nm. During the measurements, an electron beam is accelerated by an electron gun in high vacuum with several kV (~30 kV) voltage and focused by several lenses to obtain a beam diameter of a few nanometers or even less. The as-focused electron beam then hits the sample surface where

multiple different interactions occur, which can then be used for different imaging methods depending on the detector used and discussed in the following.[3]

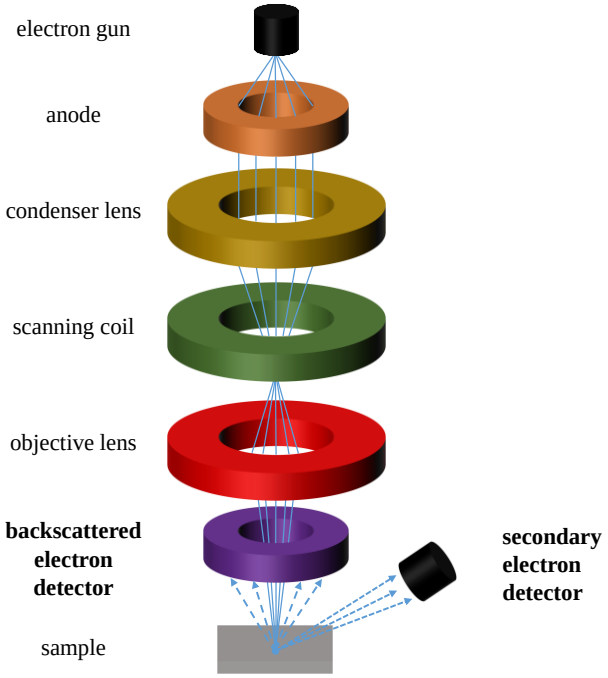

Figure 2.4: Schematic representation of the microscope column of a scanning electron microscope.[5]

Due to the interactions of the electrons with the investigated material, both secondary and backscattered electrons emerge from the sample. Secondary electrons are of low energy (typically 0 – 50 eV) and are created by an inelastic scattering process with atoms which are excited during that process. The detector for those electrons is placed outside the microscope column and gives information about the morphology of the investigated sample.

Backscattered electrons (BSE) result from an elastic scattering process of the primary electron beam with atomic nuclei and have a higher energy compared to the secondary electrons (> 50 eV). The BSEs are detected within the microscope column and their energy is dependent of the atomic number of the scattering partner, thus providing information about the elemental composition of the sample.

2.4 Photoelectron spectroscopy (PES)

Photoelectron spectroscopy is a valuable surface sensitive tool to investigate the binding energies of electrons in the investigated material and is based on the photoelectric effect.[6,7]

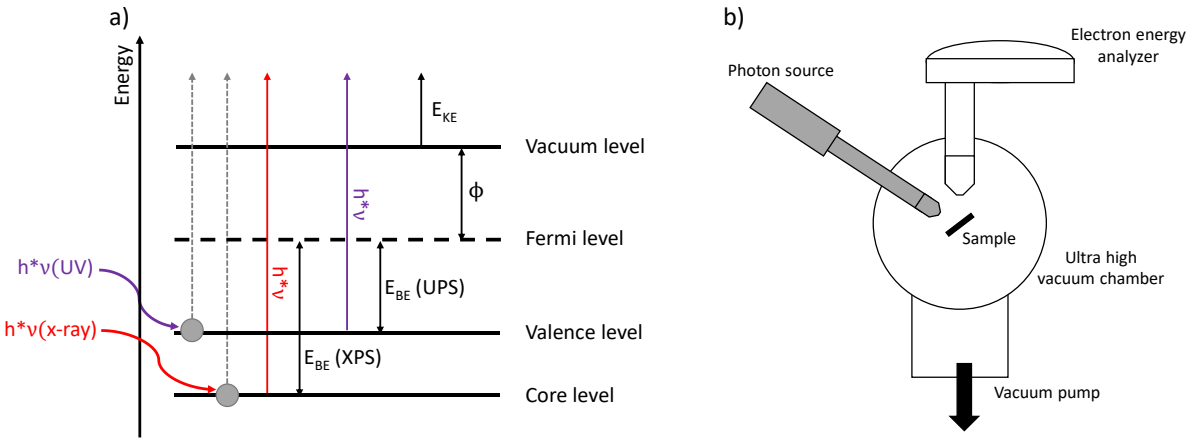

Figure 2.5: a) schematic energy diagram of UPS and XPS measurements (red lines represent the XPS energy photons and purple lines represent the UPS energy phonons), b) schematic representations of a PES setup.

In principle, the sample is irradiated with monoenergetic photons to ionize the atoms on the surface. The ejected electrons (photoelectrons) show a distribution of kinetic energies (KE) that are related to the binding energies (E_{BE}, Figure 2.5a). Generally, the sample is irradiated with high-energy radiation, either ultraviolet photons or X-rays. The ejected electrons travel from the sample to an energy analyzer where the KEs are recorded and then to a detector that counts the number of photoelectrons at various KEs (Figure 2.5b).

Utilizing Einstein's equation about the photoelectric effect we now can calculate the ionization (binding) energy of the emitted electron, knowing the work function of the investigated material:

$$E_{KE} = h\nu - E_{BE} - \phi \tag{2.3}$$

Where E_{KE} is the kinetic energy of the emitted electron, $h\nu$ the energy of the incident photon, E_{BE} the binding energy of the electron and φ is the work function of the solid sample. To obtain reliable results, the work function of the spectrometer also has to be taken into account.

The electron binding energy is distinctive for different elements and their oxidation states as for different orbitals, different kinetic energies of the emitted electrons are detected.

Depending on the energy of the incident photons, different information about the material can be accessed by PES.

2.4.1 X-Ray Photoelectron Spectroscopy (XPS)

X-ray photoelectron spectroscopy is performed using soft X-rays (energy of 200-2000 eV) and hence can be used to examine core-levels of a sample's surface. Due the rather high energy, electrons from the core-orbitals are ionized and ejected, thus providing information on the chemical composition of the surface of the investigated sample. Moreover, dependent on the number of ejected electrons, this technique provides information about the oxidation state and thus about surface reactions and changes of the surface states. Here, the fact is utilized that atoms with a higher positive oxidation state have a higher electron binding energy, a result from the additional coulombic interaction between the ejected electron and the ionized core. This leads to an observable energy shift of the emitted electrons.

2.4.2 Ultraviolet Photoelectron Spectroscopy (UPS)

While XPS is performed with (soft) x-rays, ultraviolet photoelectron spectroscopy is performed using vacuum UV radiation (energy of 10 – 45 eV). Due to the rather low energy compared to XPS, UPS is used to determine the ionization energy of the electrons in the valence levels. Here, electrons from the valence orbitals of the investigated sample are ionized and detected, providing information about the binding energy and hence about the valence band energy of the investigated material.

2.5 Ultraviolet-Visible (UV-vis) Absorption Spectroscopy

The most important information about a semiconductor is both the nature and the energy of the optical bandgap. In ultraviolet-visible (UV-Vis) absorption spectroscopy, the wavelength-dependent absorption and reflection of a sample is measured between the near-infrared, visible and UV regions of the electromagnetic spectrum. An absorption of a photon takes place when the energy of the incident photon is sufficient to excite an electron from the valence band into the conduction band of the investigated material. This absorption behavior is described by the Lambert-Beer law as shown in equation (2.4) where the absorbance A is defined as:

$$A = -log_{10}\left(\frac{I}{I_0}\right) = \alpha_{10} * l = \varepsilon * c * d \qquad (2.4)$$

The equation shows that the absorption is either dependent on the sample concentration (c), the thickness of either the cuvette containing the solution (d) and the extinction coefficient (ε) or

the thickness of the investigated solid (l) and the decadic absorption coefficient (α_{10}) of the material. I is the measured light intensity and I_0 is the incident light intensity.

To record the spectra, the wavelength of the incident light is scanned from the near-IR to the UV part with the sample while simultaneously recording I_0. By combination of I and I_0, the transmittance $T = I/I_0$ can be obtained. Typically, a dual beam spectrometer is used where the monochromatic beam is split and I_0 and I are measured simultaneously (Figure 2.6). To avoid an underestimation of I due to light scattering processes at the sample, an integrating sphere is used, which collects light transmitted through the sample at any angle and reflects it to the detector (Figure 2.6).

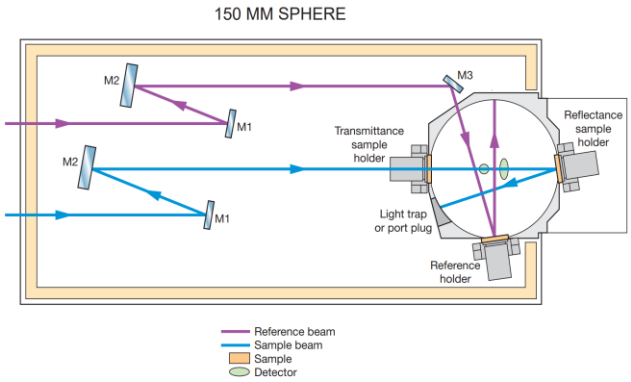

Figure 2.6: Schematic illustration of a UV/Vis setup including an integrating sphere.[8]

However, using an integrating sphere does not eliminate errors that are caused by interfacial scattering processes that occur at media with different refractive indices. Hence, before measuring a sample, a reference substrate without the sample-layer but the same architecture has to be measured both in transmittance and reflectance R and the value for the absorptance has to be corrected. This can be done by measuring the reflectance and the transmittance of the films.

$$\%A = 1 - \%T - \%R \tag{2.5}$$

Where the absorptance is given as the percentage of incident light absorbed ($\%A$). The absorbance can then be calculated using

$$A = -log_{10}(1 - \%A) \tag{2.6}$$

Hence, the absorbance of the investigated thin film is given by

$$A_{film} = A_{sample} - A_{reference} \tag{2.7}$$

To determine the optical bandgap of a thin film material, the Tauc method can be used. Here, the edge of the optical absorption can be determined with a plot of $(\alpha h\nu)^x$ against $(h\nu)$ and a linear fit of the linear region of the plot. The nature of the transition can be determined by $x = 2$ for a direct transition and $x = 1/2$ for an indirect transition.[9]

2.6 Photoluminescence Spectroscopy (PL)

Upon excitation, the charge carriers in a semiconductor can cause light emission due to band-to-band recombination, a process called luminescence. When sufficient energy is applied to a semiconductor, an electron is excited from the valence band into the conduction band, leaving behind a positively charged hole. The excitation energy can be provided by several external ways of activation such as an external bias (electroluminescence, see chapter 2.14) or light irradiation (photoluminescence, PL). The emission of PL radiation is caused by the recombination of electrons in the conduction band with holes in the valence band of the semiconductor under the emission of a photon, if the transition is dipole-allowed (Figure 2.7).[3]

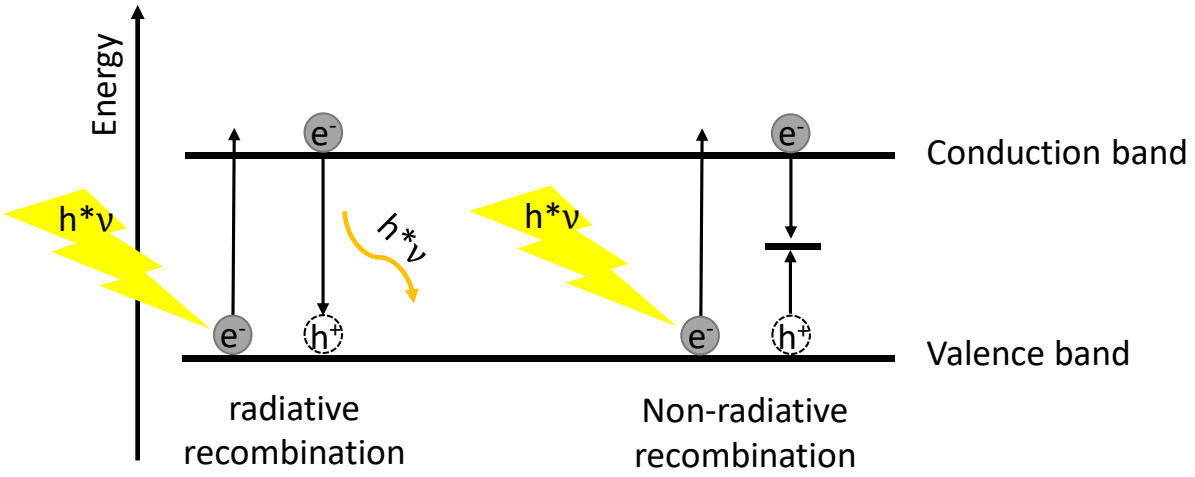

Figure 2.7: Schematic illustration of radiative and non radiative recombination upon laser excitation.

However, radiative recombination only occurs in case of band-to-band recombination. If the recombination process is trap assisted, e.g., by deep traps within the bandgap, usually the energy difference of the charge carriers is not large enough to emit light, hence the recombination process is non-radiative. Therefore, steady-state PL measurements give a good idea about the energy of the bandgap (wavelength of emitted photon), as well as the recombination process (intensity of the emission).

This type of PL measurement can also be used to determine the nature of the recombination process by measuring the intensity of the PL signal with respect to the intensity of the excitation source. A plot of the logarithmic PL signal against the logarithmic excitation intensity can be fitted with a linear fit whose slope gives insights into the recombination regime.[10]

Besides steady state measurements, time-resolved PL methods such as time-correlated single photon counting (TCSPC) are often used to investigate the recombination kinetics of photoexcited charge carriers. In principle, a short laser pulse excites the sample to start the time measurement. When a single photon of the emission process reaches the detector, the time count is stopped as shown schematically in Figure 2.8 a). By using a laser with a high repetition rate (usually MHz frequency), this measurement is performed several million times per second and leads to a histogram shown in Figure 2.8 b), where the amount of photons in counts are plotted against the corresponding time until it reached the detector.[11]

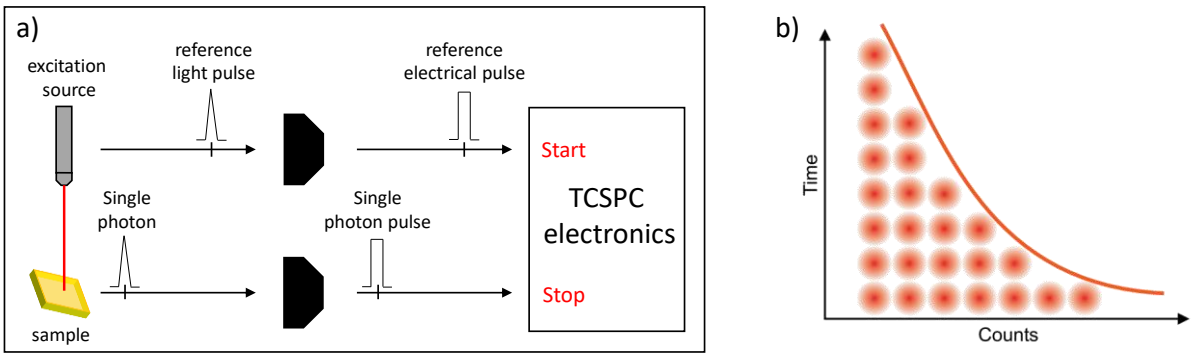

Figure 2.8: a) Schematic illustration of the experimental setup of a TCSPC measurement, b) recorded histogram during the measurement.[11,12]

As multi-photon events will affect the statistics of the histogram, only one photon per excitation must be measured. Otherwise, the early part of the decay curve will be distorted and the measurement results will be invalid. To eliminate this problem, the emission beam is attenuated.[12]

2.7 Time-Resolved Microwave Conductivity (TRMC)

Time-resolved microwave conductivity (TRMC) is a powerful tool to investigate the charge carrier mobility of the investigated material. A typical setup consists of four essential parts: A stable microwave source, a pulsed and tunable excitation source, a microwave cell with a sample holder that may be equipped with a cryostat and a sensitive detector with data acquisition system (Figure 2.9).[13]

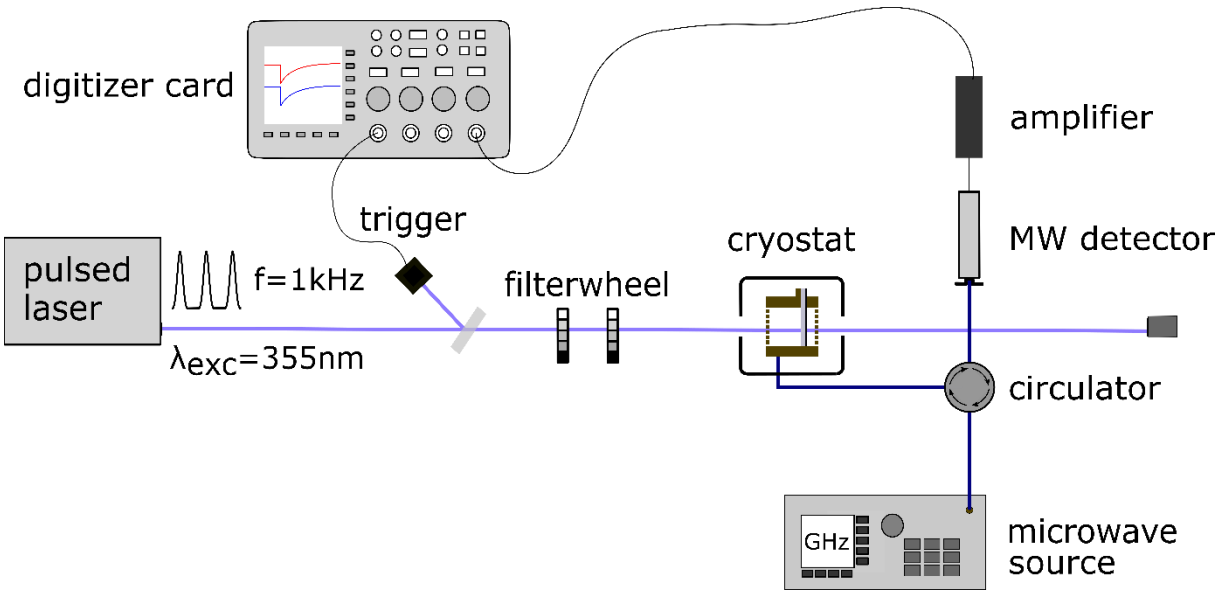

Figure 2.9: Schematic illustration of a TRMC setup (Reprinted with permission from {*ACS Appl. Energy Mater.* 2020, 3, 12, 11597–11609}. Copyright {2020} American Chemical Society).

To determine a change of the photoconductance (ΔG) of the investigated sample, it is necessary that a standing microwave with the incident power P is employed within the microwave cell. Upon photoexcitation with a pulsed laser, the change in the photoconductance is related to power-change of the reflected microwave ΔP as a function of time according to equation (2.8):

$$\frac{\Delta P(t)}{P} = -K * \Delta G(t) \tag{2.8}$$

Where P is the power of the incident microwave, $\Delta P(t)$ the power of the reflected microwave upon photoexcitation, K is the sensitivity factor of the cavity and $\Delta G(t)$ is the conductance change over time. The sensitivity factor depends on the dimension and quality of the wall of the cavity as well as the dielectric properties of the investigated sample.

While the equation gives the relation between the change of the microwave power with the change in the conductance of the investigated sample, the relation of the conductance to the actual mobility of the charge carriers remains to be evaluated. Hence, several relations are used as discussed in the following:

The conductance can also be written as in equation (2.9)

$$\Delta G = \Delta\sigma * \beta * l \tag{2.9}$$

Where $\Delta\sigma$ gives the change in conductivity and β is given by the dimensions of the cavity and l is the thickness of the sample. $\Delta\sigma$ can be defined by the charge carrier density n with the elemental charge e and the sum of the charge carrier mobilities μ_i (equation (2.10))

$$\Delta\sigma = n * e \sum_i \mu_i \tag{2.10}$$

If no recombination has taken place within the response time of the setup, the charge carrier yield ϕ can be defined as:

$$\phi = \frac{n * l}{I_0 * F_A} \tag{2.11}$$

Where n is the charge carrier density, l is the sample thickness, I_o is the intensity of the laser and F_A is the fraction of light absorbed at the excitation wavelength.

Using the abovementioned equations and the value of the maximum change in conductance ΔG_{max}, we can calculate the product of the quantum yield and the overall charge carrier mobility with equation (2.12):[13]

$$\varphi \sum_i \mu_i = \frac{\Delta G_{max}}{\beta * e * I_0 * F_A} \tag{2.12}$$

2.8 Hole-Mobility Measurements

Hole mobility measurements are a method different from TRMC to determine, how quickly a hole can move through the investigated material upon applying an external potential.[14] To measure the hole-mobility of a material, hole-only devices are used with the general architecture ITO/MoO_x/Sample/MoO_x/Au (Figure 2.10).

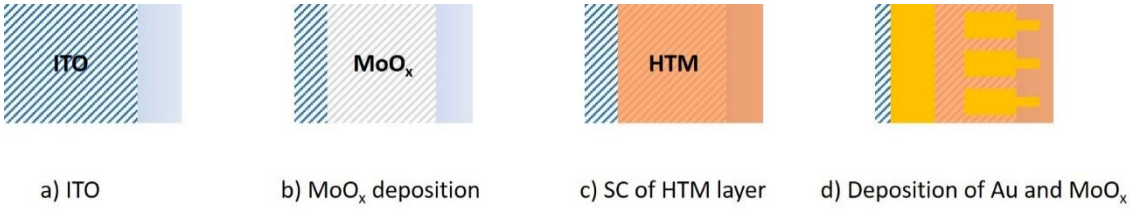

Figure 2.10: Schematic representation of the device preparation of hole-only devices. a) Shows the starting point with etching the substrate before the MoO_x layer is deposited on top via thermal

evaporation at low pressure (~10^{-7} mbar). After that, the sample layer is deposited (here, an HTM, c), followed by another layer of MoO_x and the gold electrode (d), both thermally evaporated at low pressure (10^{-7} mbar)

Here, the high work function of MoO_x efficiently blocks the electrons to selectively only extract the holes of the device. To measure the devices, an external potential is applied to build up a space charge that limits the current which then only depends on the mobility instead of the charge density. If trap-free transport and an ohmic charge injection are assumed, the Mott-Gourney law can be applied to calculate the current density with equation (2.13):[15]

$$J = \frac{9}{8} * \varepsilon_0 * \varepsilon_r * \mu * \frac{V^2}{L^3} \tag{2.13}$$

Where J is the current density, ε_0 is the vacuum permittivity, ε_r is the dielectric constant, V is the applied bias, L is the layer thickness and μ is the mobility.

2.9 Cyclic Voltammetry (CV)

Cyclic voltammetry (CV) is a potentiodynamic technique to investigate the electrochemical behavior of a material and is thus a valuable and powerful tool to determine the energy level of the highest occupied molecular orbital (HOMO) of a certain organic material. For this measurement, the sample and a supporting electrolyte are dissolved and the working and reference electrodes are immersed in the solution. For the measurement, a potential is applied which changes linearly over time and with a fixed scan rate, starting from an initial potential towards a switching potential, at which the scan is reversed and the potential swept back to the initial potential. During the whole procedure, the current is measured.

If the material features accessible oxidation states, a so-called oxidation peak in the anodic current will appear (forward scan) while the reduction peak will be visible in the cathodic current (reverse scan). For organic molecules, often an internal reference is added to the sample solution to improve the accuracy of the results. Using this internal reference (a molecule with known redox-potential, e.g., ferrocene), the HOMO energy level of the investigated material can be calculated from the current onset from the first oxidation-peak, using (2.14):[16]

$$E_{HOMO} = -\left(E_{[onset,ox\ vs\ Fc^+/Fc]} + 5.1\right)(eV) \tag{2.14}$$

Where E_{HOMO} is the energy of the HOMO level and $E_{[onset,ox\ vs\ Fc^+/Fc]}$ is the potential onset of the sample vs ferrocene (Fc^+/Fc).

2.10 Current-Voltage (*J/V*) Measurements

The most powerful tool to investigate the performance of a solar cell is the measurement of current-voltage (*J/V*) curves both under light and under dark conditions. By using this tool, the performance in terms of Power Conversion Efficiency (PCE) can directly be assessed and directly gives the quality of the solar cell. *J/V* measurements under illumination are conducted under standard conditions by means of using a standard air mass 1.5 global (AM1.5G) spectrum with an incident power of 100 mW/cm^2, also referred to the intensity of one sun.[17]

The measurement is performed by illuminating the sample and scanning with an applied external voltage in a certain range while recording the corresponding current density of the device, which is determined by the absolute current measured and the overall area of the solar cell. This measurement leads to a *J/V* curve as depicted in Figure 2.11 and shows the typical characteristics of a solar cell.

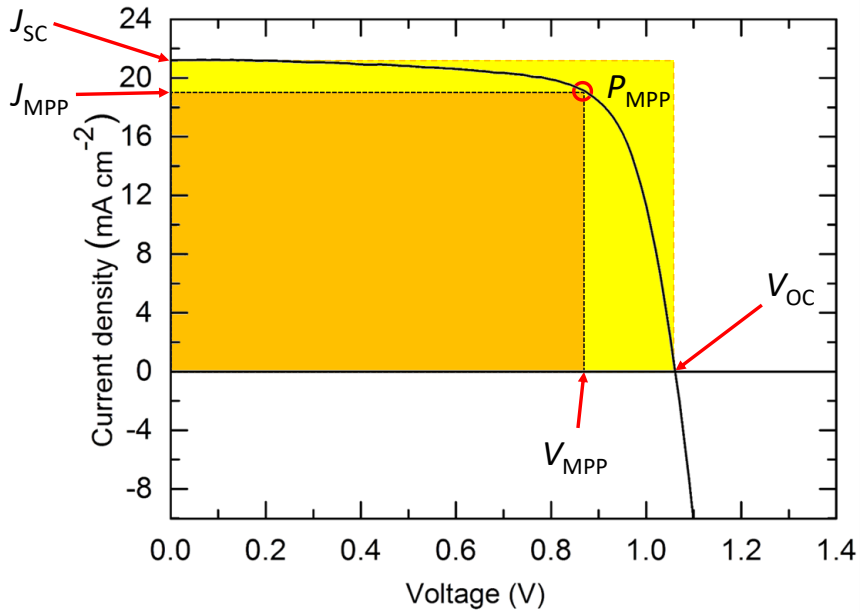

Figure 2.11: Typical *J/V*-curve obtained from a solar cell and its characteristic photovoltaic parameters.

Using a *J/V* curve, several characteristic photovoltaic parameters can be extracted to evaluate the quality of solar cells:[18]

The open circuit voltage (V_{OC}) is the figure of merit for the voltage provided by the solar cell when the net current flow through the solar cell is zero. It is influenced by several different factors, mainly by the bandgap of the material. Generally, the higher the bandgap, the larger the

V_{OC}, however, this parameter is also influenced by the ratio of non-radiative to radiative recombination, interfacial recombination and the charge carrier lifetime.

The short circuit current density (J_{SC}) gives the value of the maximum current flow across the complete active area of the solar cell while the external voltage is zero. It largely depends on the charge carrier generation, as well as the collection efficiency and is thus influenced by the incident light intensity, absorption/reflection of the material, as well as the band gap of the material (the smaller the bandgap, the larger the amount of absorbed photons creating charge carriers).

The maximum power point (*MPP*) defines the maximum power (P_{MPP}) that the solar cell can generate and is located at the intersection of the *J/V*-curve and the largest rectangular area between the curve and the coordination axes given by the product of the J_{MPP} and V_{MPP}.

The fill factor (*FF*) is defined as the ratio between the maximum power of the solar cell (represented by the orange area in Figure 2.11) and the product of J_{SC} and V_{OC} (yellow area in Figure 2.11). It is a key parameter for the evaluation of the overall quality of the solar cell and can thus provide hints about malfunctioning solar cells as it is strongly affected by internal charge carrier losses such as a large series resistance, small shunt resistance or interfacial recombination. The value of the *FF* can be described by equation (2.15):

$$FF = \frac{P_{MPP}}{V_{OC} * J_{SC}} = \frac{V_{MPP} * J_{MPP}}{V_{OC} * J_{SC}} \tag{2.15}$$

The power conversion efficiency (PCE) gives the efficiency with which the incident sun power (P_{in}) is converted into electric power and is described by equation (2.16):

$$PCE = \frac{P_{MPP}}{P_{in}} = \frac{V_{OC} * J_{SC} * FF}{P_{in}} \tag{2.16}$$

Attributed to significant ionic conductivity, especially in perovskite solar cells, these kinds of PV cells show an ‘anomalous’ *J/V* behavior, expressed as a hysteresis effect between two different *J/V* scans which leads to differently shaped *J/V* curves, depending on the direction of the voltage sweep applied (Figure 2.12).[19]

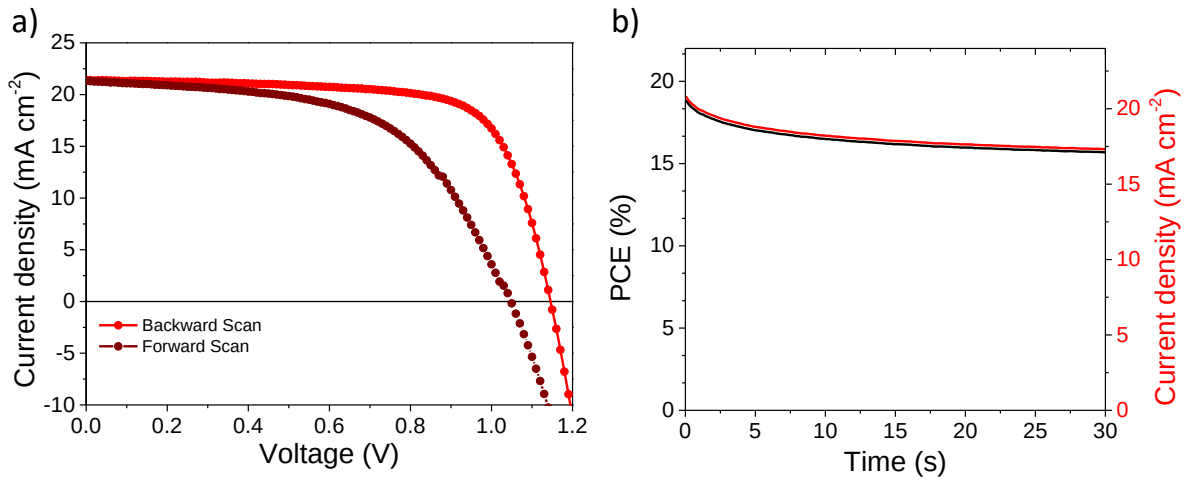

Figure 2.12: Examples for a hysteretic *J/V*-curve (a) and the stablilized power output (b).

Hence, this inconsistency between the forward and reverse scan requires an additional type of measurement where the evolution of the maximum power point is evaluated under operating conditions to assess the device efficiency in a way that is considered to be more reliable. To determine this so-called stabilized power output, a constant voltage V_{MPP} is applied and the evolution of the J_{MPP} is monitored over time under illumination (Figure 2.12 b)).

2.11 Conductivity Measurements

The electrical conductivity of a material can be determined in various ways. In this work, conductivity measurements were performed by the application of interdigitated gold-electrodes on top of a thin film of the material on glass at low pressure (~10^{-7} mbar) with various length and width (Figure 2.13).

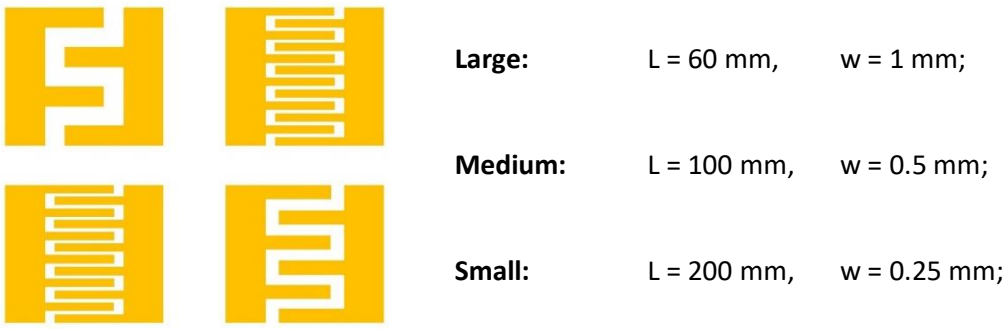

Figure 2.13: Schematic illustration of the electrode patterns used for conductivity measurements, together with the respective channel lengths (*L*) and channel widths (w).

Afterwards, *J/V* measurements in the dark are performed, measuring the current at a certain applied voltage. Using the *J/V* data, the resistance R of the material can be calculated using Ohm's law and knowing the film thickness d of the sample films, as well as the electrode dimensions (channel width w and channel length L), the conductivity σ can be calculated using equation (2.17):

$$\sigma = \frac{w}{R * L * d} \tag{2.17}$$

2.12 Light Intensity Dependent V_{OC} Measurements

As discussed in Chapter 1, a solar cell can be described as a diode. From light intensity dependent V_{OC} measurements, the ideality factor n_i of such a diode can be determined. The determination of this figure of merit is a powerful tool to determine the dominant recombination type within a thin film solar cell.[20,21]

For a perfectly contacted homogeneous absorber, the V_{OC} can be described with

$$eV_{OC} = E_g - k_B T * \ln\frac{N_C * N_V}{n * p} \tag{2.18}$$

Where E_g is the bandgap energy, e the elemental charge, and $k_B T$ the 'thermal voltage' (thermal energy) with the Boltzmann constant k_B. The second term describes the chemical potential of the electron and hole density (n and p) occupying their effective density of states (N_C and N_V respectively).

The hole- and electron densities result from the equilibrium of the charge carrier generation rate G and the recombination rate R. Since G is directly proportional to the incident light intensity, the resulting V_{OC} is light intensity-dependent. In an ideal diode, two recombination processes are dominant, resulting in different expressions for the recombination rate R:

$$R = \beta * n * p \tag{2.19}$$

for band-to-band electron-hole recombination, or

$$R = \frac{n * p}{\tau_p * n + \tau_n * p} \tag{2.20}$$

for Shockley-Read-Hall (SRH) recombination. Here, β describes the radiative recombination rate constant, while τ_n and τ_p describe the non-radiative lifetimes of the electrons and holes.

With the generation–recombination rate equilibrium $G = R$, we obtain for the V_{OC} in case of band-to-band (b2b) recombination:

$$eV_{OC,b2b} = E_g - k_B T * \ln \frac{N_C * N_V * \beta}{G} \tag{2.21}$$

And for SHR recombination

$$eV_{OC,SRH} = E_g - 2 * k_B T * \ln \frac{\sqrt{N_C * N_V}}{G(\tau_p + \tau_n)} \tag{2.22}$$

With $n = p$ for an intrinsic semiconductor.

With the light intensity-dependence of G and the recombination factor (or ideality factor) n_i being described by the value 1 (perfect band-to-band recombination) or 2 (SRH recombination), we can write

$$eV_{OC} = E_g - n_i * k_B T * \ln \frac{I_0}{I} \tag{2.23}$$

However, n_i describes the deviation from an ideal diode behavior where only recombination processes are considered to be bimolecular. Other recombination processes such as interfacial recombination can lead to ideality factors below 2 and even close to 1, despite dominant SRH recombination within the bulk. In this case, a small ideality factor does not result in a good solar cell. However, this would be also visible in a low V_{OC} values at one sun intensity of the solar cell.[20]

2.13 External Quantum Efficiency (EQE) Measurements

In photovoltaic (PV) devices, there are two types of quantum efficiency (QE): The external quantum efficiency (EQE), also referred to as internal photon to charge carrier conversion efficiency (IPCE). This QE is the ratio between the number of generated charge carriers and the number of incident photons for each wavelength. From this value, the internal quantum efficiency (IQE) can be derived, which gives the ratio between the number of absorbed photons and generated charge carriers.[22,23] Since the IQE is only a value that is calculated from the EQE measurement and the absorption spectrum of the material, only the EQE will be further explained in the following.

The basic principle to obtain the EQE of a sample solar cell is to know the ratio between the number of incident photons n_{ph} and the photogenerated carriers n_e as a function of the wavelength:

$$EQE\ (\lambda) = \frac{n_e(\lambda)}{n_{ph}(\lambda)} \tag{2.24}$$

To obtain this value, basically the short circuit current of the sample cell is measured for each wavelength and compared to the known values of a calibration diode, which was measured beforehand:

$$EQE\ _{sample}(\lambda) = \frac{I_{sample}(\lambda)}{I_{diode}(\lambda)} * EQE\ _{diode}(\lambda) \tag{2.25}$$

Another important figure of merit that can be derived from this measurement is the integrated photocurrent. This value is obtained by integration of the EQE curve and the photon flux at one sun, helping to justify and understand the J_{SC} values derived from the *J/V*-measurements of the investigated solar cell:

$$J_{int} = q \int_0^{\infty} \Phi\ (\lambda) * EQE\ _{diode}(\lambda)\ d\lambda \tag{2.26}$$

Where J_{int} is the integrated photocurrent, q is the elemental charge and $\Phi(\lambda)$ is the photon flux of one sun.

An exemplary EQE spectrum of a $Cs_2AgBiBr_6$ solar cell is shown in Figure 2.14.

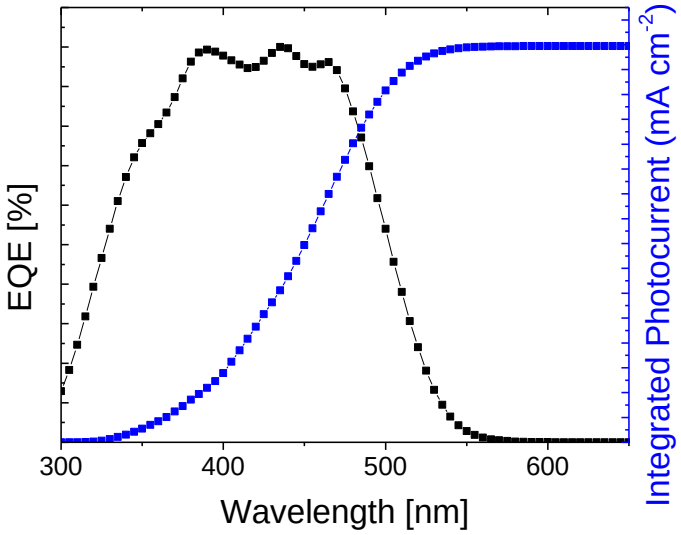

Figure 2.14: Exemplary EQE curve (black) and integrated photocurrent (blue) of a $Cs_2AgBiBr_6$ solar cell.

To justify the J_{SC} of the solar cell, the J_{int} value should be within 90 % of the J_{SC}.

2.14 Electroluminescence Spectroscopy (EL)

For electroluminescence (EL) characterization, a full solar cell is required. For this measurement, the normal operating mode of the solar cell is basically inversed and charge carriers are injected using an external forward bias, to induce recombination within the device.[3] Similar to PL measurements, the recombination must be radiative in order to detect photon emission.

Since this measurement is the reciprocal action to the standard operation of a solar cell, all important physical processes influencing the photovoltaic performance of a solar cell (recombination, resistive, and optical losses) can be determined with this technique. Hence, the EL intensity I_{EL} emitted at any surface-position is given by equation (2.27).[24]

$$I_{EL} = [1 - R] * Q_{IQE} * \Phi_{BB} * e^{\left(\frac{qV}{kT}\right)} = Q_{EQE} * \Phi_{BB} * e^{\left(\frac{qV}{kT}\right)} \qquad (2.27)$$

Where $Q_{EQE} = [1 - R] * Q_{IQE}$ is the external quantum efficiency determined by the front surface reflectance R and the internal quantum efficiency Q_{IQE}, Φ_{BB} is the spectral photon density of a blackbody, V is the internal junction voltage (resulting voltage: Applied voltage corrected with possible resistances) and kT/q is the thermal voltage.

Using this equation, almost all losses occurring in solar cells can be determined, as the external quantum efficiency (EQE) expresses the recombination and optical losses, while the internal voltage gives information about the resistive losses.

2.15 Nuclear Magnetic Resonance (NMR) Spectroscopy

Nuclear magnetic resonance spectroscopy is a very valuable tool to investigate and characterize molecules as well as solids. The method is based on the excitation of nuclear magnetic spin momenta. Due to the rotation of an atom core (spin angular momentum), a nuclear magnetic momentum $\vec{\mu}$ is induced as described by the product of the spin angular momentum $\vec{S}$ and the gyromagnetic ratio γ according to equation (2.28)

$$\vec{\mu} = \vec{S} * \gamma \tag{2.28}$$

To be NMR active, a nucleus must express this spin momentum, which occurs only if the number of protons, neutrons or both is odd. Hence, only selected isotopes such as ^{1}H, ^{13}C, ^{15}N or ^{19}F are NMR active.

The magnetic momentum of a nucleus can have different possible orientations that are defined by the quantum number I. For each quantum number $I, 2I + 1$ orientations exist that are all energetically equal in the absence of an external magnetic field. If nuclei with such a permanent spin momentum are now exposed to an external homogeneous magnetic field (eq.(2.29)), the possible quantum states I assume different energy levels:

$$\Delta E = \gamma * \hbar * B_0 \tag{2.29}$$

With ΔE for the needed excitation energy, γ the gyromagnetic ratio, $\hbar$ the reduced Planck constant and B_0 the external magnetic field.

If now a radio frequency signal is applied, and upon absorption of this energy, a transition between the quantum states can occur to fulfil the resonance condition of eq.(2.30)

$$\omega = \gamma * B_{loc} = \gamma(B_0 + B_{int}) \tag{2.30}$$

Where ω is the resonance frequency, γ the gyromagnetic ratio, and B_{loc} the local magnetic field which is derived from the external (B_0) and the internal (B_{int}) magnetic field.

The difference of the external and local magnetic field can be measured and gives information about the chemical and energetic surroundings of the investigated isotope. Depending on the chemical and electrical surroundings of, e.g., an ^{1}H isotope, the signal can split in a characteristic way and hence give information about the number and type of the neighboring nuclei and about their electronic coupling with the absorber atom. Depending on the types of atoms and their chemical environment, the obtained signals occur in a characteristic energy region of the spectrum.[25]

2.16 Thermogravimetric Analysis (TGA)

Thermogravimetric analysis is a powerful tool to investigate the thermal properties of a wide range of compounds. During the measurement, the sample is heated with a constant rate to a high temperature (between 600 and 900 °C in this work), while the mass of the sample is simultaneously tracked with a so-called thermobalance. To desorb volatile components (e.g. solvents), a constant gas flow such as nitrogen is employed during the measurement. By using TGA, degradation temperatures such as the 5 % mass-loss temperature ($T_d^{5\%}$) can be measured. Using the simultaneous thermobalance allows to perform differential scanning calometry (DSC) measurements to not only track the mass of the investigated material, but also to detect thermal effects which do not alter the mass of the material itself. With this characterization method, exothermic and endothermic processes can be detected, and material constants such as the melting temperature (T_m) or the glass transition temperature (T_g) can be measured, values that are highly important for solar cell materials.[26]

2.17 References

[1] Y. Waseda, E. Matsubara, K. Shinoda, *X-Ray Diffraction Crystallography*, Springer Berlin Heidelberg, Berlin, Heidelberg **2011**.

[2] N. Widjonarko, *Coatings* **2016**, *6*, 54.

[3] *Advanced characterization techniques for thin film solar cells*, Wiley-VCH Verlag, Weinheim, Germany **2016**.

[4] J. Schlipf, P. Müller-Buschbaum, *Adv. Energy Mater.* **2017**, *7*, 1700131.

[5] Purdue University, *Scanning Electron Microscope* **2021**, https://www.purdue.edu/ehps/rem/laboratory/equipment%20safety/Research%20Equipment/sem.html.

[6] Roger Nix, *Photoelectron Spectroscopy* **2021**, https://chem.libretexts.org/@go/page/25383.

[7] J. Benigna, *J. Chem. Educ.* **2014**, *91*, 1299.

[8] Perkin Elmer Inc. (Ed.), *Application Note on Transmission Measurements Using Integrating Spheres* **2004**.

[9] J. Tauc, R. Grigorovici, A. Vancu, *phys. stat. sol. (b)* **1966**, *15*, 627.

[10] V. Sarritzu, N. Sestu, D. Marongiu, X. Chang, S. Masi, A. Rizzo, S. Colella, F. Quochi, M. Saba, A. Mura, G. Bongiovanni, *Scientific reports* **2017**, *7*, 44629.

[11] Edinburgh Instruments, *TCSPC - What is Time-Correlated Single Photon Counting?*, https://www.edinst.com/blog/what-is-tcspc/.

[12] PicoQuant (Ed.), *Technical Note on Time-Correlated Single Photon Counting* **2014**.

[13] T. J. Savenije, A. J. Ferguson, N. Kopidakis, G. Rumbles, *J. Phys. Chem. C* **2013**, *117*, 24085.

[14] J. G. Webster, *Wiley Encyclopedia of Electrical and Electronics Engineering*, Wiley **1999**.

[15] H. J. Snaith, M. Grätzel, *Appl. Phys. Lett.* **2006**, *89*, 262114.

[16] C. M. Cardona, W. Li, A. E. Kaifer, D. Stockdale, G. C. Bazan, *Advanced materials (Deerfield Beach, Fla.)* **2011**, *23*, 2367.

[17] American Society for Testing and Materials. Committee G03 on Weathering and Durability, *Standard tables for reference solar spectral irradiances: direct normal and hemispherical on 37° tilted surface*, ASTM international **2003**.

[18] W. Tress, *Organic Solar Cells: Theory, Experiment, and Device Simulation*, Springer International Publishing, Cham, s.l. **2014**.

[19] H. J. Snaith, A. Abate, J. M. Ball, G. E. Eperon, T. Leijtens, N. K. Noel, S. D. Stranks, J. T.-W. Wang, K. Wojciechowski, W. Zhang, *The journal of physical chemistry letters* **2014**, *5*, 1511.

[20] W. Tress, M. Yavari, K. Domanski, P. Yadav, B. Niesen, J. P. Correa Baena, A. Hagfeldt, M. Graetzel, *Energy Environ. Sci.* **2018**, *11*, 151.

[21] P. Caprioglio, C. M. Wolff, O. J. Sandberg, A. Armin, B. Rech, S. Albrecht, D. Neher, M. Stolterfoht, *Adv. Energy Mater.* **2020**, *10*, 2000502.

[22] W. Ananda, in *2017 15th International Conference on Quality in Research (QiR) International Symposium on Electrical and Computer Engineering*, IEEE **72017**, p. 450.

[23] P. Hierrezuelo-Cardet, A. F. Palechor-Ocampo, J. Caram, F. Ventosinos, D. Pérez-del-Rey, H. J. Bolink, J. A. Schmidt, *Journal of Applied Physics* **2020**, *127*, 235501.

[24] U. Rau, *Phys. Rev. B* **2007**, *76*.

[25] M. Hesse, H. Meier, B. Zeeh, *Spektroskopische Methoden in der organischen Chemie*, Georg Thieme Verlag **2005**.

[26] E. Mansfield, A. Kar, T. P. Quinn, S. A. Hooker, *Analytical chemistry* **2010**, *82*, 9977.

3 The Bottlenecks of $Cs_2AgBiBr_6$ Solar Cells: How Contacts and Slow Transients Limit the Performance

This chapter is based on the following publication:

Maximilian T. Sirtl, Firouzeh Ebadi, Bas T. van Gorkom, Patrick Ganswindt, René A. Janssen, Thomas Bein* and Wolfgang Tress*, *Adv. Opt. Mater.* 2021, 2100202

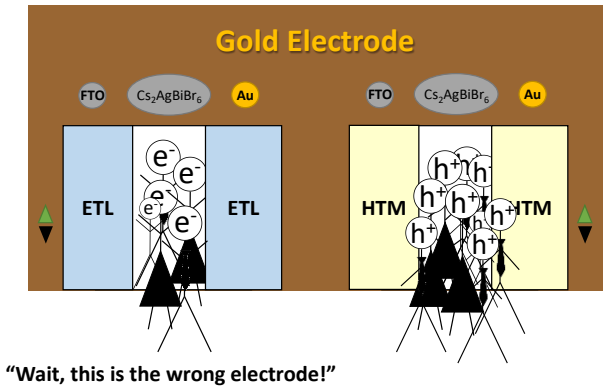

Keywords: double perovskites, electroluminescence, internal qunantum efficiency, lead-free perovskites, perovskite solar cells

3.1 Abstract

$Cs_2AgBiBr_6$ has attracted much interest as a potential lead-free alternative for perovskite solar cells. Although this material offers encouraging optoelectronic features, severe bottlenecks limit the performance of the resulting solar cells to a power conversion efficiency of below 3 %. Here, the performance-limiting factors of this material are investigated in full solar cells featuring various architectures. It is found that the photovoltaic parameters of $Cs_2AgBiBr_6$-based solar cells strongly depend on the scan speed of the *J/V* measurements, suggesting a strong impact of ionic conductivity in the material. Moreover, a sign change of the photocurrent for bias voltages above 0.9 V during the measurement of the external quantum efficiency (EQE) is revealed, which can be explained by non-selective contacts. The radiative loss of the V_{OC} from sensitive subgap-EQE measurements is calculated and it is revealed that the loss is caused by a low external luminescence yield and therefore a high non-radiative recombination, supported by the first report of a strongly red shifted electroluminescence signal between 800 and 1000 nm. Altogether, these results point to a poor selectivity of the contacts and charge transport layers, caused by poor energy level alignment that can be overcome by optimizing the architecture of the solar cell.

3.2 Introduction

Due to their attractive optoelectronic properties and processing pathways, the interest in lead-based halide perovskites ($APbX_3$; A = methylammmonium/formamidinium/Cs/Rb; X = Cl, Br, I) sky-rocketed during the last decade.[1] The nature and energy of the widely tunable bandgap, a sufficiently high charge carrier mobility, and high defect tolerance as well as the simple low-temperature processing pathways make these materials promising candidates for applications such as X-ray detectors,[2] light emitting diodes[3–5] and solar cells with power-conversion efficiencies having approached 25 %.[5–7]

Even though lead-based perovskites have outstanding potential for being implemented in solar cells, so far their large-scale application has been challenging due to the high toxicity of lead,[8] as well as several issues regarding the low stability towards ambient conditions, UV-light and humidity.[1] While stability issues can be addressed to a large extent by intelligent device- or materials-design[5,9–11] and proper encapsulation,[12] the toxicity issue can be addressed by substitution of the lead(II) ions with homovalent alternatives such as Sn^{2+} ions in a standard halide perovskite structure,[13] the use of Bi^{3+} or Sb^{3+} as a substitute for Pb^{2+} atom to form

$Cs_3Bi_2X_9$ (X = Cl/Br/I)[13] or by a combination of a monovalent and a trivalent metal ion, resulting in one of the emerging double perovskites $A_2M^IM^{III}X_6$ (A = MA, Cs; $M^I = Ag^+$, In^+, Au^+, Cu^+; $M^{III} = Bi^{3+}$, Sb^{3+}; X = Cl, Br), that have been realized both in 3D, as well as in low-dimensional Ruddlesden-Popper structures.[14–18]

Among the double perovskites investigated to date, $Cs_2AgBiBr_6$ appears to be one of the most promising candidates, featuring a long charge carrier lifetime of up to 550 ns in single crystals and above 200 ns in thin films,[19,20] high stability and good solution processability, as well as a decent theoretically possible power conversion efficiency (PCE) for solar cells.[19,21] Although first solar cell reports were published several years ago with an initial PCE of about 2.5 %,[22] researchers so far have struggled to achieve a PCE exceeding 2.84 % by using this material as absorber.[20,23–30] Besides addressing the possibility to tune the rather large and indirect bandgap and more generally the absorption onset using additives and alloying,[31–35] several studies have focused on the identification of the limiting factors hampering the performance of this material in order to overcome these issues and to push the PCE of the solar cells towards the theoretical limit. Kentsch et al. revealed a large exciton binding energy in this material,[36] and others showed that the material suffers from a rather large trap density, while a high annealing temperature of above 250 °C is necessary in order to form the perovskite film without any secondary phases in the film.[22] Most recently, Longo et al. reported on limiting factors in complete solar cells, revealing that one factor hampering the solar cell efficiency is a small electron diffusion length while the hole-diffusion length is rather large.[37] Much effort has been put into the optimization of crystallinity and orientation of thin films of $Cs_2AgBiBr_6$,[20,38] as well as interface modifications,[23,39,40] the improvement of the optoelectronic properties of single crystals[41,42] or regarding the origin of the photoluminescence (PL).[43,44] Yet, there is still no consensus on how to exactly interpret the absorption and emission features[44,45] and how to explain the severe differences between reported optical data of nominally the same material. In particular, whether and how they affect solar-cell performance remains to be understood.

In this work, we analyze the limiting factors of full solar cell devices based on $Cs_2AgBiBr_6$, comparing devices with different architectures and comprising $Cs_2AgBiBr_6$ films obtained through different synthesis methods. We investigate the radiative voltage limit using sensitive external quantum efficiency (EQE) and photo- and electroluminescence (EL) measurements. We examine the internal photovoltaic (PV) quantum efficiency as a function of voltage and

scan rate and reveal that photocurrent collection and charge carrier recombination strongly depend on the conditions set by the preceding voltage. Open circuit voltage transients provide further evidence regarding the interplay between properties of the contacts and possibly mobile ionic charges in the perovskite, thus modifying the selectivity of the contacts and interfacial recombination. We demonstrate that the latter process turns out to be a major loss mechanism.

3.3 Results and Discussion

Our recent work has established the successful synthesis of thin film solar cells based on $Cs_2AgBiBr_6$ using both the antisolvent method under inert conditions[20] and the one-step spincoating method under ambient conditions without an antisolvent.[22] After deposition of the thin films using both techniques, we obtained phase pure, yellow films that were opaque by using no antisolvent at ambient conditions (inset Figure 3.1a)) and transparent by using 2-propanol as an antisolvent inside the glovebox (inset Figure 3.1a)). The different spincoating techniques result in a large difference in the film thickness, which was determined to be around 130 ± 12 nm for the antisolvent method and 550 ± 35 nm when using no antisolvent. The layer thicknesses were determined using the SEM images in Figure S 3.1. The Bragg-Brentano X-ray diffraction (XRD) patterns in Figure 3.1 a confirm the phase-pure formation of the desired $Cs_2AgBiBr_6$ thin films after annealing at 275 °C for 5 min and at 285 °C for 5 min, respectively.

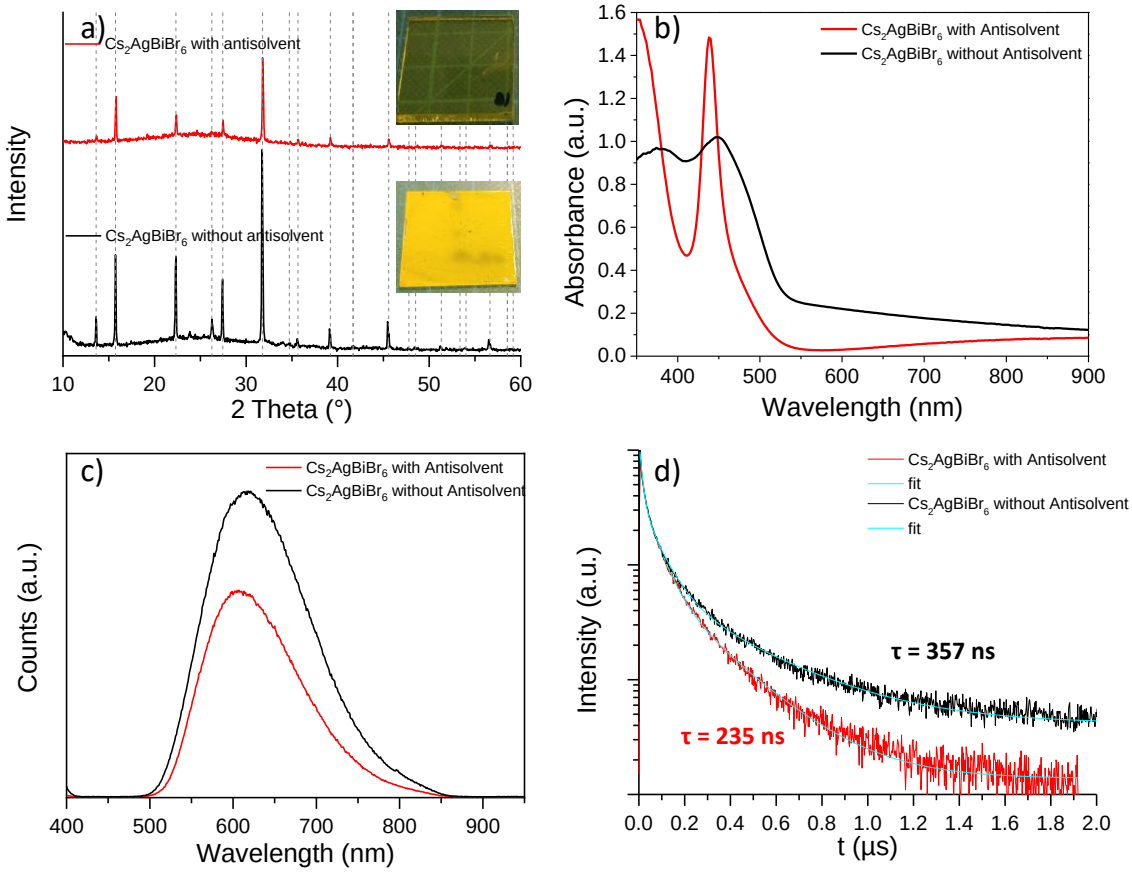

Figure 3.1: XRD patterns, PL spectra, and UV/Vis spectra of the differently spincoated $Cs_2AgBiBr_6$ thin films. a) XRD patterns measured in Bragg-Brentano geometry of the thin films spincoated without (black line) and with antisolvent (red line), with an image of the resulting films in the respective inset. The peaks of the theoretical pattern are indicated by grey, dashed droplines. b) The respective UV/Vis spectra of the thin films spincoated with (red line) and without antisolvent (black line), c) plots of the steady state PL measurements for the thin films spincoated with (red line) and without antisolvent (black line). d) Results of the TCSPC measurements with the films spincoated with (red line) and without (black line) antisolvent. Triple-exponential fits are shown in turquoise, giving the longest-living fraction of 235 ns with the antisolvent and of 357 ns without the antisolvent.

The XRD patterns show differences in the number and intensity of the peaks, which match all with the theoretical pattern obtained from single crystal data. The difference between the patterns could be explained by the large difference in the thickness of the thin films, which is more than three times greater for the films fabricated without using an antisolvent. The PL spectra in Figure 3.1c) show for both films the characteristic broad peak with a maximum around 605 and 615 nm, which is in agreement with literature reports.[22,27,28,30] The rather small difference in the peak intensity between the two synthesis methods indicates a luminescence

yield of the same order of magnitude for the films resulting from the different methods. A change can also be seen in the photoluminescence lifetimes of the different films (Figure 3.1d). While both values are in the range reported in the literature, films spincoated using the antisolvent method show a charge carrier lifetime of 235 ns (red line) while the films spincoated without antisolvent show an increase of the lifetime to 357 ns (black line). Although this trend confirms the trend in the PL intensity, it is a minor effect, which hardly influences the solar cell performance.

The biggest difference between thin films resulting from the different synthesis methods can be found in the UV/Vis spectra in Figure 3.1b) obtained from transmission measurements. Whereas the absorption onset at around 550 nm (2.3 eV) remains unmodified, the absorbance in this spectral range (450 to 550 nm) is increased for the film without antisolvent (in contrast to the sharp peaks discussed below). This trend is consistent with an increased thickness of the film without antisolvent, although not quantitatively matching the changes of the thickness by a factor of four, which might be explained by the mesoporous TiO_2 present in the film and a non-compact film. The underlying transition at the absorption onset is known from calculations to be an X to L point transition,[46] confirming the experimental reports on the indirect bandgap.[14,19] Strikingly, the absorption features peaking at 340 nm (3.6 eV) and 440 nm (2.8 eV), are less pronounced and even lower for the much thicker film. Commonly, they are attributed to direct transitions,[46] where there seems some dispute whether the narrow peak at 440 nm is due to a strongly bound exciton (direct bandgap at 387 nm (3.2 eV))[36,45] or not.[44] In our case, the decrease of the two peaks is correlated, which would be consistent with the same direct nature of the transitions (free, exciton). Nevertheless, the question remains why this transition is so strong in the thinner film and why it does not scale with the film thickness as the indirect transition at the absorption onset at 550 nm does. We speculate whether this observation could be due to a morphology effect related to a preferred orientation of the thinner film or a high presence of scattering nanocrystals.[47] An alternative explanation would be that different amounts of impurity phases (undetected by diffraction) are present in the two films. Possible crystalline secondary phases can however be excluded by the experimental XRD pattern. Moreover, the used deposition techniques are well known to produce $Cs_2AgBiBr_6$-thin films without detectable impurity phases.

The direct impact on the performance of solar cells based on the different films will be discussed further in the remainder of the paper.

3.3.1 Solar Cells

To better understand the performance limiting factors of $Cs_2AgBiBr_6$ solar cells, we fabricated devices using the architecture FTO/ETL/$Cs_2AgBiBr_6$/HTM/Au with either compact TiO_2 (c-TiO_2) or a combination of c-TiO_2 and mesoporous (mp) TiO_2 as electron transport layer (ETL), as well with either 2,2',7,7'-tetrakis[N,N-di(4-methoxyphenyl)amino]-9,9'-spirobifluorene (Spiro-OMeTAD) or poly(3-hexylthiophen) (P3HT) as hole transporting material (HTM). The solar cells that use mp-TiO_2 were fabricated without using an antisolvent, while cells comprising solely c-TiO_2 were prepared using an antisolvent-process. The active area was approximately 0.16 cm^2 and reduced to 0.083 cm^2 by an aperture for the measurements under the solar simulator.

The main focus of this study was put on a detailed investigation of solar cells with c-TiO_2 as ETL and P3HT as HTM, hence the number of solar cells using these materials exceeds the number of cells with other HTM/ETL combinations. Table 3.1 shows the parameters of the solar cells investigated in this study. The box plots of the J_{SC}, V_{OC}, *FF* and PCE data of all solar cells measured in this work can be found in Figure S 3.2, Supporting Information.

Table 3.1: Solar cell parameters of all solar cells investigated in this study using different ETL/HTM combinations. The first value shows the respective value of the champion cell while the averages with standard deviation are shown in parantheses.

Number of cells	J_{SC} [mA/cm^2] (Avg)	V_{OC} [V] (Avg)	*FF* [%] (Avg)	PCE [%] (Avg)
FTO/c-TiO_2/$Cs_2AgBiBr_6$/P3HT/Au				
170	1.35 (1.26 ± 0.13)	1.08 (0.98 ± 0.05)	71 (63 ± 5)	1.04 (0.78 ± 0.13)
FTO/c-TiO_2/$Cs_2AgBiBr_6$/Spiro-OMeTAD/Au				
44	1.38 (1.10 ± 0.10)	0.87 (0.74 ± 0.11)	57 (57 ± 8)	0.70 (0.46 ± 0.09)
FTO/c-TiO_2/mp-TiO_2/$Cs_2AgBiBr_6$/P3HT/Au				
27	2.35 (2.10 ± 0.31)	0.85 (0.90 ± 0.07)	55 (51 ± 6)	1.10 (0.95 ± 0.10)
FTO/c-TiO_2/mp-TiO_2/$Cs_2AgBiBr_6$/Spiro-OMeTAD/Au				
20	2.50 (2.38 ± 0.13)	1.02 (0.93 ± 0.09)	55 (54 ± 6)	1.40 (1.20 ± 0.12)

The results show values for the PCE that are statistically reliable for further investigation of the optoelectronic properties of the films, as well as for the determination of the performance limiting factors with PCE values between 0.7 and 1.4 %.

Cells comprising Spiro-OMeTAD on compact TiO_2 show the lowest efficiency of all cells with 0.7 % PCE for the champion cell and 0.46 % on average for more than 40 solar cells. This is

related to a rather small V_{OC} and *FF* of only 0.87 (0.74) V and 57 %, respectively. Cells comprising P3HT as HTM on compact TiO_2 show a remarkably higher PCE with values above 1 % and an increase in both *FF* and J_{SC} by 10 % and 25 % on average. Both architectures however suffer from a very low J_{SC}.

The biggest difference between all cells can be found in the J_{SC} of the mp-TiO_2 and c-TiO_2 cells, which agrees with early reports on $Cs_2AgBiBr_6$ solar cells[22] and indicates enhanced charge collection by the mesoporous structure. Moreover, using the one-step spincoating technique allows one to produce thicker films compared to the antisolvent method, however solar cells produced with this method suffer from a rather rough film morphology. Therefore, to access the benefits of a thicker layer with this technique, a mesoporous scaffold is necessary for an effective charge extraction.

The results show that a further optimization of the mp-cells is necessary as the devices fabricated on the mp scaffold suffer from a rather low *FF*. Still, the increased J_{SC} results in a higher PCE for all cells on mp-TiO_2 compared to planar devices. The comparison of the Spiro-OMeTAD cells shows an increase in the PCE by 100 % for the champion cell and even higher in average which is also caused by an increase in the V_{OC}. The P3HT devices do not show such a large improvement in the PCE, which can be related to a rather low V_{OC} in addition to the low *FF*. The results show the potential of mp-TiO_2 to help to optimize charge extraction from the $Cs_2AgBiBr_6$ double perovskites.

From all measured solar cells, we selected a smaller group that show a representative performance to investigate the impact of a fast *J/V*-scan on the chosen cells as discussed in the following.

3.3.2 Scan-Rate Dependent *J/V* Curves

The scan speed used to identify the *J/V* characteristics of solar cells reportedly shows a large influence for devices based on ionic materials such as perovskites.[48–50] This circumstance led to a standardization of the measurement protocol for lead-based perovskites and the necessity for reporting this protocol in publications.[51] However, this is not yet the case for reports on the efficiency of $Cs_2AgBiBr_6$ based solar cells, where scan speeds are commonly not reported, although hysteresis is mentioned in some publications[28,40] and the material is assumed to show ionic conductivity.[24]

To further investigate the effect of the ionic character of the material on the solar-cell performance, we performed *J/V*-scans at different scan speeds, varying from 0.01 V-steps up to 1 V-steps under 1 sun illumination for several of the solar cells discussed above. The results in Table 3.2 and Figure 3.2 show that changing the scan-speed strongly influences the photocurrent obtained from the solar cells for all architectures.

Table 3.2: Overview of the solar cells of various architectures measured with different scan speeds. The table shows the different J_{SC} values for varying scan speeds (0.01 V/step – 1 V/step where one step takes one second) together with the relative J_{SC}-change in percent. Underneath we show the resulting PCE of the corresponding cell and scan. We note that the V_{OC} and FF values for scans faster than 0.1 V/step were not reliable for calculating the PCE. The Hysteresis Index was calculated as (PCE(reverse)-PCE(forward))/PCE(reverse). The captions in the grey bars indicate the different architectures used for the solar cells.

Scan-Speed	0.01 V/step	0.05 V/step	0.1 V/step	0.5 V/step	1 V/step
FTO/c-TiO_2/$Cs_2AgBiBr_6$/Spiro-OMeTAD/Au					
J_{SC}	1.2 mA/cm^2	1.4 mA/cm^2	1.6 mA/cm^2	2.5 mA/cm^2	2.6 mA/cm^2
Increase		16 %	33 %	108 %	116 %
PCE	0.56 %	0.62 %	0.66 %		
Hysteresis Index	0.16	0.27	0.33		
FTO/c-TiO_2/mp-TiO_2/$Cs_2AgBiBr_6$/Spiro-OMeTAD/Au					
J_{SC}	1.8 mA/cm^2	2.3 mA/cm^2	2.8 mA/cm^2	3.6 mA/cm^2	3.7 mA/cm^2
Increase		27 %	56 %	100 %	1,5 %
PCE	1.23 %	1.29 %	1.33 %		
Hysteresis Index	0.27	0.36	0.35		
FTO/c-TiO_2/$Cs_2AgBiBr_6$/P3HT/Au					
J_{SC}	1.2 mA/cm^2	1.4 mA/cm^2	1.5 mA/cm^2	1.9 mA/cm^2	2.0 mA/cm^2
Increase		16 %	25 %	58 %	67 %
PCE	0.82 %	0.88 %	0.92 %		
Hysteresis Index	0.10	0.27	0.39		
FTO/c-TiO_2/mp-TiO_2/$Cs_2AgBiBr_6$/P3HT/Au					
J_{SC}	1.7 mA/cm^2	1.9 mA/cm^2	2.1 mA/cm^2	2.3 mA/cm^2	2.4 mA/cm^2
Increase		12 %	24 %	35 %	41 %
PCE	0.97 %	1.02 %	1.04 %		
Hysteresis Index	0.03	0.13	0.18		

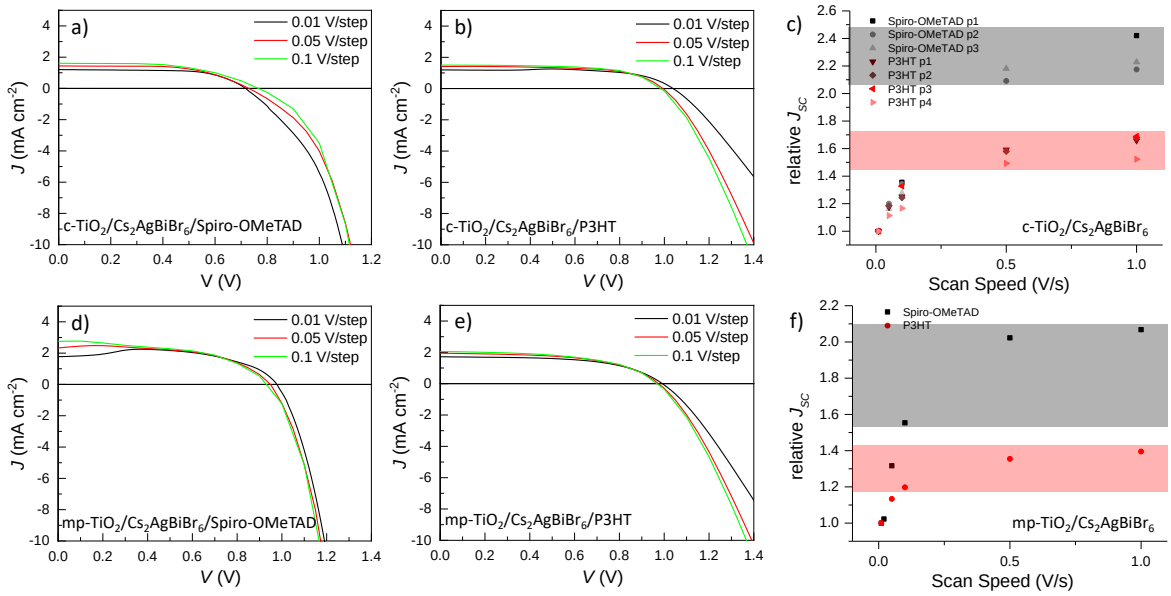

Figure 3.2: J/V-curves of different solar cell architectures measured with different scan-speeds. a) FTO/c-TiO_2/$Cs_2AgBiBr_6$/Spiro-OMeTAD/Au, b) FTO/c-TiO_2/$Cs_2AgBiBr_6$/P3HT/Au, d) FTO/c-TiO_2/mp-TiO_2/$Cs_2AgBiBr_6$/Spiro-OMeTAD/Au, e) FTO/c-TiO_2/mp-TiO_2/$Cs_2AgBiBr_6$/Spiro-OMeTAD/Au. All J/V-curves have the same color-coding with black for 0.01 V/step, red for 0.05 V/step and green for 0.1 V/step. c) Relative J_{SC}-values of several different solar cells with the architecture FTO/c-TiO2/Cs2AgBiBr6/HTM/Au with Spiro-OMeTAD (black) and P3HT (red) as HTMs. f) Relative J_{SC}-values of one solar cell each with the architecture FTO/c-TiO_2/mp-TiO_2/$Cs_2AgBiBr_6$/HTM/Au with Spiro-OMeTAD (black) and P3HT (red) as HTMs. Panels c) and f) are provided with a guidance for the eye for the value-increase of the highest J_{SC}-changes, with black for Spiro-OMeTAD as HTM and red for P3HT as HTM.

The biggest effect can be seen with cells comprising Spiro-OMeTAD as an HTM, where the J_{SC} increased from 1.2 mA/cm^2 for 0.01 V/step to 2.6 mA/cm^2 for 1 V/step for the cells on c-TiO_2, while the change on mp-TiO_2 is similar with an increase of 1.8 mA/cm^2 to 3.7 mA/cm^2 which corresponds to a relative increase of 116 % and 105 %, respectively. When using P3HT as an HTM, a similar effect was observed which, however, is not as big as for Spiro-OMeTAD with an increase of the J_{SC} from 1.2 mA/cm^2 to 2 mA/cm^2 (ΔJ_{SC} = 67 %) for c-TiO_2 and 1.7 mA/cm^2 to 2.4 mA/cm^2 (ΔJ_{SC} = 41 %) for mp-TiO_2. In Figure 3.2 a), b), d) and e), we show the *J/V* curves obtained with the measurements of up to 0.1 V/step. As expected, the PCE values of the investigated cells increase with the resulting J_{SC} by factors of 11 to 15 % for planar devices and between 7 and 8 % for the mp devices. We note that the curves show no change for the V_{OC} and the *FF*. We further observed a change in the hysteresis of the investigated cells.

Figure 3.2d) shows another remarkable effect of faster scanning: For 0.01 V/step, the *J/V*-curve expresses a large bump, which is caused by a J_{SC} smaller than the *J*-values at $V > 0$ V and may be attributed to ionic drifts within the solar cell happening on a similar time scale as the *J/V* scan. The changing density of accumulated ionic charges during the *J/V* scan results in a modified charge-carrier collection efficiency, which is reduced for lower voltages, where ions screen the built-in potential. As this trend of reduced charge collection efficiency at J_{SC} is against the electronic *J/V* curve, where charge collection efficiency increases from open circuit to short circuit, such a bump can occur.[52,53] This bump, however, vanished for faster scan speeds, which further emphasizes the scan-speed dependence of the performance of the solar cell.

While the cells measured at slow scan speeds show only very low or negligible hysteresis, this effect increases with faster scan-speed, an effect observed for all investigated cells. Interestingly, the hysteresis is smaller for P3HT as HTM and mp-TiO_2 as ETL. Especially solar cells with mp-TiO_2 and P3HT show almost no hysteresis (HI = 0.03) while cells comprising Spiro-OMeTAD in both architectures show a rather large hysteresis compared to cells with P3HT as HTM, further emphasizing the strong influence of the HTM on the effect of the ionic behavior of the solar cells.

As the results show a big impact of the *J/V*-scan speed on the solar cell performance, it is necessary to consistently report the exact measurement settings of the reported solar cells and, if possible, provide MPP tracked data.

3.3.3 Internal PV Quantum Efficiency and Transient Phenomena

While the *J/V* scan speed used to characterize the solar cells can have a large impact on the resulting performance parameters and increases the J_{SC}, the experimentally achieved current is still lower than what would be expected from optical absorption. To gain further insights, we investigated the external quantum efficiency (EQE) spectra of the solar cells and calculated the internal quantum efficiency to discriminate between absorption and charge-carrier collection losses. The black line in Figure 3.3a) shows the EQE, measured at short circuit for a planar device. The EQE of the planar device roughly follows the absorption features in Figure 3.1d) and mirrors the transmission spectrum of a perovskite film on glass/FTO, shown in blue. The EQE of the planar device cannot be enhanced with bias light and yields a current of 1.26 mA/cm^2 under AM1.5G, which is in good agreement with the solar simulator data. Contrary to

that, the EQE spectra for a mesoporous device, shown in Figure 3.3b), demonstrate that blue bias light enhances the EQE. However, this behavior is well known for dye-sensitized solar cells on mesoporous TiO_2 and attributed to reduced surface recombination of mesoporous TiO_2 for higher photogenerated charge carrier densities.[54]

In a next step, the EQE spectra were measured as a function of the applied voltage for the planar device (Figure 3.3 c). The EQEs hardly change for voltages up to 0.8 V, which is consistent with a decently high FF of these devices (>70%, Table 3.1). However, independent of bias light and the actual V_{OC} obtainable under the illumination by the EQE measurement (0.35 V without, and 0.86 V with bias), the signal changes rapidly at 0.9 V (Figure S 3.3, Supporting Information). As indicated by the massive drop in the EQE for the 0.9 V bias, the EQE signal changes sign and the (absolute) EQE increases with higher voltages. The strong drop of the EQE at 0.9 V is an indication for a built-in potential of around 0.9 V. The change of sign of the EQE and photocurrent (difference between current under illumination and in the dark) is not uncommon for emerging PV and can be explained either by a photoconductivity effect, which enhances the forward injection current, or by the current of the photogenerated charge carriers themselves changing sign. Due to the high IQEs under forward bias, we think the former is more likely.[55]

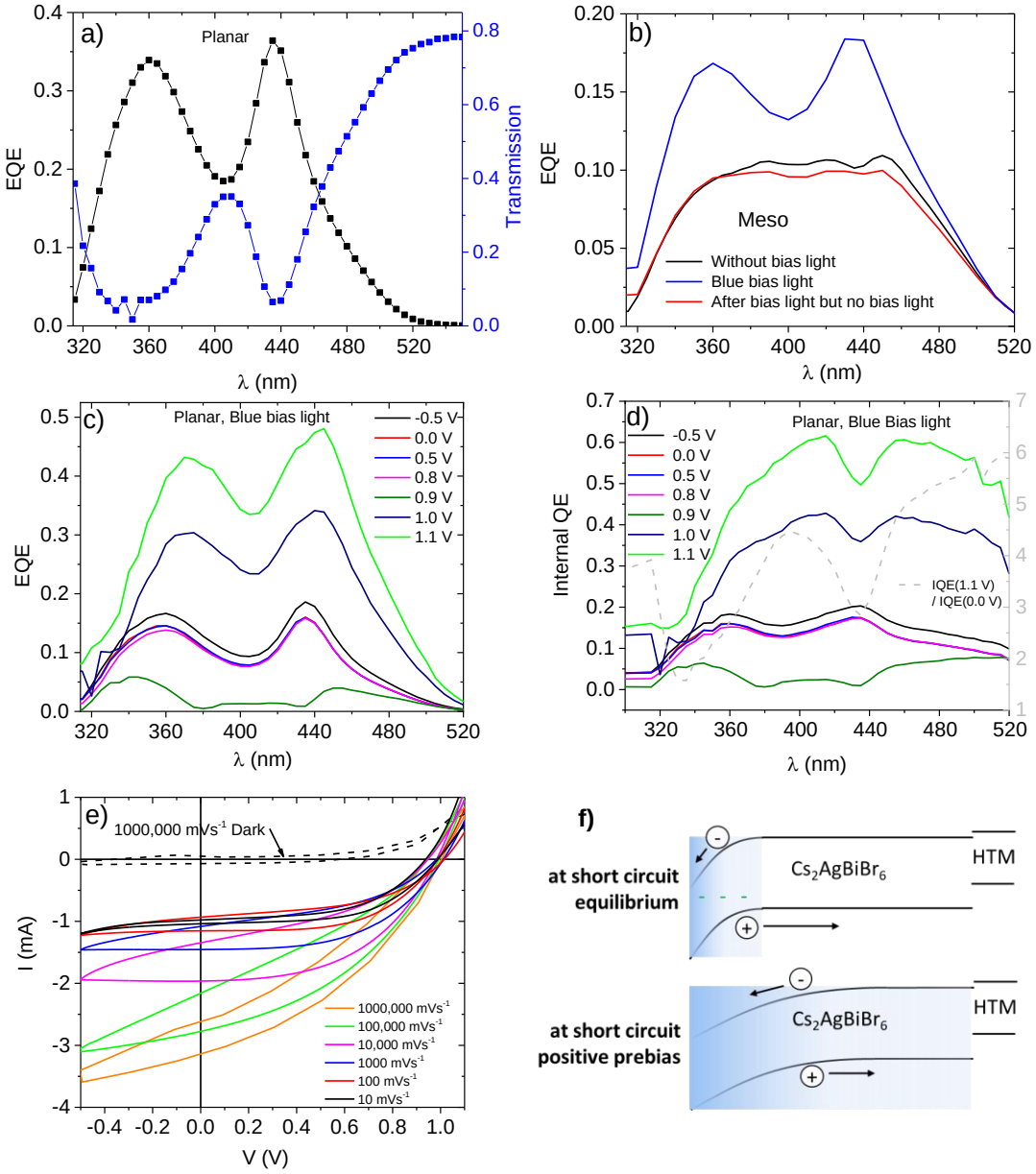

Figure 3.3: The current-collection bottleneck. a) EQE (black line) of planar device, plotted together with the transmission spectrum (blue line) of glass/FTO/$Cs_2AgBiBr_6$. b) EQE of mesoporous device with and without bias light, c) EQE of planar device for various applied voltages. For voltages larger than 0.9 V, the photocurrent changes sign. d) IQE derived from data in (c). The dashed line (right axis) shows the IQE at 1.1 V relative to those below 0.9 V. e) J/V loops at different scan rates and after prebias at 1.1 V. The dark curve at 1000 V/s shows that capacitive effects are still negligible. f) Sketch of proposed band diagrams, indicating that mainly a narrow region close to the ETL commonly contributes to photocurrent (shaded). This region gets extended after a positive prebias, possibly because negative ionic charges close to the ETL were removed.

Interestingly, not only absolute values, but the spectral shapes of the EQE change, yielding for higher voltages a more pronounced EQE in spectral regions where the EQE spectra recorded at voltages below 0.9 V have a smaller signal. To better assess this effect, we approximate the IQE (or charge carrier collection efficiency) by dividing the EQE by the absorption spectrum deduced from the measured and normalized transmission data of the film (from Figure 3.3a). Please note that for a more accurate description optical modelling would be required. However, as the subsequent layers (P3HT, Au) are hardly reflective but absorptive in the spectral range under investigation, reflection and interference effects are negligible. The IQEs obtained in this way, plotted in Figure 3.3d), are reliable and reveal a strong dependence on the wavelength. For voltages < 0.9 V, the IQE is highest in the absorption maxima, as also observed in ref. [37] where it is attributed to a low electron diffusion length reducing the collection probability of charges generated further away from the TiO_2. As the IQE of the two peaks at 360 nm and 435 nm is comparable and assuming that the absorption at 435 nm is excitonic,[36] we do not see a lower probability for harvesting photocurrent from excitonic excitations.

We do not wish to claim that we can extract a value for the diffusion length from these device measurements. The diffusion length is a parameter of a material or film, which has been reported to be larger than 100 nm for electrons and holes[56] and high EQEs have been achieved with $Cs_2AgBiBr_6$.[23] Instead, the IQE trend can as well be explained by space charge layers and field distributions arising in the solar cell due to a built-in potential, doping, and recombination processes at interfaces. Furthermore, an almost complete quenching of the $Cs_2AgBiBr_6$ photoluminescence in the device indicates that neither excitons nor immobile charges (i.e. those that do not contribute to J_{SC}) remain in the film but reach the "wrong" contacts and recombine instead (Figure S 3.4, Supporting Information). Especially on the HTL side, it is very likely that there is no energy barrier for electrons that could make this contact selective, which applies in particular for the P3HT device as the HOMO-LUMO difference of P3HT is even smaller than the bandgap of the double perovskite (Figure S 3.5, Supporting Information). Here, a heterojunction of type 1 is probably formed, which would directly explain why excitons generated in P3HT (clearly seen in the absorption in Figure S 3.6, Supporting Information) are not split at this junction and thus do not contribute to the photocurrent (no signal in the EQE).

For voltages ≥ 0.9 V, previous maxima become minima (pronounced at 435 nm). The relative normalized change (IQE(1.1 V)/ IQE(0 V)), plotted as a dashed line, clearly shows that this "inversion" holds for both absorption maxima. This means that the part of the perovskite layer

closer to the HTL is less conductive in the dark than the part close to the TiO_2. It might be possible that the forward current is driven mainly by electrons, as the hole injection barrier at the HTL is too high. The electrons would have to pass through the whole device and recombine with holes located on the HTL at the HTL interface. This electron current might profit from a conductivity enhancement within the whole layer and would be consistent with a non-selective interface at the HTL.

As already discussed above, the *J/V* curves show a rate-dependent hysteresis. Thus, we investigated the relation between hysteresis and the rather low observed EQE in more detail. We kept the solar cell under forward bias (1.1 V) for 10 s and performed a *J/V*-loop with varied sweep rate. The resulting *J/V* curves of the same device used for the EQE measurements are displayed in Figure 3.3e). The curves show that the photocurrent is higher the faster the measurement is done after the prebias. Thus, the EQE can be boosted by a factor of 3 if the electric field distribution in the device is beneficial for charge extraction. In analogy to discussions on hysteresis in the lead-based perovskites, this can be explained by mobile ionic charges that, remaining at their position set by the forward bias, are not capable of screening the field induced by the fast backward scan.[52] Interestingly, the behavior is very similar to observations in our previous work on lead-based perovskites on planar TiO_2,[57] leading us to conclude that a proper choice of charge transport layers and interface properties will allow for high IQE in the double perovskite solar cells as well.

This conclusion also holds for the open-circuit voltage, which is strongly influenced by slow transient processes as shown in Figure 3.4, where measurements on a planar device compared to a mesoporous device are shown. For both architectures, reversible transients on the timescale of seconds are observed, which indicate that recombination probabilities, most likely at interfaces, change slowly. An explanation for the (initial) increase of V_{OC} could be that the photo-induced voltage leads to a redistribution of mobile ions in the perovskite that leads to a more selective solar cell by modifying the effective built-in potential. Shifted ions would screen the electric field less and would alleviate losses by shunts, which are dominating the strong dependence of V_{OC} on light intensity at low light intensities for the planar device. In the longer run, the maximum V_{OC} for high light intensities cannot be maintained, in particular for the planar device, whereas mesoporous TiO_2 shows a stabilization effect, possibly better maintaining a certain selectivity thus further indicating the strong impact of the charge extraction layer.

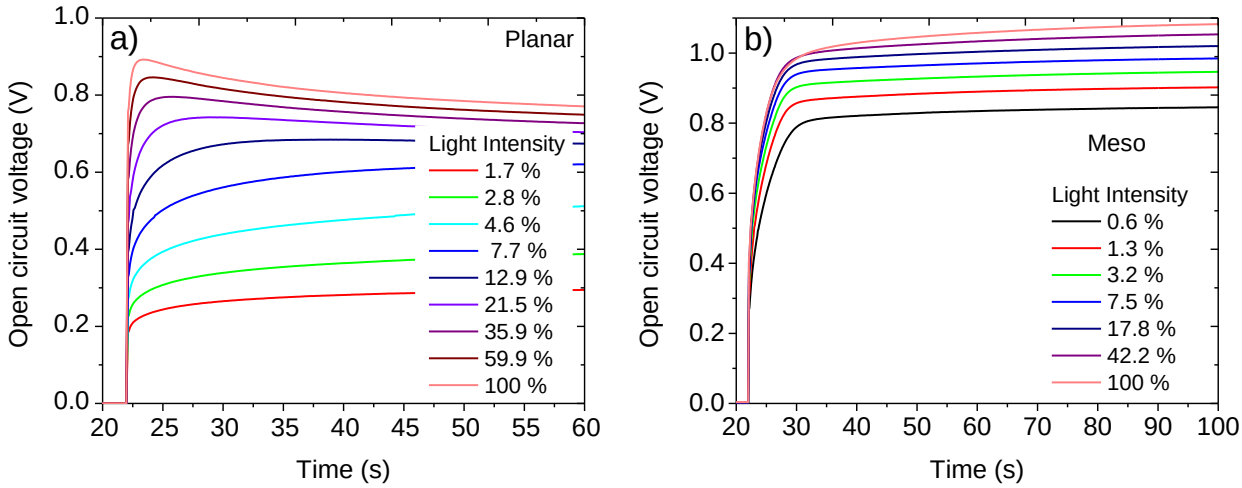

Figure 3.4: Transients of open circuit voltage. a) Planar device, b) mesoporous device. Light of different intensity is turned on at 22 s and light intensity is color-coded as indicated in the legend and is given in percent of 3 suns

3.3.4 Emission, Absorption and the Open-Circuit Voltage

We have already mentioned that the contacts are most likely a major source of recombination losses and therefore a low V_{OC}. In the following, we discuss V_{OC} in the context of absorption and emission features. The V_{OC} of the fabricated solar cells is around 1.0 V, which is a rather low value for a material that absorbs at energies > 2.3 eV and shows a PL peaking between 610 and 630 nm (about 2 eV). Therefore, we expect high non-radiative recombination losses, as already stated in ref. [37]. However, the PL peak is rather broad and various values have been reported for the bandgap of $Cs_2AgBiBr_6$.[14,19,22,27,40] Therefore, a more detailed analysis is required.

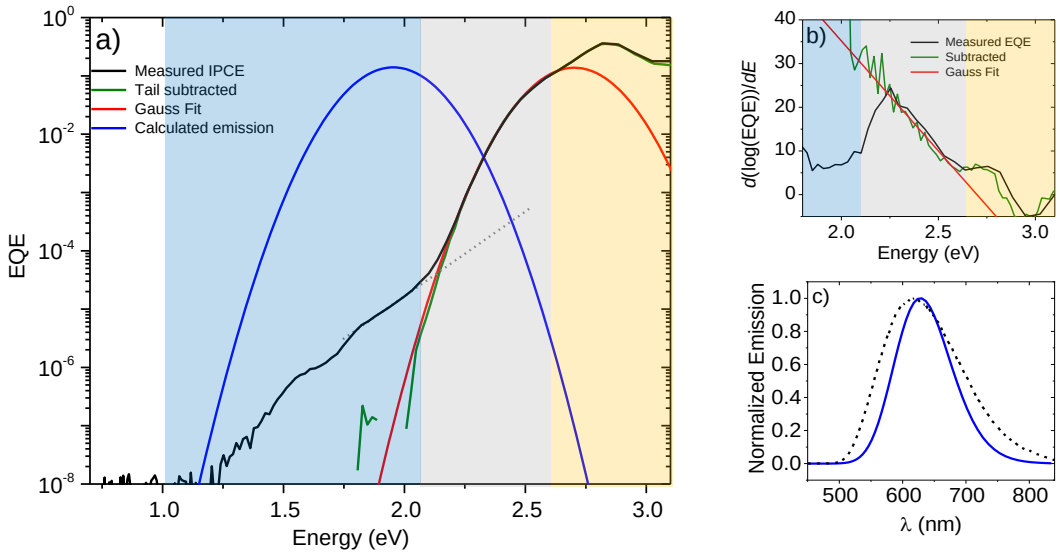

Figure 3.5: Reciprocity and tail states. a) Sensitive EQE of a planar device with Spiro-OMeTAD as HTL (black line) and calculated emission (blue line) assuming a Gaussian feature at the absorption onset, presented with a log-scale. b) Slope of the logarithm of the EQE (black line) together with the slope of the Gaussian fit (red line) and the EQE signal after subtraction of the exponential part (dark green line). c) Calculated PL emission signal on a linear scale compared with the experimental PL (black dashed line). The colored regions in panel (a) and (b) were added as a guide for the eye.

First, we determine the radiative limit of the V_{OC}, that is, the theoretical maximum, following the opto-electronic reciprocity relation introduced by Rau.[58] This approach was successfully applied to lead-based perovskite solar cells.[59] The black solid line in Figure 3.5a) shows the EQE obtained from a sensitive measurement and plotted versus energy for a device with Spiro-OMeTAD as HTL (for more devices see Figure S 3.7, Supporting Information). The peak at 2.8 eV (yellow region) corresponds to the peak in Figure 3.3 and Figure 3.1d) at 445 nm, which is commonly attributed to the direct bandgap. Below this peak, there is another broad feature, which gives rise to a shoulder at around 2.5 eV and a tail observable down to 2.1 eV (grey region). At energies below 2.1 eV there are further tail features (blue region), which we ignore for the moment. The broad onset between 2.1 eV and 2.6 eV (grey region) is also seen in absorption data from photothermal deflection spectroscopy, where an Urbach energy of 70 meV has been reported.[37] If our EQE onset is fitted with an exponential function, a characteristic ("Urbach") energy of 40 to 50 meV is determined, dependent on the selected energy range.

However, an exponential function is not ideal for fitting this spectral range (grey) as we discuss in the following.

To better understand the EQE onset, we plot the slope of log(EQE) in Figure 3.5b, where we cannot identify a constant value. Instead, the log(EQE) value decreases continuously between 2.25 and 2.6 eV (grey region), where the peak at 2.25 eV is most likely due to the overlap of the onset feature with the deep tails, which show a rather constant slope (6.7 eV^{-1}), thus exponential behavior, between 1.85 and 2.05 eV (blue region, characteristic energy 150 meV). Although we acknowledge that this tail does not describe the entire EQE below 2.05 eV, we nevertheless subtract the contribution from these deep tails (dashed line in Figure 3.5 a, obtained by an exponential fit between 1.85 and 2.05 eV, blue region) to disentangle it from the feature above 2.05 eV. The obtained EQE is plotted in dark green and shows a further increasing slope towards lower energy (Figure 3.5b). This leads us to conclude that an exponential fit in this spectral range might not be ideal. Therefore, we used a Gaussian fit in the range between 2.2 and 2.5 eV (red curve in Figure 3.5a); the log-slope is shown in Figure 3.5b) as a red line, grey area in both graphs). The Gaussian with a maximum at 2.7 eV and a width of 0.14 eV in Figure 3.5a) describes the EQE onset well, including its shoulder at 2.6 eV. The position of the fit's maximum matches with a feature reported in photoluminescence excitation spectra in ref.[44]. Here, we use the Gaussian feature to describe the whole EQE, including the part of the spectrum that is commonly assigned to the indirect bandgap,[14,19,46] whose reported values vary by at least 0.3 eV. We note that using a Gaussian is common for thermally broadened transitions, for example, in organic semiconductors.[60] If we want to describe the transition from a Gaussian defect into a continuity of states (such as a broad band), we might prefer to employ an error or a logistic function.[61] Such a fit is shown in Figure S 3.8, Supporting Information, yielding a comparable result between 2.0 and 2.5 eV. A distribution of bandgaps could be explained by a distribution in the order of the Ag Bi occupancy,[62] introduced during film formation and therefore influenced by the film "quality".

Having identified the Gaussian feature, we can calculate the emission spectrum scaled by the internal quantum efficiency $\phi_{\mathrm{Em}}(E)$ using reciprocity and detailed balance ($\phi_{\mathrm{BB}}(E)$ is the black body radiation at ambient temperature, Equation (3.1)).[58]

$$\phi_{\mathrm{Em}}(E) = \mathrm{EQE}(E)\,\phi_{\mathrm{BB}}(E) \tag{3.1}$$

The resulting emission spectrum is plotted in blue. Due to the broad absorption onset, a large Stokes shift is observed, similar to the behavior of organic solar cells.[60,63] Figure 3.5c) shows this calculated emission on a linear scale as a function of wavelength with a maximum at 630 nm. Interestingly, this spectrum looks similar to the experimental PL (dashed), although the quantitative fit is not as good as for lead-based perovskites.[59] Nevertheless, it is strong evidence that the broad and shifted PL results from the same process as the absorption, namely a broad (indirect) bandgap distribution. Hence, more complex explanations might not be required. Also, a distinction of the absorption feature and a red luminescent state[44] would possibly not be required.

Reasons for the discrepancy between measured and calculated emission can be found in the sample-to-sample variations, also seen in PL measurements with peaks ranging from 500 (accompanied by distinct narrow absorption features)[24] to 640 nm[29] and showing narrow[26], distinctive,[29] and broad[22,27,28] shape of nominally the same material that can even be further broadened by pressure alongside with the absorption.[43] These variations are strong indications that the states responsible for the absorption onset and emission are broad/distributed. Another point is that some of the deeper tail states seen in the IPCE, which might result from surfaces,[64] could contribute to the asymmetric emission between 700 and 850 nm seen in the experiment (Figure 3.1c). Furthermore, the IQE depends on the wavelength (see above), which complicates the application of the reciprocity relation.

Nevertheless, based on this analysis we attempt to calculate the radiative V_{OC} limit by Equation (3.2)

$$V_{\mathrm{OC,rad}} = \frac{k_{\mathrm{B}}T}{e}\ln\left(\frac{J_{\mathrm{SC}}}{e\int \phi_{\mathrm{Em}}(E)\mathrm{d}E} + 1\right) = 1.94\ \mathrm{V} \tag{3.2}$$

(with k_{B}: Boltzmann constant, T temperature, e elementary charge)

Here, we used J_{SC}= 1.26 mA/cm^2 derived from the EQE.

A measured V_{OC} much lower than this value implies high non-radiative recombination losses, which can be quantified by an external luminescence yield γ, Equation (3.3):

$$V_{\mathrm{OC}} = V_{\mathrm{OC,rad}} - \underbrace{\frac{k_{\mathrm{B}}T}{e}\ln\left(\frac{1}{\gamma}\right)}_{\Delta V_{\mathrm{OC,non-rad.}}} \tag{3.3}$$

For a V_{OC} of 1.1 V, γ would be 10^{-14}, which is much lower than what is reported from measurements of PL yields (0.02% in ref. [37]) of films. This discrepancy indicates high recombination at the contacts, as already discussed above. To determine γ in the solar-cell device, an electroluminescence (EL) measurement was applied, where the emission of the diode is measured under applied forward bias in the dark. As shown in Figure 3.6a), we succeeded in detecting emission for voltages > 1.1 V and determine an γ_{EL} of 10^{-8}. This value is orders of magnitude higher than expected from the measured V_{OC}. Taking this γ_{EL} and the measured V_{OC}, one would calculate a $V_{\mathrm{OC,rad}}$ that is below 1.6 V. This lower $V_{\mathrm{OC,rad}}$ could be due to the broad tail states, which we had to ignore in our analysis to make the calculations converge. Such an approach might be justified by assuming that these are non-equilibrium deep traps.[65] A $V_{\mathrm{OC,rad}}$ of 1.6 eV would match the $V_{\mathrm{OC,rad}}$ of a solar cell made of our HTL P3HT,[66] which is expected for the charge transfer and recombination in the P3HT discussed above.

Whereas Figure 3.6a) shows γ_{EL}, Figure 3.6b) displays the EL spectrum. In contrast to what is observed in lead-based perovskites, the EL spectrum does not coincide with the PL spectrum. Instead, the EL is strongly redshifted, showing a peak at around 900 nm. We can only speculate on the origin of this signal. As none of the other materials in the device are expected to emit in this range (including P3HT[67]), it is most likely that the EL results from occupation of deep tail states and the obtained γ cannot directly be used in Equation (3.3). Such deep tails are also seen in the EQE (blue region in Figure 3.5a), which we did not further quantify due to their complex signature, possibly modulated by interference effects.

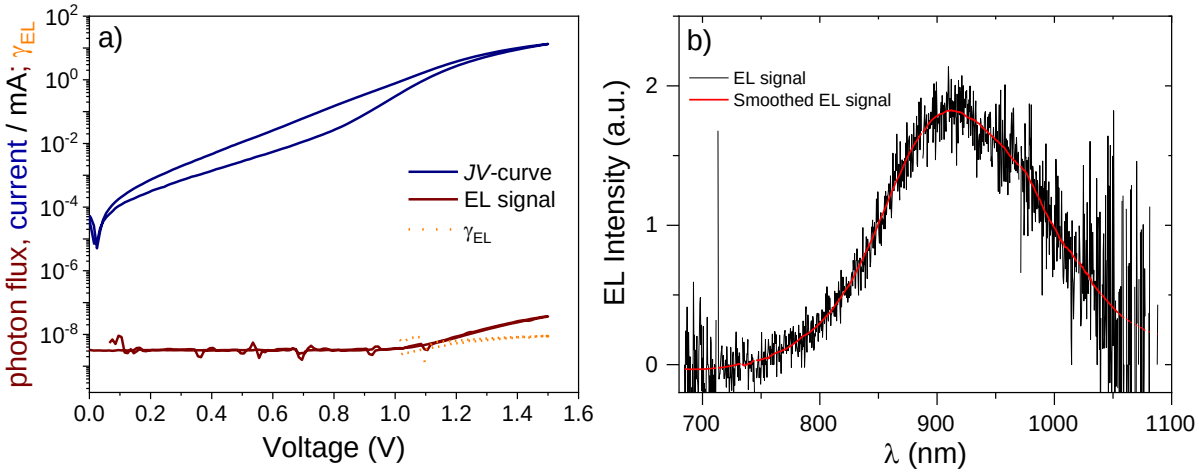

Figure 3.6: Electroluminescence. a) Current, emitted photon flux (multiplied by elementary charge) and the external EL quantum yield γ_{EL}, measured by a J/V loop starting at 0 V with a sweep rate of 10 mV/s. b) EL spectrum.

3.4 Conclusion

In this work, we successfully fabricated $Cs_2AgBiBr_6$ perovskite solar cells with different architectures where we investigated different HTMs and ETLs as well as different fabrication methods in order to find answers to the question of the bottleneck that limits $Cs_2AgBiBr_6$ solar cells to 2.8 % PCE so far. We analyzed the current-limiting processes by deriving the IQE from measured EQE. We find that the IQE depends on the location where photons are absorbed. Furthermore, it changes sign around V_{OC}, which is indicative of the importance of a built-in potential and non-selective contacts. Using scan-rate dependent *J/V* measurements, we indeed observe that charge collection strongly depends on the electric field in the device, which is affected by a slow process such as ion migration. This is consistent with transient V_{OC} measurements that provide further evidence for high recombination rates at the contacts. Therefore, we expect that understanding the exact interplay of these processes and reducing surface recombination will allow for higher photocurrents and voltages.

We analyzed emission and absorption spectra and could describe the photocurrent onset best with a Gaussian function peaking at 2.6 eV, which might be due to disorder in the $Cs_2AgBiBr_6$ perovskite. The corresponding broad emission feature was predicted at 2.0 eV (630 nm), roughly matching measured PL.

Finally, we succeeded in measuring the EL spectrum and yield of the solar cells. The EL spectrum, found in the NIR, is strongly redshifted compared to the PL, and the EL yield is of the order of 10^{-8}. Both EL spectrum and EL yield call for further studies to unravel their origin. Overall, our work opens up pathways that can address the performance-limiting factors of $Cs_2AgBiBr_6$ and related solar cells by using the right electrode material as well as suitable charge transport materials.

3.5 Experimental Section

Materials and Thin Film Synthesis

The stock solution was prepared by dissolving CsBr (212.8 mg, 1 mmol, 2 eq, Alpha Aesar, 99.999 % metals basis), $BiBr_3$ (224.4 mg, 0.5 mmol, 1 eq, Alpha Aesar, 99.9 % metals basis) and AgBr (93.9 mg, 0.5 mmol, 1 eq, Alpha Aesar, 99.998 % metals basis) in 1 mL DMSO (Sigma Aldrich, anhydrous, ≥99.9 %) at 130 °C to obtain a 0.5 M solution.

For preparing the solar cells on planar TiO_2 (see below for preparation), the thin films were deposited in a nitrogen filled glovebox by spin-coating dynamically (first at 1000 rpm for 10 s, followed by a second step at 5000 rpm for 30 s) onto the substrate (80 µL of the stock solution). After 23 s of the second step, 400 µL 2-propanol were dripped quickly on top of the substrate and the films were annealed afterwards at 275 °C for 5 minutes.

For thin films on mesoporous TiO_2, the substrates and the precursor solution were pre-heated at 85 °C on a Heidolph-hotplate with an internal temperature sensor. 100 µL of the precursor-solution were spincoated dynamically (2000 rpm, 45 s) hot onto the heated substrates at ambient conditions in air.

Solar Cell Fabrication

Fluorine-doped tin oxide coated glass sheets (7 Ω/sq) were patterned by etching with zinc-powder and 3 M HCl, cleaned with a detergent followed by washing with acetone and ethanol and dried under an air stream. Directly before applying the hole-blocking layer, the substrates were oxygen plasma cleaned for 5 min.

Compact TiO_2 (c-TiO_2)

A compact (c)-TiO_2 layer was prepared from a sol-gel precursor solution by spin-coating 100 µL onto the 3 cm x 3 cm substrates for 45 s at 2000 rpm and calcination afterwards at 500 °C for 30 min in air, resulting in a 50 nm thick layer. For the sol-gel solution, 2 M HCl (35 µL) in 2.53 mL dry 2-propanol was added dropwise to a solution of 370 µL of titanium-isopropoxide in 2.53 mL dry 2-propanol under vigorous stirring. After cooling down, the substrates were again plasma cleaned for 5 min and transferred to a nitrogen-filled glovebox. On top of the compact titania layer, the active layer was deposited as described above.

Mesoporous TiO_2 (mp-TiO_2)

After the deposition of the layer of compact TiO_2, 100 µL of a dispersion of mp-TiO_2 nanoparticles (DyeSol, 3:1 EtOH:TiO_2-paste) was spincoated on top of the c-TiO_2 layer without plasma-cleaning. Afterwards, the substrates were calcined at 500 °C for 30 min at air resulting in a 500 nm thick layer. After cooling down, the active layer was deposited on top of the TiO_2 layer as described above.

Deposition of Hole Transporting Materials (HTM)

For poly(3-hexylthiophen-2,5-diyl) (P3HT), 55 mg of the material (Ossila, batch M1011; MW: 60150; RR: 97.6 %., Mn: 28650 PDI: 2.1) was dissolved in 1 mL ortho-dichlorobenzene and deposited by spin-coating 75 µL of a 55 mg/mL solution statically at 600 rpm for 120 s at ambient conditions in air. The gold electrode (see below) was deposited directly after the HTM deposition.

For 2,2′,7,7′-tetrakis-(N,N-di-4-methoxyphenylamino)-9,9′-spirobifluorene (Spiro-OMeTAD, Borun Chemicals, 99.5 % purity), 73 mg of the material was dissolved in 1 mL of chlorobenzene. To this solution, 10 µL of 4-*tert*-butylpyridine and 30 µL of a bis(trifluoromethane)sulfonamide lithium salt solution (LiTFSI, 170 mg in 1 mL acetonitrile) were added. The resulting HTM solution was deposited *via* dynamic spincoating (1500 rpm, 45 s) in a nitrogen-filled glovebox. Afterward, the samples were stored overnight in air at < 30 R.H. to allow the HTM to oxidize.

The top electrode with the thickness of 40 nm was deposited by thermally evaporating gold under vacuum (at ~10^{-7} mbar).

Materials Characterization

X-ray Diffraction (XRD) Measurements

The thin film X-ray diffraction data were recorded using a Bruker D8 Discover Diffractometer with Ni-filtered Cu Kα radiation and a LynxEye position-sensitive detector in Bragg-Brentano Geometry.

Scanning Electron Microscopy (SEM)

SEM images were obtained with an FEI Helios G3 UC instrument with an acceleration voltage of 5 kV for the cross-sectional images and 2 kV for the top-view images. All samples were sputtered with carbon beforehand and both mirror and through-lens detectors were used.

Steady State Photoluminescence (PL)

The thin films were deposited onto the respective substrate by spin-coating as described above and all PL measurements were performed with a FluoTime 300 Spectrofluorometer (PicoQuant GmbH) in air.

To excite the samples for steady state measurements, a pulsed solid-state laser (wavelength 375 nm; LDH375, PicoQuant) with a fluence of 20 pJ/cm^2 at 40 MHz repetition rate was used in order to simulate steady state conditions.

Solar Cell Characterization

Current–voltage (*J/V*) characteristics of the perovskite solar cells were measured using a Newport OrielSol 2A solar simulator with a Keithley 2401 source meter. The devices were illuminated through a shadow mask, yielding an active area of 0.0831 cm^2. The *J/V* curves were recorded under standard AM 1.5G illumination with a xenon lamp, and calibrated to a light intensity of 100 mW cm^{-2} with a Fraunhofer ISE certified silicon diode. The input bias voltage was scanned from -1.5 to 0 V in 0.01 V steps with a rate of 0.1 V s^{-1} for the standard PCE measurements. For the experiments with different scan-speeds, we chose bigger voltage steps varying from 0.01 V to 1 V. All prepared devices show a comparable degree of hysteresis between the forward and the reverse scan.

Film Thickness Determination

The film thickness was determined using SEM cross-sectional images shown in the SI.

Sensitive EQE Measurements

Sensitive EQE measurements to characterize the sub-bandgap region were conducted using a halogen lamp (Osram 64655 HLX 250 W) as illumination source. The light was chopped using an Oriel 3502 chopper at 330 Hz and subsequently passed through a double-grating monochromator (Oriel, Cornerstone 260). Several long-pass filters were used to filter out stray light. The samples were mounted in an air tight holder filled with nitrogen to prevent air

exposure. The response was recorded from a pre-amplifier (Stanford Research, SR 570) using a lock-in amplifier (Stanford Research, SR 830) and calibrated using two Si and InGaAs reference cells.

EQE and Transmission Measurements for Figure 3.3

Measurements were performed on a homemade system with a halogen lamp, a monochromator and a silicon reference diode. The light was chopped at 330 Hz and the signal was detected through a lock-in amplifier. The setup was calibrated with a silicon solar cell, which was also used for transmission measurements, where it was placed behind the sample. Bias light was provided by blue LEDs.

***J/V* Loops and EL**

Voltage was applied and current measured with a potentiostat (Biologic SP300). Illumination was provided by a blue LED. For the ELQE, the current of a 1 cm^2 silicon diode (Hamamatsu) placed in close vicinity to the sample was measured by a second channel of the potentiostat. For the EL spectrum, a constant current of 10 mA was applied and the spectrum measured with a CCD Spectrometer (Andor with iDUS detector).

Transient Photovoltage

This measurement was performed with a Paios instrument (Fluxim) and a blue LED.

3.6 Supporting Information

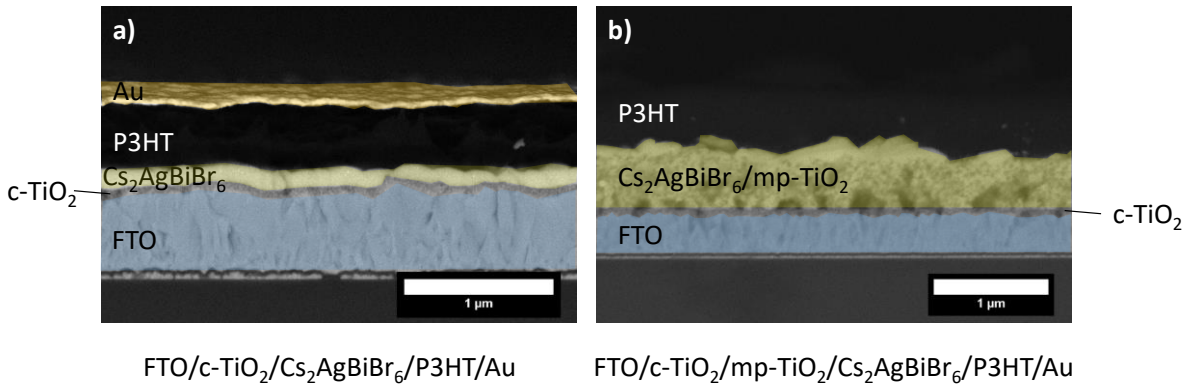

Figure S 3.1: SEM cross sections of the solar cells investigated in this work: a) on compact TiO_2 b) on mp-TiO_2

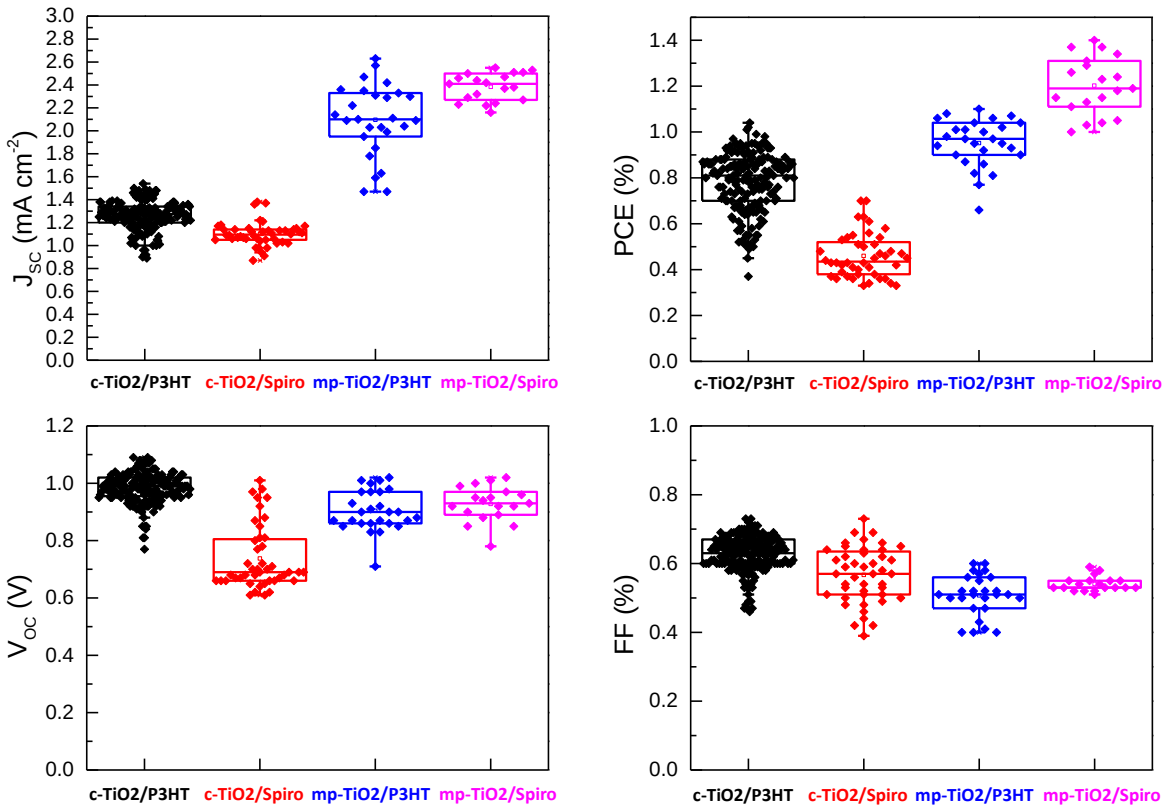

Figure S 3.2: Box plots of the photovoltaic parameters of the investigated solar cells.

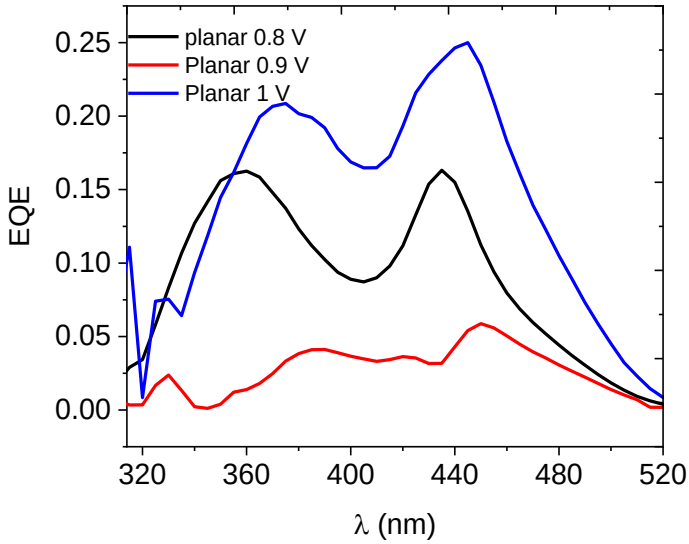

Figure S 3.3: EQE of planar device for various applied voltages without bias light. The signal changes sign at 0.9 V.

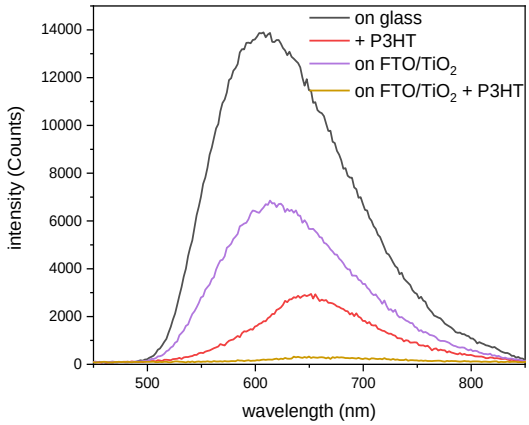

Figure S 3.4: PL of $Cs_2AgBiBr_6$ on different substrates and covered with and without P3HT.

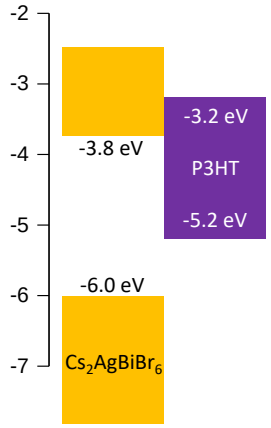

Figure S 3.5: Energy level alignment between $Cs_2AgBiBr_6$ and P3HT before contact.

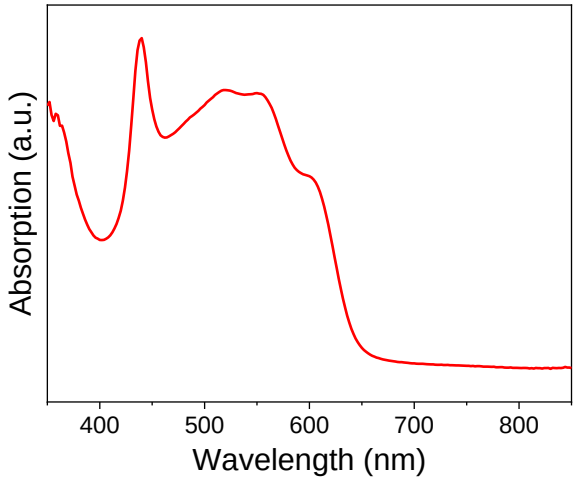

Figure S 3.6: absorption spectrum of full solar cell with the architecture FTO/c-TiO_2/$Cs_2AgBiBr_6$/P3HT/Au

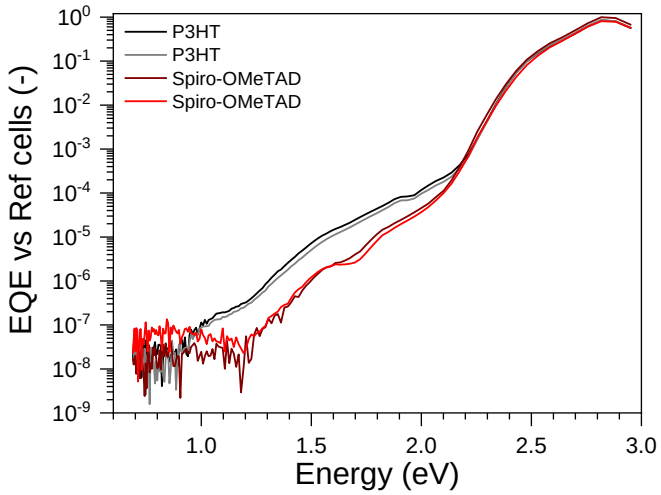

Figure S 3.7: Sensitive EQE measurements of additional planar solar cells comprising either P3HT (black and grey line) or Spiro-OMeTAD (dark red and red line) as HTM.

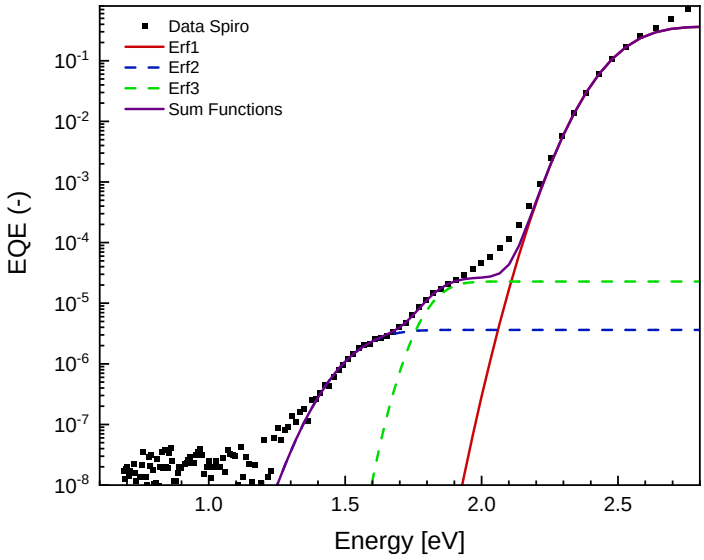

Figure S 3.8: Fitting the onset of the sensitive EQE using a superposition of error functions.

3.7 References

[1] J.-P. Correa-Baena, M. Saliba, T. Buonassisi, M. Grätzel, A. Abate, W. Tress, A. Hagfeldt, *Science (New York, N.Y.)* **2017**, *358*, 739.

[2] S. Yakunin, M. Sytnyk, D. Kriegner, S. Shrestha, M. Richter, G. J. Matt, H. Azimi, C. J. Brabec, J. Stangl, M. V. Kovalenko, W. Heiss, *Nature photonics* **2015**, *9*, 444.

[3] M. F. Aygüler, B. M. D. Puscher, Y. Tong, T. Bein, A. S. Urban, R. D. Costa, P. Docampo, *J. Phys. D: Appl. Phys.* **2018**, *51*, 334001.

[4] Z.-K. Tan, R. S. Moghaddam, M. L. Lai, P. Docampo, R. Higler, F. Deschler, M. Price, A. Sadhanala, L. M. Pazos, D. Credgington, F. Hanusch, T. Bein, H. J. Snaith, R. H. Friend, *Nature nanotechnology* **2014**, *9*, 687.

[5] M. Jeong, I. W. Choi, E. M. Go, Y. Cho, M. Kim, B. Lee, S. Jeong, Y. Jo, H. W. Choi, J. Lee, J.-H. Bae, S. K. Kwak, D. S. Kim, C. Yang, *Science (New York, N.Y.)* **2020**, *369*, 1615.

[6] H. Min, M. Kim, S.-U. Lee, H. Kim, G. Kim, K. Choi, J. H. Lee, S. I. Seok, *Science (New York, N.Y.)* **2019**, *366*, 749.

[7] H. Lu, Y. Liu, P. Ahlawat, A. Mishra, W. R. Tress, F. T. Eickemeyer, Y. Yang, F. Fu, Z. Wang, C. E. Avalos, B. I. Carlsen, A. Agarwalla, X. Zhang, X. Li, Y. Zhan, S. M. Zakeeruddin, L. Emsley, U. Rothlisberger, L. Zheng, A. Hagfeldt, M. Grätzel, *Science (New York, N.Y.)* **2020**, *370*.

[8] A. Babayigit, A. Ethirajan, M. Muller, B. Conings, *Nature materials* **2016**, *15*, 247.

[9] M. L. Petrus, K. Schutt, M. T. Sirtl, E. M. Hutter, A. C. Closs, J. M. Ball, J. C. Bijleveld, A. Petrozza, T. Bein, T. J. Dingemans, T. J. Savenije, H. Snaith, P. Docampo, *Adv. Energy Mater.* **2018**, *8*, 1801605.

[10] M. L. Petrus, J. Schlipf, C. Li, T. P. Gujar, N. Giesbrecht, P. Müller-Buschbaum, M. Thelakkat, T. Bein, S. Hüttner, P. Docampo, *Adv. Energy Mater.* **2018**, *8*, 1703396.

[11] Y. Hu, M. F. Aygüler, M. L. Petrus, T. Bein, P. Docampo, *ACS Energy Lett.* **2017**, *2*, 2212.

[12] R. Cheacharoen, C. C. Boyd, G. F. Burkhard, T. Leijtens, J. A. Raiford, K. A. Bush, S. F. Bent, M. D. McGehee, *Sustainable Energy Fuels* **2018**, *2*, 2398.

[13] N. Glück, T. Bein, *Energy Environ. Sci.* **2020**, *13*, 4691.

[14] E. T. McClure, M. R. Ball, W. Windl, P. M. Woodward, *Chem. Mater.* **2016**, *28*, 1348.

[15] L.-Y. Bi, Y.-Q. Hu, M.-Q. Li, T.-L. Hu, H.-L. Zhang, X.-T. Yin, W.-X. Que, M. S. Lassoued, Y.-Z. Zheng, *J. Mater. Chem. A* **2019**, *7*, 19662.

[16] M. K. Jana, S. M. Janke, D. J. Dirkes, S. Dovletgeldi, C. Liu, X. Qin, K. Gundogdu, W. You, V. Blum, D. B. Mitzi, *J. Am. Chem. Soc.* **2019**, *141*, 7955.

[17] H. C. Sansom, G. Longo, A. D. Wright, L. R. V. Buizza, S. Mahesh, B. Wenger, M. Zanella, M. Abdi-Jalebi, M. J. Pitcher, M. S. Dyer, T. D. Manning, R. H. Friend, L. M. Herz, H. J. Snaith, J. B. Claridge, M. J. Rosseinsky, *Journal of the American Chemical Society* **2021**, *143*, 3983.

[18] S. Rieger, B. J. Bohn, M. Döblinger, A. F. Richter, Y. Tong, K. Wang, P. Müller-Buschbaum, L. Polavarapu, L. Leppert, J. K. Stolarczyk, J. Feldmann, *Phys. Rev. B* **2019**, *100*.

[19] A. H. Slavney, T. Hu, A. M. Lindenberg, H. I. Karunadasa, *J. Am. Chem. Soc.* **2016**, *138*, 2138.

[20] M. T. Sirtl, M. Armer, L. K. Reb, R. Hooijer, P. Dörflinger, M. A. Scheel, K. Tvingstedt, P. Rieder, N. Glück, P. Pandit, S. V. Roth, P. Müller-Buschbaum, V. Dyakonov, T. Bein, *ACS Appl. Energy Mater.* **2020**, *3*, 11597.

[21] W. Xiang, W. Tress, *Advanced materials (Deerfield Beach, Fla.)* **2019**, *31*, e1902851.

[22] E. Greul, M. L. Petrus, A. Binek, P. Docampo, T. Bein, *J. Mater. Chem. A* **2017**, *5*, 19972.

[23] X. Yang, Y. Chen, P. Liu, H. Xiang, W. Wang, R. Ran, W. Zhou, Z. Shao, *Adv. Funct. Mater.* **2020**, *30*, 2001557.

[24] M. Ghasemi, L. Zhang, J.-H. Yun, M. Hao, D. He, P. Chen, Y. Bai, T. Lin, M. Xiao, A. Du, M. Lyu, L. Wang, *Adv. Funct. Mater.* **2020**, *30*, 2002342.

[25] W. Gao, C. Ran, J. Xi, B. Jiao, W. Zhang, M. Wu, X. Hou, Z. Wu, *Chemphyschem* **2018**, *19*, 1696.

[26] F. Igbari, R. Wang, Z.-K. Wang, X.-J. Ma, Q. Wang, K.-L. Wang, Y. Zhang, L.-S. Liao, Y. Yang, *Nano Lett.* **2019**, *19*, 2066.

[27] C. Wu, Q. Zhang, Y. Liu, W. Luo, X. Guo, Z. Huang, H. Ting, W. Sun, X. Zhong, S. Wei, S. Wang, Z. Chen, L. Xiao, *Adv. Sci. (Weinh.)* **2018**, *5*, 1700759.

[28] M. Wang, P. Zeng, S. Bai, J. Gu, F. Li, Z. Yang, M. Liu, *Sol. RRL* **2018**, *2*, 1800217.

[29] P. Fan, H.-X. Peng, Z.-H. Zheng, Z.-H. Chen, S.-J. Tan, X.-Y. Chen, Y.-D. Luo, Z.-H. Su, J.-T. Luo, G.-X. Liang, *Nanomaterials (Basel, Switzerland)* **2019**, *9*.

[30] B. Wang, L. Yang, C. Dall'Agnese, A. K. Jena, S.-I. Sasaki, T. Miyasaka, H. Tamiaki, X.-F. Wang, *Sol. RRL* **2020**, *4*, 2000166.

[31] E. M. Hutter, M. C. Gélvez-Rueda, D. Bartesaghi, F. C. Grozema, T. J. Savenije, *ACS Omega* **2018**, *3*, 11655.

[32] N. Pai, J. Lu, M. Wang, A. S. R. Chesman, A. Seeber, P. V. Cherepanov, D. C. Senevirathna, T. R. Gengenbach, N. V. Medhekar, P. C. Andrews, U. Bach, A. N. Simonov, *J. Mater. Chem. A* **2020**, *8*, 2008.

[33] K.-Z. Du, W. Meng, X. Wang, Y. Yan, D. B. Mitzi, *Angewandte Chemie (International ed. in English)* **2017**, *56*, 8158.

[34] Z. Li, S. R. Kavanagh, M. Napari, R. G. Palgrave, M. Abdi-Jalebi, Z. Andaji-Garmaroudi, D. W. Davies, M. Laitinen, J. Julin, M. A. Isaacs, R. H. Friend, D. O. Scanlon, A. Walsh, R. L. Z. Hoye, *J. Mater. Chem. A* **2020**, *8*, 21780.

[35] F. Ji, J. Klarbring, F. Wang, W. Ning, L. Wang, C. Yin, J. S. M. Figueroa, C. K. Christensen, M. Etter, T. Ederth, L. Sun, S. I. Simak, I. A. Abrikosov, F. Gao, *Angew. Chem. Int. Ed.* **2020**, *132*, 15303.

[36] R. Kentsch, M. Scholz, J. Horn, D. Schlettwein, K. Oum, T. Lenzer, *J. Phys. Chem. C* **2018**, *122*, 25940.

[37] G. Longo, S. Mahesh, L. R. V. Buizza, A. D. Wright, A. J. Ramadan, M. Abdi-Jalebi, P. K. Nayak, L. M. Herz, H. J. Snaith, *ACS Energy Lett.* **2020**, *5*, 2200.

[38] J. Xiu, Y. Shao, L. Chen, Y. Feng, J. Dai, X. Zhang, Y. Lin, Y. Zhu, Z. Wu, Y. Zheng, H. Pan, C. Liu, X. Shi, X. Cheng, Z. He, *Materials Today Energy* **2019**, *12*, 186.

[39] G. Yan, B. Jiang, Y. Yuan, M. Kuang, X. Liu, Z. Zeng, C. Zhao, J.-H. He, W. Mai, *ACS applied materials & interfaces* **2020**, *12*, 6064.

[40] M. Pantaler, K. T. Cho, V. I. E. Queloz, I. García Benito, C. Fettkenhauer, I. Anusca, M. K. Nazeeruddin, D. C. Lupascu, G. Grancini, *ACS Energy Lett.* **2018**, *3*, 1781.

[41] C. W. Ahn, J. H. Jo, J. Chan Kim, H. Ullah, S. Ryu, Y. Hwang, J. San Choi, J. Lee, S. Lee, H. Jeen, Y.-H. Shin, H. Y. Jeong, I. W. Kim, T. H. Kim, *Journal of Materiomics* **2020**, *6*, 651.

[42] M. Keshavarz, E. Debroye, M. Ottesen, C. Martin, H. Zhang, E. Fron, R. Küchler, J. A. Steele, M. Bremholm, J. van de Vondel, H. I. Wang, M. Bonn, M. B. J. Roeffaers, S. Wiedmann, J. Hofkens, *Advanced materials (Deerfield Beach, Fla.)* **2020**, *32*, e2001878.

[43] C. Lv, X. Yang, Z. Shi, L. Wang, L. Sui, Q. Li, J. Qin, K. Liu, Z. Zhang, X. Li, Q. Lou, D. Yang, J. Zang, R. Liu, B. Liu, C.-X. Shan, *J. Phys. Chem. C* **2020**, *124*, 1732.

[44] A. Schmitz, L. L. Schaberg, S. Sirotinskaya, M. Pantaler, D. C. Lupascu, N. Benson, G. Bacher, *ACS Energy Lett.* **2020**, *5*, 559.

[45] L. Schade, A. D. Wright, R. D. Johnson, M. Dollmann, B. Wenger, P. K. Nayak, D. Prabhakaran, L. M. Herz, R. Nicholas, H. J. Snaith, P. G. Radaelli, *ACS Energy Lett.* **2019**, *4*, 299.

[46] M. R. Filip, S. Hillman, A. A. Haghighirad, H. J. Snaith, F. Giustino, *J. Phys. Chem. Lett.* **2016**, *7*, 2579.

[47] Y. Bekenstein, J. C. Dahl, J. Huang, W. T. Osowiecki, J. K. Swabeck, E. M. Chan, P. Yang, A. P. Alivisatos, *Nano letters* **2018**, *18*, 3502.

[48] W. Tress, *The journal of physical chemistry letters* **2017**, *8*, 3106.

[49] R. S. Sanchez, V. Gonzalez-Pedro, J.-W. Lee, N.-G. Park, Y. S. Kang, I. Mora-Sero, J. Bisquert, *The journal of physical chemistry letters* **2014**, *5*, 2357.

[50] E. L. Unger, A. Czudek, H.-S. Kim, W. Tress, *Characterization Techniques for Perovskite Solar Cell Materials*, Elsevier **2020**.

[51] R. B. Dunbar, B. C. Duck, T. Moriarty, K. F. Anderson, N. W. Duffy, C. J. Fell, J. Kim, A. Ho-Baillie, D. Vak, T. Duong, Y. Wu, K. Weber, A. Pascoe, Y.-B. Cheng, Q. Lin, P. L. Burn, R. Bhattacharjee, H. Wang, G. J. Wilson, *J. Mater. Chem. A* **2017**, *5*, 22542.

[52] W. Tress, N. Marinova, T. Moehl, S. M. Zakeeruddin, M. K. Nazeeruddin, M. Grätzel, *Energy Environ. Sci.* **2015**, *8*, 995.

[53] S. E. Richardson, *Energy Environ. Sci* **2016**, *9*, 1476.

[54] T. Trupke, P. Würfel, I. Uhlendorf, *J. Phys. Chem. B* **2000**, *104*, 11484.

[55] W. Tress, *Organic Solar Cells: Theory, Experiment, and Device Simulation*, Springer International Publishing, Cham, s.l. **2014**.

[56] W. Ning, F. Wang, B. Wu, J. Lu, Z. Yan, X. Liu, Y. Tao, J.-M. Liu, W. Huang, M. Fahlman, L. Hultman, T. C. Sum, F. Gao, *Advanced materials (Deerfield Beach, Fla.)* **2018**, *30*, e1706246.

[57] J. P. Correa Baena, L. Steier, W. Tress, M. Saliba, S. Neutzner, T. Matsui, F. Giordano, T. J. Jacobsson, A. R. Srimath Kandada, S. M. Zakeeruddin, A. Petrozza, A. Abate, M. K. Nazeeruddin, M. Grätzel, A. Hagfeldt, *Energy Environ. Sci.* **2015**, *8*, 2928.

[58] U. Rau, *Phys. Rev. B* **2007**, *76*.

[59] W. Tress, N. Marinova, O. Inganäs, M. K. Nazeeruddin, S. M. Zakeeruddin, M. Graetzel, *Adv. Energy Mater.* **2015**, *5*, 1400812.

[60] K. Vandewal, K. Tvingstedt, A. Gadisa, O. Inganäs, J. V. Manca, *Nature materials* **2009**, *8*, 904.

[61] C. M. Sutter-Fella, D. W. Miller, Q. P. Ngo, E. T. Roe, F. M. Toma, I. D. Sharp, M. C. Lonergan, A. Javey, *ACS Energy Lett.* **2017**, *2*, 709.

[62] J. Yang, P. Zhang, S.-H. Wei, *The journal of physical chemistry letters* **2018**, *9*, 31.

[63] W. Tress, B. Beyer, N. Ashari Astani, F. Gao, S. Meloni, U. Rothlisberger, *The journal of physical chemistry letters* **2016**, *7*, 3936.

[64] D. Bartesaghi, A. H. Slavney, M. C. Gélvez-Rueda, B. A. Connor, F. C. Grozema, H. I. Karunadasa, T. J. Savenije, *J. Phys. Chem. C* **2018**, *122*, 4809.

[65] N. Zarrabi, O. J. Sandberg, S. Zeiske, W. Li, D. B. Riley, P. Meredith, A. Armin, *Nature communications* **2020**, *11*, 5567.

[66] J. Yao, T. Kirchartz, M. S. Vezie, M. A. Faist, W. Gong, Z. He, H. Wu, J. Troughton, T. Watson, D. Bryant, J. Nelson, *Phys. Rev. Applied* **2015**, *4*.

[67] K. Tvingstedt, K. Vandewal, A. Gadisa, F. Zhang, J. Manca, O. Inganäs, *Journal of the American Chemical Society* **2009**, *131*, 11819.

4 Optoelectronic Properties of $Cs_2AgBiBr_6$ Thin Films: The Influence of Precursor Stoichiometry

This chapter is based on the following publication:

Maximilian T. Sirtl‡, Melina Armer‡, Lennart K. Reb, Rik Hooijer, Patrick Dörflinger, Manuel A. Scheel, Kristofer Tvingstedt, Phillipp Rieder, Nadja Glück, Pallavi Pandit, Stephan Roth, Peter Müller-Buschbaum, Vladimir Dyakonov and Thomas Bein*, *ACS Appl. Energy Mater.* 2020, **3**, 11597-11609

‡ These Authors equally contributed to this work

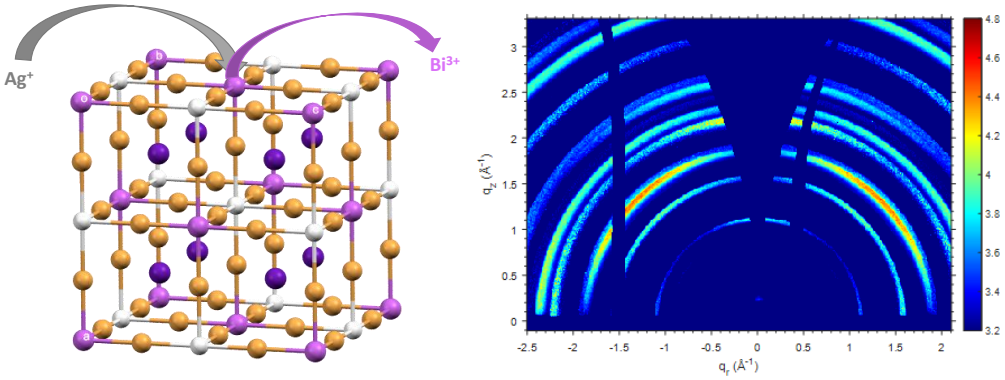

Keywords: double perovskite, elpasolite, lead-free perovskite, perovskite solar cell, $Cs_2AgBiBr_6$, oriented thin films, microwave conductivity

4.1 Abstract

Lead-free double perovskites have recently attracted growing attention as a possible alternative to lead-based halide perovskites in photovoltaics and other optoelectronics applications. The most prominent compound $Cs_2AgBiBr_6$, however, presents issues such as a rather large and indirect bandgap, high exciton binding energies and poor charge carrier transport, especially in thin films. In order to address some of these challenges, we systematically modified the stoichiometry of the precursors used for the synthesis of thin films towards a $BiBr_3$-deficient system. In combination with a stoichiometric excess of AgBr, we obtained highly oriented double perovskite thin films. These modifications directly boost the lifetime of the charge carriers up to 500 ns as observed by time-resolved photoluminescence spectroscopy. Moreover, time-resolved microwave conductivity studies revealed an increase of the charge carrier mobility from 3.5 $cm^2/(Vs)$ to around ~5 $cm^2/(Vs)$. Solar cells comprising the modified films as planar active layers reached power conversion efficiency (PCE) values up to 1.11 %, exceeding the stoichiometric reference film (~0.97 %), both on average and with champion cells. The results in this work underline the importance of controlling the nanomorphology of the bulk film. We anticipate that control of precursor stoichiometry will also offer a promising approach for enhancing the efficiency of other perovskite photovoltaic absorber materials and thin films.

4.2 Introduction

Hybrid metal halide perovskite solar cells have recently attracted much attention due to the easy preparation and outstanding optoelectronic properties of the respective lead-containing perovskite materials. Since their introduction in 2009, this family of solar cell absorber materials has enabled an enormous increase in performance, from about 3.8 % in the beginning to reaching over 25 % in state-of-the-art devices.[1–3] However, lead-based halide perovskites present several challenging issues, such as the high toxicity of lead as well as the rather low stability toward air, humidity and light without special encapsulation.[4–7] Hence, recent research interest has also addressed the search for finding alternative materials, in addition to achieving a higher stability of the lead-based solar cells.[8,9]

One promising idea to overcome these challenges is the homovalent substitution of lead ions using Sn^{2+}, which has so far resulted in photovoltaic efficiencies of up to 9.2 %.[10] However, Sn^{2+} readily oxidizes to Sn^{4+} when exposed to air which negatively affects the long-term

stability of the prepared solar cells, thus resulting in fast degradation of the active layer under ambient conditions, although many improvements were recently achieved.[11–13]

In order to find new long-term stable materials and adequate alternatives for lead, computational studies have delivered promising results, but also revealed multiple issues for the resulting perovskite materials such as the thermodynamic stability as well as the solubility of the materials and their optoelectronic properties.[14–20] One of the promising materials is $Cs_2AgBiBr_6$, showing a long charge carrier lifetime, high charge carrier mobility in single crystals as well as calculated effective charge carrier masses comparable to those calculated for lead-based perovskites.[21–24] Moreover, the material shows a superior stability towards ambient conditions and has a bandgap between 1.9 and 2.3 eV which is, however, indirect.[21–26] After some of us have recently demonstrated a viable solar cell design for this double perovskite, achieving a power conversion efficiency (PCE) of up to 2.5 %, several solar cell preparation methods were published, including vapor assisted annealing or vapor deposition.[26–30] As crystallinity, crystallite orientation and film quality play an important role for efficient solar cells,[31–37] Xiu et al. developed a capillary-assisted dip-coating method, achieving crystalline $Cs_2AgBiBr_6$ films at 160 °C and a preferred orientation parallel to the (002) plane.[38] Moreover, Igbari et al. recently showed that the optoelectronic properties of $Cs_2AgBiBr_6$ films can be improved by keeping the exact stoichiometry of the compound.[27]

Here, we investigate the influence of precursor stoichiometry on the properties of $Cs_2AgBiBr_6$ thin films by changing the amount of AgBr and $BiBr_3$ added to the stock solution. By combining an AgBr excess with a $BiBr_3$ deficiency, a significant increase in the orientation and crystallinity of the films could be observed, which was analyzed by in-film Bragg-Brentano X-Ray diffraction and grazing-incidence wide-angle X-Ray scattering (GIWAXS) measurements. Moreover, the modified films exhibit a higher charger carrier mobility in comparison to the in-batch stoichiometric reference, as well as a longer charge carrier lifetime of over 500 ns, obtained by means of photoluminescence (PL) and time-resolved microwave conductivity (TRMC) measurements, respectively. Our approach shows a simple and universal way to tailor the properties of this material using a two-step spin-coating process, which results in an improvement of solar cell efficiency. Our work offers a facile way to tune the optoelectronic properties of $Cs_2AgBiBr_6$ thin films by increasing their preferred orientation and henceforth the charge carrier mobility as well as charge carrier lifetime, which ultimately leads to an increase in efficiency of the resulting solar cells.

4.3 Results and Discussion

For the thin-film synthesis we dissolved CsBr, AgBr and $BiBr_3$ in DMSO at elevated temperature (130 °C) to obtain a 0.5 M solution. Afterwards, we spin-coated the solution on the substrates using a two-step anti-solvent method, followed by an annealing step at 275 °C for 5 minutes as shown in Figure 4.1 and as described in the experimental part (Table S 4.1).

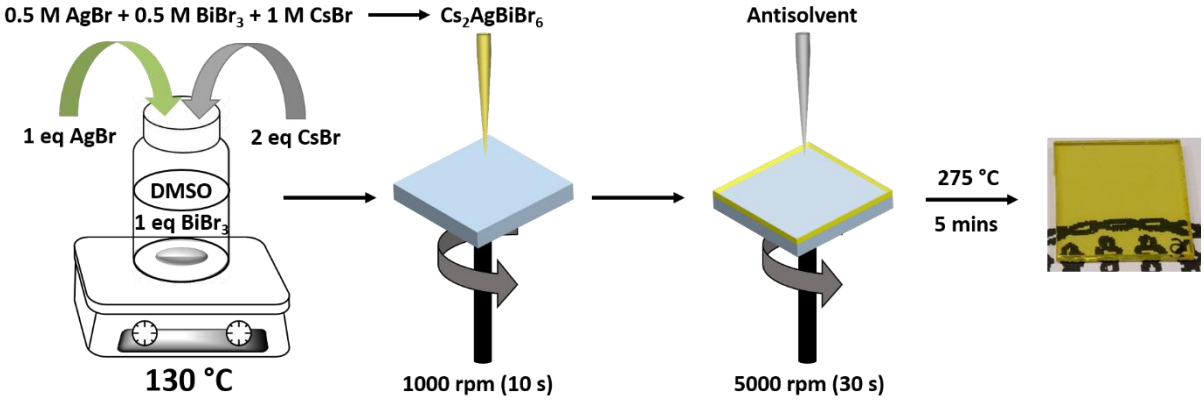

Figure 4.1. Synthesis protocol for the double perovskite thin films. First, the precursors were dissolved in DMSO at 130 °C and afterwards spin-coated with a two-step anti-solvent method. The phase pure double perovskite films were obtained after an additional annealing step at 275 °C for 5 minutes.

For the preparation of the double perovskite films, we first screened a variety of different antisolvents. Here, we obtained the best films in terms of coverage and morphology using 2-propanol (isopropanol, IPA) in a nitrogen filled glovebox, which has been reported to be a good anti-solvent for the preparation of $Cs_2AgBiBr_6$ thin films.[27,30] SEM analysis of the synthesized double perovskite film surfaces (top-view images in Figure S 4.1, Supporting Information) reveals that using IPA as an anti-solvent results in the best film formation with a complete coverage (Figure S 4.1). Therefore, the processing with IPA in a nitrogen filled glovebox was chosen for the following investigations.

Table 4.1 gives an overview of the changes in the stoichiometry that were made in order to investigate the influence of precursor ratio on the film properties. Phase purity and high crystallinity are considered to be very important parameters for the performance of double perovskite films when used as an absorber in solar cells.[26–30,39,40] With regards to phase purity however, it has been shown for lead-based hybrid halide perovskites, that working with a PbI_2 excess is beneficial for the solar cell devices in terms of performance and trap density.[41–43]

Therefore, the first step in this work was to investigate the influence of different precursor stoichiometries on the orientation and crystallinity of the obtained double perovskite films.

Table 4.1. Overview of concentration changes of the $Cs_2AgBiBr_6$ precursors. While the amount of CsBr was always kept constant, the concentrations of AgBr and $BiBr_3$ were changed from 10 to 20%.

AgBr (A)	$BiBr_3$ (B)	CsBr	abbreviation
-10 %	1	1	*0.90:1*
1	-10 %	1	*1:0.90*
+10%	+10%	1	*1.10:1.10*
+10%	1	1	*1.10:1*
+10%	-10%	1	*1.10:0.90*
1	+10%	1	*1:1.10*
-15%	1	1	*0.85:1*
+15%	1	1	*1.15:1*
1	-15%	1	*1:0.85*
1	+15%	1	*1:1.15*
+15%	-15%	1	*1.15:0.85*
-15%	+15%	1	*0.85:1.15*
+15%	+15%	1	*1.15:1.15*
-20%	1	1	*0.80:1*
+20%	1	1	*1.20:1*
1	-20%	1	*1: 0.80*
1	+20%	1	*1:1.20*
+20%	-20%	1	*1.20:0.80*
-20%	+20%	1	*0.80:1.20*
+20%	+20%	1	*1.20:1.20*

To achieve the crystallization conditions of a corresponding solar cell device, we deposited the perovskite layer by spin-coating on top of a layer of compact TiO_2 on an FTO substrate and investigated the films using XRD (Figure 4.2, Figure Figure S 4.2). The results show that changing from Bi^{3+} rich and/or Ag^+ poor conditions (Figure 4.2, orange (*1:1.2*), green (*1.2:1.2*) and dark yellow (*0.8:1*) lines) to Ag^+ rich and Bi^{3+} poor conditions (Figure 4.2, turquoise

(*1.2:1*), magenta (*1:0.8*) and blue (*1.2:0.8*) line) strongly increases the crystallinity and preferred crystallite orientation in the film. Powder X-Ray diffraction (PXRD) patterns of the films resulting from different precursor stoichiometries however reveal a small amount of a side phase, which is discussed further below.

As all films have the same thickness of ~150 nm, the increasing ratio between the peaks of the perovskite and the FTO peaks indicate an increase in crystallinity, which drastically changes with the stoichiometry for Bi deficiency (*1:1-x*—films) and for Bi deficiency combined with Ag excess (*1+x:1-x*—films). An increase in crystallite orientation within the film is indicated by the lack of peaks from the stoichiometric reference (e.g. (111) or (022)), while the only Bragg peaks in the XRD data can be ascribed to the (002) and (004) planes for the above described precursor changes. Figure 4.2 displays the effect of changes in stoichiometry by 20 mol%, as this had the highest impact on the crystallinity and orientation of the films. The smaller impact for changes by 10 mol%, which increases for changes by 15 mol%, can be found in Figure S 4.2 of the Supporting Information.

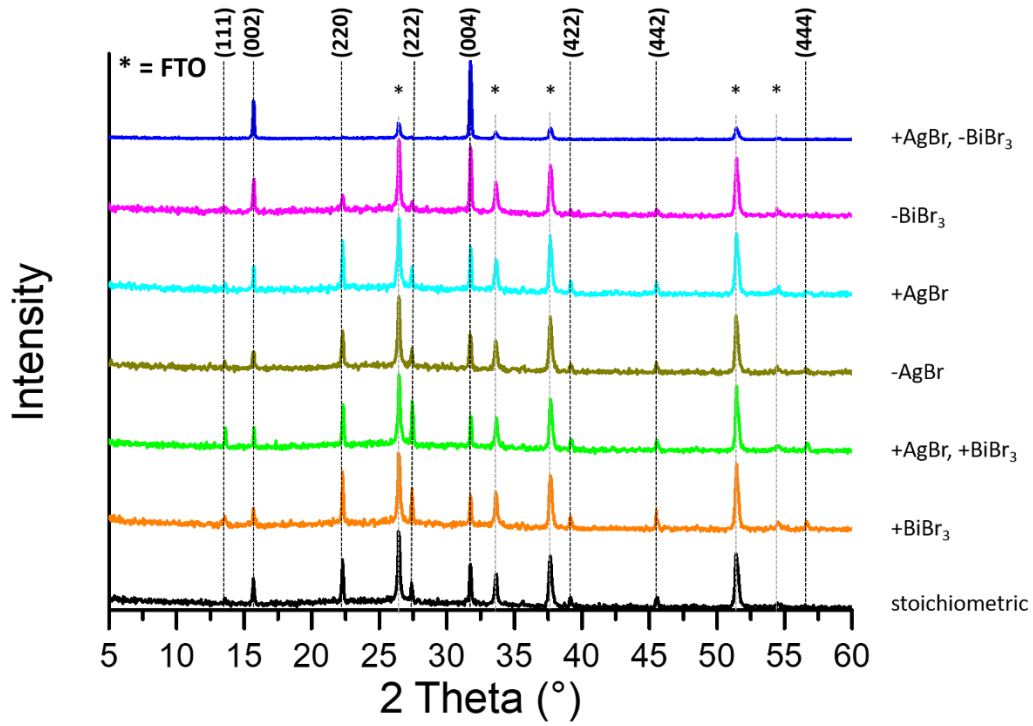

Figure 4.2. XRD data of films obtained by changing the precursor ratio by 20 % as indicated in the legend. The impact of crystallinity is visible through comparison of the (002) and (004) Bragg peak intensities with respect to the FTO substrate peaks (marked with asterisks and gray dashed dropline).

The stoichiometry changes are as indicated in the legend and the different observable planes are indicated with the black dashed droplines as well as the (hkl) Miller indices.

To directly compare the impact of concentration on the crystallite orientation of the obtained films, displays XRD data of films with $BiBr_3$ excess (*1:1+x*; Figure 4.3 a), $BiBr_3$ deficiency (*1:1-x*; Figure 4.3 b), a combination of $BiBr_3$ excess and AgBr deficiency (*1+x:1-x*; Figure 4.3 c), and pure AgBr excess ((*1+x:1*); d) with x = 0.1, 0.15 and 0.2 for changes of 10, 15 and 20 mol%, respectively.

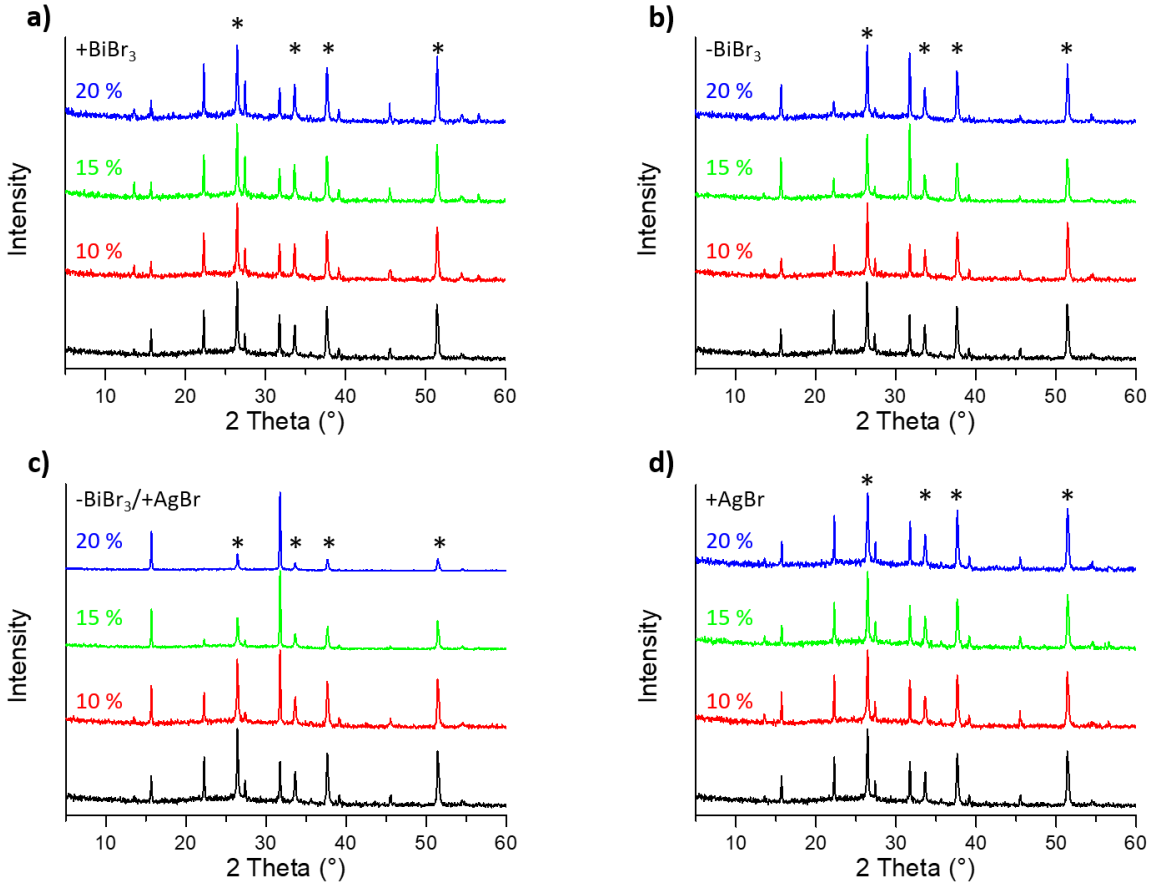

Figure 4.3. XRD data of the obtained double perovskite films with the largest changes in crystallinity and orientation. a) films with $BiBr_3$ excess; b) films with $BiBr_3$ deficiency; c) films with $BiBr_3$ deficiency combined with AgBr excess; d) films with AgBr excess. In all panels, the black line represents the film obtained with stoichiometric precursors while red, green and blue lines indicate 10 mol%, 15 mol% and 20 mol% changes, respectively. The asterisks indicate the Bragg reflections of the FTO substrate.

The XRD data in Figure 4.3 indicate that the orientation and crystallinity of the films are strongly influenced by the amount of $BiBr_3$ in the stock solution. Figure 4.3 a shows the XRD data of (*1:1+x*)—films. It can be seen that the crystal orientation of these films remains similar regarding the number of visible peaks of the different planes. Moreover, the Bragg peak intensities related to the (111) direction, as well as to the (022) direction are increased toward 15 mol% while decreasing again at a change of 20 mol%. Figure 4.3b shows the XRD data of (*1:1-x*)—films. The patterns show an increase in orientation, which is indicated by a decrease of the Bragg peaks for the above-mentioned planes. This effect is strongly boosted by an additional AgBr excess by the same amount, which results in a pattern where only the Bragg peaks for the (002) and the (004) planes are visible (Figure 4.3c), while the patterns of the film do not change towards a preferred orientation upon using a pure AgBr excess (Figure 4.3d). Moreover, not only the orientation of the (*1+x:1-x*)—films, but also their crystallinity seems to increase which is indicated by the strong increase of the ratio between the peaks of the (002) and (004) plane and the FTO peaks (indicated with asterisks). The increase in crystallinity is also indicated by the decrease of the FMWH of the (004)-peak at 31.8° *2*θ from 0.21 ° for the stoichiometric reference to 0.16 ° for the (*1+x:1-x*)—films, which corresponds to domain sizes of around 660 nm and 850 nm, respectively. These values match well with the findings from SEM analysis (Figure S 4.3). To gain further insight regarding the crystallite orientation within the films, we performed grazing-incidence wide-angle X-ray scattering (GIWAXS) measurements for films with 15 mol% changes. This method is a powerful tool to evaluate the preferred orientation of the crystalline phase within a thin film.[44–46]

The GIWAXS data obtained from films comprising AgBr excess with $BiBr_3$ deficiency and from the stoichiometric reference are shown in Figure 4.4. Figure 4.4a shows that standard films comprising the $Cs_2AgBiBr_6$ double perovskite obtained from a stoichiometric ratio of precursors do not present a preferred crystallite orientation, as reported in the literature.[26,28–31] Figure 4.4b,c, however, show a change in behavior as the Bragg peaks of the (002) and of the (004) reflection (red circle) gain intensity in surface normal direction (low χ values, Figure 4.4d) if the stoichiometry of the films (their precursor ratio) is changed towards (*1.15:0.85*) and (*1.20:0.80*), respectively. To directly compare the different films and to extract quantitative information of different degrees of orientation, a plot of the azimuthal cut along the (002) reflection and the corresponding fits are shown in Figure 4.4d. Here, the plot shows the strongest intensity towards χ = 0° for all three films (stoichiometric reference: light grey scatters

with the corresponding fit in light red; (*1.15:0.85*)—films: dark grey with red fit; (*1.20:0.80*)—films: black with dark-red fit).

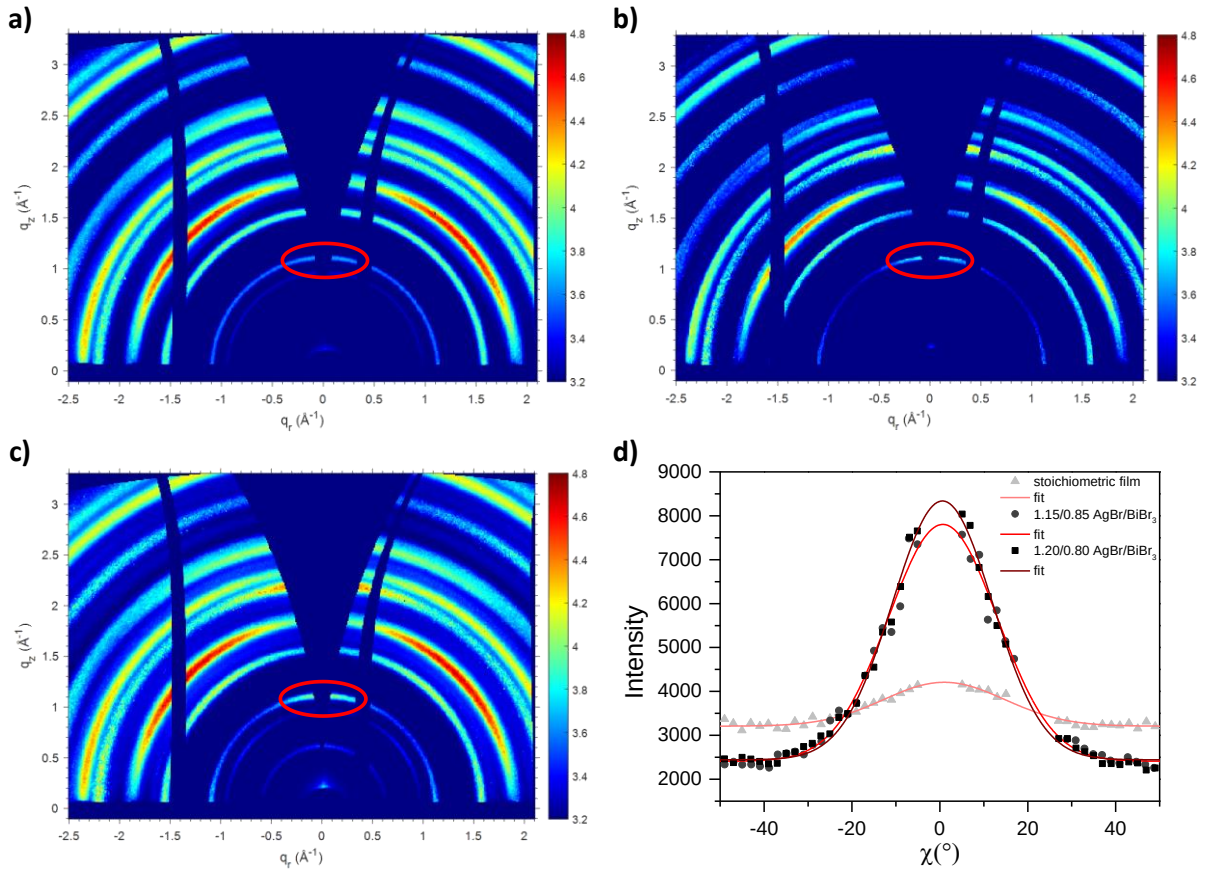

Figure 4.4. GIWAXS data of the investigated films. a) Stoichiometric films; b) films with $BiBr_3$ deficiency, combined with AgBr excess (*1.15:0.85;* 15 mol%); c) films with $BiBr_3$ deficiency, combined with AgBr excess (*1.20:0.80;* 20 mol%); d) azimuthal cut of (002) reflection (marked with a red ellipse in a) to c)) to show the comparison of the intensities with fit for the stoichiometric films (light grey triangles, light red fit), *1.15:0.85*-films (dark grey circles, red fit) and *1.20:0.80*-films (black squares, dark red fit).

Furthermore, the data show a continuous increase in central peak intensity towards the 20 mol% change with the biggest change going towards the 15 mol% film. The high-intensity peaks at q ~ 1.9 (Å^{-1}) are assigned to the FTO reflection of the substrate which moreover overlaps the (113) reflection. The GIWAXS data in Figure S 4.4 confirm that a similar change in the orientation of the films could not be observed for (*1:0.85*)— or (*1:1.15*)—films which is in agreement with the diffraction patterns obtained by in-film Debye-Scherrer XRD that indicated the exact same trend. Moreover, the same results were observed with thin films which were

spin-coated on top of pure glass substrates (Figure S 4.5) and sapphire, respectively (Figure S 4.6).

To investigate the phase purity of the resulting double perovskite films, PXRD measurements were performed with powders obtained by scratching off the as-synthesized thin films. The XRD data are shown in Figure 4.6 and reveal secondary phases for the films with different stoichiometric ratios. As expected from the chemical equations in Figure S 4.7, the (*1.15:1*)—films show peaks at 2θ = 30.81°, 44.13° and 54.86° belonging to the AgBr secondary phase (Figure 4.6a).[47] Films with the (*1:1.15*) ratio exhibit additional peaks at similar angles, however a peak at 54° is not visible, which indicates cubic $BiBr_3$ as a secondary phase (Figure 4.6b) and is expected from Figure S 4.7.[48] For (*1:0.85*)—films, the secondary phase Cs_2AgBr_3 would be expected from the reaction scheme in Figure 4.5).

$$2\ CsBr + AgBr + 0.85\ BiBr_3 \longrightarrow 0.85\ Cs_2AgBiBr_6 + 0.15\ Cs_2AgBr_3$$

Figure 4.5: Reaction scheme of proposed side phase formation for the *(1:0.85)*-films.

The peaks of the secondary phase observed, however, belong to $CsAgBr_2$.[49] From the reaction scheme in Figure S 4.7, it is visible that in this case CsBr should also have formed as a secondary phase, yet the peaks of this material are obscured by the main peaks of the $Cs_2AgBiBr_6$ double perovskite (Figure 4.6c).[50] The complete CRD patterns can be found in Figure S 4.8. For the (*1.15:0.85*)—films, $CsAgBr_2$ is observed as the only secondary phase. This was confirmed by additional experiments where $CsAgBr_2$ was synthesized and precipitated for PXRD measurements (Figure S 4.9a). Moreover, thin films of this material were deposited by spin-coating and the corresponding film-XRD was recorded (Figure S 4.9b). Interestingly, the characteristic peak at 2θ = 8° for the Cs_2AgBr secondary phase is not visible in the film-XRD data of the double perovskite films, but only in the PXRD data and slightly in the GIWAXS data (Figure 4.4c), which possibly results from a very small ratio of this secondary phase within the film, as well as a possibly low crystallinity of $CsAgBr_2$ compared to the $Cs_2AgBiBr_6$ double perovskite. The formation of the secondary phase in case of the *(1.15/0.85)*-thin films was confirmed with EDX-measurements of the scraped-off powders, shown in in the supporting information (Figure S 4.10, Table S 4.2).

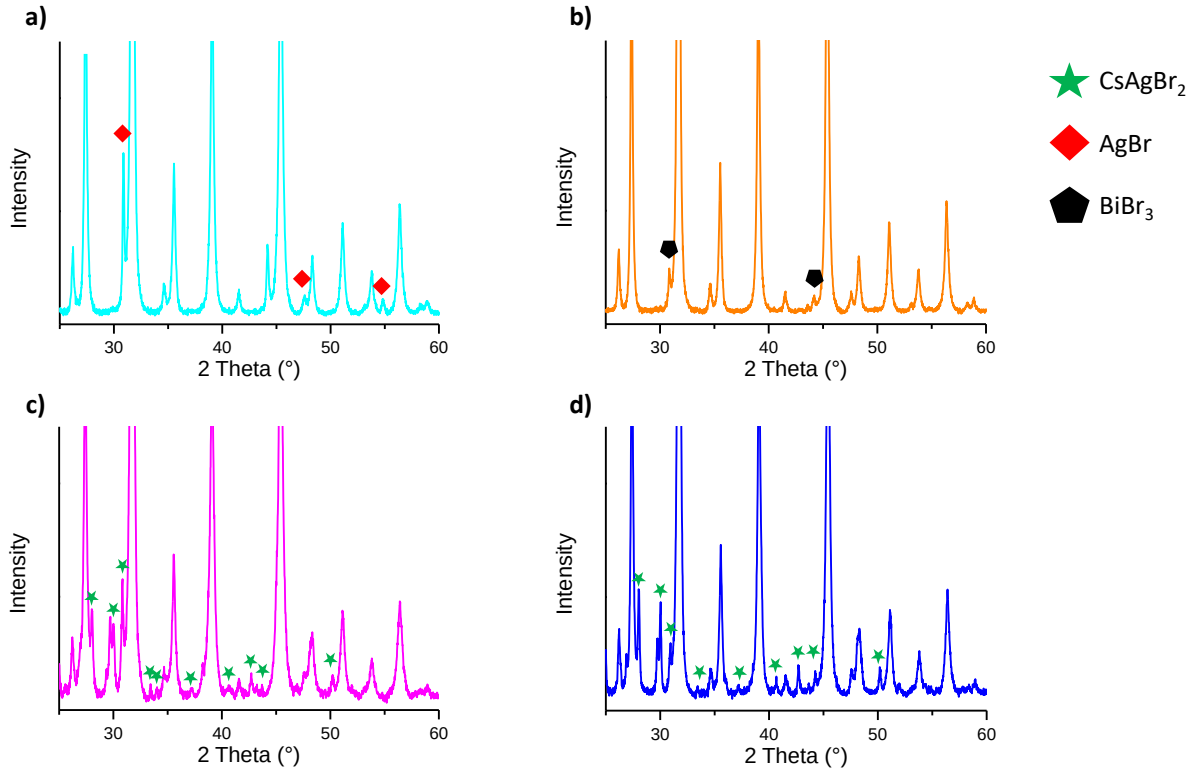

Figure 4.6. PXRD data of the different double perovskite films. a) (*1.15:1*)—film, b) (*1:1.15*)—film, c) (*1:0.85*)—film, d) (*1.15:0.85*)—film. The Bragg peak positions of the secondary phases are indicated with different symbols: red rectangle: AgBr; black pentagon: $BiBr_3$ and green star: $CsAgBr_2$. The full PXRD patterns can be found in Figure S 4.8.

Hence, to investigate the influence of this secondary phase on the crystallization behavior, stoichiometric double perovskite films were fabricated by spin-coating their precursors on top of a thin film of $CsAgBr_2$ and XRD measurements of the films were performed. The results in Figure S 4.8c show that the orientation of the film does not change in the same manner as it did for films produced directly from $BiBr_3$ deficiency combined with an AgBr excess. By intentionally adding $CsAgBr_2$ to the stoichiometric $Cs_2AgBiBr_6$ stock solution at several concentrations, we did not achieve a similar orientation and crystallinity in the thin films as compared to the (*1.20:0.80*)—films, as shown in the film-XRD data in Figure S 4.9c. Even by adding $CsAgBr_2$ at high concentration (35 %), the crystallite orientation of the films is not comparable to the ones where the above excess/deficiency combination was applied. However, all films synthesized with added secondary phase, show a strong reflection at $2\theta = 8°$, which cannot be found in the patterns of the highly oriented double perovskite thin films. This shows

that the $CsAgBr_2$ secondary phase has almost no influence on the structural properties of the thin films investigated in this work.

A high orientation along the (001) plane has been proven to be beneficial for charge transport in lead-based perovskite systems.[41–43] These findings inspired us to perform PL and TRMC measurements to investigate the influence of the orientation and change in stoichiometry of our double perovskite thin films on the optoelectronic properties.

Figure 4.7a shows the different PL intensity spectra of double perovskite thin films with different precursor ratios with respect to an in-batch reference that was deposited from a stoichiometric solution. The steady-state spectra were recorded on five different spots of the corresponding films and the results were averaged. To prevent any influence of FTO or TiO_2 substrates, all films for these measurements were deposited by spin-coating on glass substrates. All films show a strongly Stokes-shifted and broad PL peak around 2.0-2.1 eV, which is in good agreement with literature reports and can be attributed both to the indirect bandgap emission and trap-assisted recombination.[23,28,40]

To rule out any possible influence of $CsAgBr_2$ on the optoelectronic properties of the investigated films, we also performed the same UV/Vis and PL measurements with thin films of this secondary phase (Figure S 4.11). The results reveal that the secondary phase does not have any photoluminescence or absorption in the visible region. Therefore, the secondary phase does not influence the optoelectronic properties of the investigated double perovskite thin films, apart from introducing optically inactive volume to the film.

While the UV/Vis absorption of the stoichiometrically altered thin films does not change remarkably apart from a slight decrease in absorption for the (*1.0:0.85*)—films (Figure S 4.12), the PL results show the highest intensity for these $BiBr_3$ deficient films. Moreover, a slight increase of the intensity compared to the stoichiometric reference is also observed for the (*1.15:0.85*)—and (*1.20:0.80*)—films which show a lower UV/Vis absorption than the stoichiometric reference. Additionally, for the combination of AgBr excess with $BiBr_3$ deficiency, the PL data show that the change of 15 mol% is most beneficial, as the (*1.10:0.90*)—and (*1.20:0.80*)—films show reduced intensity in comparison (Figure S 4.13). The (*1.15:0.85*)—films show a minor red-shift, which increases the Stokes shift slightly. A higher steady state intensity implies a larger amount of (steady state) free charge carriers,[39] beneficial for open-circuit voltage and thus PCE of operational solar cells. The results suggest that the

additional amount of Bi^{3+} is detrimental for the film performance as an increase of the $BiBr_3$ amount seems to have the largest negative impact on the photoluminescence of the films. In the case of AgBr excess, only the combination with a $BiBr_3$ deficiency results in an improvement of the PL signal, further strengthening the point that the Bi^{3+} amount is the crucial part of the stoichiometry changes.

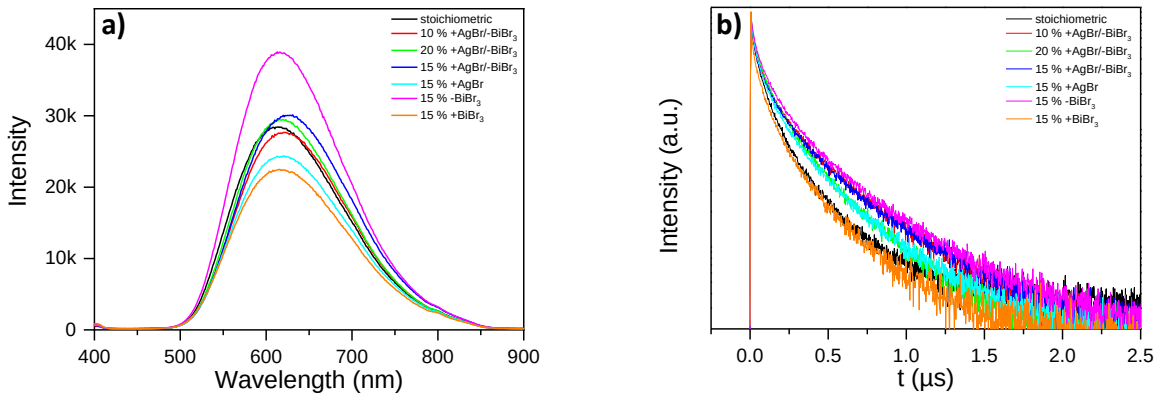

Figure 4.7. Photoluminescence of different precursor ratio films. (a) Steady state emission with an artifact of the setup 800 nm which is caused by the 400 nm longpass filter used. (b) Time-resolved emission dynamics obtained through TCSPC. The different precursor ratios are color coded as indicated in the legend: stoichiometric reference (black), (*1+x:1-x*)—films (red, blue and green), (*1.15:1*)—, (*1:0.85*)— and (*1:1.15*)—films (turquoise, magenta and orange).

To gain further insight into the charge carrier lifetime and the influence of the precursor stoichiometry, we performed time-correlated single photon counting (TCSPC) measurements as shown in Figure 4.7b). The traces were fitted with a triple exponential function to accommodate all contributions, as done in the literature to evaluate transient photoluminescence data for $Cs_2AgBiBr_6$. This conventional evaluation has been chosen in order to compare the different films based on suggested recombination mechanisms corresponding to the different decay contributions discussed by Slavney et al. and other groups.[23,29,51] The traces for every film with corresponding fits are shown in the Supporting Information (Figure S 4.14), and the values of the charge carrier lifetimes are shown in Table 4.2.

For all films, a fast decay component was observed, usually faster than 20 ns. Moreover, a second, slower component with lifetimes around 80—150 ns was observed, as well as a third fraction with even slower decay and the largest contribution to the signal.

Table 4.2 Overview of TCSPC results and the tri-exponential fits. All three decay components are given in ns and the contributions towards the overall signal intensity are given in brackets.

Film	τ_1 (ns) [contribution in %]	τ_2 (ns) [contribution in %]	τ_3 (ns) [contribution in %]	τ_{AVG} (ns)
Stoichiometric	13.0 ± 1.4 [7.1]	82.5 ± 1.7 [50.0]	**303.5** ± 5.5 [42.9]	172.3
10 mol% +AgBr/-$BiBr_3$	17.7 ± 1.4 [7.8]	116.6 ± 2.6 [38.5]	**445.3** ± 5.5 [53.7]	285.5
15 mol% +AgBr/-$BiBr_3$	18.3 ± 1.5 [8.4]	122.8 ± 2.9 [39.8]	**464.4** ± 6.6 [51.8]	291.1
20 mol% +AgBr/-$BiBr_3$	19.6 ± 1.6 [8.3]	110.4 ± 2.1 [44.2]	**363.1** ± 4.8 [47.5]	223.0
15 mol% +AgBr	16.8 ± 1.3 [8.0]	101.9 ± 2.0 [42.5]	**378.3** ± 4.9 [49.5]	232.0
15 mol% -$BiBr_3$	25.4 ± 1.7 [9.7]	143.9 ± 2.8 [44.0]	**505.2** ± 6.8 [46.3]	299.5
15 mol% +$BiBr_3$	7.2 ± 8.5 [5.0]	76.2 ± 1.7 [45.0]	**307.1** ± 5.2 [50.0]	187.6

While the origin of the first two decay contributions so far remains unclear in literature, the third fraction τ_3 could be attributed to a first order decay and therefore a trap assisted recombination process.[23,29,51]

A comparison of this long living component (τ_3) reveals a superior lifetime for films either comprising a sole $BiBr_3$ deficiency (505.2 ns) or a combination with AgBr excess (464.4 ns). This indicates a slower recombination *via* trap states and should thus result in a better performance in solar cells. On average, the correlation between films featuring the highest steady-state PL intensity with the longest charge carrier lifetime certifies a reduced non-radiative recombination rate irrespective of its origin.

These results further reinforce the findings from the steady state measurements that the trap density is reduced by moving towards a Bi^{3+} deficient system which is in agreement with the

calculations of Li et al.[52] Although the (*1+x:1-x*)—films have both reduced PL intensity and lifetime compared to the (*1.0:0.85*)—films, the contributions of the lifetime components that are caused by trap assisted recombination are reduced while simultaneously those fractions are long living, indicating a lower overall trap density.

Although fitting TRPL results with three exponentials is the common evaluation method, it cannot fully address all processes that contribute to the signal. Therefore, to enhance our understanding of the defect-related dynamic behavior of the different films, we performed both fluence-dependent steady state and time-resolved photoluminescence measurements of the stoichiometric and the (*1.15:0.85*)—films as for between these two, the stoichiometric difference is the largest within the 15 mol% change. The results in Figure S 4.15 and Figure S 4.16 show a similar behavior of both films for both measurements.

The fluence-dependent steady state measurements reveal two different slopes between 1 mW/cm^2 and 1000 mW/cm^2. In the low intensity regimes, a slope of 1.4 was found for both films. This is in agreement with literature and indicates a recombination pathway dominated by Shockley-Read-Hall and therefore trap assisted recombination.[53] For high excitation intensity, a slope of m = 1 was found, which could be assigned to an excitonic contribution since a higher excitation intensity leads to a strongly increased amount of charge carriers, which in turn leads to a smaller ratio of free charge carriers to excitons as stated by the Saha-Langmuir equation.[54]

The graphs of the fluence dependent TRPL measurements in the Supporting Information show a similar behavior of both films as well, consistent with the results of the steady-state measurements. This indicates again the same recombination pathways for both films which is in agreement with the steady state measurements. Moreover, neither of the films show fluence dependency of their TRPL which is in agreement with results from other groups.[39]

After PL, which consists of several contributions due to radiative and non-radiative exciton and/or charge carrier recombination, we performed time-resolved microwave conductivity (TRMC) measurements on the films to gain insight in the intrinsic charge carrier properties of the material. Because the PL results suggest the (*1+x:1-x*)—films of 15 mol% to be the most promising, we focused our studies on this particular stoichiometry change of 15 mol% in the following. The TRMC transients can be found in the Suppporting Information (Figure S 4.17).

In TRMC, the photoconductance (ΔG) is measured as a function of time upon pulsed optical excitation of the sample.[55] For this purpose, the sample was placed in a TRMC cavity and

excited well above the bandgap at 355 nm. Ideally, the product of the free carrier generation quantum yield ϕ and the sum of electron and hole mobility $\sum \mu$ is directly proportional to ΔG as expressed in eq (4.1):

$$\varphi \sum \mu = \frac{\Delta G_{max}}{\beta e I_0 F_A} \quad (4.1)$$

Where I_0 is the number of incident photons, F_A is the fraction of absorbed light, e is the elemental charge, and β is the ratio of the inner dimensions of the TRMC cell.

In 2018, Bartesaghi *et al.* first investigated $Cs_2AgBiBr_6$ single crystals with TRMC and revealed that the material presents a large number of surface traps, as well as a mobility of at least 0.1 $cm^2/(Vs)$.[21] Using a similar setup and microwave frequency range, we performed intensity dependent ϕΣμ measurements at room temperature. For high excitation intensity, a relatively small value of ϕΣμ can be observed, although a high charge carrier density prevails which is indicated by the strong absorption at 355 nm. Therefore, the higher amount of charges leads to a faster recombination within the response time of the setup, as well as a reduced ratio of free charges to excitons. This altogether leads to a quantum yield below 1.[51] As shown in Figure 4.8, the product of quantum yield and mobility does not saturate for the lower laser intensity. As the mobility in general is considered to be intensity-independent, this further strengthens the assumption that the free carrier quantum yield is substantially lower than 1 and that a large amount of strongly bound Frenkel excitons are created. To reach a quantum yield of 1, a considerably smaller excitation intensity is required. However, at lower intensity, we were not able to obtain TRMC traces with a sufficient signal to noise ratio, which can be ascribed to the large exciton binding energy proposed for this material.[51] Hence, we will only be able to give a lower estimate for the charge carrier mobility of the investigated films. To rule out any different behavior due to different film thickness, as well as absorption behavior, we recorded the absorption spectra (Figure S 4.12) and determined the thickness of the different films *via* profilometry (Table 4.3). Please note that here we have different film thickness compared to the PL part, as the TRMC measurements were performed on sapphire-glass with a lower surface roughness compared to FTO covered glass.

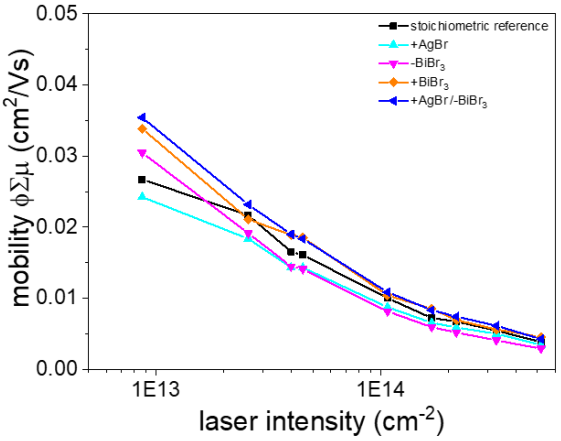

Figure 4.8. Intensity dependent mobility values obtained by TRMC measurements at RT. The product of the quantum yield and the charge carrier mobility is dependent on the excitation intensity given in photons/cm^2. The product of mobility and quantum yield does not saturate at low intensity, which can be attributed to the exciton formation. The black line shows the values of the stoichiometric films, the blue line of the (*1.15:0.85*)—film, the turquoise line of the (*1.15:1*)—film, the magenta line of the (*1:0.85*)—film, and the orange line of the (*1:1.15*)—film.

In agreement with literature, the product of the quantum yield and the mobility of the different films drops with an increase of laser intensity.[21] This can be related to the smaller quantum yield at higher intensity caused, as discussed above, by the smaller ratio of free charge carriers to excitons and fast recombination. The results show that the product of quantum yield and charge carrier mobility is the highest for the (*1.15:0.85*)—films at all laser intensities. At lower laser intensity, both the stoichiometric and the (*1:1.15*)—films show comparable values. Kentsch et al. have recently calculated the exciton binding energy in a $Cs_2AgBiBr_6$ thin film to be 268 meV, which is more than 10fold higher compared to the lead-based MAPI perovskite.[51] As excitonic contributions are generally not taken into account for the general TRMC equation (4.1), the charge carrier mobility values we obtained are significantly underestimated since the quantum yield is strongly dependent on the high exciton binding energy and should be well below 1.

To determine the absolute and corrected values of the charge carrier mobility, the quantum yield was corrected with the Saha-Langmuir equation (4.2)[54]

$$\frac{x^2}{1-x} = \frac{1}{n}\left(\frac{2\pi m^* k_B T}{h^2}\right)^{\frac{3}{2}} e^{-\frac{E_B}{k_B T}} \qquad (4.2)$$

Where x is the fraction of free charge carriers, n is the total charge carrier density, T is the absolute temperature, k_B is the Boltzmann constant, E_B the exciton binding energy and m^* the reduced exciton mass which was determined by Feng et al.[56] With this correction, we were able to estimate the charge carrier mobility as shown in Table 4.3. We note that a fraction of the free charge carriers recombines within the response time of the TRMC setup. Therefore, the $\phi\Sigma\mu$ values presented here can be considered as a lower limit to the actual mobility in these double perovskites.

Table 4.3. Quantum yield, products of mobility and quantum yield, estimated mobilities and thicknesses for the different stoichiometric films.

Film parameter	Quantum yield	$\varphi\Sigma\mu$ [$cm^2/(Vs)$]	$\Sigma\mu$ [$cm^2/(Vs)$]	d [nm]
Stoichiometric reference	0.0064	0.027	4.2	116 ± 20
1.15:1	0.0069	0.024	3.5	134 ± 19
1:1.15	0.0067	0.034	5.1	125 ± 16
1:0.85	0.0064	0.031	4.8	101 ± 21
1.15:0.85	0.0072	0.036	5.0	136 ± 18

With the Saha-Langmuir correction, we observed a higher charge carrier mobility for the (*1.15:0.85*)—films compared to all other films, as already suggested by the measured product of the quantum yield and the mobility in Figure 4.8 and Table 4.3. However, in earlier reports on mobilities in lead-free double perovskites, excitonic contributions and the resulting low quantum yield were not taken into account and therefore, the earlier reported products of quantum yield and mobility measured by Bartesaghi *et al.* on $Cs_2AgBiBr_6$ films are lower than the values presented here.[21] However, as we accounted for the low quantum yield of the samples, we have been able to get a more precise estimate of the lower boundary of the actual mobility of lead-free perovskites.

Altogether, the results confirm the trend observed from the PL measurements that suggest improved charge carrier dynamics for the (*1.15:0.85*)—film.

In addition to optoelectronic investigations, we integrated the different double perovskite thin films as active layers in solar cells with the architecture FTO/TiO_2/$Cs_2AgBiBr_6$/P3HT/Au. To exclude a varying absorption due to different layer thicknesses, the thickness for all films was fixed at 150 nm.

Solar cells with abnormal *J-V*-curves as well as shorted cells were left out of the statistics since those results were not reliable. The obtained parameters of the solar cells are shown in Table 4.4 and Figure 4.9, and the *J-V*-curves of the champion cells of the stoichiometric reference and the (*1.15:0.85*)—films are shown in Figure S 4.19. An exemplary EQE spectrum can be found in Figure S 4.20.

Table 4.4. Parameters of solar cells comprising double perovskite thin films made with different stoichiometric precursor ratios. The table shows the V_{OC} in V, the J_{SC} in mA/cm^2, the *FF*, and the PCE in %. For every stoichiometric ratio, the champion device is shown, while the average of all devices is given in the bracket.

FTO/TiO_2/$Cs_2AgBiBr_6$/P3HT/Au				
Precursor stoichiometry [# of cells]	J_{SC} (mA/cm^{-2}) [Avg]	V_{OC} (V) [Avg]	*FF* (%) [Avg]	PCE (%) [Avg]
Stoichiometric [40]	1.40; [1.16 ± 0.14]	1.03; [0.93 ± 0.07]	67; [62 ± 8]	0.97; [0.68 ± 0.14]
+AgBr/-$BiBr_3$ [36]	1.48; [1.32 ± 0.12]	1.05; [0.92 ± 0.09]	71; [65 ± 9]	1.11; [0.75 ± 0.19]
-$BiBr_3$ [41]	1.33; [1.03 ± 0.15]	1.05; [0.91 ± 0.09]	74; [67 ± 6]	1.02; [0.63 ± 0.17]
+AgBr [28]	1.48; [1.26 ± 0.10]	0.91; [0.72 ± 0.13]	72; [59 ± 10]	0.91; [0.55 ± 0.18]
+$BiBr_3$ [30]	1.15; [1.10 ± 0.13]	1.02; [0.86 ± 0.13]	67; [58 ± 8]	0.79; [0.56 ± 0.16]

For each data point, 28 to 41 cells were taken into account with most cells (41) contributed from the (*1.00:0.85*)—films. The cells with the stoichiometric reference showed a slightly lower reproducibility with 36 working devices. The performance of the cells reached 1.11 % for the (*1.15:0.85*)—films which also showed the highest average PCE amongst the prepared solar cells. The stoichiometric films featured a maximum PCE of 0.97 % with a lower average value compared to the (*1.15:0.85*)—films. For (*1.15:1*)— or (*1:0.85*)—films, as well as for films with the (*1:1.15*) precursor stoichiometry, the average PCE drops in comparison to the stoichiometric reference, which confirms the trend we observed with the PL and TRMC measurements.

The origin of the difference in PCE of the (*1.15:0.85*) device compared to the stoichiometric one can be found in the change in the J_{SC} and *FF* of the cells. In the case of the (*1.15:0.85*)—films, the average J_{SC} is increased by 13 %, while the *FF* is increased by 3 % absolute value compared to the stoichiometric reference. The increase in average J_{SC} results from an improvement of the charge carrier dynamics as shown above by TRMC and TCSPC measurements, as well as the film morphology. This is further supported by the larger *FF*. For the champion cell, the V_{OC} of the (*1.15:0.85*)—films is increased as well while the average is the same. This is in agreement with our results from the optoelectronic studies.

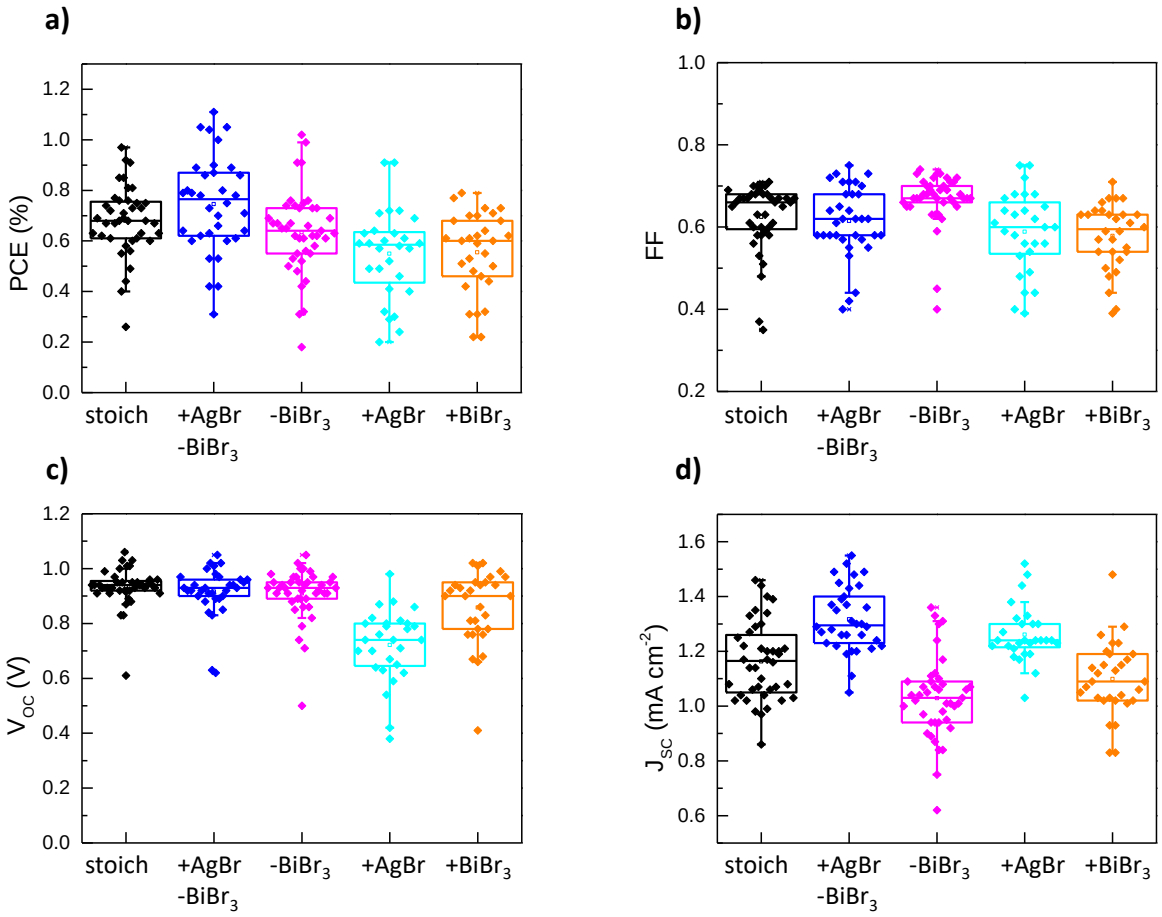

Figure 4.9. Box plots of the solar cell parameters of the cells: black: stoichiometric reference; blue: *(1.15:0.85)*—films; magenta: *(1:0.85)*—films; turquoise: *(1.15:1)*—films; orange: *(1:1.15)*—films. Panel (a) shows the PCE of the solar cells in %, panel (b) shows the FF of the solar cells, panel (c) shows the V_{OC} in V and panel (d) gives the J_{SC} in mA/cm2.

The results show that changing the precursor stoichiometry of the films to an AgBr excess combined with a $BiBr_3$ deficiency by 15 mol% improves the photovoltaic performance of the system. An increase in the J_{SC}, as well as in the *FF* can be observed suggesting that the modified films allow for enhanced charge transport and charge carrier extraction, which is in agreement with our TRMC and PL measurements.

Altogether, the results for the solar cells are consistent with findings for lead-based perovskites indicating that by increasing the crystallite orientation along the (001)-direction, the charge extraction is increased, leading to a rise in J_{SC} and hence an enhancement of the overall performance of the resulting solar cells as charge transport along this direction is favored.[32–35]

4.4 Conclusion

In conclusion, we present a way to improve the optoelectronic properties of $Cs_2AgBiBr_6$ thin films by controlling domain orientation and crystallization. This was achieved by tuning the stoichiometry of the precursors and working in an AgBr-excessive and $BiBr_3$-deficient system or a combination of both (*$AgBr:BiBr_3$ = 1:1.15/1:0.85/1.15:1/1.15:0.85*). We examined the structural properties of the prepared films using both film XRD and GIWAXS techniques to show a strong increase in orientation along the (001)-direction of (*1.15:0.85)*-films. The analysis moreover revealed the formation of a small amount of the secondary-phase $CsAgBr_2$, which was found to not influence the structural and optoelectronic properties of the material.

Investigating the optoelectronic properties of the prepared films revealed an enhancement of the PL lifetime for the (*1.15:0.85)* and (*1:0.85)*-films from ~250 ns to ~500 ns compared to the stoichiometric reference, while the other stoichiometric combinations showed reduced lifetime. Moreover, TRMC measurements revealed a strong increase in mobility and conductivity which ultimately resulted in an enhancement of the photovoltaic properties of the material. Solar cells with the architecture FTO/TiO_2/$Cs_2AgBiBr_6$/P3HT/Au reached PCEs up to 1.11 % using the (*1.15:0.85)*-films, which also outperformed the stoichiometric reference due to an enhancement of the J_{SC} by 13 % in average. The increase in J_{SC} as a result of controlled crystal domain orientation is consistent with literature reports regarding oriented Pb-based perovskite solar cells.

This work introduces a way to easily tune the properties of the $Cs_2AgBiBr_6$ perovskite by changing the stoichiometry of the AgBr and $BiBr_3$ precursors used in thin-film deposition. The optimized crystallographic orientation of the films opens possibilities of enhanced charge transport as well as improved charge extraction and is a valuable tool to enhance the performance of lead-free double perovskite solar cells. The results of this study further show the importance of charge carrier transport in this system, the determinants of which deserve further study.

4.5 Methods

Materials and Thin Film Synthesis

The Stock solution was prepared by dissolving CsBr (212.8 mg, 1 mmol, Alpha Aesar, 99.999 % metals basis), $BiBr_3$ (224.4 mg, 0.5 mmol, Alpha Aesar, 99.9 % metals basis) and

AgBr (93.9 mg, 0.5 mmol, Alpha Aesar, 99.998 % metals basis) in 1 mL DMSO (Sigma Aldrich, anhydrous, ≥99.9 %) at 130 °C to obtain a 0.5 M solution for the stoichiometric reference films. To change the stoichiometry, we changed the amounts of AgBr and $BiBr_3$ according to Table S 4.1. In a nitrogen filled glovebox, the thin films were deposited by spin-coating dynamically (first at 1000 rpm for 10 s, followed by a second step at 5000 rpm for 30 s) onto the substrate (80 µL of the stock solution). After 23 s of the second step, 400 µL 2-propanol was dripped quickly on top of the substrate, and the films were annealed at 275 °C for 5 minutes.

Solar Cell Fabrication

Fluorine-doped tin oxide coated glass sheets (7 Ω/sq) were patterned by etching with zinc-powder and 3 M HCl, cleaned with a detergent followed by washing with acetone and ethanol and dried under an air stream. Directly before applying the hole blocking layer the substrates were plasma cleaned with oxygen for 5 min. A compact TiO2 layer was prepared from a sol-gel precursor solution by spin-coating 300 µL onto the 3 cm x 3cm substrates for 45 s at 2000 rpm and calcination afterwards at 500 °C for 30 min in air resulting in a 50 nm thick layer. For the sol-gel solution, 2 M HCl (35 µL) in 2.53 mL dry 2-propanol was added dropwise to a solution of 370 µL titanium isopropoxide in 2.53 mL dry 2-propanol under vigorous stirring. After cooling down, the substrates were again plasma cleaned for 5 min and transferred to a nitrogen-filled glovebox. On top, of the titania layer, the active layer was deposited as described above.

For P3HT, 55 mg of the material (Ossila, batch M1011; MW: 60150; RR: 97.6 %., M_n: 28650 PDI: 2.1) was dissolved in 1 mL ortho-dichlorobenzene and deposited dynamically by spin-coating 90 µL of a 55 mg/mL solution at 600 rpm for 120 s at ambient conditions.

The top electrode with a thickness of 40 nm was deposited subsequently by thermal evaporation of gold under vacuum (~10^{-6} mbar).

Materials Characterization

X-ray diffraction (XRD) Measurements

The thin film X-Ray diffraction data were recorded using a Bruker D8 Discover Diffractometer with Ni-filtered Cu K_α radiation and a LynxEye position-sensitive detector in Bragg-Brentano geometry.

The Powder X-Ray diffraction data were recorded using a STOE STADI P diffractometer with Ge-filtered Cu K_α radiation and a DECTRIS solid-state strip detector MYTHEN 1K in Debye-Scherrer geometry.

Grazing-Incidence Wide-Angle X-Ray Scattering (GIWAXS)

GIWAXS measurements were carried out at the Micro- and Nano focus X-Ray Scattering (MiNaXS) beamline P03 located at PETRA III (DESY, Hamburg, Germany).[57] A photon energy of 12.6 keV with corresponding wavelength (λ = 0.986 Å) was used. The incidence angle of the beam impinging onto the films was 0.4°, which was above the critical angle (total reflection angle) of the double perovskite thin films. Thus, the bulk film was probed by the X-ray beam to obtain structure information. A 2D detector with pixel size 172 × 172 μm^2 (Pilatus 300K, Dectris Ltd., Switzerland) was placed at a sample-to-detector distance of 119 mm to collect the scattered X-rays. To protect the detector from overexposure, the direct beam was shielded by a beamstop. To avoid beam damage, all films were measured on several different spots with short exposure times. The 2D detector patterns were reshaped, corrected and further processed using the GIXSGUI software.[58]

Scanning Electron Microscopy (SEM)

SEM images were obtained with an FEI Helios G3 UC instrument with an acceleration voltage of 5 kV for the cross-sectional images and 2 kV for the top-view images and EDX studies. All samples were sputtered with carbon beforehand and both mirror and through the lens detectors were used.

Steady State Photoluminescence (PL) and Time-Correlated Single Photon Counting (TCSPC)

The thin films were deposited onto the respective substrate by spin-coating as described above and all PL measurements were performed with a FluoTime 300 Spectrofluorometer (PicoQuant GmbH) in air.

To excite the samples for steady state measurements, a pulsed solid-state laser of 375 nm wavelength (LDH375, PicoQuant) with a fluence of 20 pJ/cm^2 at 40 MHz repetition rate was used, in order to obtain steady state conditions.

For TCSPC, the samples were excited using a pulsed solid-state laser of 375 nm wavelength (LDH375 PicoQuant) with the following power and repetition rates: AgBr:$BiBr_3$ = 1:1.15 (4.1 µW; 0.25 MHz) 1:0.85 (3.8 µW; 0.23 MHz); 1.15:1 (4.9 µW; 0.29 MHz); 1.10:0.90 (4.2 µW; 0.26 MHz); 1.15:0.85 (3.8 µW; 0.23 MHz); 1.20:0.80 (4.6 µW; 0.28 MHz). The illuminated area was 100 µm.

The emission of the sample was collimated, focused on the entrance slit of a monochromator, and reduced with a neutral density filter such that the photomultiplier tube (PMT) behind the monochromator could only detect one single photon at a time. The time difference between laser triggering and the PMT detecting a photon was measured and collected in a histogram, which after a large number of counts (usually several thousands) represents the decay kinetics of the emissive state. The wavelength for excitation was determined by the steady state measurements and fixed. To obtain the lifetime of the charge carriers, the decay was fitted with a triple exponential function as shown in Figure S 4.14.

Fluence-dependent TCSPC measurements were carried out with an FLS-980s (Edinburgh Instruments) spectrometer. As excitation source a pulsed 375 nm laser (EPL-375) was used with a repetition rate of 0.2 kHz for all samples. The excitation fluence was varied between 9.2 nJ/cm² and 0.5 nJ/cm² by the use of neutral density filters.

Fluence-dependent steady state PL was measured using a 415 nm LED (Solis-415C, Thorlabs). The sample was placed at a 45° angle towards the excitation beam, so that measurements were performed in a reflection configuration. A silicon diode was placed in the emission pathway in order to monitor the resulting integrated photoluminescence.

Time Resolved Microwave Conductivity Measurements

The stoichiometrically altered $Cs_2AgBiBr_6$ films were fabricated on sapphire substrates with the technique used for all other films. The thin films on sapphire substrates were placed in a microwave cavity. The TRMC technique was used to measure the change in reflected microwave (9 GHz) power after pulsed excitation (repetition rate 1 kHz) of the samples at 355 nm using the third harmonic of an Nd:YAG laser. The layers were illuminated from the back side.[55] The exact Setup is shown in the SI.

Absorption Measurements

We recorded the linear absorption spectra of the films comprising different precursor stoichiometry on a Lambda 950 (Perkin Elmer) instrument with an integrating sphere.

Solar Cell Characterization

Current–Voltage (*J-V*) characteristics of the perovskite solar cells were measured using a Newport OrielSol 2A solar simulator with a Keithley 2401 source meter. A spectral mismatch factor of 1.002 was estimated following a previously established protocol.[59] The devices were illuminated through a shadow mask, yielding an active area of 0.0831 cm^2. The J-V curves were recorded under standard AM 1.5G illumination from a xenon lamp, and calibrated to a light intensity of 100 mW cm^{-2} with a Fraunhofer ISE certified silicon diode. The input bias voltage was scanned from -1.5 to 0 V in 0.05 V steps with a rate of 0.2 V s^{-1}. All prepared devices show a comparable degree of hysteresis between the forward and the reverse scan, which is negligible small.

To obtain the EQE spectra, the respective solar cell was illuminated with chopped monochromatic light of a tungsten light source. The resulting current response was recorded via a lock-in amplifier (Signal Recovery 7265) at a chopping frequency of 14Hz. The current response of a reference diode was used to obtain the incident light power in order to calculate EQE(λ). By integrating the resulting EQE curve over the reference solar spectral irradiance (global tilt, American Society for Testing and Materials, ASTM G173), the theoretical short circuit current under one sun condition is extracted.

4.6 Supporting Information

Table S 4.1: Overview of stock solution preparation for the stoichiometric ratios investigated in this work.

Film	AgBr [mg]	$BiBr_3$ [mg]	CsBr [mg]
(1:1.15)	93.9	258.0	212.8
(1:0.85)	93.9	190.7	212.8
(1.15:1)	108.0	224.4	212.8
(1.15:0.85)	108.0	190.7	212.8

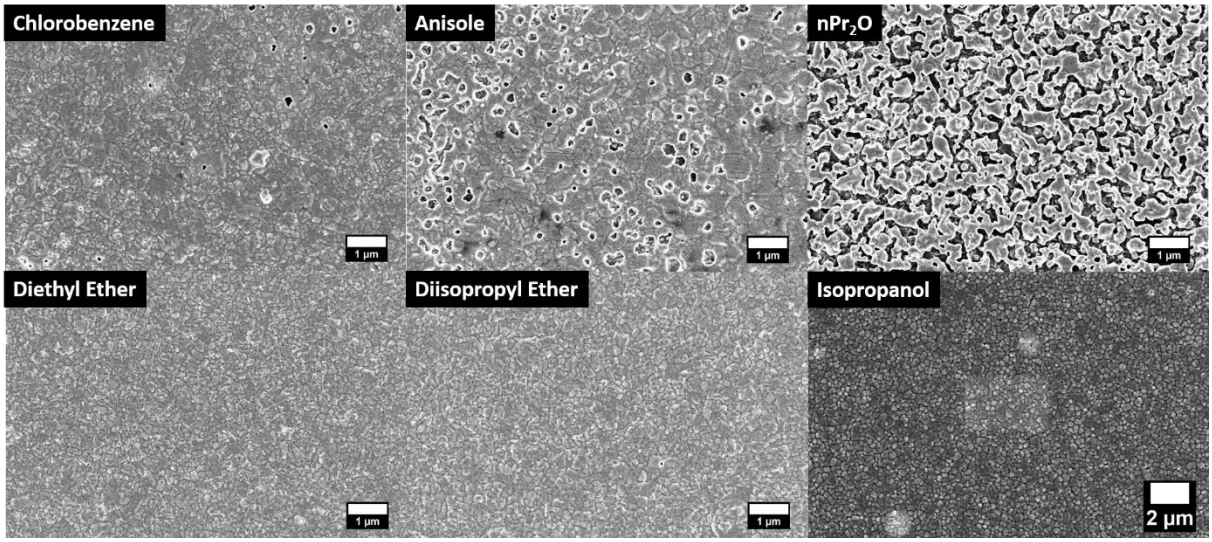

Figure S 4.1: Top-view SEM images of films spincoated with different antisolvents. As we want to show also the great surface coverage in larger areas, we zoomed out of the top view image of the film produced with isopropanol as antisolvent.

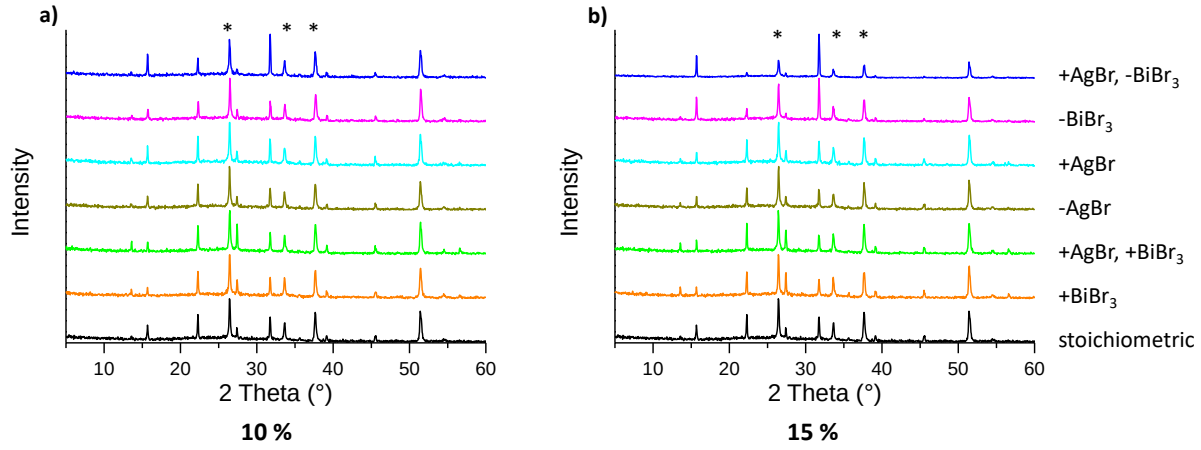

Figure S 4.2: XRD data of $Cs_2AgBiBr_6$ double perovskite films with stoichiometry changes of 10 mol% (a) and 15 mol% (b). The stoichiometry changes are as indicated in the legend: dark blue: *(1+x:1-x)*—films, magenta: *(1:1-x)*—films, turquoise: *(1+x:1)*—films, dark yellow: *(1-x:1)*—films, green: *(1+x:1+x)*—films, orange: *(1:1+x)*—films and black: stoichiometric film. The peak positions of the FTO substrate are indicated with asterisks.

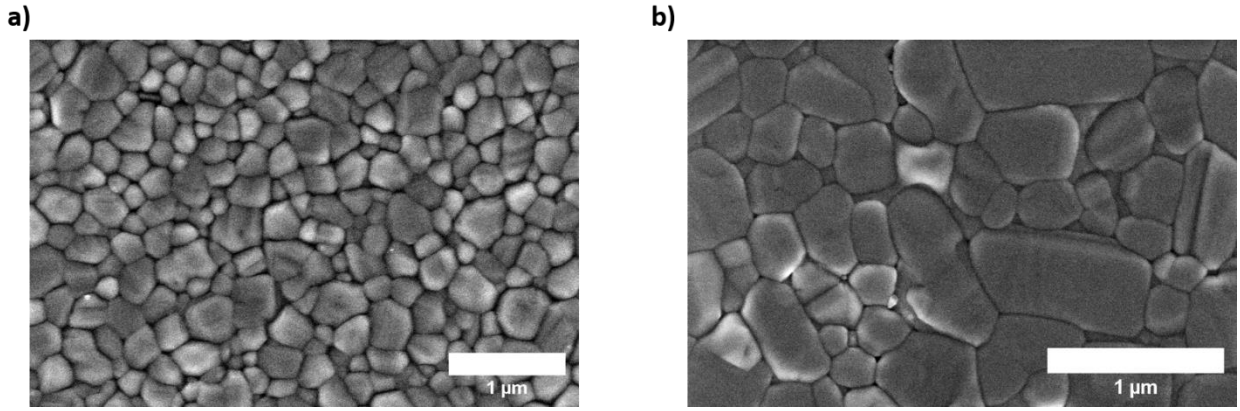

Figure S 4.3: Top view SEM of the stoichiometric film (a) and the (*1.15:0.85*)—film.

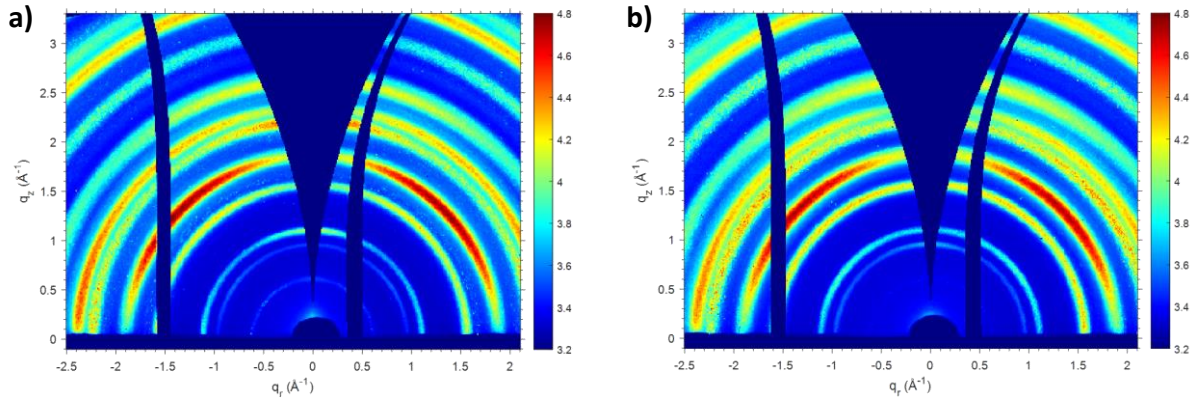

Figure S 4.4: 2D GIWAXS data of the (*1:0.85*)–film (a) and the (*1:1.15*)—film (b).

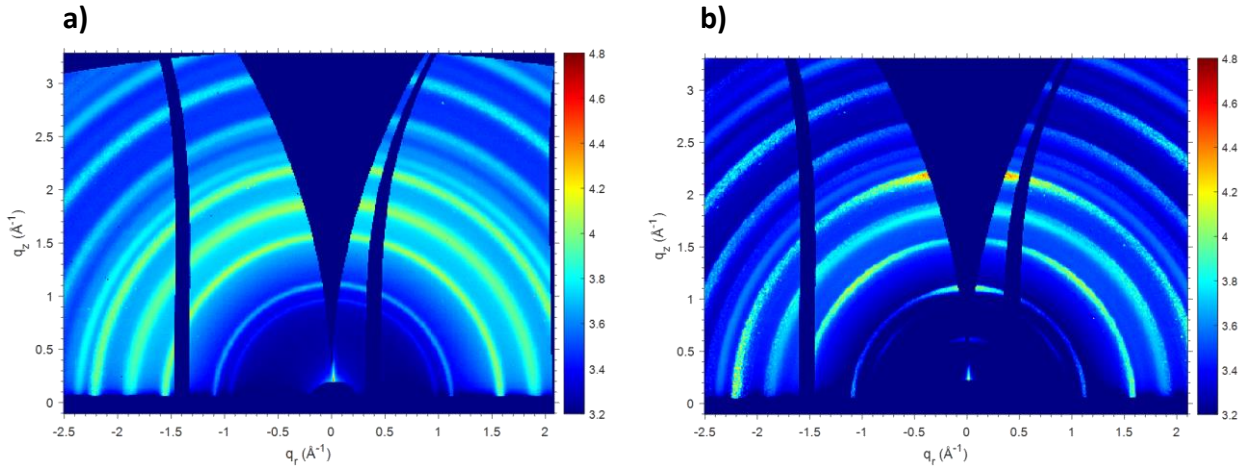

Figure S 4.5: GIWAXS data of $Cs_2AgBiBr_6$ double perovskite films on glass substrate: a) stoichiometric reference, b) (*1.15:0.85*)—film.

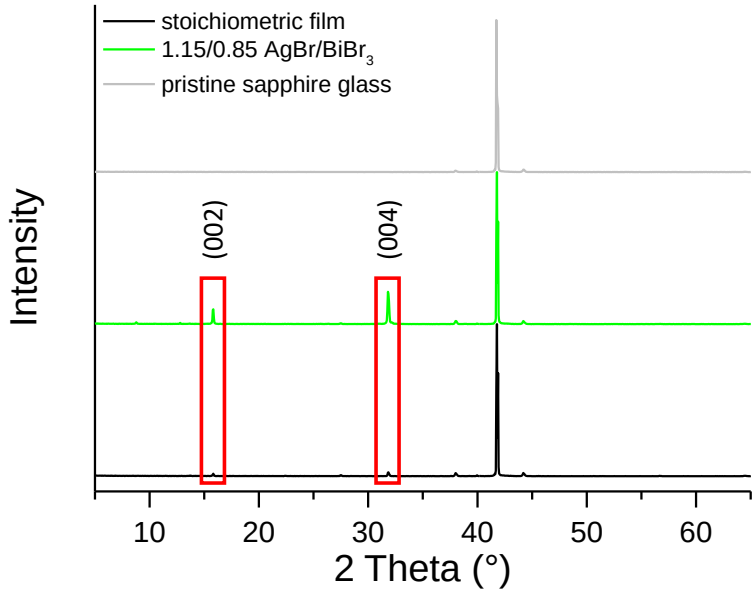

Figure S 4.6: XRD patterns of $Cs_2AgBiBr_6$ double perovskite thin films spincoated on sapphire substrates. The green line shows the pattern of the (*1.15:0.85*)—films while the black line shows the pattern of the stoichiometric reference. The (002) and (004) reflexes are shown with red boxes and the pattern of a plain sapphire substrate is shown in grey.

stoichiometric film	$2\ CsBr + AgBr + BiBr_3 \longrightarrow Cs_2AgBiBr_6$
(1.15/1)-film	$2\ CsBr + 1.15\ AgBr + BiBr_3 \longrightarrow Cs_2AgBiBr_6 + 0.15\ AgBr$
(1/1.15)-film	$2\ CsBr + AgBr + 1.15\ BiBr_3 \longrightarrow Cs_2AgBiBr_6 + 0.15\ BiBr_3$
(1/0.85)-film	$2\ CsBr + AgBr + 0.85\ BiBr_3 \longrightarrow 0.85\ Cs_2AgBiBr_6 + 0.15\ CsAgBr_2 + 0.15\ CsBr$
(1.15/0.85)-film	$2\ CsBr + 1.15\ AgBr + 0.85\ BiBr_3 \longrightarrow 0.85\ Cs_2AgBiBr_6 + 0.3\ CsAgBr_2$

Figure S 4.7: Proposed chemical reactions for the formation of the side phases formed due to the stoichiometric changes.

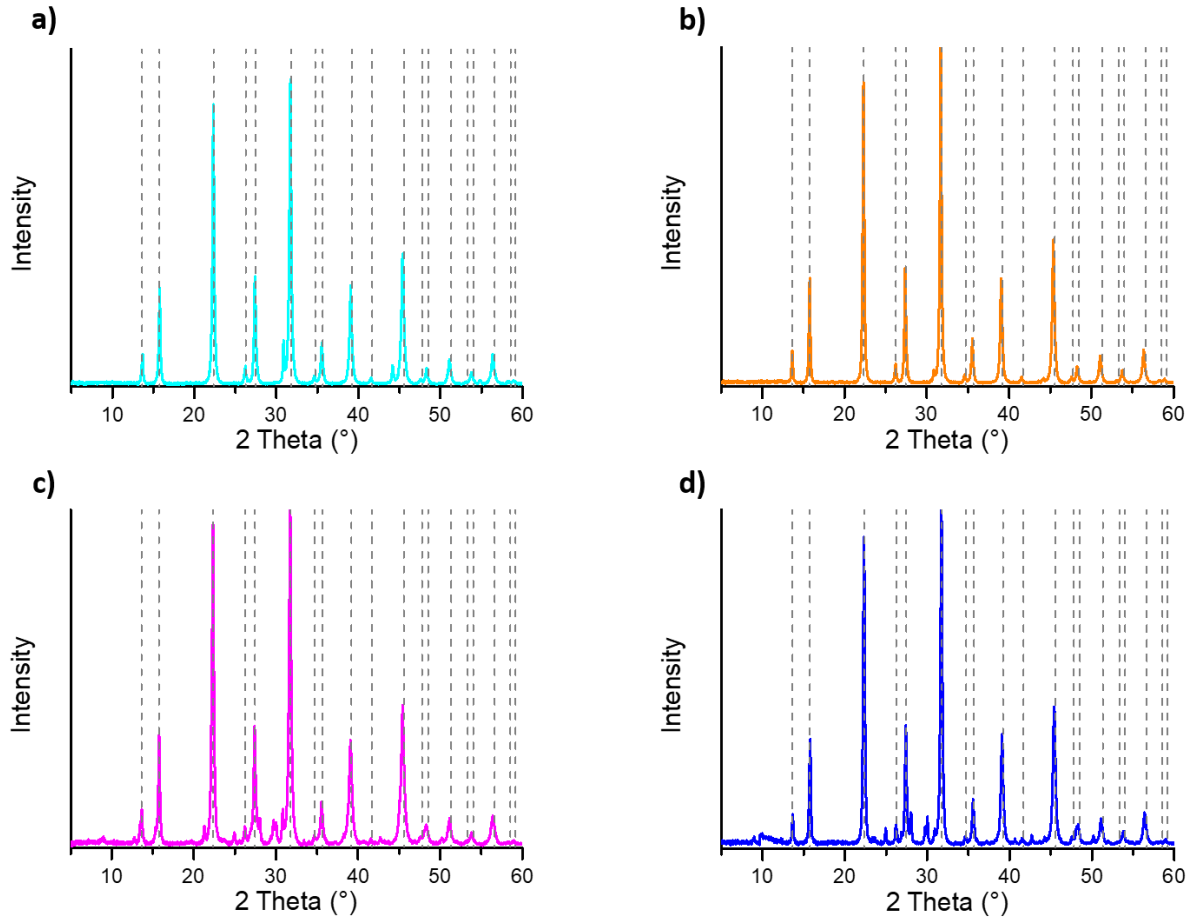

Figure S 4.8: PXRD data of the different $Cs_2AgBiBr_6$ double perovskite films. a) (*1.15:1*)—film, b) (*1:1.15*)—film, c) (*1:0.85*)—film, d) (*1.15:0.85*)—film. The theoretical Bragg peak positions of the stoichiometric reference are indicated by the grey dashed droplines.

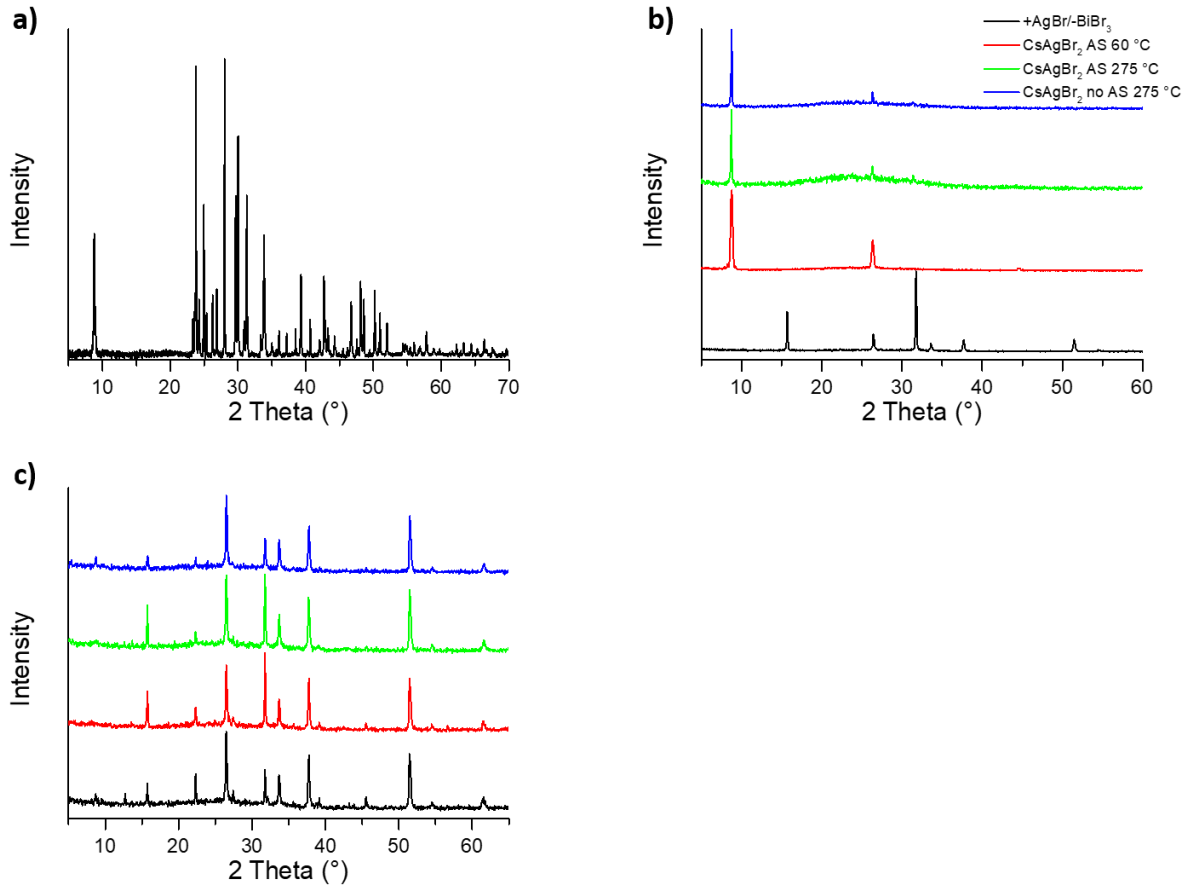

Figure S 4.9: PXRD (a) and film XRD data (b—c) of $CsAgBr_2$ side phase; b) (*1.15:0.85*)—films (black line); pure $CsAgBr_2$ spin-coated with 60 °C annealing with isopropanol as antisolvent (red line), pure $CsAgBr_2$ spin-coated with 275 °C annealing with isopropanol as antisolvent (green line), pure $CsAgBr_2$ spin-coated with 275 °C annealing without antisolvent (blue line); c) film XRD after addition of $CsAgBr_2$ compound to stock solution (7 %, red line; 15 %, green line; 35 %; blue line) compared to stoichiometric film (black line).

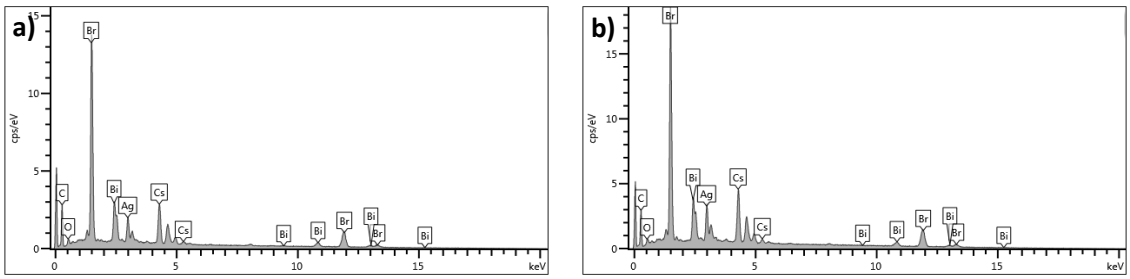

Figure S 4.10: Graphs of atom-% distribution resulting from the EDX-measurements with the powders obtained from a) the stoichiometric $Cs_2AgBiBr_6$ double perovskite thin films and b) the (*1.15:0.85*)—films.

Table S 4.2**:** Overview over the atom-% distribution in the powders of the stoichiometric $Cs_2AgBiBr_6$ double perovskite thin film and the *(1.15:0.85)* thin film obtained from the EDX-measurements.

Element	**stoichiometric film (atom %)**	***(0.15:0.85)*—film (atom %)**
Br	60.04	57.14
Ag	10.59	12.73
Cs	19.84	21.60
Bi	9.58	8.53
Total	100	100

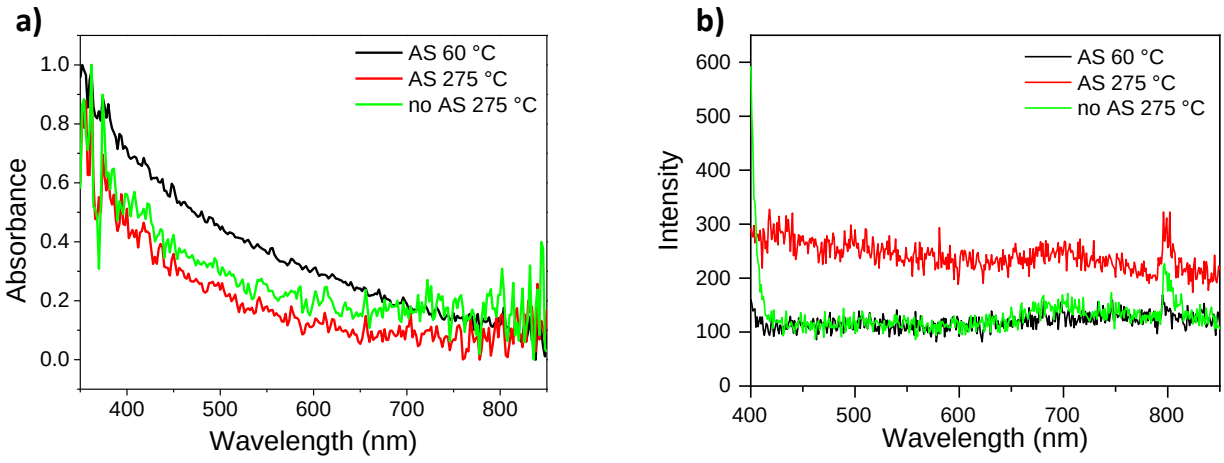

Figure S 4.11: UV/vis absorption (a) and PL emission spectra (b) of films consisting of the pure $CsAgBr_2$ side phase. Black line indicates films with annealing at 60 °C and isopropanol as antisolvent, red line indicates films with annealing at 275 °C and isopropanol as antisolvent, green line indicates films with annealing at 275 °C without antisolvent.

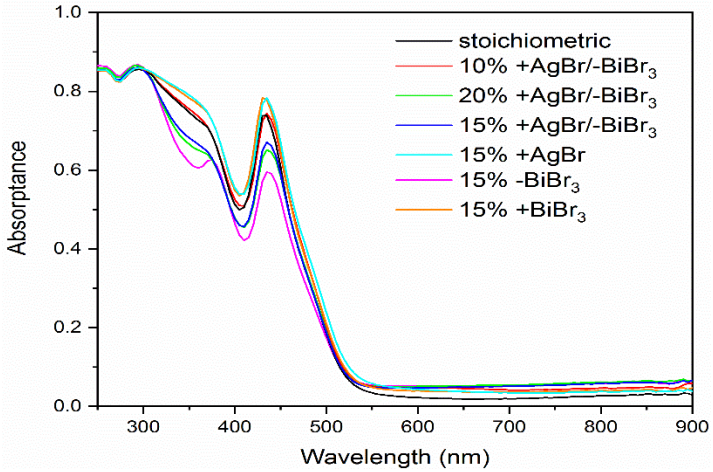

Figure S 4.12: UV/vis absorption spectra of the films with different stoichiometric ratios: The black line shows the stoichiometric films, the red, green and blue lines show the *(1+x:1-x)*—films, the turquoise line shows the (*1.15:1*)—film, the magenta line shows the (*1:0.85*)—film and the orange line shows the (*1:1.15*)—film.

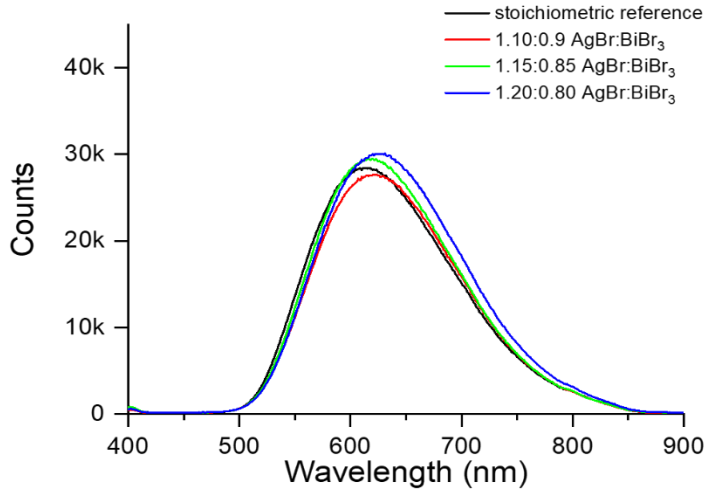

Figure S 4.13: steady state PL spectra of the (*1+x:1-x*)—films compared with the stoichiometric reference. The black line shows the stoichiometric reference, the red, green and blue lines show the different stoichiometric changes**.**

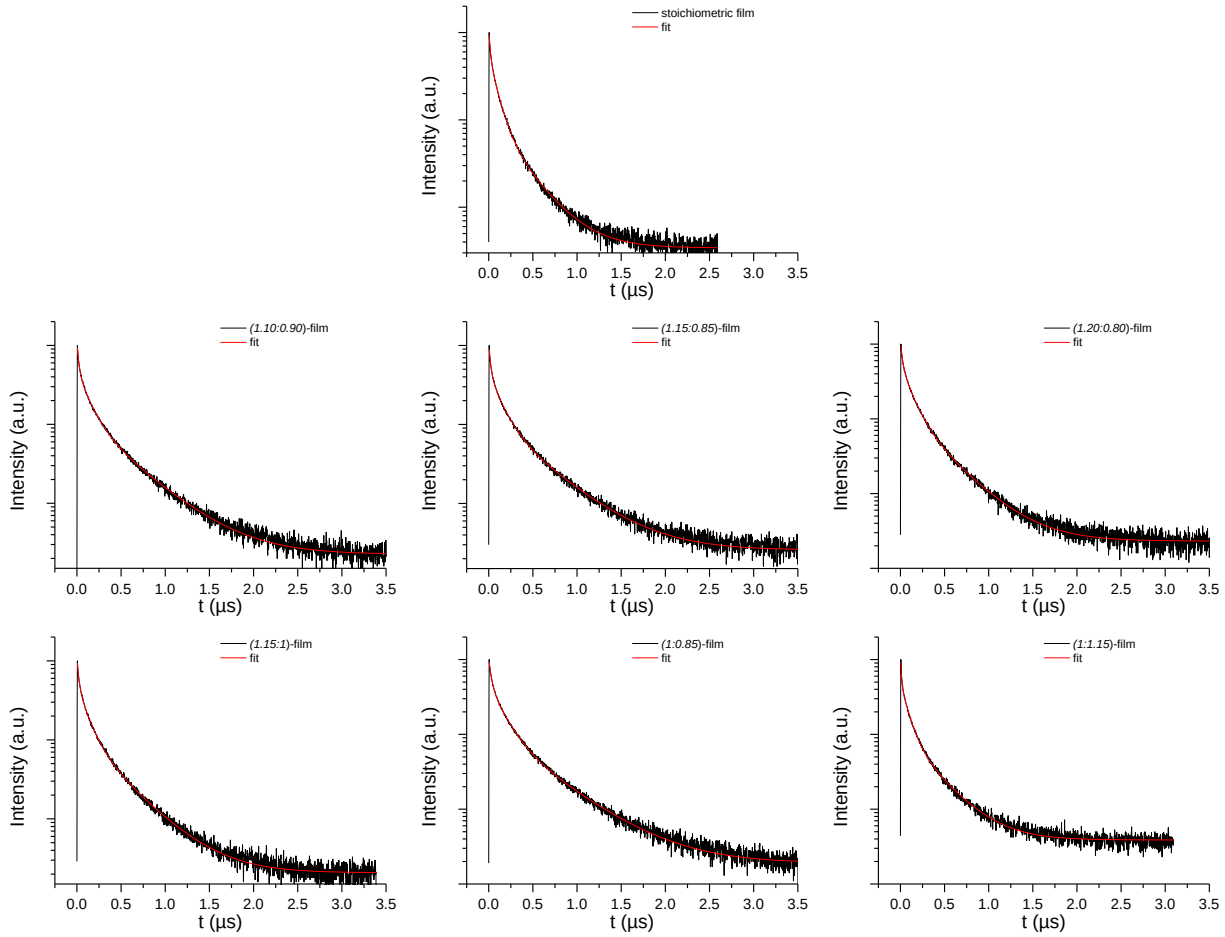

Figure S 4.14: TCSPC traces of the different films. Stoichiometry changes as indicated in the legend; black curve is the measured decay, the red line is the corresponding fit. The graphs were plotted semi-logarithmic.

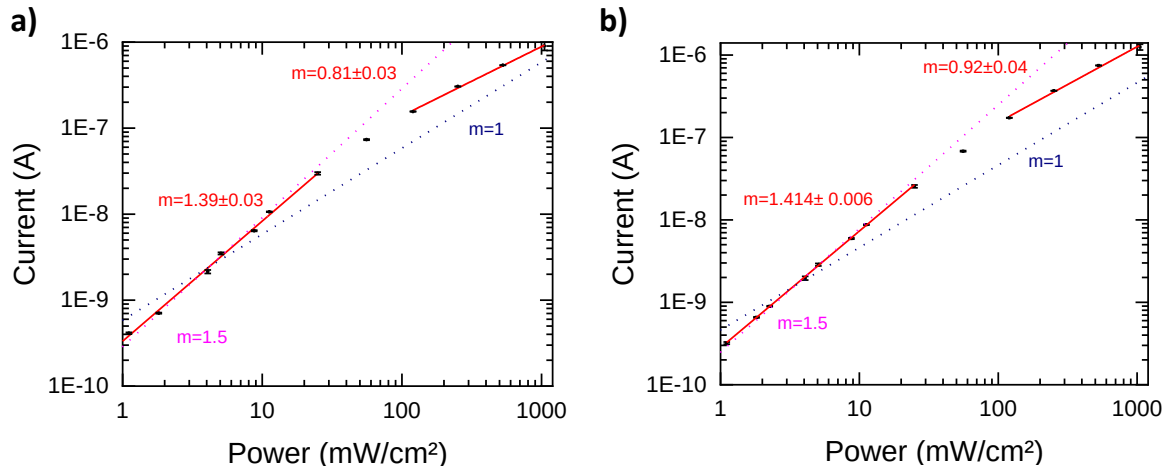

Figure S 4.15: Fluence-dependent steady state measurements of the a) stoichiometric reference $Cs_2AgBiBr_6$ double perovskite film and b) of the (*1.15:0.85*)—film. Red lines represent the fits to the data with the obtained slopes m shown in red. Pink and blue dotted lines represent guides to the eye for slopes of m = 1.5 (pink) and m = 1 (blue).

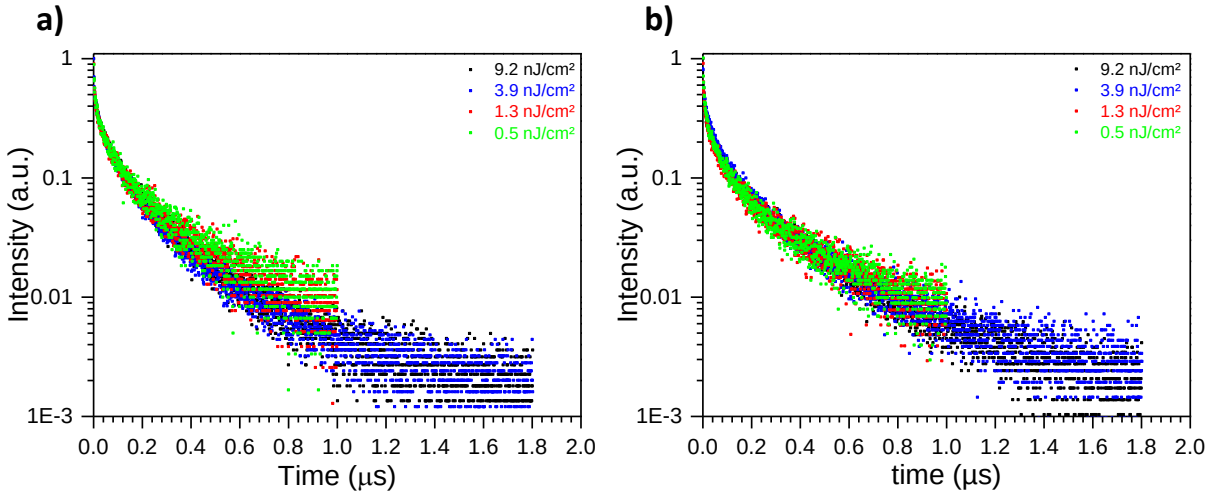

Figure S 4.16: Fluence-dependent TRPL data of a) the stoichiometric reference $Cs_2AgBiBr_6$ double perovskite film and b) the (*1.15/0.85*)—film. The different fluences are indicated as follows: black dots for 9.2 nJ/cm^2, blue dots for 3.2 nJ/cm^2, red dots for 1.3 nJ/cm^2 and green dots for 0.5 nJ/cm^2.

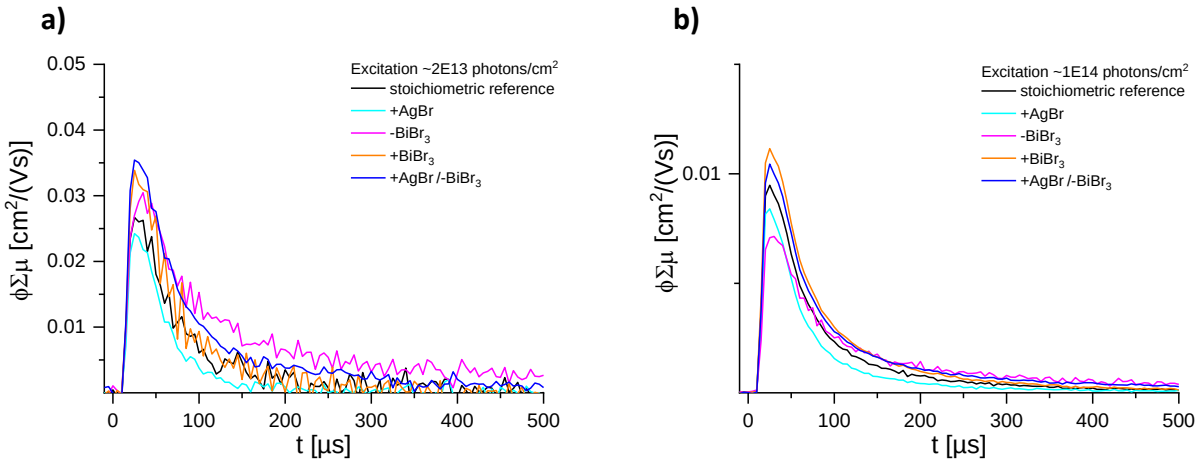

Figure S 4.17: TRMC traces for different laser excitation intensities; a) $2*10^{13}$ photons and b) 10^{14} photons. Stoichiometric changes in 15 mol%; black line shows the stoichiometric reference, the blue line shows the (*1.15:0.85*)—film, the turquoise line shows the (*1.15:1*)—film, the magenta line shows the (*1:0.85*)—film and the orange line shows the (*1:1.15*)—film.

TRMC Setup

Fig. S18 shows a schematic representation of the TRMC setup, used for the photoconductance measurements. The microwave resonator, operates in the commonly used TE_{102} mode. Two sides of the resonator are equipped with a vertical grating that allows the sample to be illuminated. Microwave radiation is coupled directly into the resonator and a circulator allows separating the reflected microwaves. A tunnel diode converts the reflected microwaves into a DC signal, which is amplified and send to a digitizer card. The signal thus obtained is proportional to the reflected microwave power P.

To illuminate the sample, the third harmonic of a Nd:YAG laser is used (355 nm) with a pulse duration of 80 ps. After the laser beam is widened, an aperture is used to guarantee a homogeneous illumination profile. A series of filter wheels with neutral density filters allows controlling the incident photon fluence by several orders of magnitude.

By combining a dark and illuminated measurement, one can calculate the normalized change in reflected microwave power ΔP/P, which is related to the change in conductance ΔG as followed:

$$\Delta G = -K\frac{\Delta P}{P}$$

The sensitivity factor K connects the change in reflected microwave power with the change in conductance. The calculation of the mobility and determination of the sensitivity factor K is done according to [60]

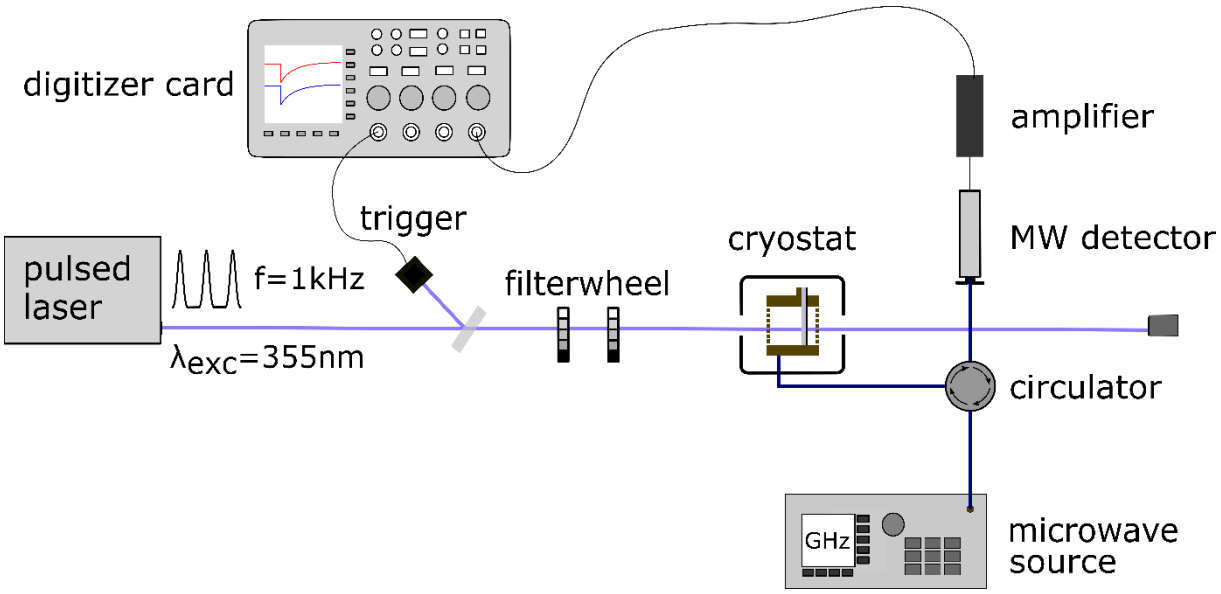

Figure S 4.18: Schematic representation of TRMC Setup used in this work.

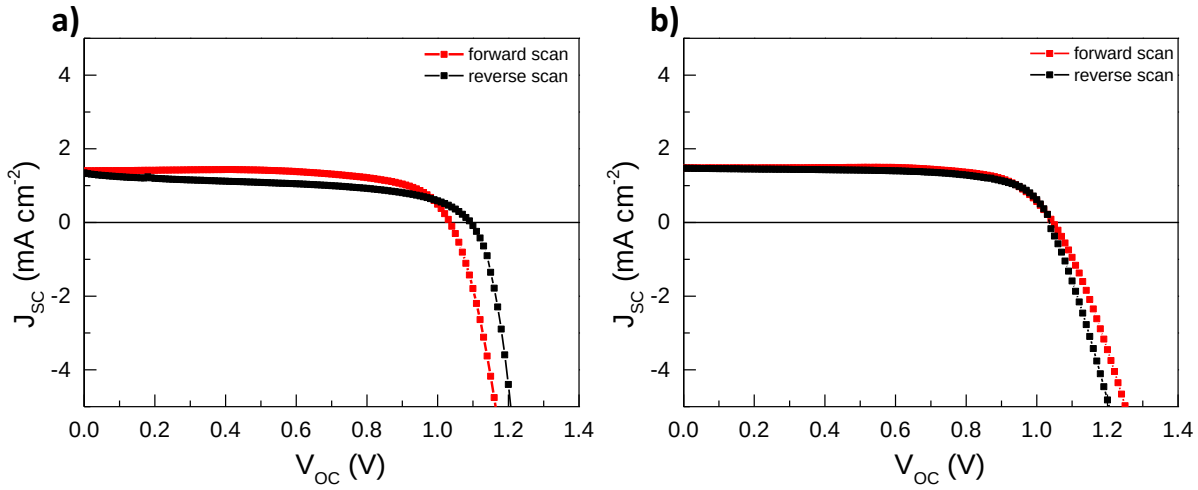

Figure S 4.19: J/V-curves of the champion cells of the stoichiometric reference $Cs_2AgBiBr_6$ double perovskite film and the (*1.15:0.85*)—film. a) stoichiometric reference, b) (*1.15:0.85*)—film.

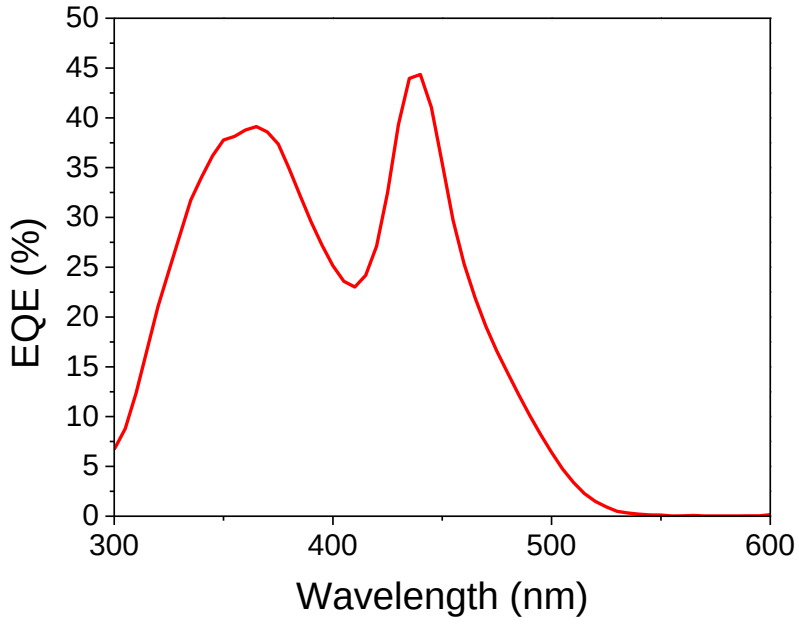

Figure S 4.20: EQE spectra of the stoichiometric $Cs_2AgBiBr_6$ double perovskite solar cell. The integrated current (1.74 mA/cm^2) matches well with the stabilized value for J_{SC} under 1 sun condition (1.81 mA/cm^2).

4.7 References

[1] A. Kojima, K. Teshima, Y. Shirai, T. Miyasaka, *J. Am. Chem. Soc.* **2009**, *131*, 6050.

[2] E. H. Jung, N. J. Jeon, E. Y. Park, C. S. Moon, T. J. Shin, T.-Y. Yang, J. H. Noh, J. Seo, *Nature* **2019**, *567*, 511.

[3] M. A. Green, E. D. Dunlop, J. Hohl-Ebinger, M. Yoshita, N. Kopidakis, A. W. Y. Ho-Baillie, *Prog. Photovolt. Res. Appl.* **2019**, *28*, 3.

[4] A. Binek, M. L. Petrus, N. Huber, H. Bristow, Y. Hu, T. Bein, P. Docampo, *ACS applied materials & interfaces* **2016**, *8*, 12881.

[5] A. M. A. Leguy, Y. Hu, M. Campoy-Quiles, M. I. Alonso, O. J. Weber, P. Azarhoosh, M. van Schilfgaarde, M. T. Weller, T. Bein, J. Nelson, P. Docampo, P. R. F. Barnes, *Chem. Mater.* **2015**, *27*, 3397.

[6] M. L. Petrus, Y. Hu, D. Moia, P. Calado, A. M. A. Leguy, P. R. F. Barnes, P. Docampo, *ChemSusChem* **2016**, *9*, 2699.

[7] M. L. Petrus, J. Schlipf, C. Li, T. P. Gujar, N. Giesbrecht, P. Müller-Buschbaum, M. Thelakkat, T. Bein, S. Hüttner, P. Docampo, *Adv. Energy Mater.* **2017**, *7*, 1700264.

[8] M. L. Petrus, K. Schutt, M. T. Sirtl, E. M. Hutter, A. C. Closs, J. M. Ball, J. C. Bijleveld, A. Petrozza, T. Bein, T. J. Dingemans, *Adv. Energy Mater.* **2018**, *8*, 1801605.

[9] M. L. Petrus, A. Music, A. C. Closs, J. C. Bijleveld, M. T. Sirtl, Y. Hu, T. J. Dingemans, T. Bein, P. Docampo, *J. Mater. Chem. A* **2017**, *5*, 25200.

[10] K. Nishimura, M. A. Kamarudin, D. Hirotani, K. Hamada, Q. Shen, S. Iikubo, T. Minemoto, K. Yoshino, S. Hayase, *Nano Energy* **2020**.

[11] Q. Tai, X. Guo, G. Tang, P. You, T.-W. Ng, D. Shen, J. Cao, C.-K. Liu, N. Wang, Y. Zhu, C.-S. Lee, F. Yan, *Angewandte Chemie (International ed. in English)* **2019**, *58*, 806.

[12] E. W.-G. Diau, E. Jokar, M. Rameez, *ACS Energy Lett.* **2019**, *4*, 1930.

[13] Z. Yang, M. Zhong, Y. Liang, L. Yang, X. Liu, Q. Li, J. Zhang, D. Xu, *Adv. Funct. Mater.* **2019**.

[14] Z. Xiao, K.-Z. Du, W. Meng, J. Wang, D. B. Mitzi, Y. Yan, *Journal of the American Chemical Society* **2017**, *139*, 6054.

[15] G. Volonakis, A. A. Haghighirad, H. J. Snaith, F. Giustino, *J. Phys. Chem. Lett.* **2017**, *8*, 3917.

[16] M. R. Filip, X. Liu, A. Miglio, G. Hautier, F. Giustino, *J. Phys. Chem. C* **2018**, *122*, 158.

[17] X.-G. Zhao, J.-H. Yang, Y. Fu, D. Yang, Q. Xu, L. Yu, S.-H. Wei, L. Zhang, *J. Am. Chem. Soc.* **2017**, *139*, 2630.

[18] Z. Xiao, W. Meng, J. Wang, Y. Yan, *ChemSusChem* **2016**, *9*, 2628.

[19] K.-Z. Du, W. Meng, X. Wang, Y. Yan, D. B. Mitzi, *Angewandte Chemie (International ed. in English)* **2017**, *56*, 8158.

[20] G. Volonakis, M. R. Filip, A. A. Haghighirad, N. Sakai, B. Wenger, H. J. Snaith, F. Giustino, *J. Phys. Chem. Lett.* **2016**, *7*, 1254.

[21] D. Bartesaghi, A. H. Slavney, M. C. Gélvez-Rueda, B. A. Connor, F. C. Grozema, H. I. Karunadasa, T. J. Savenije, *J. Phys. Chem. C* **2018**, *122*, 4809.

[22] M. R. Filip, S. Hillman, A. A. Haghighirad, H. J. Snaith, F. Giustino, *J. Phys. Chem. Lett.* **2016**, *7*, 2579.

[23] A. H. Slavney, T. Hu, A. M. Lindenberg, H. I. Karunadasa, *J. Am. Chem. Soc.* **2016**, *138*, 2138.

[24] F. Wei, Z. Deng, S. Sun, F. Zhang, D. M. Evans, G. Kieslich, S. Tominaka, M. A. Carpenter, J. Zhang, P. D. Bristowe, A. K. Cheetham, *Chem. Mater.* **2017**, *29*, 1089.

[25] E. T. McClure, M. R. Ball, W. Windl, P. M. Woodward, *Chem. Mater.* **2016**, *28*, 1348.

[26] E. Greul, M. L. Petrus, A. Binek, P. Docampo, T. Bein, *J. Mater. Chem. A* **2017**, *5*, 19972.

[27] F. Igbari, R. Wang, Z.-K. Wang, X.-J. Ma, Q. Wang, K.-L. Wang, Y. Zhang, L.-S. Liao, Y. Yang, *Nano Lett.* **2019**, *19*, 2066.

[28] W. Ning, F. Wang, B. Wu, J. Lu, Z. Yan, X. Liu, Y. Tao, J.-M. Liu, W. Huang, M. Fahlman, *Adv. Mater.* **2018**, *30*, 1706246.

[29] C. Wu, Q. Zhang, Y. Liu, W. Luo, X. Guo, Z. Huang, H. Ting, W. Sun, X. Zhong, S. Wei, *Adv. Sci.* **2018**, *5*, 1700759.

[30] W. Gao, C. Ran, J. Xi, B. Jiao, W. Zhang, M. Wu, X. Hou, Z. Wu, *ChemPhysChem* **2018**, *19*, 1696.

[31] A. E. Maughan, A. M. Ganose, D. O. Scanlon, J. R. Neilson, *Chem. Mater.* **2019**, *31*, 1184.

[32] R. Quintero-Bermudez, A. Gold-Parker, A. H. Proppe, R. Munir, Z. Yang, S. O. Kelley, A. Amassian, M. F. Toney, E. H. Sargent, *Nat. Mater.* **2018**, *17*, 900.

[33] Q. Liang, J. Liu, Z. Cheng, Y. Li, L. Chen, R. Zhang, J. Zhang, Y. Han, *J. Mater. Chem. A* **2016**, *4*, 223.

[34] P. Docampo, F. C. Hanusch, N. Giesbrecht, P. Angloher, A. Ivanova, T. Bein, *APL Mater.* **2014**, *2*, 81508.

[35] N. Cho, F. Li, B. Turedi, L. Sinatra, S. P. Sarmah, M. R. Parida, M. I. Saidaminov, B. Murali, V. M. Burlakov, A. Goriely, *Nat. Commun.* **2016**, *7*, 13407.

[36] G. Niu, H. Yu, J. Li, D. Wang, L. Wang, *Nano Energy* **2016**, *27*, 87.

[37] N. Giesbrecht, J. Schlipf, L. Oesinghaus, A. Binek, T. Bein, P. Müller-Buschbaum, P. Docampo, *ACS Energy Lett.* **2016**, *1*, 150.

[38] J. Xiu, Y. Shao, L. Chen, Y. Feng, J. Dai, X. Zhang, Y. Lin, Y. Zhu, Z. Wu, Y. Zheng, *Mater. Today Energy* **2019**, *12*, 186.

[39] R. L. Z. Hoye, L. Eyre, F. Wei, F. Brivio, A. Sadhanala, S. Sun, W. Li, K. H. L. Zhang, J. L. MacManus-Driscoll, P. D. Bristowe, *Adv. Mater. Interfaces* **2018**, *5*, 1800464.

[40] M. Pantaler, K. T. Cho, V. I. E. Queloz, I. García Benito, C. Fettkenhauer, I. Anusca, M. K. Nazeeruddin, D. C. Lupascu, G. Grancini, *ACS Energy Lett.* **2018**, *3*, 1781.

[41] M. Jiang, Y. Wu, Y. Zhou, Z. Wang, *AIP Adv.* **2019**, *9*, 85301.

[42] Y. Cheng, H.-W. Li, J. Qing, Q.-D. Yang, Z. Guan, C. Liu, S. H. Cheung, S. K. So, C.-S. Lee, S.-W. Tsang, *J. Mater. Chem. A* **2016**, *4*, 12748.

[43] T. Du, C. H. Burgess, J. Kim, J. Zhang, J. R. Durrant, M. A. McLachlan, *Sustain. Energy Fuels* **2017**, *1*, 119.

[44] N. Giesbrecht, J. Schlipf, I. Grill, P. Rieder, V. Dyakonov, T. Bein, A. Hartschuh, P. Müller-Buschbaum, P. Docampo, *J. Mater. Chem. A* **2018**, *6*, 4822.

[45] J. Schlipf, P. Müller-Buschbaum, *Adv. Energy Mater.* **2017**, *7*, 1700131.

[46] A. Hexemer, P. Müller-Buschbaum, *IUCrJ* **2015**, *2*, 106.

[47] M. Boukhtouta, S. Lamraoui, S. Touam, H. Meradji, S. Ghemid, F. El Haj Hassan, *Phase Transit.* **2015**, *88*, 357.

[48] H. von Benda, *Z. Kristallogr. – Cryst. Mater.* **1980**, *151*, 271.

[49] S. Hull, P. Berastegui, *J. Solid State Chem.* **2004**, *177*, 3156.

[50] C. Kim, G. Pilania, R. Ramprasad, *Chem. Mater.* **2016**, *28*, 1304.

[51] R. Kentsch, M. Scholz, J. Horn, D. Schlettwein, K. Oum, T. Lenzer, *J. Phys. Chem. C* **2018**, *122*, 25940.

[52] T. Li, X. Zhao, D. Yang, M.-H. Du, L. Zhang, *Phys. Rev. Appl.* **2018**, *10*, 41001.

[53] V. Sarritzu, N. Sestu, D. Marongiu, X. Chang, S. Masi, A. Rizzo, S. Colella, F. Quochi, M. Saba, A. Mura, *Sci. Rep.* **2017**, *7*, 44629.

[54] V. D'innocenzo, G. Grancini, M. J. Alcocer, A. R. Kandada, S. D. Stranks, M. M. Lee, G. Lanzani, H. J. Snaith, A. Petrozza, *Nat. Commun.* **2014**, *5*, 3586.

[55] T. J. Savenije, A. J. Ferguson, N. Kopidakis, G. Rumbles, *J. Phys. Chem. C* **2013**, *117*, 24085.

[56] H.-J. Feng, W. Deng, K. Yang, J. Huang, X. C. Zeng, *J. Phys. Chem. C* **2017**, *121*, 4471.

[57] A. Buffet, A. Rothkirch, R. Döhrmann, V. Körstgens, M. M. Abul Kashem, J. Perlich, G. Herzog, M. Schwartzkopf, R. Gehrke, P. Müller-Buschbaum, *J. Synchrotron Radiat.* **2012**, *19*, 647.

[58] Z. Jiang, *J. Appl. Crystallogr.* **2015**, *48*, 917.

[59] H. J. Snaith, *Energy Environ. Sci.* **2012**, *5*, 6513.

[60] T. J. Savenije, A. J. Ferguson, N. Kopidakis, G. Rumbles, *J. Phys. Chem. C* **2013**, *117*, 24085.

5 2D/3D Hybrid $Cs_2AgBiBr_6$ Double Perovskite Solar Cells: Improved Energy Level Alignment for Higher Contact-Selectivity and Large Open Circuit Voltage.

This chapter is based on the following publication:

Maximilian T. Sirtl,[1] Rik Hooijer,[1] Melina Armer,[2] Firouzeh G. Ebadi,[3] Mahdi Mohammadi,[3] Clément Maheu,[4] Andreas Weis,[1] Bas T. van Gorkom,[5] Sebastian Häringer,[1] René A. J. Janssen,[5] Thomas Mayer,[4] Vladimir Dyakonov,[2] Wolfgang Tress[3] and Thomas Bein[1]

Manuscript under Revision

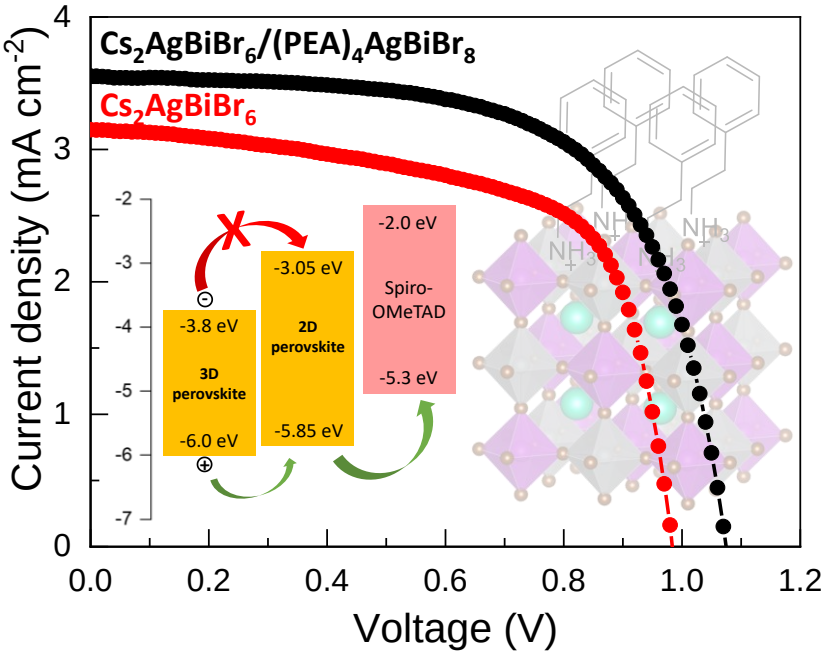

keywords: Double Perovskite; $Cs_2AgBiBr_6$; 2D/3D hybrid perovskite; double perovskite solar cells; 2D perovskite

5.1 Abstract

Since their introduction in 2017, the efficiency of lead-free halide perovskite solar cells based on $Cs_2AgBiBr_6$ did not exceed 3 %. The limiting bottlenecks were attributed to a low electron diffusion length, self-trapping events and poor selectivity of the contacts, leading to large non-radiative V_{OC} losses. Here, we introduce 2D/3D hybrid double perovskites for the first time, using phenethyl ammonium as the constituting cation. The resulting solar cells show an increased efficiency of up to 2.5 % for the champion cells and 2.03 % on average, marking an improvement by 10 % compared to the 3D reference on mesoporous TiO_2. The main effect was due to a V_{OC} improvement by up to 70 mV on average, yielding a maximum V_{OC} of 1.18 V using different PEA^+ concentrations. While these are among the highest reported V_{OC} values for $Cs_2AgBiBr_6$ solar cells, the effect was attributed to a change in recombination behavior within the full device and a better selectivity at the interface towards the hole transporting material (HTM). This explanation was supported by voltage-dependent external quantum efficiency, as well as photoelectron spectroscopy, revealing better energy level alignment and thus a better hole-extraction and an improved electron blocking at the HTM interface.

5.2 Introduction

Halide double perovskites have recently attracted much interest in the photovoltaic community as they are seen as a possibility to solve several issues arising from their lead-based cousins featuring excellent optoelectronic properties.[1] Changing the simple perovskite ABX_3 structure to a 2x2x2 supercell, halide double perovskites have the general formula $A_2B^IB^{III}X_6$ where two bivalent cations B^{2+} are exchanged by a combination of one monovalent cation B^+ (e.g. Cu^+, Ag^+, Au^+, In^+) and one trivalent cation B^{3+} (e.g. Bi^{3+}, Sb^{3+}).[2] Several theoretical calculations have been performed on this structural motif, providing a large variety of proposed thermodynamically stable compounds of which $Cs_2AgBiBr_6$ proved to be the most promising material so far.[3–7] $Cs_2AgBiBr_6$ was characterized first by McClure et al. in 2016[8] and, being long-term stable at ambient conditions and providing alternative element combinations that exclude toxic elements,[2] this material was moved into the focus of research, especially due to promising optoelectronic properties of single crystals (for instance a charge carrier lifetime of >500 ns)[9,10] and the possibility to solution-process the material for thin films synthesis.[11]

After the first report on solar cells using $Cs_2AgBiBr_6$ as an active layer in 2017,[11] several groups reported solar cells implementing different architectures and contact layers. In order to

optimize the optoelectronic properties and charge extraction behavior, the stoichiometric precursor ratio,[12,13] organic interface layers,[14] charge transport layers[15–18] and n-i-p, as well as p-i-n[19] structures have been investigated. Ultimately, these efforts led to power conversion efficiencies (PCE) that did not exceed 3 % within several years of research.[16] Hence, present research activities aim at the investigation of the intrinsic bottlenecks of this material to find ways to overcome them and to push the solar cell efficiency further.

While the energy level alignment between the valence band maximum (VBM) of the double perovskite and the highest occupied molecular orbital (HOMO) energy level of the commonly used hole-transport materials (HTM) is non-optimal for solar cell functions,[15] the position of the conduction band minimum (CBM) leads to a low selectivity of the contacts within the full solar cell.[17] Moreover, a short electron diffusion length in deposited thin film structures.[20] ultra-fast self-trapping of free charge carriers[21] and large non-radiative V_{OC} losses have been found,[17] while it remains unclear whether a large exciton binding energy is hampering the solar cell efficiency[22,23] and how the PL signal of the thin films can be explained.[13,17,24]

Another challenge is the rather large and indirect bandgap of 2.3 eV, especially since the stabilization of the related double perovskite Cs_2AgBiI_6 has not yet been realized due to the low thermodynamic stability of this compound.[25] While tuning of the absorption onset is pursued by using additives and alloying,[26–30] as well as high pressure modification,[31] a promising pathway to stabilize iodine based Ag-Bi double perovskites is the introduction of a large A-site cation in order to form 2D double perovskites, as first introduced by Connor et al. in 2018 using bromide.[32] Following this procedure, Jana et al. synthesized the first iodine based Ag-Bi double perovskite by using a oligothiophene based double cation 5,5′-diylbis(aminoethyl)-[2,2′-bithiophene] to stabilize $(AE2T)_4AgBiI_8$, which expressed a reduced bandgap of 2 eV that moreover was direct.[33] Going further, several other groups managed to stabilize the iodine phase using different spacer cations.[34,35] Due to the insulating properties of large organic cations, however, experience with lead-based perovskites shows a reduced efficiency of the pure 2D structures compared with their pure 3D counterpart.[36,37] To overcome this issue, either the formation of a quasi 2D perovskite (n >= 2) can be achieved by using small amounts of a small A^+ cation to partially substitute the large cation, or the formation of a hybrid perovskite can be pursued, using a 3D layer and combining it with a very thin 2D layer on top.[36,38–41]

In this work, we introduce the first 2D/3D hybrid double perovskite to date. By using the simple aromatic phenethyl ammonium bromide salt in 2-propanol, we show the formation of a $(PEA)_4AgBiBr_8$ layer on top of a 3D $Cs_2AgBiBr_6$ thin film. Moreover, we achieved the formation of a pure 2D $(PEA)_4AgBiBr_8$ thin film that shows excellent coverage and uniformity to determine the optical properties where we calculated the bandgap to be direct. Using an ultra-thin $(PEA)_4AgBiBr_8$ layer on top of the 3D film, we show that the efficiency of the resulting solar cell is boosted from 2.1 % to 2.5 % which we assigned to a large increase of the V_{OC} and J_{SC} both for the champion cells and the cells showing average performance. Especially the V_{OC} values are the highest so far reported for this material, reaching up to 1.14 V. We assign these changes to an increase in the selectivity of the contact, while the recombination behavior seems to remain the same, and support these findings with voltage dependent external quantum efficiency (EQE) measurements, as well as ultraviolet photoelectron spectroscopy (UPS), X-ray photoelectron spectroscopy (XPS) and photoluminescence measurements (PL). Overall, we show that utilizing 2D/3D hybrid double perovskites offers opportunities to address the issues regarding poor energy level alignment towards the HTM side and to easily fine-tune the contact-selectivity, ultimately boosting the overall solar cell efficiency. Moreover, we provide a technique to use 2D Ag-Bi double perovskites to provide pathways towards iodine-based compounds in lead free double perovskite solar cells.

5.3 Results and Discussion

5.3.1 Formation of the Hybrid Phase

In the field of 2D/3D hybrid perovskites, one approach to form such a layer is the deposition of the spacer cation on top of the already formed 3D film. This leads to the formation of a very thin 2D or 2D/3D hybrid top layer.[36,42] In our work, we adapted this approach and prepared the 3D layer first by spincoating the preheated $Cs_2AgBiBr_6$ stock solution on top of preheated glass substrates. This was followed by high temperature annealing (Figure 5.1). After the formation of the 3D film, we introduced the spacer cation by spincoating phenethyl ammonium bromide (PEABr) on top, which is well known to form a 2D silver-bismuth perovskite phase.[43–45] We tested the hybrid perovskite formation with different PEABr concentrations in 2-propanol (*iso*propanol, IPA) ranging from 0.01 mol*L^{-1} (0.01 M) to 0.1 M.

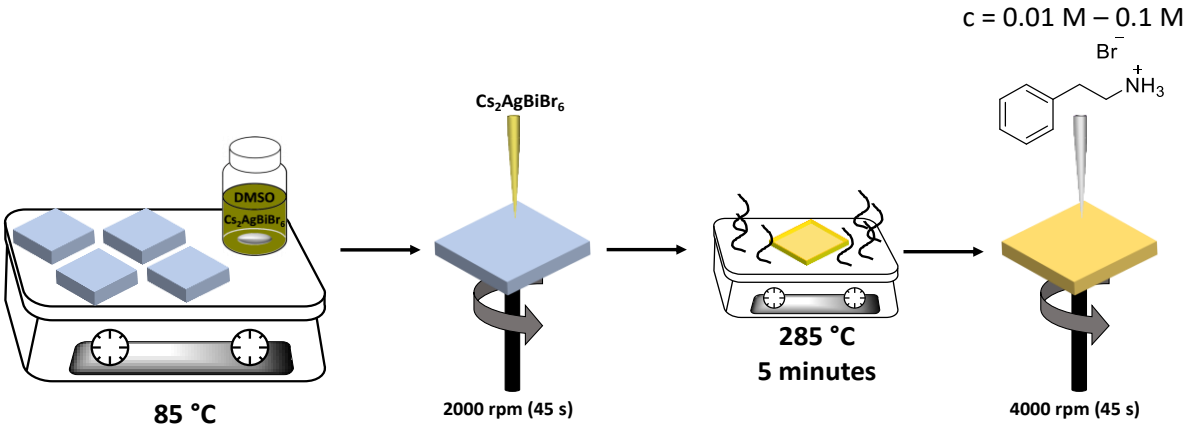

Figure 5.1: Schematic synthesis scheme of the 2D/3D hybrid double perovskite thin films. In a first step, we deposited the 3D double perovskite thin film by spincoating a preheated solution (85 °C) on a preheated substrate (85 °C) at 2000 rpm. After thermal annealing at 285 °C for 5 minutes, the spacer cation was spincoated on top of the 3D film at various concentrations (in IPA at 4000 rpm) to form a 2D/3D hybrid double perovskite film on top of the pure 3D layer.

The insertion of long cations into a 3D perovskite leads to the formation of 2D phases with an increased lattice constant, which can be observed by the emergence of small angle XRD reflections.[32] To investigate the formation of a 2D layer on top of our 3D films, we performed both X-ray diffraction in Bragg-Brentano geometry and grazing incident wide angle X-ray scattering (GIWAXS) and compared the obtained patterns of the hybrid films (c(PEABr)= 0.1 M, 0.06 M and 0.01 M) with the results for pure 3D films and the theoretical PXRD pattern of the n = 1 $(PEA)_4AgBiBr_8$ structure (obtained from ref[43]) as shown in Figure 5.2 for the small angle region between 2 and 12 ° 2θ.

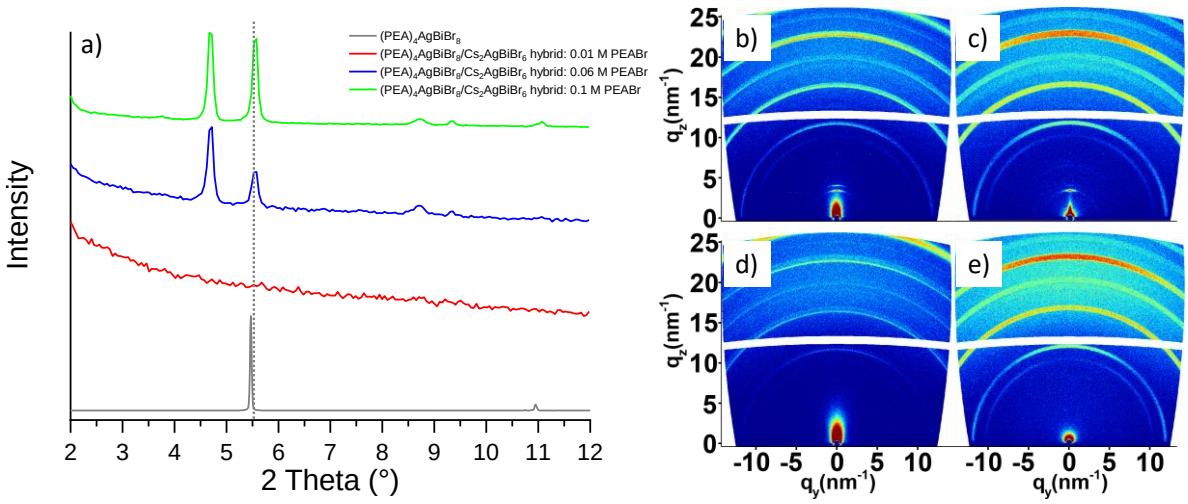

Figure 5.2 XRD pattern and GIWAXS detector images of the investigated thin films. a) Bragg-Brentano XRD pattern of modified thin films between 2 and 12 °2θ. Green (0.1 M PEABr), blue (0.06 M PEABr) and red line (0.01 M PEABr) show the hybrid thin films while the grey line shows the theoretical pattern of the pure 2D $(PEA)_4AgBiBr_8$ double perovskite. The dashed grey line was added as a guide for the eye to emphasize the low-angle reflection. b)-e) show the GIWAXS detector images of the 0.1 M (b), 0.06 M (c) and 0.01 M (d) hybrid, as well as the 3D reference (e).

The here measured films were spincoated on top of an FTO/c-TiO_2/mp-TiO_2 scaffold to simulate the same crystallization behavior utilized for the construction of solar cells.

Figure 5.2a confirms the formation of the $(PEA)_4AgBiBr_8$ 2D-phase upon spincoating the spacer cation on top of the pure 3D films for PEABr concentrations higher than 0.06 M. The comparison of the XRD pattern of the hybrid film with the calculated pattern of the pure 2D $(PEA)_4AgBiBr_8$ shows the formation of the characteristic reflection at low angles of 5.5 ° 2θ. However, the formation of this reflection cannot be observed using the lowest PEABr concentrations of 0.01 M. This suggests the formation of a rather thin 2D layer for low PEABr concentrations, which we confirmed through further GIWAXS measurements. Interestingly, one can see the formation of a second phase of the 2D perovskite at even smaller angles (~4.5 °2θ). This can be related to the formation of 2D layers with n values bigger than one, which leads to a further increase of one unit cell dimension and hence to a shift of the reflection toward smaller angles. The full patterns in Figure S 5.1 show that all films are phase-pure with respect to undesired side phases such as AgBr, CsBr or $BiBr_3$, as well as $Cs_3Bi_2Br_9$ and $(PEA)_3Bi_2Br_9$. The only additional reflections visible are gold-related peaks, which is expected as the XRD patterns were recorded on full solar cells.[46]

The GIWAXS measurements confirm the findings from the XRD measurements. Thin films treated with higher concentrated PEABr solutions (Figure 5.1 b, c) show the formation of two peaks at low scattering vectors q, proving the presence of a low-dimensional phase. Using the same integration time, these reflections cannot be found for thin films treated with very low concentrated PEABr solutions (0.01 M). However, by increasing the integration time by the factor 6, reflections at very small scattering vectors appear as shown in Figure S 5.2 (Supporting Information), demonstrating the formation of different 2D phases.

To further investigate the ultrathin 2D layers, SEM top-view images were recorded using the through-lens (TLD) and circular backscatter detector (CBS) as shown in the SI and Figure 5.3. The images compare the morphology of the above discussed thin films with the 3D reference and the films obtained by spincoating PEABr solutions with the concentrations 0.1 M and 0.01 M.

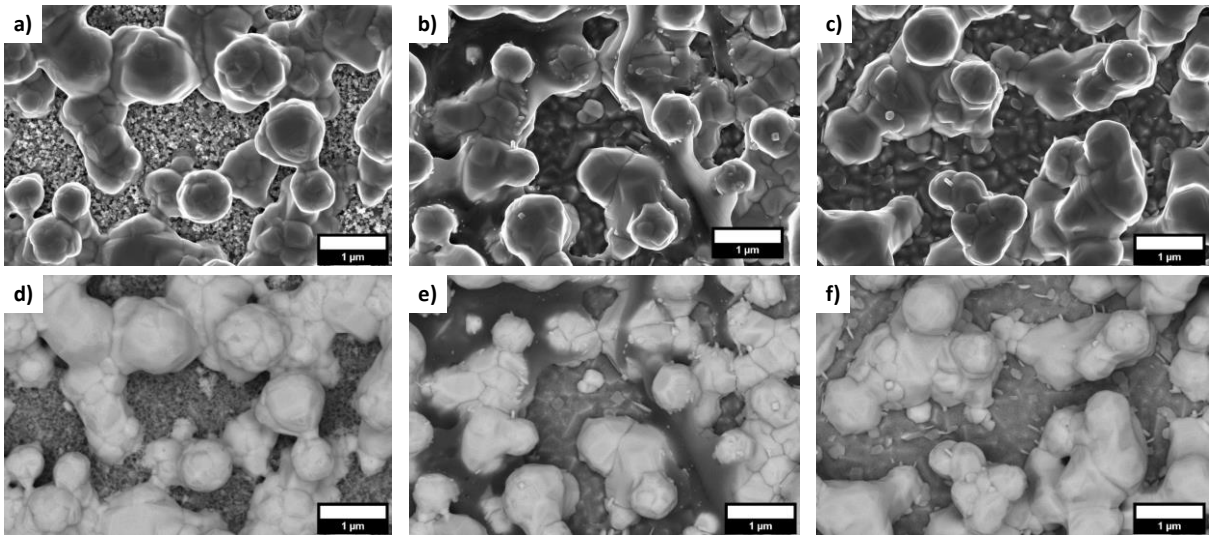

Figure 5.3: SEM top view images of the 3D reference (a,d), the 0.1 M hybrid (b,e) and the 0.01 M hybrid (c,f). The images a) to c) show the SEM top views obtained with a through-lens (TLD) and the images d) to f) show the images obtained with a circular backscatter detector (CBS). A smaller magnification can be found in the Supporting Information.

Figure 5.3 shows a zoom of the images shown in the SI. The morphology suggests the formation of rather big perovskite crystallites (> 1µm) that stick out from the mp-TiO_2 scaffold, which leads to rather large voids between the respective perovskite crystallites. However, this morphology has been proven to work well in solar cells[11] and the images clearly indicate the formation of a new layer for both PEABr concentrations. While the new layer forms big slabs

within the voids of the 3D layer, the formation of this film can be seen from the back-scatter images in Figure 3 f) as well for very low PEABr concentrations. Hence, we were able to confirm the formation of an additional low-dimensional double perovskite layer by spincoating a spacer cation on top of the 3D layer. We will now discuss the solar cells comprising this material as an active layer.

5.3.2 Solar Cell Performance

In the lead-halide perovskite community, it is well known that the hybridization of 3D films towards a 2D/3D structure can lead to an improvement of the photovoltaic performance of the resulting solar cells. This improvement has been assigned to better interfaces within the solar cells, as well as trap passivation, resulting in a significant increase in V_{OC}.[38,41]

$Cs_2AgBiBr_6$ double perovskite solar cells, however, are known to suffer from a rather small electron diffusion length, a fast localization and self-trapping of charge carriers and, more importantly, from rather large non-radiative V_{OC} losses and non-selective contacts.[17,20,21]

To investigate the influence of the above discussed lead-free 2D/3D hybrid perovskite, we employed the thin films in solar cells with the architecture FTO/c-TiO_2/mp-TiO_2/$Cs_2AgBiBr_6$/$(PEA)_4AgBiBr_8$/Spiro-OMeTAD/Au. The results are shown in Figure 5.4 and in Table 5.1. Please note that the PEABr concentrations of 0.01 M and 0.06 M were chosen after a screening process, during which the thin films comprising these parameters have shown to improve the solar cells in comparison to other concentrations and the 3D reference.

Table 5.1: Photovoltaic parameters of the investigated solar cells with the architecture FTO/c-TiO_2/mp-TiO_2/perovskite/Spiro-OMeTAD/Au

FTO/c-TiO_2/mp-TiO_2/perovskite/Spiro-OMeTAD/Au				
Perovskite [# of cells]	J_{SC} (mA/cm^{-2}) [Avg]	V_{OC} (V) [Avg]	*FF* (%) [Avg]	PCE (%) [Avg]
pure 3D [60]	3.33; [3.06 ± 0.18]	1.06; [0.99 ± 0.05]	60; [60 ± 5]	2.15; [1.84 ± 0.21]

2D/3D-hybrid, 0.06 M [68]	3.50; [2.99 ± 0.28]	1.07; [1.07 ± 0.05]	66; [61 ± 3]	2.47; [1.95 ± 0.23]
2D/3D-hybrid, 0.01 M [72]	3.55; [3.21 ± 0.22]	1.08; [1.05 ± 0.05]	64; [60 ± 5]	2.46; [2.03 ± 0.23]

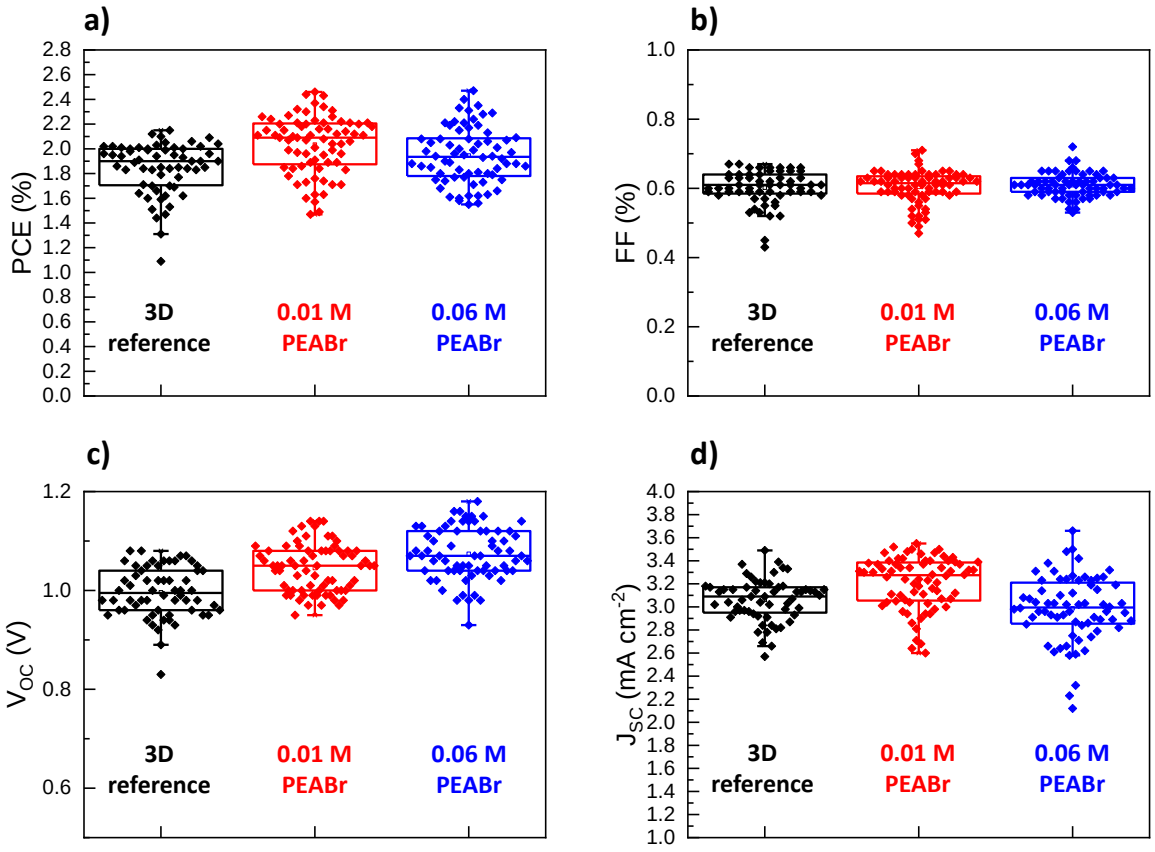

Figure 5.4: Box plots of the solar cell parameters of the investigated cells: black: 3D reference, red: 0.01 M hybrid, blue: 0.06 M hybrid. Panel a) shows the PCE of the solar cells in %, panel b) shows the FF of the solar cells, panel c) shows the V_{OC} in V and panel d) shows the J_{SC} in mA/cm^2.

The values show a clear improvement of the solar cell efficiency by using 2D/3D hybrid perovskite active layers in the solar cells. The average results show an optimum cation concentration of 0.01 mol/L PEABr in IPA, as solar cells with this cation-concentration achieve the highest efficiencies, both in the champion and the average values. Solar cells made with

0.06 M PEABr do show a champion cell with 2.5 % PCE as well, the average values though are lower than compared to the 0.01 M cells.

For both 2D/3D hybrid double perovskite solar cells, a maximum PCE of up to 2.46 % (0.01 M PEABr) and 2.47 % (0.06 M PEABr) were achieved, which is an improvement of 13 % compared to the 3D reference where the champion cell reached up to 2.15 % PCE. *J/V*-curves of high-performance solar cells are shown in Figure S 5.4. While the high PCE of almost 2.5 % is highly reproducible for the low concentrated (0.01 M PEABr, in the following called 0.01 M hybrid) hybrid, this value was only achieved once for the higher concentrated (0.06 M PEABr, in the following called 0.06 M hybrid) hybrid. This can be seen in the average values where the 3D reference results in 1.84 % over 60 solar cells, while the 0.06 M hybrid shows an improvement to 1.95 % over 68 devices. The 0.01 M hybrid double perovskite achieves also on average the highest PCE with 2.03 %, which is almost 10 % better compared to the 3D reference.

To find the reasons for the increase in efficiency, the different PV parameters need to be investigated. Figure 5.4 shows the different boxplots of the solar cells investigated in this work. While the *FF* only changes for the respective champion cells, it does not have any influence on the average improvement of the solar cells as it has values of 60 % for both the 3D reference and the 0.01 M hybrid and only improves to 61 % for the 0.06 M hybrid solar cells. The biggest changes in the photovoltaic (PV) parameters can be found in the V_{OC} and the J_{SC}. For both parameters, an improvement is observed for the 0.01 M hybrid compared to the 3D reference, both for the champion device and the average of all devices. On average, the 0.01 M hybrid solar cells express an improvement in their V_{OC} by 60 mV from 0.99 V to 1.05 V, which translates to 6 %. For the 0.06 M hybrid, the V_{OC} improvement is even larger with 80 mV, leading to an average value of 1.07 V. For the J_{SC}, an improvement can only be found for the 0.01 M hybrid. Here, the average value increases by 5 % from 3.06 mA/cm^2 for the 3D reference to 3.21 mA/cm^2 for the hybrid cell. For the 0.06 M hybrid, the average J_{SC} is reduced compared to the 3D reference with a value of 2.99 mA/cm^2. These effects are well within expectation and can be explained with the nature of the 2D perovskite. The addition of a 2D layer on top of a 3D layer is beneficial for the V_{OC} of the perovskite solar cells as already reported for lead-based perovskites.[36,38,41] Yet, a 2D layer is defined by its organic large cation, here a phenethyl ammonium cation. This leads to an insulating barrier on top of the 3D layer. While a thick 2D layer leads to a large improvement of the V_{OC}, it hampers charge transport from the 3D layer

towards the back electrode. The thinner this layer becomes, the more charge carriers can travel through this layer, hence the J_{SC} is improved. Another reason for the improvement of the J_{SC} can be found in the structure of the formed 2D perovskite: While for the 0.06 M hybrid, two phases with different n-values are formed, the only reflection found for the hybrids with concentrations < 0.04 M is for a phase with a n value bigger than 1. This translates to thicker octahedral layers in between the insulating PEA-layers and thus only a few insulation layers.

To further understand the improvement of the solar cells, additional measurements were performed.

5.3.3 Photoluminescence and Light Intensity Dependent V_{OC}

For lead-based 2D/3D hybrid perovskites, the corresponding reports discuss the improvement in the PCE and especially the V_{OC} with an increase in the signal of steady state photoluminescence, as well as an increase in the charge carrier lifetime obtained using time-resolved photoluminescence (TRPL).[36,38,41] Hence, we performed the same set of experiments as shown in Figure 5.5.

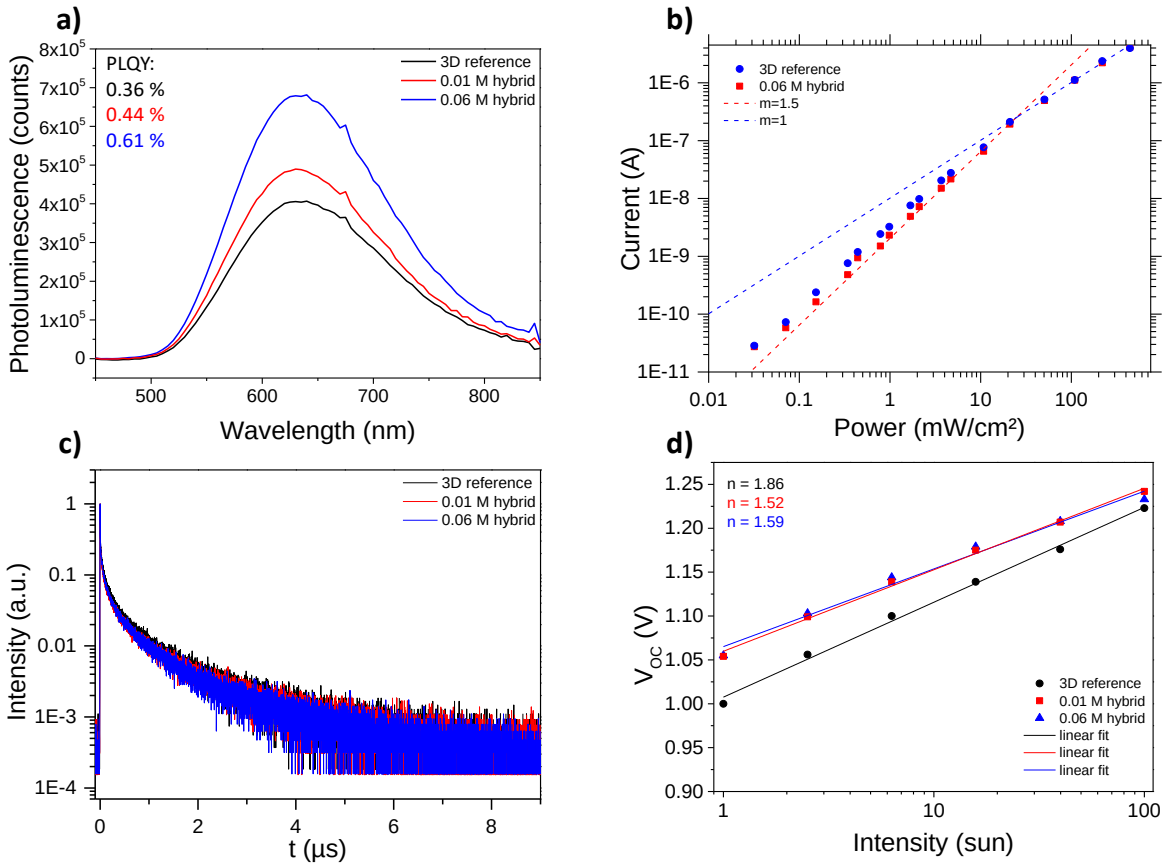

Figure 5.5: a) Steady state PL of the different films spincoated on glass, b) shows the fluence dependent PL with m giving the slopes at different incident laser power, c) gives the PL decay of the different films. d) shows the light intensity dependent V_{OC} measurements with the respective ideality factor given as n-value. All panels have the same color-coding: black: 3D reference, red: 0.01 M hybrid, blue: 0.06 M hybrid.

In contrast to lead-based perovskites, we did not observe any significant changes in the charge carrier behavior, both in the steady state and time resolved photoluminescence. This behavior is counter-intuitive, as we would expect a change in the recombination behavior of our thin films, especially the hybrids, following the V_{OC} trend from the solar cells. First, we measured the PLQY of our thin films.

A small increase in the signal of the PL signal can be found (Figure 5.5 a) for the 0.01 M hybrid, while the PL signal of the 0.06 M hybrid is almost double in intensity compared to the 3D film. To exclude measurement artifacts, every film was measured several times at several different spots. PLQY values show an improvement of the thin films from ~0.36 % for the 3D reference up to 0.61 % for the 0.06 M hybrid, while the 0.01 M hybrid lies at around 0.44 %. While all of

these values are the highest so far reported for this material, they match well with the observed trend of the V_{OC} values of the solar cells.[20] Yet, the PLQY values are only sufficient to explain an increase of the V_{OC} by 20 mV in case of the 0.06 M hybrid films.[47] This shows that the dominant recombination regime might not change significantly, as no significant change in the radiative recombination was observed. To investigate this further, we additionally measured fluence dependent steady state PL (Figure 5.5 c) of the thin films on glass, comparing the 0.06 M hybrid with the 3D reference (as only for the 0.06 M hybrid, bigger changes are visible so far). While the slopes in the fluence dependent PL do change going from lower to higher laser intensity, it is expected from our previous work and can be explained as a shift from trap assisted recombination towards excitonic recombination as at higher laser intensity, the ratio of free charge carriers to excitons is smaller compared to lower light intensity.[13,48] Among the different architectures, however, the data points do not show different values. This suggests that the dominating recombination behavior of the 2D/3D hybrid films is the same as for the 3D reference,[49] while all films have a change of the recombination regime going from low to high laser intensities (Figure 5.5 b), which again indicates the formation of a hybrid phase instead of a simple passivation effect. Time resolved measurements (Figure 5.5 c) do not show significant changes either, detecting a charge carrier lifetime from 331 ns for the 3D reference up to 352 ns for the 0.01 M hybrid and 356 ns for the 0.06 M hybrid, respectively. Hence, we can conclude that the lifetime of the charge carriers does not contribute significantly to the observed V_{OC}.

As an increased V_{OC} not only indicates changed recombination behavior in the pristine film, but can also be linked to better contact selectivity leading to a reduction of charge carrier recombination rates at the interface,[50,51] light intensity dependent V_{OC} measurements were performed as they are a valuable tool to determine the ideality factor of the diode that represents a solar cell. While fluence dependent steady state PL gives information about the recombination regime within the pristine film, the ideality factor does the same within the full device where n=1 should indicate a perfect bimolecular recombination and n=2 indicates a perfect trap assisted recombination. The ideality factor can be deduced using the following equation (5.1):[52]

$$V_{OC} \sim n * \frac{kT}{e} * \ln(I) \tag{5.1}$$

Where kT/e has a value of 0.02527 V at room temperature.

However, if the recombination behavior is dominated by interfacial recombination, the ideality factor may be equal to 1 as well and eventually reach values below 1.[52,53] In this case, the initial V_{OC} of the respective solar cell should be lower than 1 V, which is not the case in this work.

Figure 5.5 d shows the graphs obtained from measuring the three different solar cells, the values of the ideality factors obtained from the linear fit of the values in a ln plot (Figure S 5.5) are written in the figure. Contrary to the fluence dependent PL measurements, the devices show in fact a change in the recombination behavior. While the 3D reference expresses an ideality factor of 1.86 at 395 nm excitation, indicating a mere trap assisted recombination behavior, the hybrid solar cells show values of 1.52 (0.06 M) and 1.59 (0.01 M) respectively. This could indicate a change of the recombination behavior towards bot perfect bimolecular, or interfacial recombination.[52,53] As discussed above, however, a dominant interfacial recombination process would be associated with a rather low V_{OC} below 1 V. This is not the case in this work with average values of 1.07 and 1.05 V for 0.06 M and 0.01 M cells respectively. Hence, the results indicate that for the 2D/3D hybrids, the recombination behavior is less dominated by interfacial and trap assisted recombination than compared to the 3D reference. This indicates a large improvement of the selectivity of the contacts, which we recently determined as one of the major bottlenecks.[17] The improvement of the charge carrier recombination in the full devices is further evidenced by EL EQE measurements we performed using cells comprising the 3D reference and the 0.01 M hybrid solar cells. Here, an improvement of the ELQE from $4*10^{-8}$ to 10^{-7} at the start of the measurement and from $1.5*10^{-8}$ to 10^{-7} after 170 s does show an increase of almost one order of magnitude for the 2D/3D hybrid solar cell (Figure S 5.6, Supporting Information). While the value of the 3D reference is comparable to that from ref.[17], the 0.01 M cell indicates a significant improvement of the recombination behavior and thus explains a reduction of non-radiative V_{OC} losses.

Moreover, the measurement shows an improvement of the stability of the hybrid compared to the 3D reference. This is also evidenced by MPP tracking performed over a time-span of 3600 s. While both solar cells show a rather high stability of over 90 %, the 0.01 M cell has an improved value of maintaining 99.6 % of the initial PCE compared to the 3D reference (98.5 %, Figure S 5.6, Supporting Information).

To further investigate the origin of the higher selectivity and the improved J_{SC}, we proceeded with quantum efficiency measurements and band-energy determination.

5.3.4 PV Quantum Efficiency and Energy Level Alignment

The 0.06 M hybrid and the 0.01 M hybrid show very comparable behavior regarding the optoelectronic measurements, especially regarding the light intensity dependent V_{OC} measurements. The 0.01 M films, however, show superior efficiency in solar cells, resulting from an improvement in both the J_{SC} and the V_{OC}. Hence, we will continue to discuss only the 0.01 M hybrid in the remainder of this paper.

Solar cells comprising the 0.01 M hybrid show an improved J_{SC} compared to the 3D reference (from 3.06 to 3.21 mA/cm^2 on average). This can also be seen in the EQE spectra in Figure 5.6 a. Here, the cells measured with the 0.01 M hybrid show a higher EQE compared to the 3D reference. Please note that we chose pixels (solar cell devices) for this measurement with a PCE well within the average of the solar cells described above. The biggest difference in the EQE is observable for the peak at ~450 nm, where the absorption is the highest (dashed lines in Figure 5.6 c and d). Here, the EQE is at 50 % for the 2D/3D hybrid, while the EQE of the 3D reference only reaches 40 %. Overall, an average increase of 10 % in the EQE can be observed for the 2D/3D hybrid perovskite solar cells, which directly leads to an increased integrated photocurrent by almost 25 % (2.3 mA/cm^2 to ~2.9 mA/cm^2) which matches well with the obtained J_{SC} values from the solar cells (2.6 mA/cm^2 for the 3D reference and 2.8 mA/cm^2 for the hybrid). It confirms the trend visible from average values of all measured devices as shown in the section above. To further investigate the trap density and recombination behavior of the solar cells, subgap-EQE measurements were performed (Figure 5.6 b). The spectra show no significant change in the trap density, observable by the signal in the spectral region below 2 eV. In fact, a slight increase in signal is observed for the 2D/3D hybrid double perovskite solar cells. This indicates that the hybrid cells express a slightly higher amount of gap-states and deep tails and confirms that no trap passivation occurred by hybridizing the 3D perovskite. It supports the finding that the boost in V_{OC} dies not come from simple trap passivation.

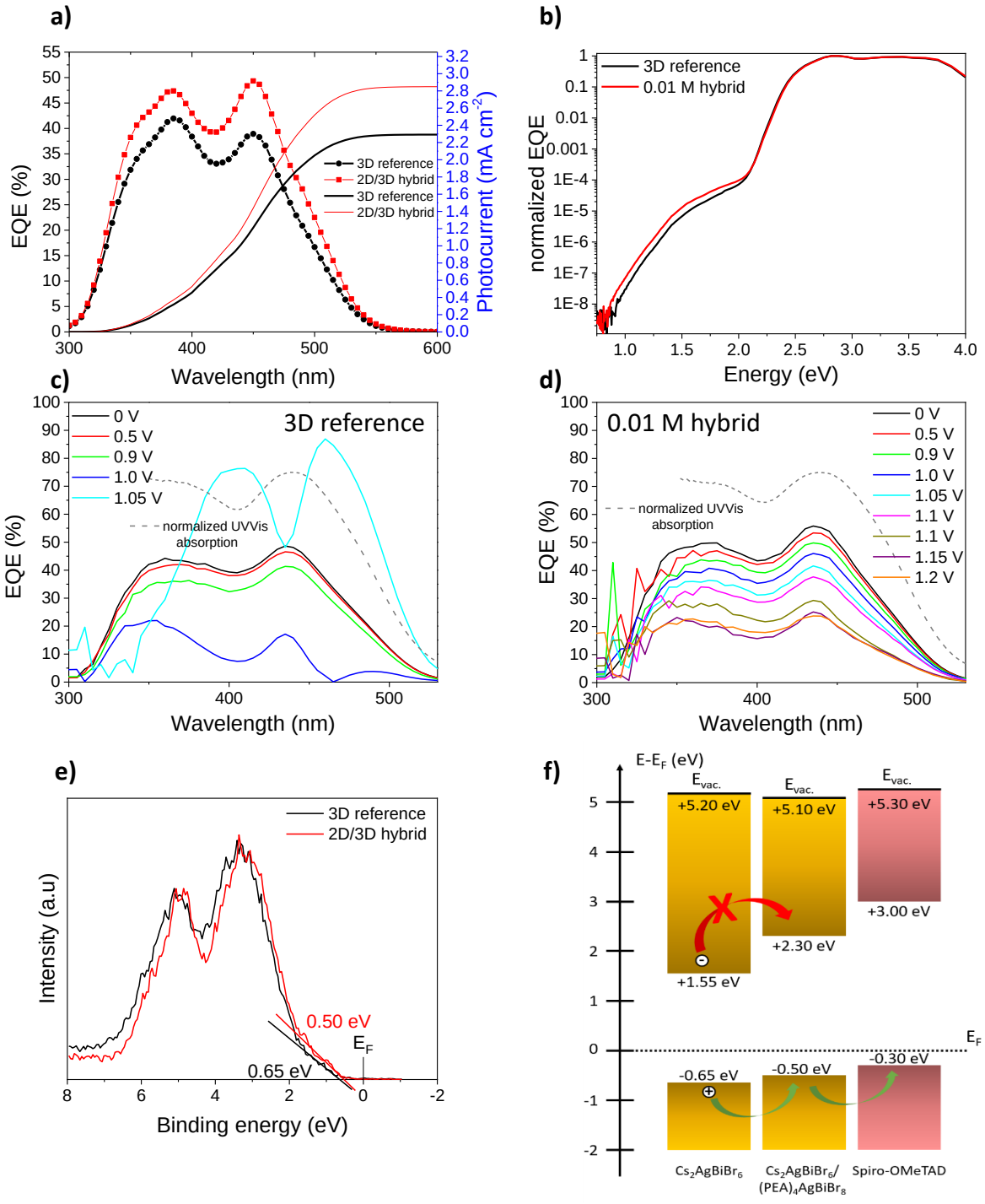

Figure 5.6: EQE and UPS spectra measured in this work. a) gives the EQE spectra obtained from the 3D reference (red line) and the 0.01 M hybrid (black line), plotted together with the integrated photocurrent. Panel b) shows the subgap EQE spectra of the 3D reference (red line) and the 0.01 M hybrid (black line). Panels c) and d) show the voltage dependent EQE measurements of the 3D reference and the 0.01 M hybrid respectively. Different applied volages are shown in the legend. The dashed grey line shows the respective UV-Vis absorption spectrum to guide the eye. Panel e) shows the XPS spectra

of the valence shell energies of the hybrid double perovskite (red line) in respect to the 3D reference (black line). Panel f) shows a schematic energy level diagram obtained from the XPS values of the VBM and the optical bandgap obtained from the tauc plot in the Supporting Information.

In our recent publication, we observed a change of sign of the EQE by measuring the spectra as a function of the applied voltage, which was indicated by a large drop of the EQE at voltages > 0.9 V.[17] While the bias causing this effect is much higher compared to our last work, we do see a very similar effect with the 3D solar cells: At voltages higher 1.00 V, we observe a drop in the EQE before it rises again strongly up to 80 % (at 1.05 V external bias). The higher external voltage required compared to our recent report is well within the increase in the V_{OC} (0.9 V on average in ref.[17] compared to 0.98 V on average in the present work) and indicates either a larger built-in potential of 1 V that could be caused by the choice of Spiro-OMeTAD as HTM instead of P3HT. The first has a higher LUMO level compared to the latter, allowing a better electron blocking and therefore a better overall selectivity.[54] In the present work, we again observe not only an increase of the absolute EQE values, but also a change in the shape. While the shape of the EQE spectra below 1 V external bias exactly follows the absorption peaks of the UV-Vis spectrum (grey dashed line in Figure 5.6 c), this shape is inverted after applying voltages above 1.00 V. Now, the EQE maxima are located at the spectral range of the absorption minima, which indicates that the charge carriers created more homogeneously in the perovskite layer result in a higher photocurrent. The high EQE value can only be explained by a photomultiplication effect due to a photoenhanced forward current. Given the well-aligned conduction band of TiO_2 and perovskites, this current is most likely carried by electrons, which recombine with holes on the HTM. This further confirms the findings of our recent work that we indeed have rather non-selective contacts and thus reduce the charge carrier collection.[17]

For the 2D/3D hybrid perovskite, no such change in the EQE is observed, at least for voltages up to 1.20 V. Here, the value of the EQE steadily decreases, as also observed for the 3D reference. Upon reaching voltages higher than 1.25 V, the solar cell rapidly degrades and the measured values are not reliable. The absence of the photocurrent inversion for the 2D/3D hybrid double perovskite solar cells indicates a large improvement of the selectivity within the solar cell as not only the V_{OC} of the solar cell is increased (indicating an even larger internal voltage, as well as built-in potential), but also the photocurrent direction shows no change at all, indicating a higher selectivity of the contacts. These results, together with the absence of trap passivation, support the indications of an increased contact selectivity, as well as reduced

interface recombination leading to the vast improvement of the V_{OC} values of the resulting solar cells as observed with light intensity dependent V_{OC} measurements.

To investigate the energy levels, photoelectron spectroscopy measurements were performed on the perovskites deposited on FTO substrates as shown in Figure 5.6 e), Figure S 5.7 and Figure S 5.8 (Supporting Information).

Since the films were deposited at ambient conditions in air, contamination with oxygen could not be excluded. Hence, not UV irradiation but X-rays were used to determine the valence band maxima of the two different films. To confirm the presence of the spacer cation for the 2D/3D hybrid thin films, we determined the core-level energies of the different samples. Figure S 5.8 exhibits the survey and the core level XPS spectra for the 3D reference and a 2D/3D hybrid. Binding energy positions of each element agree with a previous report.[12] The presence of nitrogen in the 2D/3D hybrid thin film confirms the presence of the spacer cation. A narrowing of the core level emission lines is also observed when the spacer cation is added. On average, the FWHM decreases to 100 meV and for the Br 3d spectra, it leads to more defined emission lines. This is in agreement with an ordering of the perovskite after a 3D to 2D transition[43,44] and confirms the presence of a 2D/3D hybrid phase. The nitrogen spectrum (N1s) can only be found for the 2D/3D hybrid material. However, the Cs 3d emission lines are visible as well, evidencing that the contribution of the 3D phase to the PES spectra cannot be dismissed. This can be linked to the morphology of the investigated thin films as shown in Figure 5.3 and Figure S 5.3, Supporting Information, showing the µm-sized 3D perovskite crystallite penetration out of the 2D layer.

Figure 5.6 e shows a shift of the VBM after the addition of a spacer cation. It evidences that the VBM of the 2D material is 150 meV closer to the Fermi level, compared to the 3D reference. This is supported by the similar shifts of 100 meV (Bi4f, Ag3d) or 150 meV (Br3d, Cs3d) that are observed on the core level emission lines (Figure S 5.8, Supporting Information). As all measurements are performed relative to the Fermi level of the sample, such global shift toward lower energy indicates a change in the Fermi level position of the perovskite absorber.

To determine the energy of the conduction band minimum, we measured the optical bandgap of a pure 2D $(PEA)_4AgBiBr_8$ thin film (Figure S 5.10, Supporting Information). The thin film was deposited on a FTO substrate to simulate the same environment as for the 3D thin films, resulting in fully covered, smooth thin films (inset in Figure S 5.10 a, Supporting Information).

To determine the nature of the optical bandgap of the material, we calculated the band structure using first principle DFT calculations (Figure S 5.11, Supporting Information). The PBE-SOC-TS band structure of $(PEA)_4AgBiBr_8$, shows a drastic change in the band gap nature compared to the 3D reference perovskite with the lowest band transition being centered at the Γ point in the Brillouin zone.[32] We note that although the bandgap is significantly underestimated, we can assume that the DFT-PBE method provides accurate predictions about the electronic nature of the calculated structure.[55,56] Hence, a direct bandgap with an energy of 2.8 eV was measured (Figure S 5.10, Supporting Information), enhancing the energy by 0.6 eV compare to the 3D $Cs_2AgBiBr_6$.[17]

Combining the optical bandgap, the VBM and the work function measured by UPS (Figure S 5.9, Supporting Information), the full band diagram can be constructed (Figure 5.6 f). To provide more insight on the charge carrier collection of our device, the energy levels of the HTM, a LiTFSI-doped Spiro-OMeTAD were determined and added to the diagram. The VBM and the work function were measured with UPS (Figure S 5.10, Supporting Information) and the band gap was assumed to be 3.3 eV, although the absorption energy of the oxidized species is slightly lower.[57] The 2D perovskite has a CBM of +2.3 eV (relatively to the Fermi level) which is 750 meV above the one of the 3D counterpart and 700 meV below the LUMO of the HTM. As the electrons are photogenerated inside the 3D material, the presence of the 2D layer enhances the electron blocking behavior of the resulting hybrid thin films. In addition, the VBM of the 2D/3D hybrid double perovskite is 150 meV closer to the HOMO energy level of the HTM compared to the 3D reference. It optimizes the holes extraction and therefore, it reduces the amount of interfacial recombination.

This altogether confirms the findings of the EQE measurement that indicate a significant change in the selectivity of the contacts in the solar cell. It leads to the observed boost in the V_{OC} of the solar cells and addresses one of the major issues of solar cells based on Pb-free perovskites.

5.4 Conclusions

In this work, we successfully synthesized an Ag-Bi based 2D/3D hybrid double perovskite for the first time, using phenethyl ammonium bromide as large cation salt to form $(PEA)_4AgBiBr_8/Cs_2AgBiBr_6$ thin films. After confirmation of the film formation, we implemented this material in perovskite solar cells, obtaining a significant increase in the PCE from 1.84 % on average for the 3D reference to 2.03 % for the 2D/3D hybrid. The champion

cells comprising the 2D/3D hybrid thin film even reach efficiencies up to 2.5 %. While the J_{SC} shows an improvement of 10 % on average, the V_{OC} is improved on average by 70 mV to reach values up to 1.14 and 1.18 V, which are among the highest values reported for $Cs_2AgBiBr_6$ solar cells. This boost in the V_{OC} is attributed to a large enhancement of the selectivity of the contacts in the solar cell, which was shown by comprehensive EQE and PL studies. Photoelectron spectroscopy reveals a shift in the valence band maximum of the 2D/3D hybrid perovskite thin film of 150 meV towards the Fermi level energy. This improves the energy level alignment and allows for a better hole-extraction towards the doped Spiro-OMeTAD layer. In combination with an increased bandgap of the 2D material, which was calculated to be direct, the XPS results predict an energy barrier of 750 meV between the 2D and the 3D perovskite, improving the contact selectivity in the solar cell. In this work, we show a way to easily tune the perovskite/HTM energy level alignment, as well as to improve the charge carrier selectivity of the contacts in the solar cell. Hence, this work offers a toolbox to efficiently address some of the bottlenecks that have been identified for the behavior of lead-free double perovskite solar cells.

5.5 Experimental

Materials and Thin Film Synthesis

The stock solution was prepared by dissolving CsBr (Alpha Aesar, 99.999 % metals basis), $BiBr_3$ (Alpha Aesar, 99.9 % metals basis) and AgBr (Alpha Aesar, 99.998 % metals basis) in 1 mL DMSO (Sigma Aldrich, anhydrous, ≥99.9 %) by vigorous stirring at 130 °C for 60 minutes to obtain a 0.5 M solution. Weighing the precursors was performed in a nitrogen-filled glovebox, while all other steps, including the DMSO addition to the precursors, were done at ambient conditions in air.

Prior to the spincoating step, the substrates and the solution were placed on a hotplate (Heidolph with internal temperature sensor) at 85 °C to be preheated. The stock solution was constantly stirred. The thin films were fabricated by spincoating the warm solution dynamically (2000 rpm for 45 s) onto the preheated substrates (100 µL of the stock solution). After the spincoating, the thin films were annealed at 285 °C for 5 minutes at ambient conditions in air.

Solar Cell Fabrication

Fluorine-doped tin oxide coated glass sheets (7 Ω/sq) were patterned by etching with zinc-powder and 3 M HCl, cleaned with a detergent followed by washing with acetone and ethanol and dried under an air stream. Directly before applying the hole-blocking layer, the substrates were oxygen plasma cleaned for 5 min.

Compact TiO_2 (c-TiO_2)

A compact TiO_2 layer was prepared from a sol-gel precursor solution by spin-coating 100 µL onto the 3 cm x 3 cm substrates for 45 s at 2000 rpm and calcination afterwards at 500 °C for 30 min in air, resulting in a 50 nm thick layer. For the sol-gel solution, 2 M HCl (35 µL) in 2.53 mL dry 2-propanol was added dropwise to a solution of 370 µL of titanium-isopropoxide in 2.53 mL dry 2-propanol under vigorous stirring. After cooling down, the substrates were again plasma cleaned for 5 min and transferred to a nitrogen-filled glovebox.

Mesoporous TiO_2 (mp-TiO_2)

After the deposition of the layer of compact TiO_2, 100 µL of a dispersion of mp-TiO_2 nanoparticles (DyeSol, 3:1 EtOH:TiO_2-paste) was spincoated on top of the c-TiO_2 layer without plasma-cleaning. Afterwards, the substrates were calcined at 500 °C for 30 min in air resulting in a 500 nm thick layer. After cooling down, the active layer was deposited on top of the TiO_2 layer as described above.

Deposition of Hole Transporting Materials (HTM)

73 mg of 2,2′,7,7′-tetrakis-(N,N-di-4-methoxyphenylamino)-9,9′-spirobifluorene (Spiro-OMeTAD, Borun Chemicals, 99.5 % purity) were dissolved in 1 mL of chlorobenzene. To this solution, 10 µL of 4-tert-butylpyridine and 30 µL of a bis(trifluoromethane)sulfonamide lithium salt solution (LiTFSI, 170 mg in 1 mL acetonitrile) were added. The resulting HTM solution was deposited via dynamic spincoating (1500 rpm, 45 s) in a nitrogen-filled glovebox. Afterward, the samples were stored overnight in air at < 30 R.H. to allow the hole transporting material to oxidize.

The top electrode with the thickness of 40 nm was deposited by thermally evaporating gold under vacuum (at ~10^{-7} mbar).

DFT Calculations

First-principle DFT calculations were based on a plane wave basis set and norm-conversing Vanderbilt pseudopotentials as implemented in the Quantum Espresso package.[58,59] Furthermore, the PBE exchange−correlation functional and the Tkatchenko−Scheffler (TS) dispersion scheme were used.[60,61] The latter is necessary to accurately describe the structural properties in low-dimensional perovskite materials.[62] Additionally, spin-orbit coupling was included to treat the heavy Bi atom. The structure, starting from the single crystal data of Schmitz et al.,[45] was optimized until all residual forces on the nuclei were below 1.0 x 10^{-3} a.u.. Thereby, the following equilibrium unit cell parameters were obtained:

a = 11.4661 Å, b = 11.5138 Å, c = 17.0237 Å, α = 106.6141°, β = 99.6955°, γ = 90.7676°

A kinetic energy cutoff of 50 Ry for the wavefunctions and 400 Ry for the charge density was used. A 4x4x1 k-point grid was utilized.

Materials Characterization

Powder X-Ray Diffraction (PXRD) Measurements

The patterns were recorded using a Bruker D8 Discover Diffractometer with Ni-filtered Cu K_α radiation and a LynxEye position-sensitive detector.

2D Grazing-Incidence Wide Angle X-Ray Scattering (GIWAXS)

GIWAXS measurements were carried out on a ANTON-PAAR SAXSPOINT 2.0 with a PRIMUX 100 microfocus source with Cu-$K_{\alpha 1}$ radiation (λ = 1.5406 Å) and a DECTRIS EIGER R 1M 2D Detector.

Scanning Electron Microscopy (SEM)

SEM data were taken with a FEI Helios NanoLab G3 UC field emission scanning electron microscope equipped with an additional concentric backscattered detector.

Photoelectron Spectroscopy (PES)

Even though the samples were prepared under ambient conditions in air, to minimize contaminations, samples were shipped under nitrogen. They were opened in a glovebox and transferred to the ultra high vacuum system.

PES measurements were performed with a Thermo Fisher VG Escalab 250 spectrometer. It is equipped with a monochromatic X-ray source (Al Kα = 1486.6 eV) set at 13 mA and 15 kV. The pressure inside the analytic chamber was monitored below 5.10^{-9} mbar. Measurements were performed in "dark conditions" as discussed in[63] to avoid undesired photovoltage and misinterpretation of the energy levels.

Survey spectra were acquired with a pass energy of 50 eV, a step size of 0.1 and a dwell time of 50 ms per measurement point. The detailed scans were acquired with a lower pass energy (10 eV) and a lower step size (0.05 eV). UPS measurements were performed with the same spectrometer; He I (21.2 eV) discharge was used.

XPS spectra were calibrated using the Fermi level of silver (0 eV) measured by XPS as well as the binding energy of the Au 4f7/2 emission line (84.0 eV), the Ag 3d5/2 emission line (368.26 eV – FWHM at a pass energy of 10 eV was equal to 0.52 eV), and the Cu 2p3/2 emission line (932.67 eV). The Femi level of silver was also measured with UPS to calibrate the corresponding spectra. The Fermi level value was determined with a sigmoid fit and taking the position where the intensity is at 50%. All calibration samples were cleaned with Ar sputtering prior to the measurement (3 kV, for 180 s). The Fermi level of the cleaned silver was also used to determine the instrumental resolution: 0.35 eV for XPS (pass energy of 10 eV) and 0.24 eV for UPS (pass energy of 2.5 eV).

Semi quantitative analysis was performed using the Thermo Avantage software. Core levels were fitted using modified Shirley background subtraction and Gauss-Lorentz convolution. Quantification was made with the machine-corrected atomic sensitivity factors based on Scofield's calculations.

Photoluminescence Quantum Yield (PLQY), Fluence Dependent Steady State PL and Time-Correlated Single Photon Counting (TCSPC)

The PLQY was measured using a laser with 405 nm wavelength, a power of 71.0 mW/cm^2 and an integrating sphere. The spot size was 0.0152 cm^2.

The TRPL was recorded using a 375 nm laser with a repetition rate of 10 µs, a power of $5.5x10^{-7}$ W and a spotsize of 290 µm.

All spectra were measured using a Edinburgh Instruments FLS 980 and in reflection using a Si diode for detection.

Fluence-dependent steady state PL was measured using a 415 nm LED (Solis-415C, Thorlabs). The sample was placed at an 45° angle towards the excitation beam, so that measurements were performed in a reflection configuration. A silicon diode was placed in the emission pathway in order to monitor the resulting integrated photoluminescence.

EQE Measurements for Figure 6

Measurements were performed on a home made system with a halogen lamp, a monochromator and a silicon reference diode. The light was chopped at 330 Hz and the signal was detected through a lock-in amplifier. The setup was calibrated with a silicon solar cell and no bias light was applied.

Sensitive EQE Measurements

Sensitive EQE measurements to characterize the sub-bandgap region were conducted using a halogen lamp (Osram 64655 HLX 250 W) as illumination source. The light was chopped using an Oriel 3502 chopper at 330 Hz and subsequently passed through a double-grating monochromator (Oriel, Cornerstone 260). Several long-pass filters were used to filter out stray light. The samples were mounted in an air tight holder filled with nitrogen to prevent air exposure. The response was recorded from a pre-amplifier (Stanford Research, SR 570) using a lock-in amplifier (Stanford Research, SR 830) and calibrated using two Si and InGaAs reference cells.

Absorption Measurements

The absorption spectra of the films were taken on a Lambda 1050 (Perkin Elmer) instrument with an integrating sphere.

Solar Cell Characterization

Current–voltage (*J-V*) characteristics of the perovskite solar cells were measured using a Newport OrielSol 2A solar simulator with a Keithley 2401 source meter. The devices were illuminated through a shadow mask, yielding an active area of 0.0831 cm^2. The *J-V* curves were recorded under standard AM 1.5G illumination from a xenon lamp, and calibrated to a light intensity of 100 mW cm^{-2} with a Fraunhofer ISE certified silicon diode. The input bias voltage was scanned from -1.5 to 0 V in 0.01 V steps with a rate of 0.1 V s^{-1} for the standard PCE measurements. For the experiments with different scan-speeds, we chose bigger voltage steps

varying from 0.01 V to 1 V. All prepared devices show a comparable degree of hysteresis between the forward and the reverse scan.

5.6 Supporting Information

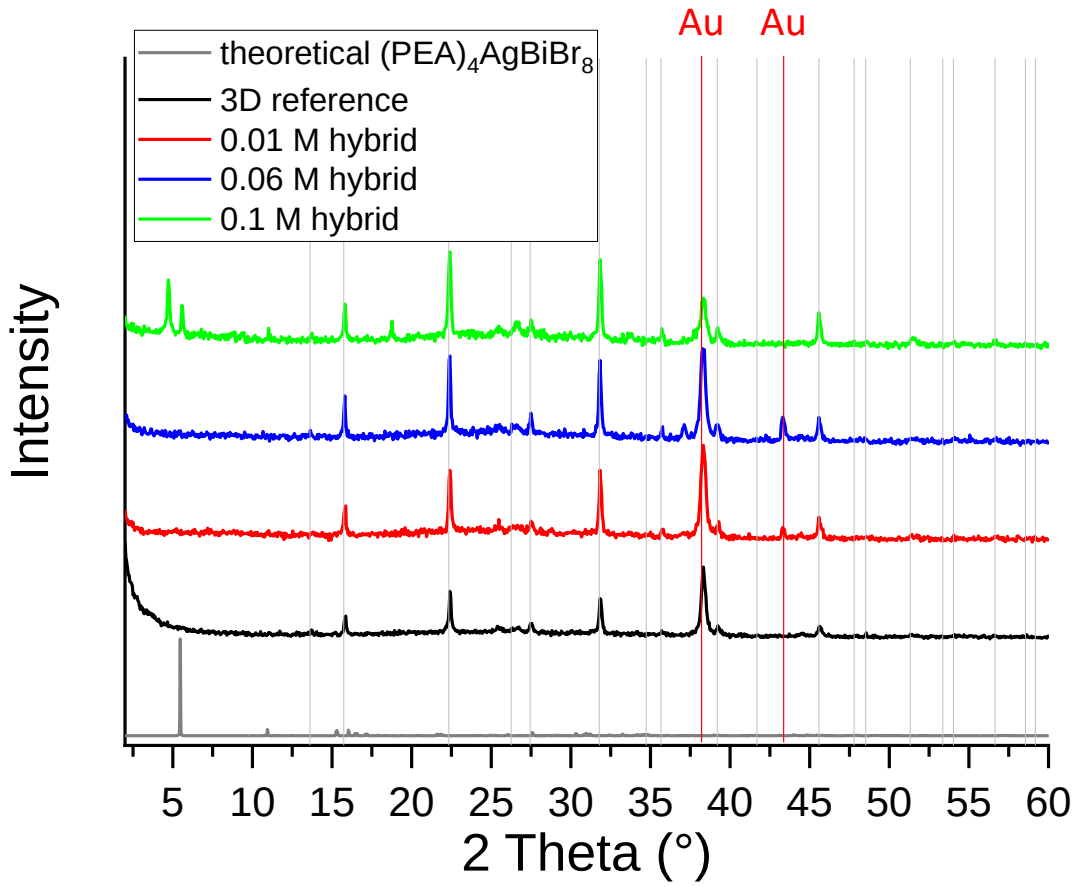

Figure S 5.1: Full XRD patterns of the different thin films recorded in Bragg Brentano Geometry. The grey line shows the theoretical pattern of $(PEA)_4AgBiBr_8$ perovskite. The grey drop lines indicate the theoretical pattern of the 3D double perovskite $Cs_2AgBiBr_6$. The black line is the obtained pattern from the pure 3D Solar cell, the red line shows the experimental pattern of the solar cell with the 0.01 M hybrid as active layer, the blue and green line show the experimental patterns of solar cells comprising the 0.06 M and 0.1 M hybrid respectively. The red drop line indicates the reflections arising from the gold electrode.

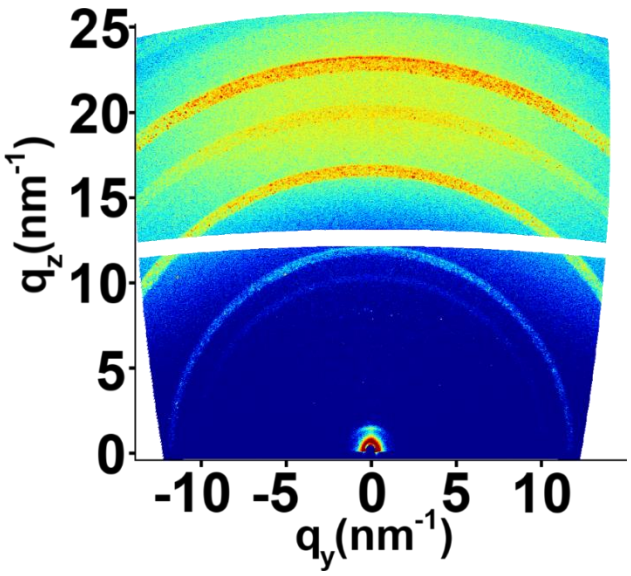

Figure S 5.2: Detector-image of GIWAXS measurements performed on thin films treated with 0.01 M PEAr and measured with an increased integration time.

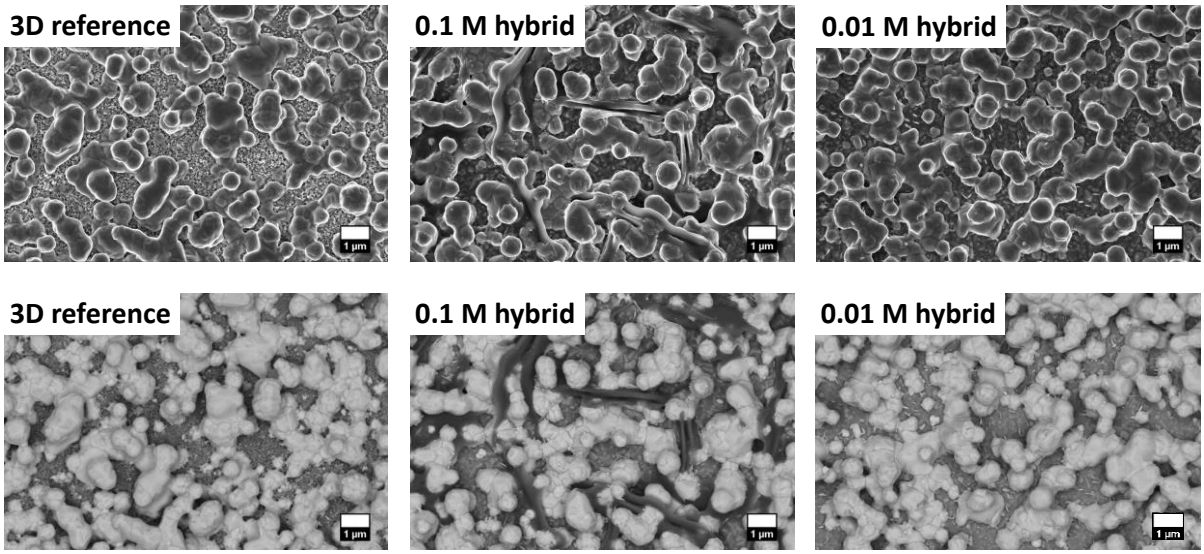

Figure S 5.3: SEM topview images of the investigated thin films. Top line shows the through the lense detector (TLD) images. Lower line shows the images obtained with a circular backscatter detector (CBS). The 3D reference is shown on the left side, the 0.1 M hybrid in the middle and the 0.01 M hybrid on the right side.

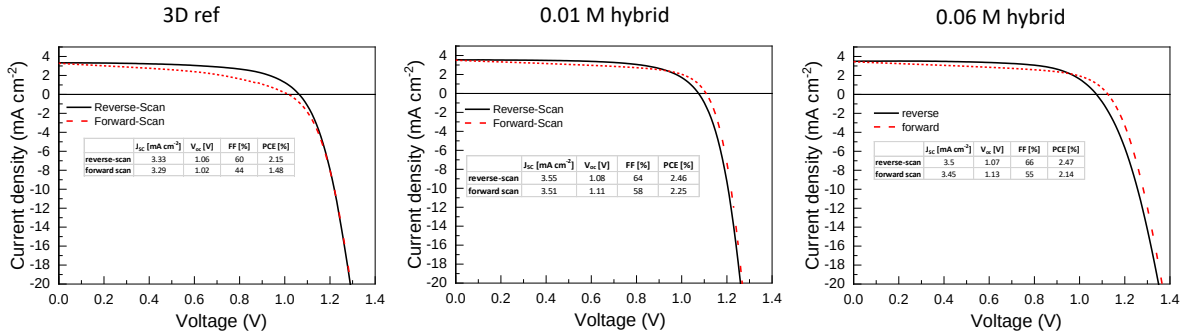

Figure S 5.4: J-V curves of the solar cells investigated in this paper. The curves show negligble hysteresis between the forward and the reverse scan.

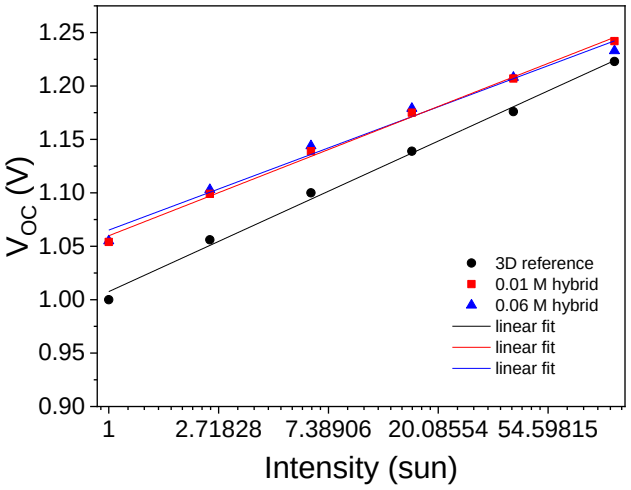

Figure S 5.5: semi-ln plots of the light intensity dependent V_{OC} measurements. The parameters are shown as indicated in the legend.

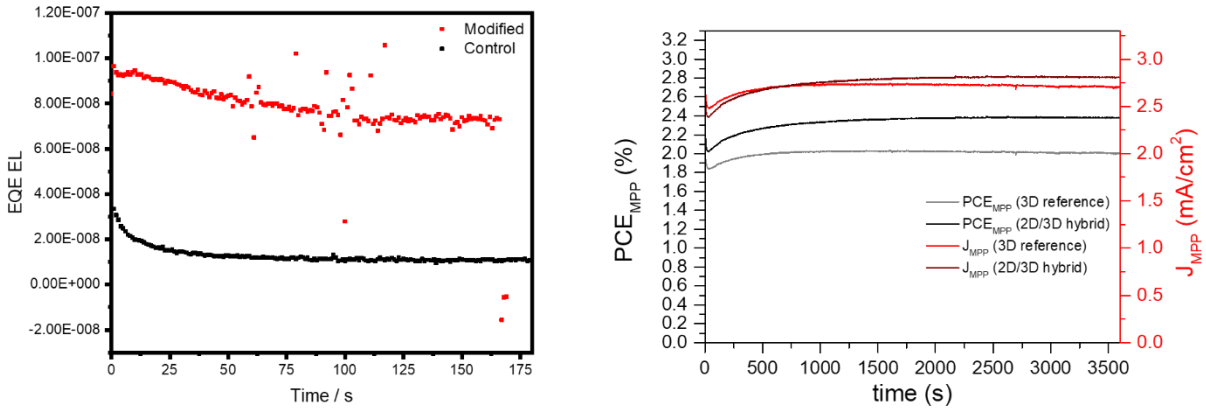

Figure S 5.6: EQE EL and MPP measurements of the 0.01 M (red line) and the 3D reference (black line).

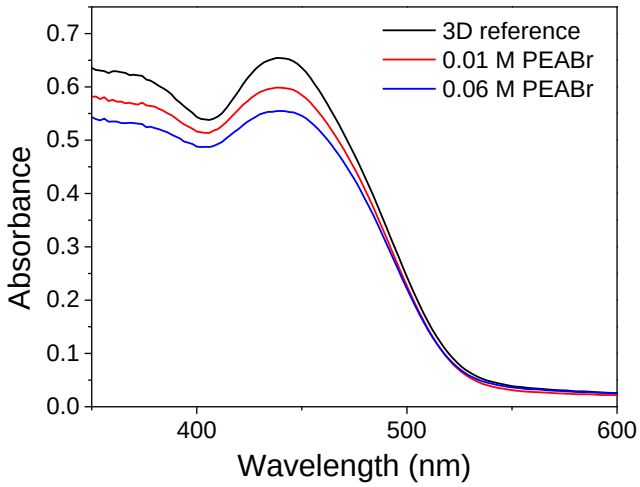

Figure S 5.7: UV-Vis absorption spectra obtained from thin films on FTO substrates. Color coding as indicated in the legend.

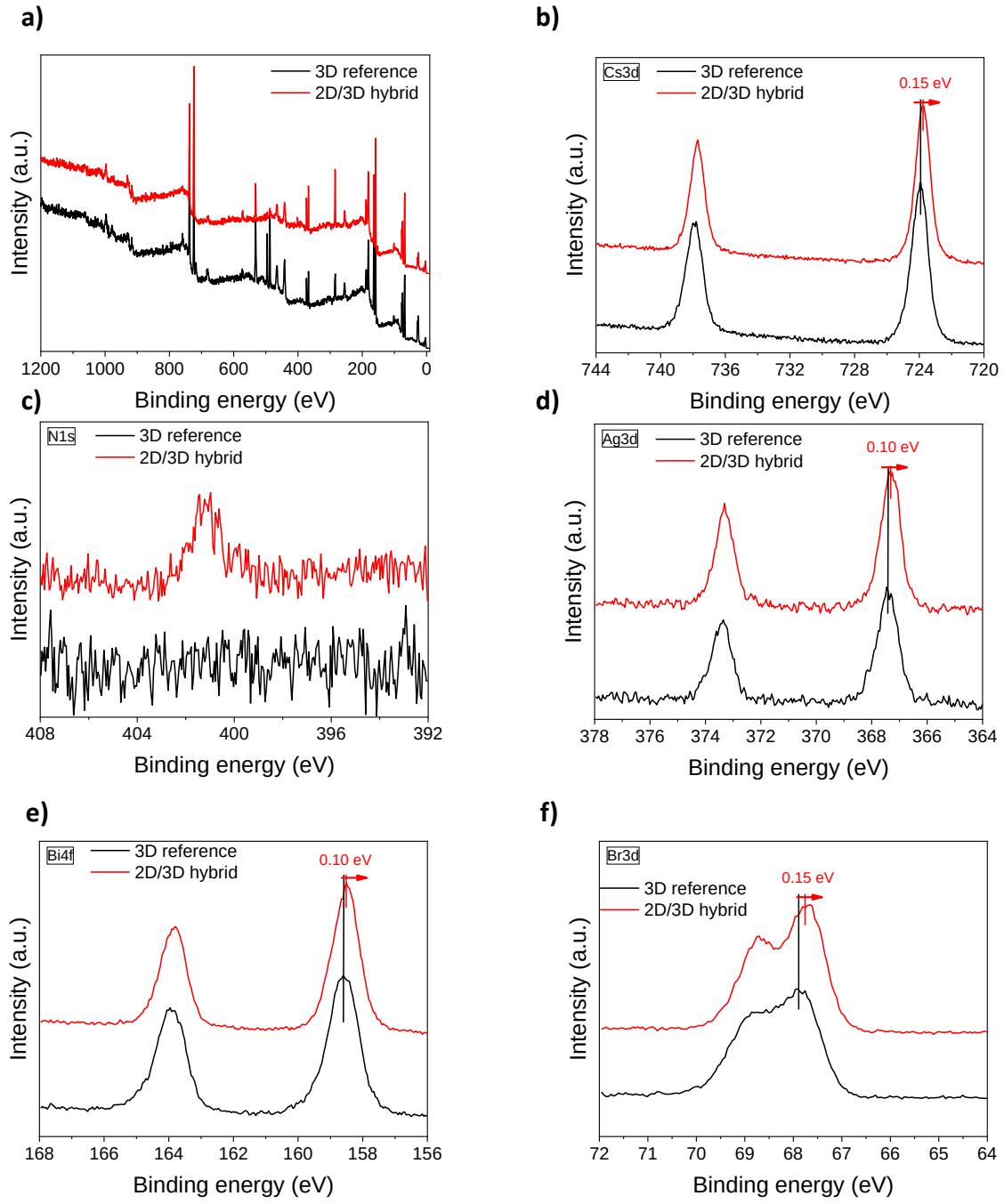

Figure S 5.8: XPS spectra of the 2D/3D hybrid (red lines) and 3D reference (black line) thin films. a) survey b) Cs3d c) N1s d) Ag3d e) Bi4f f) Br3d, all expressing shifts of 100 or 150 meV.

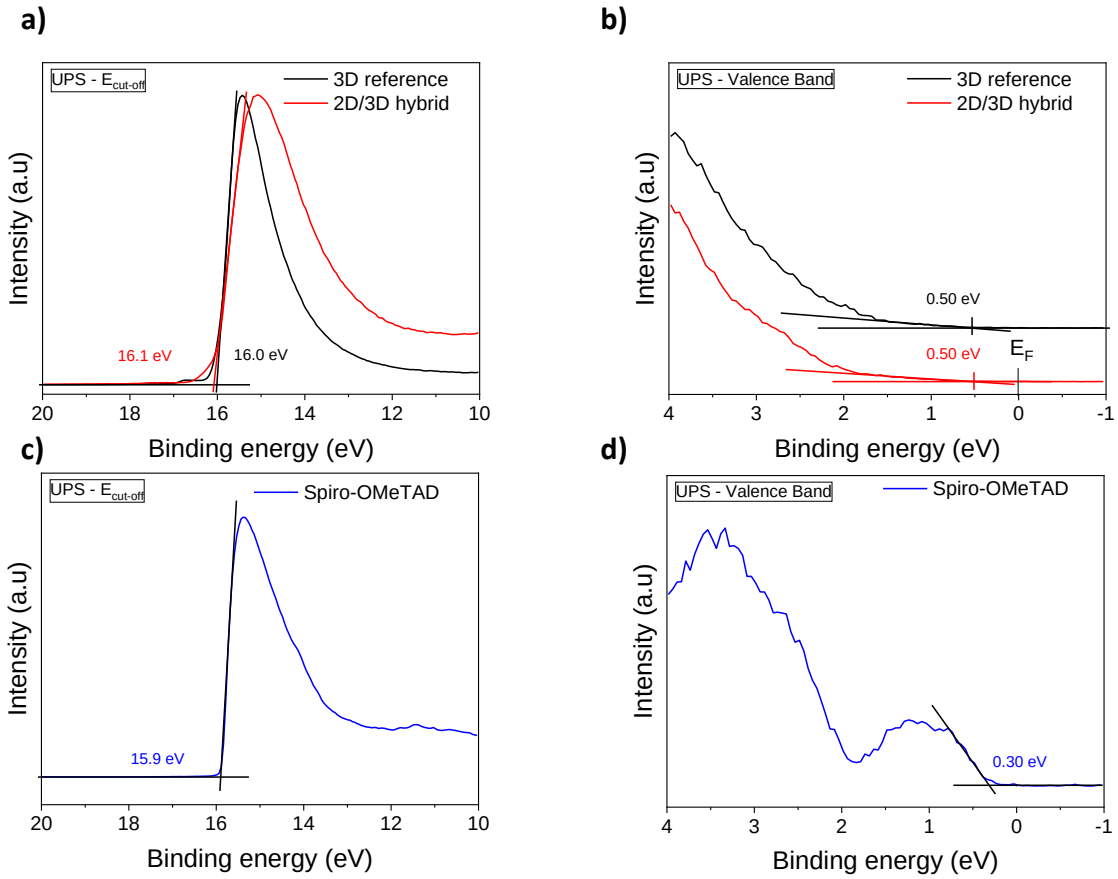

Figure S 5.9: UPS spectra of the 2D/3D hybrid (red lines) and 3D reference (black line) thin films. a) Cut-off measured by applying a 6V bias b) Valence band edge. UPS spectra of doped Spiro-OMeTAD with LiTFSI thin film. c) Cut-off measured by applying a 6V bias d) Valence band edge.

The Cut-off ($E_{cut-off}$) provides the work function (W_f) of the material (the distance between the vacuum level and the Fermi level) through this equation: $W_f = h\nu - E_{cut-off}$, with $h\nu$ the excitation energy, i.e. the He I discharge (21.2 eV).

The doped Spiro-OMeTAD thin film was prepared inside the ultra-high vacuum system and directly transferred to the analytic chamber for UPS analysis. It was prepared by the co-evaporation of LiTSFI and Spiro-OMeTAD. The base pressure of the deposition chamber was $6.0.10^{-8}$ mbar and it increased to $2.5.10^{-7}$ mbar during the deposition process. A current of 625 mA and of 434 mA was applied to the Al_2O_3 crucibles containing, respectively, Spiro-OMeTAD and LiTFSI. Co-evaporation lasts 2 hours.

The VBM of the 3D reference and the 2D/3D hybrid perovskite are measured equal with UPS. We believe that the preparation or the transfer of the samples to Darmstadt might have induced

some surface contaminations. The escape depth of the photoelectrons is higher for XPS than for UPS. Therefore, XPS measurements are less influenced by theses contaminations and are more reliable. However, it should be pointed out that the main conclusion of this section is unchanged if we take the VBM difference obtained with XPS or with UPS. Because of the optical band gap difference a 0.15 eV (XPS) difference or a 0 eV (UPS) difference still induce an additional electron blocking layer at the 2D|3D interface

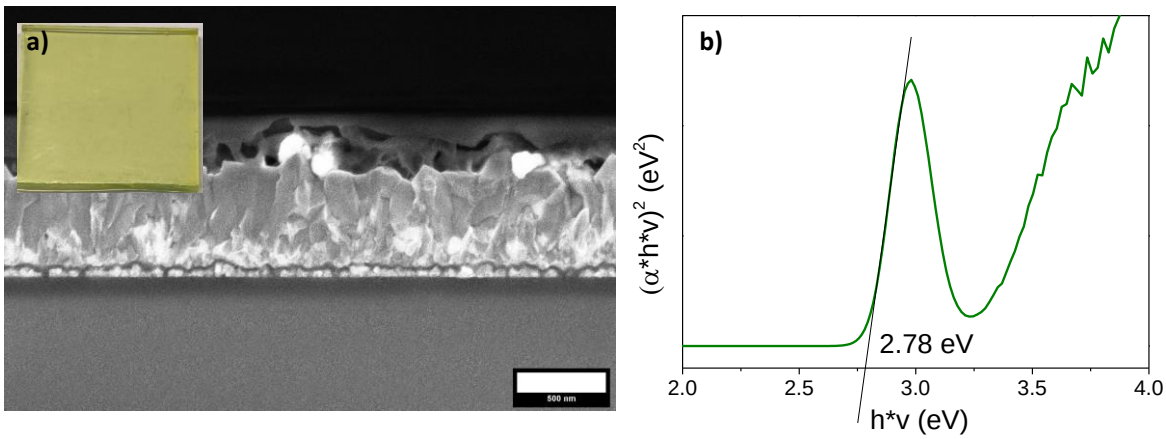

Figure S 5.10: a) SEM cross-sectional image of the measured $(PEA)_4AgBiBr_8$ thin films with a photograph in the inset. b) direct tauc plot of pure $(PEA)_4AgBiBr_8$ thin films on FTO.

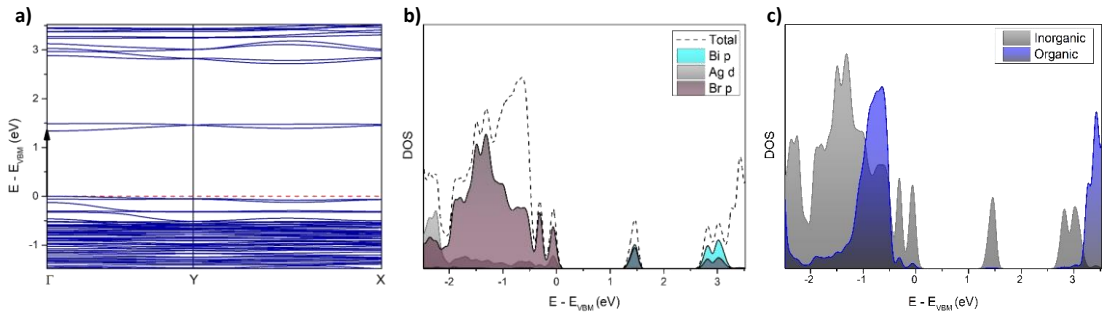

Figure S 5.11: a) shows the PBE-SOC-TS band structure of $(PEA)_4AgBiBr_8$, showcasing the characteristic conduction band splitting of the Bi 6p orbitals (b), already well described for $Cs_2AgBiBr_6$.[6] Furthermore, the band gap nature changes drastically, with the lowest band transition being centered at the Γ point in the Brillouin zone.[32] The absolute band gap is underestimated significantly (~ 1.3 eV), a known deficiency of the DFT-PBE method, whereas other characteristics like the electronic nature are expected to be predicted accurately.[55] The atomic contribution to the frontier orbitals is also identical to other previous published 2D Ag-Bi phases, consisting of mostly halide p and Ag d orbitals in the valence band, with the conduction band predominantly made of Bi p and a contribution of halide p orbitals.

5.7 References

[1] M. Green, E. Dunlop, J. Hohl-Ebinger, M. Yoshita, N. Kopidakis, X. Hao, *Prog. Photovolt. Res. Appl.* **2021**, *29*, 3.

[2] X.-G. Zhao, J.-H. Yang, Y. Fu, D. Yang, Q. Xu, L. Yu, S.-H. Wei, L. Zhang, *J. Am. Chem. Soc.* **2017**, *139*, 2630.

[3] Z. Xiao, W. Meng, J. Wang, Y. Yan, *ChemSusChem* **2016**, *9*, 2628.

[4] M. R. Filip, X. Liu, A. Miglio, G. Hautier, F. Giustino, *J. Phys. Chem. C* **2018**, *122*, 158.

[5] G. Volonakis, M. R. Filip, A. A. Haghighirad, N. Sakai, B. Wenger, H. J. Snaith, F. Giustino, *J. Phys. Chem. Lett.* **2016**, *7*, 1254.

[6] M. R. Filip, S. Hillman, A. A. Haghighirad, H. J. Snaith, F. Giustino, *J. Phys. Chem. Lett.* **2016**, *7*, 2579.

[7] G. Volonakis, A. A. Haghighirad, H. J. Snaith, F. Giustino, *J. Phys. Chem. Lett.* **2017**, *8*, 3917.

[8] E. T. McClure, M. R. Ball, W. Windl, P. M. Woodward, *Chem. Mater.* **2016**, *28*, 1348.

[9] A. H. Slavney, T. Hu, A. M. Lindenberg, H. I. Karunadasa, *J. Am. Chem. Soc.* **2016**, *138*, 2138.

[10] R. L. Z. Hoye, L. Eyre, F. Wei, F. Brivio, A. Sadhanala, S. Sun, W. Li, K. H. L. Zhang, J. L. MacManus-Driscoll, P. D. Bristowe, R. H. Friend, A. K. Cheetham, F. Deschler, *Adv. Mater. Interfaces* **2018**, *5*, 1800464.

[11] E. Greul, M. L. Petrus, A. Binek, P. Docampo, T. Bein, *J. Mater. Chem. A* **2017**, *5*, 19972.

[12] F. Igbari, R. Wang, Z.-K. Wang, X.-J. Ma, Q. Wang, K.-L. Wang, Y. Zhang, L.-S. Liao, Y. Yang, *Nano Lett.* **2019**, *19*, 2066.

[13] M. T. Sirtl, M. Armer, L. K. Reb, R. Hooijer, P. Dörflinger, M. A. Scheel, K. Tvingstedt, P. Rieder, N. Glück, P. Pandit, S. V. Roth, P. Müller-Buschbaum, V. Dyakonov, T. Bein, *ACS Appl. Energy Mater.* **2020**, *3*, 11597.

[14] X. Yang, Y. Chen, P. Liu, H. Xiang, W. Wang, R. Ran, W. Zhou, Z. Shao, *Adv. Funct. Mater.* **2020**, *30*, 2001557.

[15] B. Wang, L. Yang, C. Dall'Agnese, A. K. Jena, S.-I. Sasaki, T. Miyasaka, H. Tamiaki, X.-F. Wang, *Sol. RRL* **2020**, *4*, 2000166.

[16] B. Wang, N. Li, L. Yang, C. Dall'Agnese, A. K. Jena, S.-I. Sasaki, T. Miyasaka, H. Tamiaki, X.-F. Wang, *J. Am. Chem. Soc.* **2021**, *143*, 2207.

[17] M. T. Sirtl, F. Ebadi, B. T. Gorkom, P. Ganswindt, R. A. J. Janssen, T. Bein, W. Tress, *Adv. Optical Mater.* **2021**, *9*, 2100202.

[18] C. Wu, Q. Zhang, Y. Liu, W. Luo, X. Guo, Z. Huang, H. Ting, W. Sun, X. Zhong, S. Wei, S. Wang, Z. Chen, L. Xiao, *Adv. Sci. (Weinh.)* **2018**, *5*, 1700759.

[19] W. Gao, C. Ran, J. Xi, B. Jiao, W. Zhang, M. Wu, X. Hou, Z. Wu, *Chemphyschem* **2018**, *19*, 1696.

[20] G. Longo, S. Mahesh, L. R. V. Buizza, A. D. Wright, A. J. Ramadan, M. Abdi-Jalebi, P. K. Nayak, L. M. Herz, H. J. Snaith, *ACS Energy Lett.* **2020**, *5*, 2200.

[21] A. D. Wright, L. R. V. Buizza, K. J. Savill, G. Longo, H. J. Snaith, M. B. Johnston, L. M. Herz, *J. Phys. Chem. Lett.* **2021**, *12*, 3352.

[22] D. Bartesaghi, A. H. Slavney, M. C. Gélvez-Rueda, B. A. Connor, F. C. Grozema, H. I. Karunadasa, T. J. Savenije, *J. Phys. Chem. C* **2018**, *122*, 4809.

[23] R. Kentsch, M. Scholz, J. Horn, D. Schlettwein, K. Oum, T. Lenzer, *J. Phys. Chem. C* **2018**, *122*, 25940.

[24] S. J. Zelewski, J. M. Urban, A. Surrente, D. K. Maude, A. Kuc, L. Schade, R. D. Johnson, M. Dollmann, P. K. Nayak, H. J. Snaith, P. Radaelli, R. Kudrawiec, R. J. Nicholas, P. Plochocka, M. Baranowski, *J. Mater. Chem. C* **2019**, *7*, 8350.

[25] P. Vishnoi, R. Seshadri, A. K. Cheetham, *J. Phys. Chem. C* **2021**, *125*, 11756.

[26] N. Pai, J. Lu, M. Wang, A. S. R. Chesman, A. Seeber, P. V. Cherepanov, D. C. Senevirathna, T. R. Gengenbach, N. V. Medhekar, P. C. Andrews, U. Bach, A. N. Simonov, *J. Mater. Chem. A* **2020**, *8*, 2008.

[27] Z. Li, S. R. Kavanagh, M. Napari, R. G. Palgrave, M. Abdi-Jalebi, Z. Andaji-Garmaroudi, D. W. Davies, M. Laitinen, J. Julin, M. A. Isaacs, R. H. Friend, D. O. Scanlon, A. Walsh, R. L. Z. Hoye, *J. Mater. Chem. A* **2020**, *8*, 21780.

[28] F. Ji, J. Klarbring, F. Wang, W. Ning, L. Wang, C. Yin, J. S. M. Figueroa, C. K. Christensen, M. Etter, T. Ederth, L. Sun, S. I. Simak, I. A. Abrikosov, F. Gao, *Angew. Chem. Int. Ed.* **2020**, *132*, 15303.

[29] E. M. Hutter, M. C. Gélvez-Rueda, D. Bartesaghi, F. C. Grozema, T. J. Savenije, *ACS Omega* **2018**, *3*, 11655.

[30] A. Karmakar, M. S. Dodd, S. Agnihotri, E. Ravera, V. K. Michaelis, *Chem. Mater.* **2018**, *30*, 8280.

[31] Q. Li, Y. Wang, W. Pan, W. Yang, B. Zou, J. Tang, Z. Quan, *Angew. Chem. Int. Ed.* **2017**, *56*, 15969.

[32] B. A. Connor, L. Leppert, M. D. Smith, J. B. Neaton, H. I. Karunadasa, *J. Am. Chem. Soc.* **2018**, *140*, 5235.

[33] M. K. Jana, S. M. Janke, D. J. Dirkes, S. Dovletgeldi, C. Liu, X. Qin, K. Gundogdu, W. You, V. Blum, D. B. Mitzi, *J. Am. Chem. Soc.* **2019**, *141*, 7955.

[34] L.-Y. Bi, Y.-Q. Hu, M.-Q. Li, T.-L. Hu, H.-L. Zhang, X.-T. Yin, W.-X. Que, M. S. Lassoued, Y.-Z. Zheng, *J. Mater. Chem. A* **2019**, *7*, 19662.

[35] Y. Yao, B. Kou, Y. Peng, Z. Wu, L. Li, S. Wang, X. Zhang, X. Liu, J. Luo, *Chem. Commun.* **2020**, *56*, 3206.

[36] Y. Hu, J. Schlipf, M. Wussler, M. L. Petrus, W. Jaegermann, T. Bein, P. Müller-Buschbaum, P. Docampo, *ACS Nano* **2016**, *10*, 5999.

[37] J. Schlipf, Y. Hu, S. Pratap, L. Bießmann, N. Hohn, L. Porcar, T. Bein, P. Docampo, P. Müller-Buschbaum, *ACS Appl. Energy Mater.* **2019**, *2*, 1011.

[38] Y. Liu, S. Akin, L. Pan, R. Uchida, N. Arora, J. V. Milić, A. Hinderhofer, F. Schreiber, A. R. Uhl, S. M. Zakeeruddin, A. Hagfeldt, M. I. Dar, M. Grätzel, *Sci. Adv.* **2019**, *5*, eaaw2543.

[39] D. Liang, C. Dong, L. Cai, Z. Su, J. Zang, C. Wang, X. Wang, Y. Zou, Y. Li, L. Chen, L. Zhang, Z. Hong, A. El-Shaer, Z.-K. Wang, X. Gao, B. Sun, *Small (Weinheim an der Bergstrasse, Germany)* **2021**.

[40] R. Yang, R. Li, Y. Cao, Y. Wei, Y. Miao, W. L. Tan, X. Jiao, H. Chen, L. Zhang, Q. Chen, H. Zhang, W. Zou, Y. Wang, M. Yang, C. Yi, N. Wang, F. Gao, C. R. McNeill, T. Qin, J. Wang, W. Huang, *Adv. Mater.* **2018**, *30*, e1804771.

[41] T. Liu, J. Guo, Di Lu, Z. Xu, Q. Fu, N. Zheng, Z. Xie, X. Wan, X. Zhang, Y. Liu, Y. Chen, *ACS Nano* **2021**, *15*, 7811.

[42] Y. Hu, L. M. Spies, D. Alonso-Álvarez, P. Mocherla, H. Jones, J. Hanisch, T. Bein, P. R. F. Barnes, P. Docampo, *J. Mater. Chem. A* **2018**, *6*, 22215.

[43] W. Yuan, G. Niu, Y. Xian, H. Wu, H. Wang, H. Yin, P. Liu, W. Li, J. Fan, *Adv. Funct. Mater.* **2019**, *29*, 1900234.

[44] X. Wang, K. Li, H. Xu, N. Ali, Y. Wang, Q. Shen, H. Wu, *Chem. Commun.* **2020**, *56*, 7917.

[45] F. Schmitz, J. Horn, N. Dengo, A. E. Sedykh, J. Becker, E. Maiworm, P. Bélteky, Á. Kukovecz, S. Gross, F. Lamberti, K. Müller-Buschbaum, D. Schlettwein, D. Meggiolaro, M. Righetto, T. Gatti, *Chem. Mater.* **2021**, *33*, 4688.

[46] E. R. Jette, F. Foote, *The Journal of Chemical Physics* **1935**, *3*, 605.

[47] K. Tvingstedt, O. Malinkiewicz, A. Baumann, C. Deibel, H. J. Snaith, V. Dyakonov, H. J. Bolink, *Sci. Rep.* **2014**, *4*, 6071.

[48] V. D'Innocenzo, G. Grancini, M. J. P. Alcocer, A. R. S. Kandada, S. D. Stranks, M. M. Lee, G. Lanzani, H. J. Snaith, A. Petrozza, *Nat. Commun.* **2014**, *5*, 3586.

[49] V. Sarritzu, N. Sestu, D. Marongiu, X. Chang, S. Masi, A. Rizzo, S. Colella, F. Quochi, M. Saba, A. Mura, G. Bongiovanni, *Scientific reports* **2017**, *7*, 44629.

[50] E. J. Juarez-Perez, M. Wuβler, F. Fabregat-Santiago, K. Lakus-Wollny, E. Mankel, T. Mayer, W. Jaegermann, I. Mora-Sero, *J. Phys. Chem. Lett.* **2014**, *5*, 680.

[51] Y. Zhang, M. Liu, G. E. Eperon, T. C. Leijtens, D. McMeekin, M. Saliba, W. Zhang, M. de Bastiani, A. Petrozza, L. M. Herz, M. B. Johnston, H. Lin, H. J. Snaith, *Mater. Horiz.* **2015**, *2*, 315.

[52] W. Tress, M. Yavari, K. Domanski, P. Yadav, B. Niesen, J. P. Correa Baena, A. Hagfeldt, M. Graetzel, *Energy Environ. Sci.* **2018**, *11*, 151.

[53] P. Caprioglio, C. M. Wolff, O. J. Sandberg, A. Armin, B. Rech, S. Albrecht, D. Neher, M. Stolterfoht, *Adv. Energy Mater.* **2020**, *10*, 2000502.

[54] J. Jiménez-López, W. Cambarau, L. Cabau, E. Palomares, *Sci. Rep.* **2017**, *7*, 6101.

[55] P. J. Hasnip, K. Refson, M. I. J. Probert, J. R. Yates, S. J. Clark, C. J. Pickard, *Philos. Trans. A Math. Phys. Eng. Sci.* **2014**, *372*, 1.

[56] N. Giesbrecht, A. Weis, T. Bein, *J. Phys. Energy* **2020**, *2*, 24007.

[57] M. L. Petrus, K. Schutt, M. T. Sirtl, E. M. Hutter, A. C. Closs, J. M. Ball, J. C. Bijleveld, A. Petrozza, T. Bein, T. J. Dingemans, T. J. Savenije, H. Snaith, P. Docampo, *Adv. Energy Mater.* **2018**, *8*, 1801605.

[58] P. Giannozzi, S. Baroni, N. Bonini, M. Calandra, R. Car, C. Cavazzoni, D. Ceresoli, G. L. Chiarotti, M. Cococcioni, I. Dabo, A. Dal Corso, S. de Gironcoli, S. Fabris, G. Fratesi, R. Gebauer, U. Gerstmann, C. Gougoussis, A. Kokalj, M. Lazzeri, L. Martin-Samos, N. Marzari, F. Mauri, R. Mazzarello, S. Paolini, A. Pasquarello, L. Paulatto, C. Sbraccia, S. Scandolo, G. Sclauzero, A. P. Seitsonen, A. Smogunov, P. Umari, R. M. Wentzcovitch, *J. Phys. Condens. Matter.* **2009**, *21*, 395502.

[59] D. R. Hamann, *Phys. Rev. B* **2013**, *88*.

[60] Perdew, Burke, Ernzerhof, *Phys. Rev. Lett.* **1996**, *77*, 3865.

[61] A. Tkatchenko, M. Scheffler, *Phys. Rev. Lett.* **2009**, *102*, 73005.

[62] R. L. Z. Hoye, P. Schulz, L. T. Schelhas, A. M. Holder, K. H. Stone, J. D. Perkins, D. Vigil-Fowler, S. Siol, D. O. Scanlon, A. Zakutayev, A. Walsh, I. C. Smith, B. C. Melot,

R. C. Kurchin, Y. Wang, J. Shi, F. C. Marques, J. J. Berry, W. Tumas, S. Lany, V. Stevanović, M. F. Toney, T. Buonassisi, *Chem. Mater.* **2017**, *29*, 1964.

[63] T. Hellmann, C. Das, T. Abzieher, J. A. Schwenzer, M. Wussler, R. Dachauer, U. W. Paetzold, W. Jaegermann, T. Mayer, *Adv. Energy Mater.* **2020**, *10*, 2002129.

6 Hydrazone-based Hole Transporting Material Prepared *via* Condensation Chemistry as Alternative for Cross-Coupling Chemistry for Perovskite Solar Cells.

This chapter is based on the following publication:

Michiel L. Petrus,‡ Maximilian T. Sirtl,‡ Anna C. Closs, Thomas Bein, Pablo Docampo, *Mol. Syst. Des. Eng.*, 2018, **3**, 734-740.

‡ These Authors contributed equally to this work

All figures and content were reproduced with permission from the Royal Society of Chemistry

Please note that reference 11 was changed to reference 1 as these references were identical. Hence, the original manuscript consists of 41 references instead of only 40 as it is the case in this chapter

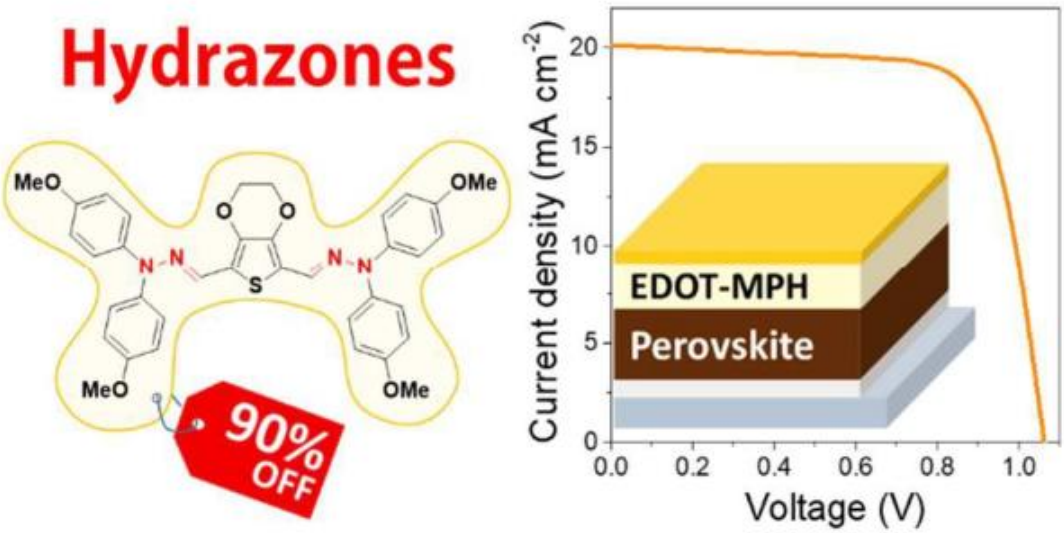

6.1 Abstract

Perovskite solar cells have shown an exceptionally fast increase in performance. So far, most high performing devices comprise expensive hole transport material (HTM) which are synthesized using tedious synthetic procedures, resulting in a high cost and thereby limit the potential use in large-scale applications. In a quest to find low-cost chemistry to link the building blocks, in this work we explore hydrazone-based small molecules. These materials can be synthesized in a simple condensation reaction, with water being the only side product leading to a low material cost of less than 10 $/g. When used as hole transporting layers in perovskite solar cells, highly reproducible performance was obtained, similar to state-of-the-art materials, with the main difference being a small open-circuit voltage loss due to increased interfacial recombination. Thus, we show that hydrazone-based materials have the potential to compete in performance with materials obtained *via* cross-coupling reactions at a fraction of their cost.

6.2 Design, System, Application

Conjugated hole transporting materials are generally designed by linking building blocks with interesting opto-electronic properties together by using aryl-aryl coupling chemistry. However, these coupling reactions have several disadvantages, such as the inherent formation of side-products, the use of (transition) metal catalysts and their use require stringent reaction conditions, leading to a high product cost. Condensation chemistry offers an excellent alternative to these complicated coupling chemistries, as water is the only side-product and metal catalysts are not required, simplifying product workup and therefore drastically reducing the cost of these materials. In this work we introduce a hydrazone-based small molecule (EDOT-MPH) as hole transporting material for perovskite solar cells. EDOT-MPH can be synthesized using a simple condensation reaction resulting in an estimated material cost of less than $10 per gram. The charge transporting properties of EDOT-MPH are at least as good as those of state-of-the-art Spiro-OMeTAD, while the energy levels match with the perovskite. When employed as charge transporting layer in photovoltaic devices, very reproducible results are obtained, which approach the power conversion efficiencies of state-of-the-art HTMs in a direct comparison. We demonstrate that hydrazone-based HTM have the potential to compete with state-of-the-art materials in performance at only a fraction of the cost, making this class of materials highly interesting for large-scale production.

6.3 Introduction

Perovskite based solar cells are attracting great interest, motivated by the potential to prepare low-cost photovoltaics with excellent performance and the possibility to be flexible and lightweight. However, high quality hole transporting materials (HTMs) leading to record efficiencies are generally synthesized in palladium cross-coupling reactions that require stringent reactions.[1–6] These chemistries suffer from side reactions and traces of the metal catalyst will stay behind, extensive product purification is required. As a result of the tedious synthesis and workup, not only the cost of these materials is generally high, but it also limits the scalability and impacts the environment as was pointed out by several researchers.[1,7–10]

Recent research mainly focussed on reducing the cost of HTMs by decreasing the amount of synthetic steps.[1,11,12] In addition to that, we also focused on drastically reducing the synthetic complexity, cost of materials and the environmental impact of organic HTMs, by moving away from transition metal based cross-coupling reactions.[8,9,13] Instead, condensation chemistry has been explored, offering an interesting alternative as we showed in our previous work, where we introduced azomethine-based (-CH=N-) HTMs, which were synthesized in a Schiff-base condensation reaction and purified in a simple washing step while the synthesis itself was performed without chlorinated solvents.[8,14,15] The simple chemistry and product workup resulted in an estimated material costs of $10 per gram.[8] More recent work showed that the cost can be even further reduced to $4 per gram by varying the core of the small-molecule HTMs, while these materials have good moisture barrier properties.[9] Daskeviciene et al. explored condensation chemistry by synthesizing an enamine-based HTM termed “V950”, which resulted in impressive power conversion efficiencies of 17.8%.[16] Hydrazone-based (-CH=N-NRR’) HTMs can also be synthesized in a simple and clean condensation reaction, and have shown good performance as electron donor in organic photovoltaics and have potential as hole transporting materials in dye sensitized solar cells with high charge carrier mobilities and tunable thermal properties.[17–21] However, to the best of our knowledge, these materials have not been examined in perovskite solar cells. In this work we explore the potential of a hydrazone-based HTM, synthesized using a simple and clean low-cost procedure, in perovskite solar cells and compare the optoelectronic properties to other HTMs prepared *via* condensation chemistry. We study the charge transporting properties and the effect of conductivity-enhancing additives. Our results show that the hydrazone-based HTM has good charge transporting properties, and shows photovoltaic performance close to state-of-the-art materials when used

in planar heterojunction devices. Devices based on hydrazone HTMs have improved reproducibility, demonstrating the potential of simple condensation chemistry for organic electronic applications.

6.4 Results and Discussion

6.4.1 Synthesis

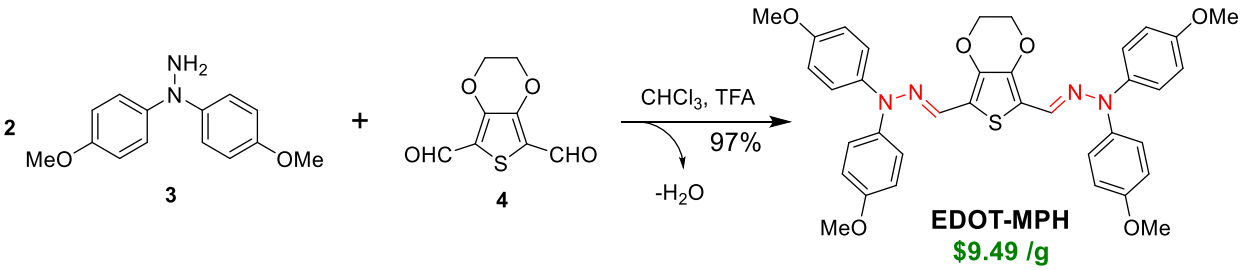

Scheme 6.1. Reaction scheme and molecular structure of EDOT-MPH. The hydrazone bond is highlighted and the estimated material cost is shown in green.

The hydrazine precursor 3 was synthesized following published procedures (Scheme 6.1 and Scheme S 6.1),[22–24] and was directly used in the condensation reaction with dialdehyde (4), resulting in the hydrazone product (EDOT-MPH) which was obtained as a bright orange, crystalline powder (Figure S 6.1 and Figure S 6.2) in a near quantitative yield of 97%.

The material cost of the HTM was estimated following a procedure established by Osedach et al. and introduced to the field of HTMs for perovskites by our group.[7,8] The estimated materials cost on a lab scale is $9.49 per gram for EDOT-MPH (details in the supporting information). In comparison, the material cost of Spiro-OMeTAD is estimated to be approximately 10 times higher.[8] The low cost of EDOT-MPH is ascribed to the simple chemistry that doesn't require expensive metal catalysts and with water as the only side-product, which simplifies the purification of the product. We found that especially purification *via* column chromatography is very costly. Additionally, as relatively few chemicals are required, this HTM can be considered more environmentally friendly. However, the major environmental concern of perovskite solar cells will be the toxicity of lead, for which several solutions are currently being explored.[13,25,26] For a better understanding of the environmental impact of organic materials, Sheldon introduced the term E factor, which is defined as kg waste per kg product.[27] For EDOT-MPH we calculated an E value of 400, while Spiro-OMeTAD has an E factor of 3600,

clearly showing the difference in chemical waste from the synthesis between these materials on a lab scale.

6.4.2 Thermal Properties

As solar cells can reach temperatures up to 80 °C under operational conditions, it is important that phase transitions of the materials are well above this temperature to ensure a good stability. Therefore, the thermal properties were studied by thermogravimetric analysis (TGA) and differential scanning calorimetry (DSC).

The degradation temperature of EDOT-MPH was determined to be 255 ˚C (Table 6.1 and Figure S 6.3), although this is relatively low for HTMs used in perovskite solar cells, it is well above the standard operating temperature of the solar cells. No glass transition (T_g) was observed by DSC measurements in the temperature range from 0 to 200 ˚C. While hot-stage microscope measurements revealed a melting transition of the material at 244 ˚C, which is well above the operation temperature of a solar cell. Apart of being a crucial requirement for the materials to be used as an HTM, high melting temperatures are beneficial as they indicate a close molecular packing of the molecule, which has shown to lead to good photovoltaic performance when the materials are used as HTM in perovskite solar cells.[9]

6.4.3 Optoelectronic Properties

A good energy alignment between the highest occupied molecular orbital (HOMO) of the HTM and the valance band of the perovskite is important in order to obtain efficient hole extraction. We determined the HOMO energy from the oxidation onset obtained from cyclic voltammetry (CV) measurements (Figure 6.1a). The obtained value of -5.08 eV is slightly higher than Spiro-OMeTAD (Figure 6.1b and Table 6.1). The lowest unoccupied molecular orbital (LUMO) energy level was determined by adding the bandgap to the HOMO energy level and resulted in a value of -2.7 eV. The high LUMO energy level is expected to result in an efficient electron blocking layer.

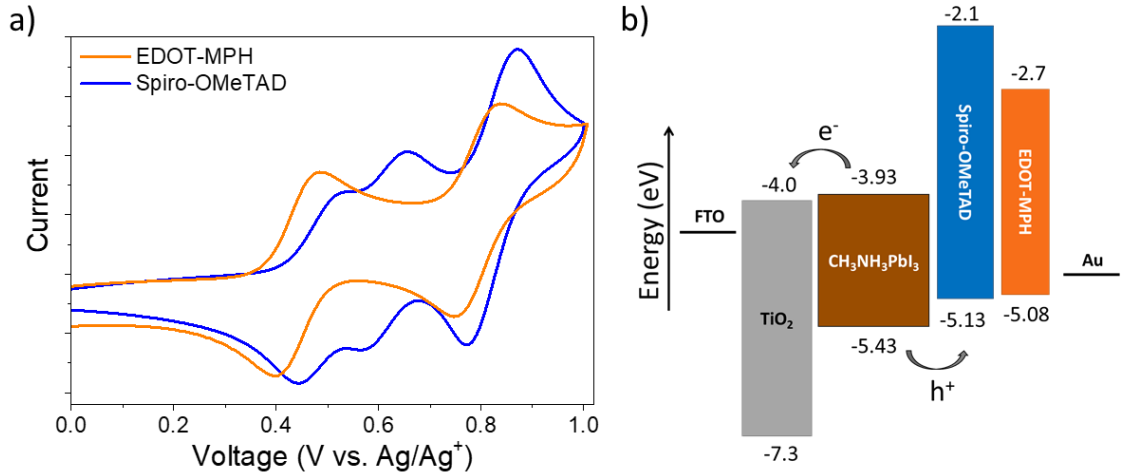

Figure 6.1: Electronic Properties. a), Cyclic voltammogram of EDOT-MPH measured in a CH_2Cl_2 solution containing 1 M $tBuNPF_4$ as electrolyte. B), Energy level diagram showing the energy levels of EDOT-MPH and their alignment with the perovskite.

To gain insights into the geometric and electronic structure of EDOT-MPH, density functional theory (DFT) geometry optimization (B3LYP/6-31G(d,p) level) were performed in vacuum and in dichloromethane (DCM) as the solvent, by means of the conductor-like polarizable continuum model (CPCM) as implemented in the Gaussian 09 program package (Figure 6.2 and Figure S 6.4). Following the procedure published by Chi et al.,[28] the highest occupied molecular orbital (HOMO) energy level was calculated to be -5.09 eV, which is in excellent agreement with the experimentally obtained value. Figure 6.2 b) shows that the HOMO is distributed over the core of the HTM and *via* the hydrazone bond to one of the phenyl rings on each side. The other phenyl ring is twisted out of the plane of the molecule, which explains why the HOMO is not localized there. The lowest unoccupied molecular orbital (LUMO) is mostly distributed on the core and the hydrazone-bond of the molecule. Additionally, the electron density mapping of the molecules was calculated as shown in Figure 6.2 c). The more electronegative part is indicated by the red color while the more positive parts are blue. The results show a directional dipole within the molecule, that could assist in the formation of a close molecular packing, resulting in good intermolecular charge transport, as was pointed out in our recent work.[9]

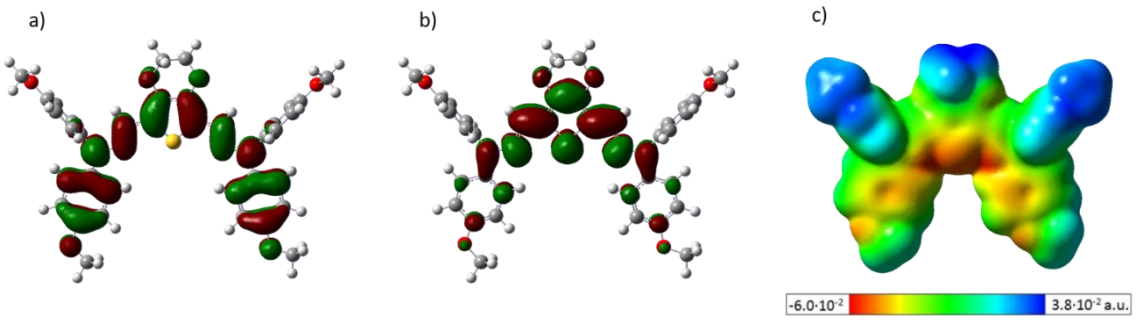

Figure 6.2: The optimized molecular geometry and energy level distribution of EDOT-MPH obtained from DFT calculations in DCM. Distribution of the electronic energy levels of a) the HOMO and b) the LUMO orbitals. c) Electrostatic surface potential map, revealing the strong dipole in the core.

Table 6.1: Optoelectronic and thermal properties of EDOT-MPH.

	λ_{max} (nm)	λ_{onset} (nm)	E_g (eV)	$E_{HOMO, DFT}$ (eV)[a]	$E_{HOMO, CV}$ (eV)[b]	E_{LUMO} (eV)[c]	T_m (°C)	T_d (°C)
EDOT-MPH	458	520	2.38	-5.09	-5.08	-2.70	244	259

[a] DFT calculation in DCM corrected following the procedure published by Chi *et al.*[21] [b] Experimental value obtained from cyclic voltammetry. [c] Estimated by adding the optical bandgap to the HOMO energy level. T_m = melting temperature, T_d = degradation temperature (5% wt. loss)

6.4.4 Conductivity and Mobility

Lithium bis(trifluoromethanesulfonyl)imide (LiTFSI) is a commonly used additive to assists in the oxidation of the HTM in order to increase to conductivity.[29] We studied the effect of adding LiTFSI to EDOT-MPH by recording its light absorption spectrum as a function of the additive concentrations (Figure 6.3). Upon addition of LiTFSI to EDOT-MPH, we observe the formation of one or more new species with absorption maxima at 660 and 740 nm. Upon increasing the LiTFSI concentration, the intensity of the new species increases, while the absorption of the pristine material bleaches. This indicates that EDOT-MPH is oxidized and forms an oxidized or double oxidized species which shows a red shifted absorption profile compared to the pristine material.

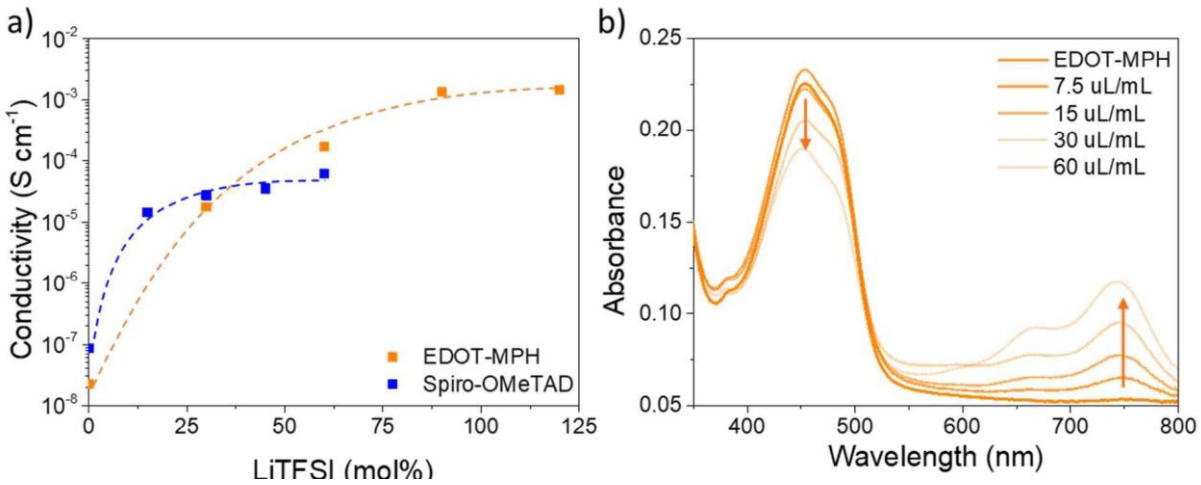

Figure 6.3: Charge transporting properties of EDOT-MPH. a), The measured electrical conductivity as a function of the amount of LiTFSI added to the solution used for spincoating the films. The dotted line is added as a guide to the eye. b), UV-Vis absorption spectra, of EDOT-MPH films as a function of added LiTFSI. The UV-vis spectra show the formation of the oxidized species in the range of 600 – 800 nm, while the peak of the pristine material bleaches.

In order to characterize the charge transporting properties, hole mobility and conductivity measurements were performed. "Hole-only" devices with a commonly used architecture were prepared to measure the hole mobility (indium-doped tin oxide (ITO)/MoO_x/EDOT-MPH/MoO_x/Au).[30,31] *J-V* curves were recorded in the dark, with the current assumed to be space-charge limited at higher voltages (Figure S 6.5). From this, the charge carrier mobility can be estimated using the Mott-Gurney equation. EDOT-MPH shows a hole mobility of 2.8 x 10^{-5} cm^2 V^{-1} s^{-1}, which is comparable to the hole mobility measured for pristine Spiro-OMeTAD,[32] and other azomethine- and hydrazone-based HTMs.[9,21,33,34]

Besides the mobility, the conductivity is an important parameter for charge transport. We measured the conductivity using interdigitating electrodes and studied the effect of oxidizing the HTM with LiTFSI. The initial conductivity is low (2 x 10^{-8} S cm^{-1}), but comparable to Spiro-OMeTAD.[29] Upon addition of LiTFSI, a clear increase in conductivity is observed which seems to plateau at around 100 mol% LiTFSI and a conductivity of 2 x 10^{-3} S cm^{-1}. At a LiTFSI concentration of 40 mol% (which is later used for preparing the hole transporting layer in perovskite solar cells) the conductivity of EDOT-MPH is comparable to that of Spiro-OMeTAD containing 30 mol%.[29] Based on these results, a good charge transport to the electrode is expected when EDOT-MPH is used as HTM in a perovskite solar cell, which will minimize the series resistance.

6.4.5 Photovoltaic Properties

The photovoltaic properties of a perovskite device containing EDOT-MPH as HTM were studied by preparing planar perovskite solar cells (Figure 6.4, Figure S 6.6 and Figure S 6.7) and were tested under ambient conditions. As perovskite absorber, the standard methylammonium lead iodide ($MAPbI_3$) and the more recently introduced high performance perovskite $(FA_{0.79}MA_{0.16}Cs_{0.05})Pb(I_{0.83}Br_{0.17})_3$ (FAMACs) were used.[35–37] The deposition of EDOT-MPH was optimized for spincoating from a chloroform/chlorobenzene (1:4 ratio) solution at 40 °C, resulting in a film thickness of approximately 100 nm (Figure 6.4b). Similarly to previously studied small molecules accessed *via* condensation chemistry, also this material shows to have good film forming properties, which allows the preparation of relatively thin homogeneous films.[9] In contrast, small molecules synthesized *via* cross-coupling reactions often show their best performance with relatively thick layers (200 – 300 nm),[6,38] which requires more material and thereby further increases the cost. The high quality of our HTM layer furthermore results in a relatively narrow distribution of the photovoltaic performance, especially when compared to Spiro-OMeTAD (Table 6.2). Additionally, high quality films show an improved stability and due to the lack of pinholes also function as a moisture barrier.[9]

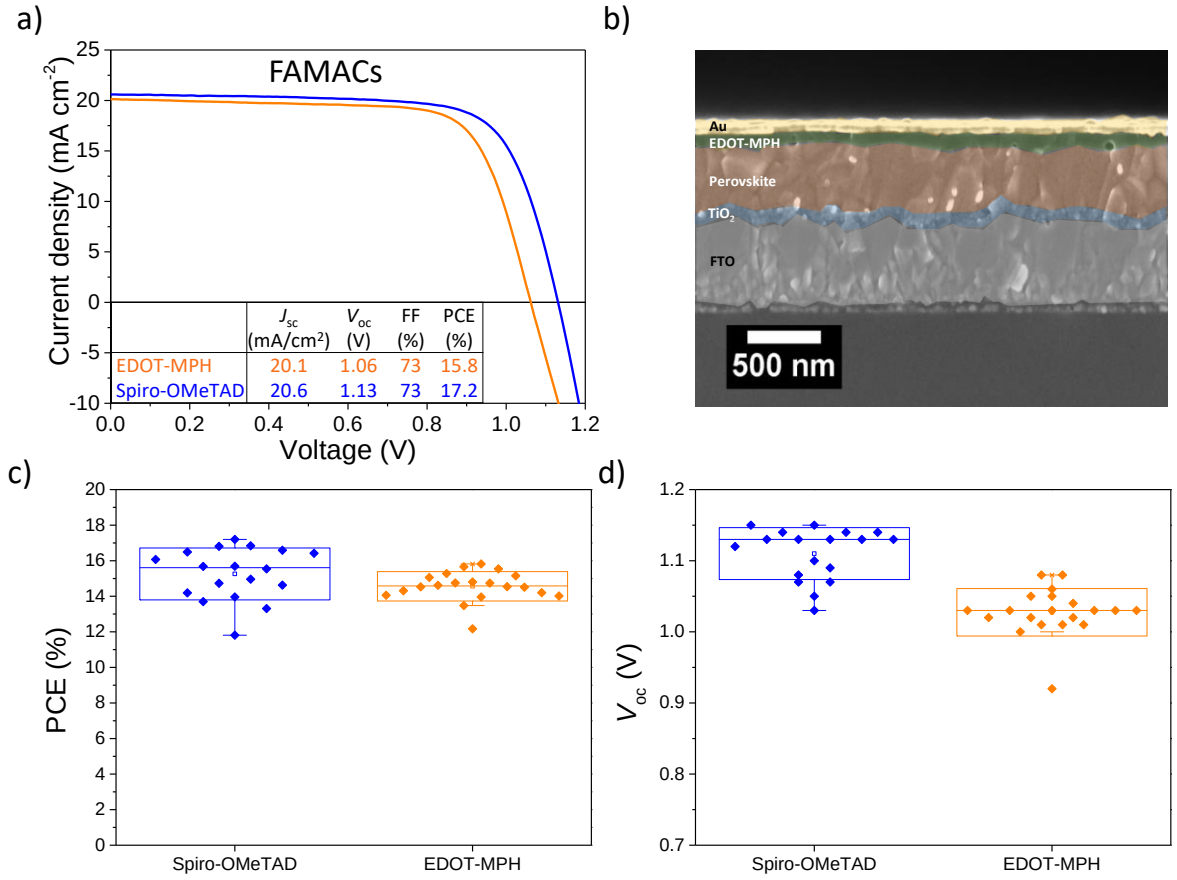

Figure 6.4. Photovoltaic peroformance and reproducibility of FAMACs perovskite solar cells comprising EDOT-MPH or Spiro-OMeTAD as HTM. a) *J/V* curves collected under AM 1.5G simulated sunlight of the champion devices comprising EDOT-MPH and Spiro-OMeTAD in the following device architecture: FTO/compact TiO_2/FAMACs/HTM/Au. b) SEM cross-section c), d), Box-plot of 38 individual devices prepared showing the comparison of the power conversion efficiency and open-circuit voltage of devices comprising either EDOT-MPH or Spiro-OMeTAD as HTM.

Devices comprising FAMACs as perovskite absorber show a better performance than those with $MAPbI_3$. However, the same trends in photovoltaic performance were observed when EDOT-MPH was used instead of Spiro-OMeTAD (Figure 6.4 and Table S 6.3). With EDOT-MPH as hole transporter, higher FFs are obtained while the J_{SC} is slightly sacrificed. The V_{OC} however is significantly lower than devices comprising Spiro-OMeTAD. This loss might partly result from the higher HOMO energy level of EDOT-MPH but could also hint to a higher interfacial charge recombination and/or slow charge carrier injection.[39] Despite the lower V_{OC}, the average PCE of the devices comprising EDOT-MPH is comparable to those with Spiro-OMeTAD, and even shows to be slightly higher for EDOT-MPH when combined with $MAPbI_3$.

Also the stabalized power output shows to be very comparable (Figure S 6.8). The high average PCE is mainly attributed to the narrow distribution in performance when EDOT-MPH is used.

Table 6.2. Overview of the average device performance prepared using different perovskites

Perovskite	**HTM**	J_{SC} **(mA/cm^2)**	V_{OC} **(V)**	**FF (%)**	**PCE (%)**
$MAPbI_3$	EDOT-MPH	19.6 ± 0.4	1.01 ± 0.02	68 ± 6	13.5 ± 1.4
$MAPbI_3$	Spiro-OMeTAD	19.0 ± 0.8	1.05 ± 0.04	64 ± 7	13.2 ± 1.8
FAMACs	EDOT-MPH	19.4 ± 0.3	1.03 ± 0.03	73 ± 2	14.6 ± 0.8
FAMACs	Spiro-OMeTAD	20.8 ± 0.5	1.11 ± 0.04	66 ± 4	15.3 ± 1.5

6.4.6 Time Resolved Photoluminescence

Time resolved photoluminescence (TRPL) has been used to study the lifetime of the charge carriers and their recombination dynamics in a perovskite/HTM bilayer. The decays were acquired timecorrelated single-photon counting (TCSPC) technique.

Steady state photoluminescence spectra of the $MAPbI_3$/HTM films show a single emission peak with a maximum around 770 nm, which is significant lower compared to a pristine $MAPbI_3$ film. Especially EDOT-MPH shows a strong reduction of the PL intensity, which indicates a fast hole injection from the perovskite to the HTM and/or significant interfacial recombination. PL decay measurements of bilayers consisting of $MAPbI_3$/EDOT-MPH and $MAPbI_3$/Spiro-OMeTAD were obtained at the same acquisition time (Figure 6.5 and Figure S 6.9). The initial rise in the PL intensity is slightly lower for EDOT-MPH, which has been linked to a fast hole injection.[40] However, EDOT-MPH shows a significant faster decay, implying a higher recombination of the charge carriers, which may account for the lower open-circuit voltage and hence lower device efficiency. These results are very comparable to our recently studied azomethine-based HTM, EDOT-OMeTPA, where also a fast charge injection in combination with a high interfacial recombination was observed.[39]

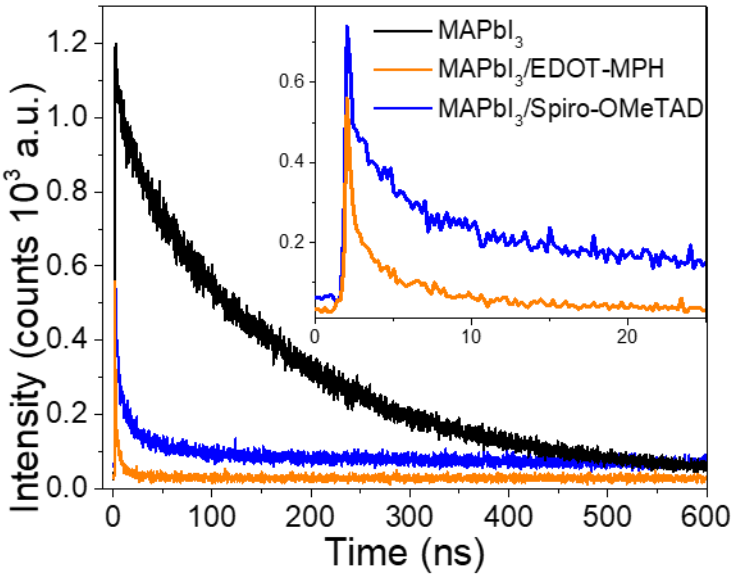

Figure 6.5. Time resolved photoluminescence decay of $MAPbI_3$ films and bilayers consisting of $MAPbI_3$/HTM, obtained for the same acquisition time.

By tuning the molecular structure, the HOMO energy level can easily be fine-tuned, which is expected to result in a higher V_{OC}.[9] Further tuning of the molecular structure could also improve the interface between the perovskite and the HTM to reduce interfacial charge recombination. By increasing the V_{OC}, it is likely that hydrazone-based materials can outperform devices comprising Spiro-OMeTAD as a result of the good reproducibility. We therefore believe that hydrazone-based materials have a high potential, especially since materials prepared *via* condensation chemistry can be produced at significant lower cost.

6.5 Conclusion

In conclusion, we introduce a new class of HTMs that are based on a hydrazone-backbone to the field of perovskite solar cells. Our hydrazone-based HTM, EDOT-MPH, is prepared *via* a simple and clean condensation reaction in which water is the only side product, resulting in a low cost and low environmental impact. EDOT-MPH shows charge transporting properties that compete with current state-of-the-art materials. When applied in perovskite solar cells, a small loss in V_{OC} is observed which likely originates from an unoptimized energy alignment and interfacial recombination. Nevertheless, the average PCE is comparable to devices comprising Spiro-OMeTAD, mainly as a result of the excellent reproducibility which is linked to the high quality of the HTM layer. These results demonstrate that hydrazone-based HTMs can be

produced at a fraction of the cost of current state-of-the-art materials while their performance shows the potential to outperform them.

6.6 Supporting Information

Methods

General Characterization Techniques

UV-Vis spectra were recorded using a Perkin Elmer Lambda 1050 spectrometer with an integrating sphere**.** FTIR were obtained using a Perkin Elmer FT-Infrared Spectrometer Paragon 1000. ^{1}H- and ^{13}C-NMRspectra were recorded using a Bruker spectrometer Avance III HD 400 MHz. All spectra where referenced to the solvent (^{1}H-NMR: $CDCl_3$ **δ = 7.26 ppm;** **^{13}C-NMR:** $CDCl_3$ **δ = 77.0 ppm). HRMS measurements were carried out using a Thermo Finnigan MAT 95.**

Cyclic Voltammetry

Cyclic voltammetry experiments were performed using a Metrohm Potentiostat (PGSTAT302N) with platinum working and counter electrode and an Ag/AgCl reference electrode. Experiments were performed in anhydrous and degassed dichloromethane solutions of the hole transporter with 0.1 M tetrabutylammonium hexafluorophosphate (tBuNPF6) as electrolyte and a scan rate of 100 mV s^{-1}. HOMO levels were calculated according to literature with the formal potential of the Fc^{+}/Fc redox positioned at −5.1 eV vs. vacuum. [41]

Thermal Characterization

Thermogravic analysis (TGA) was performed using a Netzsch STA 449 C Jupiter under nitrogen atmosphere with a scan rate of 10 °C min^{-1}. Differential scanning calorimetry (DSC) was performed under nitrogen atmosphere using a Perkin Elmer DSC8000 at a heating rates in the range of 10–50 °C min^{-1}. Melting behavior was confirmed using a melting point apparatus.

Powder X-Ray Diffraction (PXRD)

Powder X-ray diffraction analysis of HTM crystal structures was carried out in transmission mode using a STOE Stadi PM diffractometer with Cu $K\alpha_1$-radiation (λ = 1.5406 Å) operating at 40 kV and 40 mA, equipped with a DECTRIS MYTHEN 1 K solid-state strip detector.

Preparation of $MAPbI_3$ and FAMACs Devices

Substrate Etching and Cleaning

All chemicals were purchased from Sigma Aldrich unless stated otherwise. Fluorine-doped tin oxide (FTO) coated glass substrates (Pilkington TEC 7) were patterned and then etched with 2 M HCl and zinc powder. Substrates were scrubbed with detergent (2% Hellmanex in water) and then washed with water, acetone and ethanol. The FTO was treated in oxygen plasma for 5 min immediately prior to the spin-coating the electron transporting layer.

Electron Transport Layer Deposition

A compact TiO_2 layer was prepared from a sol-gel precursor solution by spincoating onto the freshly prepared substrates for 45 s at 2000 rpm. The substrates were afterwards calcinated at 500 °C for 30 min at air. For the sol-gel solution a 2 M solution of HCl in dry 2-propanol was added dropwise to a vigorously stirring 0.43 mM solution of Ti-isopropoxide (99.999 %) in dry 2-propanol.

FAMACs Perovskite pPecursor Solution and Film Deposition

1.5 M $Cs_{0.05}(FA_{0.83}MA_{0.17})_{0.95}Pb(I_{0.83}Br_{0.17})_3$ with excess lead iodide was prepared with 215 mg FAI, 28 mg MABr (Dyesol), 634 mg PbI_2 (TCI), and 92 mg $PbBr_2$ (TCI). A 1.875 M solution of CsI in DMSO was then diluted into the precursor solution. The perovskite solution was prepared in a mixture of anhydrous DMF (800 µL) and DMSO (200 µL) and stirred in nitrogen atmosphere on a hot plate at 70 °C for 15. After filtration, the room temperature precursor solution was deposited on FTO/TiO_2 substrates in a nitrogen filled glove box and spin-coated at 1000 rpm for 10 s and then at 6000 rpm for 20 s (ramp of 2000 rpm s^{-1}). 500 µL of chlorobenzen was quickly dispensed onto the substrate 10 s before the end of spin-coating, and then the substrate was annealed on a hot plate at 100 °C for 45 min. After deposition of the HTM, the films were stored at < 30 % relative humidity overnight.

$MAPbI_3$ Perovskite Precursor Solution and Film Deposition

For the $MAPbI_3$ precursor solution methylammonium iodide (Dyesol; 0.2 g; 1.25 mmol) and PbI_2 (TCI, >98%; 0.61 g; 1.3 mmol) were dissolved in *N*,*N*-dimethylformamide (DMF) : dimethyl sulfoxide (DMSO) solvent mixture (1:4 vol/vol; 1 mL) under stirring at 100 °C. The solution was spin-coated dynamically (80 µL; first at 1000 rpm for 10 s, followed by a second

step at 5000 rpm for 30 s) onto the substrate. After 20 s, chlorobenzene (400 µL) was added on top of the spinning substrate and afterwards the substrate was annealed on a hotplate (first at 40 °C for 40 min, followed by a second step at 100 °C for 10 min). After deposition of the HTM, the films were stored at < 30 % relative humidity over night.

Hole Transport Layer and Electrode Deposition

The hole transport material (HTM) 2,2',7,7'-tetrakis(N,N'-di-p-methoxyphenylamine)-9,9'-spirobifluorene (spiro-OMeTAD) was prepared by dissolving 75 mg spiro-OMeTAD (Borun chemicals) in 1 mL anhydrous chlorobenzene. To this solution 30 µL of a lithium bis(trifluoromethanesulfonyl)imide (Li-TFSI) solution (170 mg mL^{-1}in acetonitrile) and 10 µL tert-butylpyridine (tBP) were added. 80 µL of this solution was spincoated dynamically onto the substrate at 1500 rpm.

For the deposition on FAMACs, to 20 mg of EDOT-MPH 800 µL anhydrous chlorobenzene and 200 µL anhydrous chloroform along with 10 µL tBP and 20 µL of a Li-TFSI solution (170 mg mL^{-1} in acetonitrile) were added. The mixture was heated at 60 °C for 5-10 minutes until the solution became transparent, and was then passed through a Chromafil 0.45 µm PET-45/15 MS syringe filter while hot. The filtered solution was left on a hot plate at 40 °C while spin-coating. 80 µL of the EDOT-MPH solution was quickly dispensed onto the substrates while they were spinning at 1000 rpm for 45 s.

For deposition on $MAPbI_3$. To 15 mg of EDOT-MPH 800 µL anhydrous chlorobenzene and 200 µL anhydrous chloroform along with 10 µL tBP and 20 µL of a Li-TFSI solution (170 mg mL^{-1} in acetonitrile) were added. The mixture was heated at 80 °C for 5-10 minutes until the solution became transparent, and was then passed through a Chromafil 0.45 µm PET-45/15 MS syringe filter while hot. The filtered solution was left on a hot plate at 60 °C while spin-coating. 80 µL of the EDOT-MPH solution was quickly dispensed onto the substrates while they were spinning at 1000 rpm for 45 s.

The substrates were left in a desiccator box for 24 h for the HTM to oxidize before thermally evaporating a 50 nm gold electrode under vacuum of < 9 x 10^{-6} mbar.

Solar Cell Characterization

J/V-curves of solar cells were recorded under ambient conditions under simulated AM 1.5 sunlight, with an incident power of approximately 100 mW cm-2, which was corrected for the

exact light intensity using a Fraunhofer ISE certified silicon cell. The active area of the solar cells was defined with a square metal aperture mask of 0.0831 cm^2. The reported device characteristics were estimated from the measured *J/V*-curves obtained from the reverse scan (from V_{OC} to J_{SC}) which was recorded at a scan rate of 0.2 V s-1 after pre-biasing at 1.5 V for 5 s under illumination using a Newport OrielSol 2A solar simulator with a Keithley 2401 source meter. All as-prepared devices show a comparable degree of hysteresis between the forward and reverse scan.

Charge Transport Measurements

Hole-Only Device Preparation and Characterization.

ITO-substrates (1.5 x 2.0 cm, VisionTek, 12 Ω/sq to 15 Ω/sq) were etched and cleaned. The substrates were plasma cleaned prior to the thermal deposition of the MoO_x layer (10 nm) under vacuum (~$1 \cdot 10^{-6}$ mbar). The substrates were exposed to air and stored in a nitrogen-filled glovebox. Next, the EDOT-MPH was spincoated from a chlorobenzene:chloroform mixture as described above at a concentration of 10 mg mL^{-1}. A top electrode of MoO_x (10 nm), followed by a layer of gold (40 nm) was deposited under vacuum (~$1 \cdot 10^{-6}$ mbar). The active area of the device was 0.16 cm^2. Current-voltage characteristics were recorded in air in the dark using a Metrohm potentiostat (PGSTAT302N) at a scan rate of 0.1 V s^{-1}. The layer thickness which was around 50 nm was determined for the individual films by using atomic force microscopy (AFM) measurements, which were performed in tapping mode using a NanoInk DPN Stage microscope, or with a Veeco Dektak 150.

Conductivity Device Preparation and Characterization.

Glass substrates with a thin compact layer of Al_2O_3 were used to improve the wetting of the HTMs on the substrate. EDOT-MPH was spincoated at 1000 rpm from a chloroform:chlorobenzene mixture as described above containing the given amount of LiTFSI as oxidant, resulting in a film thickness of approximately 50 nm. The films allowed to oxidize for 24 h in a desiccator at a relative humidity < 30 %. 40 nm thick gold electrodes were thermally deposited under vacuum (~10^{-6} mbar). The electrode pattern was designed for two point probe measurements with a channel length of 250, 500 and 1000 µm, a channel width of 0.2, 0.1 and 0.056 m respectively. No significant differences were observed depending on the electrode pattern and the measured values were averaged over at least 8 individual devices. *JV*-

curves were recorded under ambient conditions without illumination using a Keithley 2400 source meter at a scan rate of 1 V s^{-1} in the range from -5 to 5 V.

Computational Study.

The geometry optimization and electronic structure calculations were carried out using Gaussian09 program package. Density functional theory (DFT) geometry optimizations using the B3LYP/6-31G(d,p) basis set were performed in vacuum and in dichloromethane as the solvent, by means of the conductor-like polarizable continuum model (CPCM). The calculated HOMO energy level was obtained by adding 0.624 eV to the HOMO energy level obtained from DFT calculations using DCM as solvent.[28]

Synthetic Details

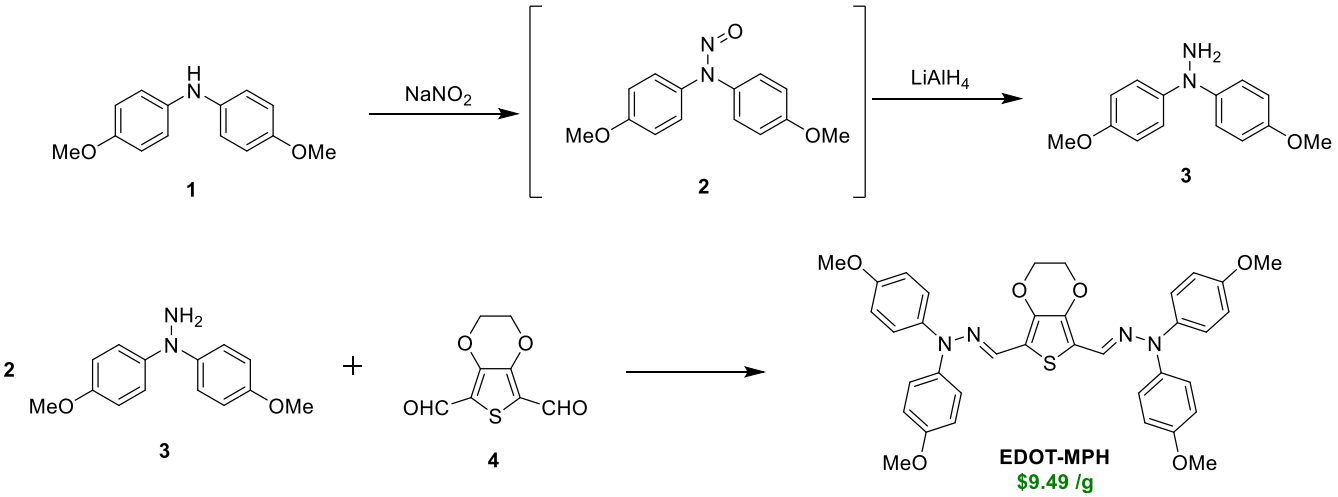

Scheme S 6.1: Synthesis of EDOT-MPH and its starting material.

Synthesis of 1,1-Bis(methoxyphenyl)amine (1)

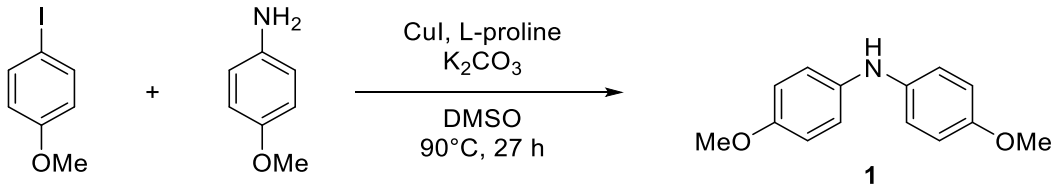

A mixture of K_2CO_3 (17.44 g, 125 mmol, 2 eq), CuI (1.22 g, 6.29 mmol, 0.1 eq) and L-proline (1.47 mg, 12.58 mmol, 0.2 eq) was added to a solution of 4-Iodoanisole (1.8 g, 62.9 mmol, 1 eq) DMSO (150 mL), resulting in a black color. *p*-anisolidine, (12.8 g, 103.8 mmol, 1.5 eq) was added, and the mixture stirred at 90 °C for 2 days. After filtration of the suspension, the

solution was extracted with ethyl acetate (3 x 200 mL). The combined organic layers were washed with brine and dried with Na_2SO_4. After filtration the solvent was removed *in vacuo* and the product was recrystallized from diethyl ether. After a short silica-column (Eluent: Ethyl acetate/hexane 7:1), the product was obtained as red-orange crystals in a yield of 52 %.

^{1}H-NMR ($CDCl_3$, 400 MHz): δ= 6.934 (d_t, 4 H, *J*= 8.8 Hz), 6.827 (d_t, 4 H, *J*= 8.8 Hz), 5.249 (s, 1 H), 3.784 (s, 6 H) ppm.

Characterization in agreement with literature.[24]

Synthesis of N,N-bis(4-mothoxyphenyl)nitrous amide (2)

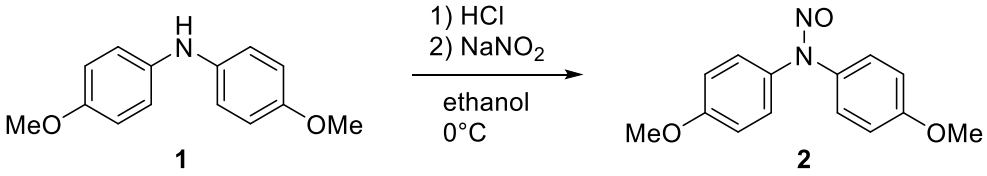

HCl (37 %, 20 mL) was added to a solution of Bis(4-methoxyphenyl)amine (5 g, 21.8 mmol, 1 eq in 120 mL ethanol) at 0°C and and the orange solution was stirred vigorously for 5 min. To this mixture, 50 mL of a 0.47 M solution of $NaNO_2$ in water was added dropwise, leading to a white precipitate which was formed immediately. After stirring at 0 °C for 1 h, the product was filtered off as a colorless powder and dried *in vacuo*. The product was obtained in a good yield of 91 % and stored in the glovebox.

^{1}H-NMR ($CDCl_3$, 400 MHz): δ= 7.332 (d_t, 2 H, *J*= 8.8 Hz), 7.076–7.033 (m, 6 H), 3.795 (d, 6 H) ppm.

^{13}C-NMR ($CDCl_3$, 100 MHz): δ= 159.51, 158.48, 135.50, 129.74, 128.35, 122.19, 114.91, 114.67, 55.48, 55.44 ppm.

Characterization in agreement with literature.[22]

Synthesis of 1,1-bis(4-methoxyphenyl)hydrazine (3)

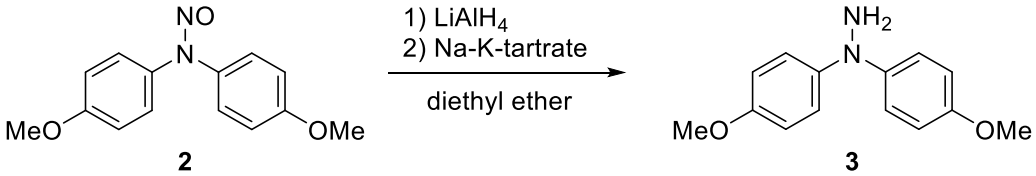

To a solution of the as received nitrous amide **2** (5 g, 19.37 mmol, 1 eq in 300 mL diethyl ether), $LiAlH_4$ (1 g, 26.2 mmol, 1.4 eq in 40 mL diethyl ether) was added dropwise, leading to an off-white suspension which was stirred for 2 h at room temperature. After the careful addition of a saturated Na-K-tartrate solution in water, the organic layer was extracted with diethyl ether (3 x 150 mL). HCl (37 %) was added to the combined organic layers, resulting in a white precipitation of the product. After addition of a 0.75 M NaOH solution (50 mL in water), the product was extracted with diethyl ether (3 x 150 mL) and the combined organic layers were dried with $MgSO_4$. The solvent was removed *in vacuo* and the product was obtained as a red crystalline powder in a medium yield of 58.4 %.

^{1}H-NMR ($CDCl_3$, 400 MHz): δ= 7.074 (d_t, 4 H, *J*= 8.8 Hz), 6.839 (d_t, 4 H, *J*= 9.2 Hz), 4.046 (s, 2 H), 3.790 (s, 6 H) ppm.

Characterization in agreement with literature.[22]

Synthesis of EDOT-MPH (5)

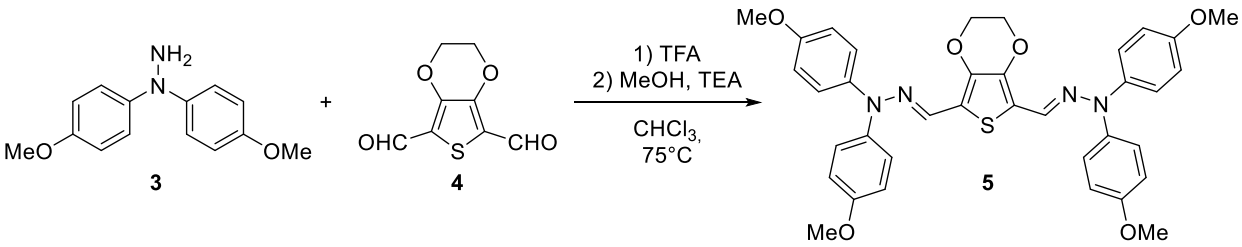

To the red solution of **3** (0.33 g, 1.35 mmol, 2.3 eq) in 10 mL dry chloroform, compound **4** (0.12 eq, 0.59 mmol, 1 eq)[5] was added, together with one drop of trifluoro acetic acid. After the mixture was stirred over night at room temperature, it was heated to reflux for 4 hours. After cooling down, the product was crushed out by adding 50 mL methanol. After the addition of 0.1 mL triethylamine in order to neutralize the suspension, the product was filtered off a bright orange powder and washed with methanol. The product was dried under vacuum and obtained in a high yield of 97 %. The whole workup of the molecules was done under ambient conditions, indicating the stability of the molecule at air.

^{1}H-NMR ($CDCl_3$, 400 MHz): δ= 7.218 (s, 2 H), 7.103 (d_t, 4 H, *J*= 8.8 Hz), 6.946 (d_d, 4 H, *J*= 8.8 Hz), 4.086 (s, 4 H), 3.831 (s, 12 H) ppm.

^{13}C-NMR ($CDCl_3$, 100 MHz): δ= 156.60, 139.12, 137.33, 126.31, 123.55, 115.47, 115.05, 64.77, 55.61 ppm.

HRMS (FAB^+) m/z: $[M]^+$ calculated for $C_{36}H_{34}O_6N_4S$: 650.2199; found: 650.2224

FTIR: $\nu(cm^{-1})$: 3050 (vw), 3000 (w), 2927 (w), 2831 (w), 1602 (m, **C=N-N**), 1548 (w), 1500 (vs), 1435 (s), 1368 (s), 1299 (m), 1244 (vs), 1199 (vs), 1112 (s), 1065 (vs), 952 (s), 816 (vs).

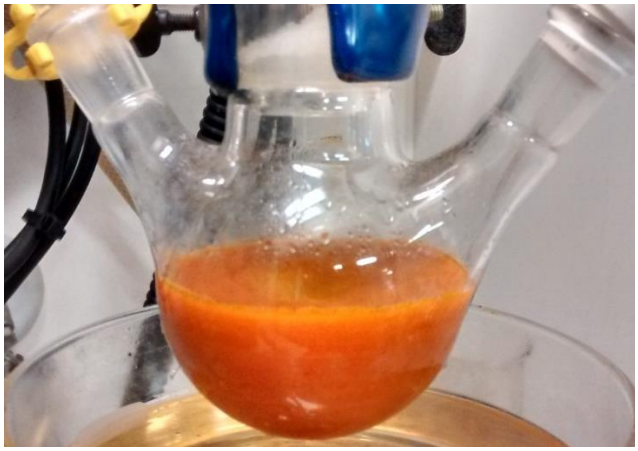

Figure S 6.1 Crude product. Reaction vessel showing the bright orange product right before filtering it off.

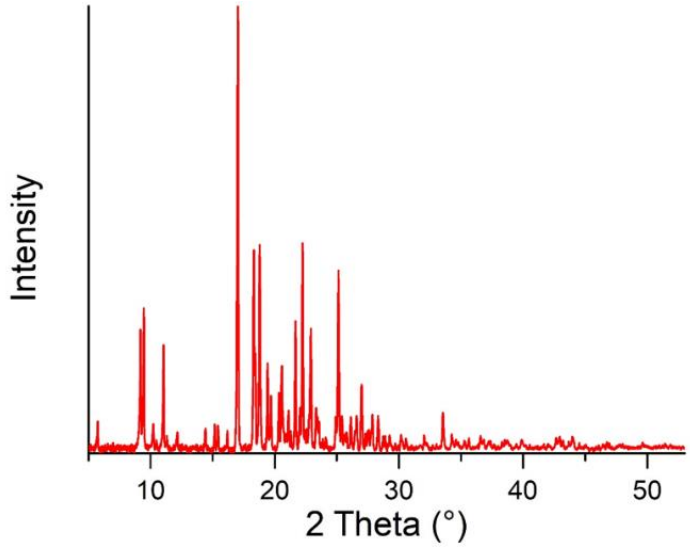

Figure S 6.2: PXRD patterns of EDOT-MPH, demonstrating that the materil is crystalline.

Cost estimation

In order to make an estimate of the cost of the different hole transporting materials using the cost model as was described by Osedach *et al.*[7] which was implemented by ourselves for HTMs for perovskite solar cells.[8,9] For every synthetic step the required amounts of reactants, catalysts, reagents and solvents are calculated to obtain 1 gram of the final product.

Additionally, the required materials for workup and purification were estimated using the procedure as published.

1. Quenching/neutralization. The required amounts were evaluated on a case-by-case basis. For neutralization a stoichiometric amount of the acid or base were assumed to be necessary.

2. Extraction: The use of 150 mL solvent (three times 50 mL) and 1 gram of drying agent (Na_2SO_4 , or $MgSO_4$) were assumed to be required to obtain 1 gram of the (intermediate) product.

3. Column chromatography. We assume that to obtain 1 gram of the (intermediate) product, 400 mL of solvent and a column filled with 263 g of 60 μm silica gel was used. The amounts are based on the assumption that the separation (R_f>0.3) and sample loading would be ideal.

4. Recrystallization. We assume that 1 gram of product requires 100 mL of solvent and that the procedure is only performed once.

5. Distillation/sublimation. We assume no chemicals are required and no chemical waste, the energy was similar to other steps not included.

6. Washing. We assume 100 mL of solvent is required to wash 1 gram of the (intermediate) product.

7. Filtering. We assume 50 mL of solvent is required to filter 1 gram of the (intermediate) product.

The quantities are based on published procedures where the synthesis, workup and purification are performed on a lab scale. Upscaling to a multi-kilogram scale might reduce the quantities, especially materials used in the purification, considerably. For example, multiple steps could possibly be combined to reduce the number of isolation steps (“telescoping”). Also solvents might be replaced for cheaper (and/or environmentally friendly) alternatives or reused to reduce materials and waste cost. For this reason the estimated material cost could be seen as an upper limit.

The starting materials and therefore the amount of synthetic steps could be a topic of debate, however most of the used starting materials are common starting materials for the different synthetic routes. In example, 4-iodoaniline has been used as starting material for all three protocols.

In order to estimate the cost, quotes (for bulk quantities when possible) have been collected from major chemical suppliers (Sigma-Aldrich, Acros Organics and Fischer Chemicals) for all used chemicals. The costs were multiplied by the quantities that are required for the synthesis and the sum of all costs was calculated to estimate to total material cost.

Different synthetic routes were evaluated in order to find the most cost effective route. We found that especially

procedures that require column chromatography for purification add significantly to the cost, as a result of the high prices of silica gel together with the large amounts of solvent used. Also upscaling of column chromatography to a multi-kilogram scale will be challenging.

Furthermore, production on a large scale could have an influence on the price of starting materials. The cost of starting materials might be reduced significantly. Also by finding other suppliers of chemicals the cost of (especially organic) starting materials could be further reduced. In example, 3,4-ethylenedioxythiophene (EDOT) is commercially available at Sigma-Aldrich and Acros organics in small quantities at prices exceeding $5,000 per kilogram, while other suppliers offer the same material in an even higher purity in bulk quantities at prices below $250 per kilogram.

We also note that the material cost only takes into account the cost of materials used. Equipment, energy consumption, maintenance, waste treatment, labor, profit and various other overhead charges are not taken into account. Depending on the synthesis and purification steps this could also have a significant influence on the cost. For example, palladium cross-coupling reactions require stringent conditions, making the upscaling significant more costly than simple reactions that can be performed at ambient conditions. In the case of pharmaceutical drugs, for example, the materials cost accounts for only 20-45% of the total cost of drug synthesis.

The cost analysis presented here is based on lab scale synthesis and gives a rough estimate of the material cost. The procedure is based on previous publications by ourselves[5,6] and Osedach *et al*.[7]

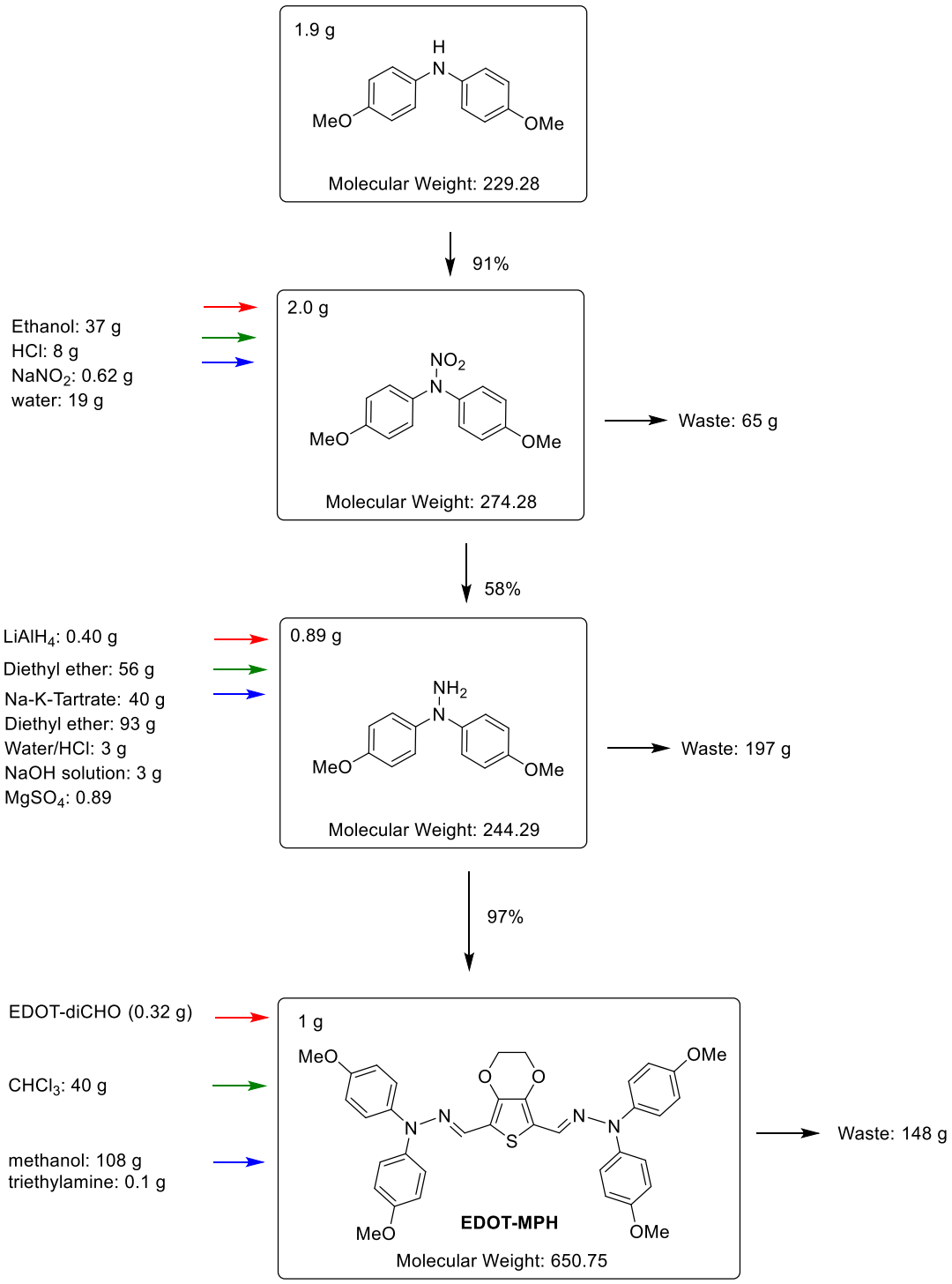

Scheme S 6.2: Synthesis scheme for cost estimation and chemical waste.

Table S 6.1: Cost analysis and overall cost for the synthesis of 1 g EDOT-MPH.

Chemical	Weight reagent (g)	Weight solvent (g)	Weight workup (g)	Total weight	Chemical cost ($/kg)	Cost ($/g product)	Cost ($/step)
Amine	1.9			1.9	$1,666.00	$3.17	$3.32
Ethanol		37		37	$3.16	$0.12	
HCl		8		8	$3.39	$0.03	
$NaNO_2$		0.62		0.62	$17.12	$0.01	
Water		19		19	$0.00	$0.00	
$LiAlH_4$	0.4			0.4	$522.80	$0.21	$4.48
DEE		56		56	$22.89	$1.28	
Na-K-Tartrate			40	40	$19.46	$0.78	
DEE			93	93	$22.89	$2.13	
HCl			3	3	$3.39	$0.01	
NaOH			3	3	$7.56	$0.02	
MgSO4			0.89	0.89	$54.24	$0.05	
EDOT	0.32			0.32	4262.36	$1.36	$1.69
TFA	0.02			0.02	$141.12	$0.00	
chloroform		40		40	$2.60	$0.10	
methanol			108	108	$1.98	$0.21	
triethylamine			0.1	0.1	$23.18	$0.00	

Total	**3**	**160**	**248**	**411**			**$9.49**

Thermal Properties

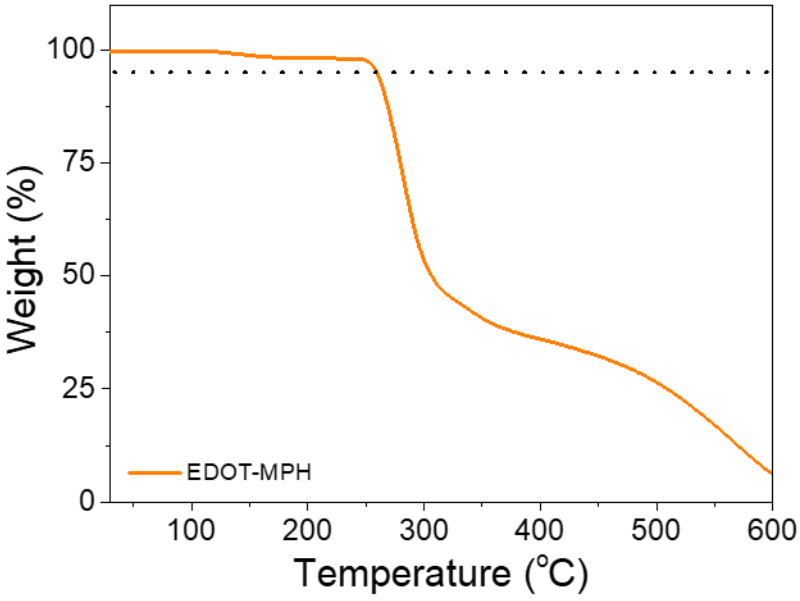

Figure S 6.3: TGA thermogram of EDOT-MPH recorded under nitrogen atmosphere with a heating rate of 10 °C/min. The dotted black line indicates the 5% weight loss.

Geometry Optimization

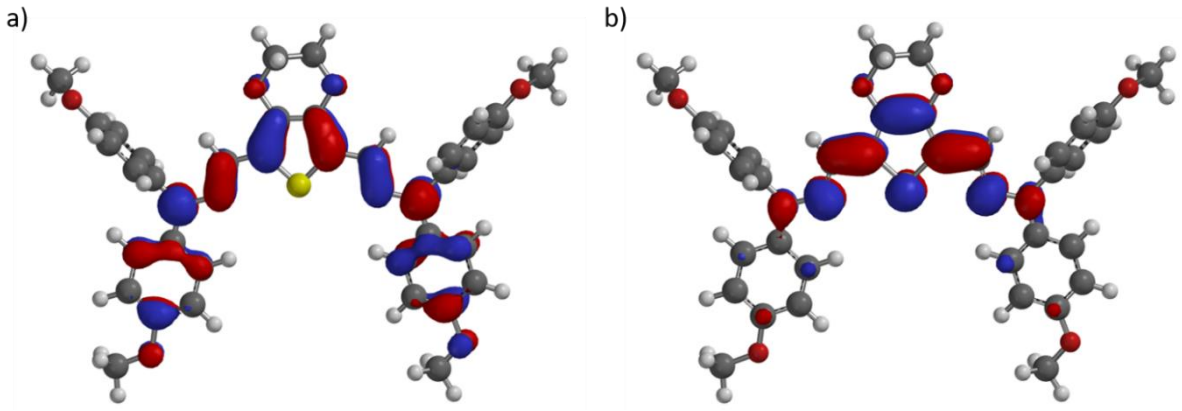

Figure S 6.4: Frontier molecular orbital distributions. Distribution of the HOMO (a) and LUMO (b) levels, obtained from DFT calculations in vacuum.

Charge Carrier Mobility

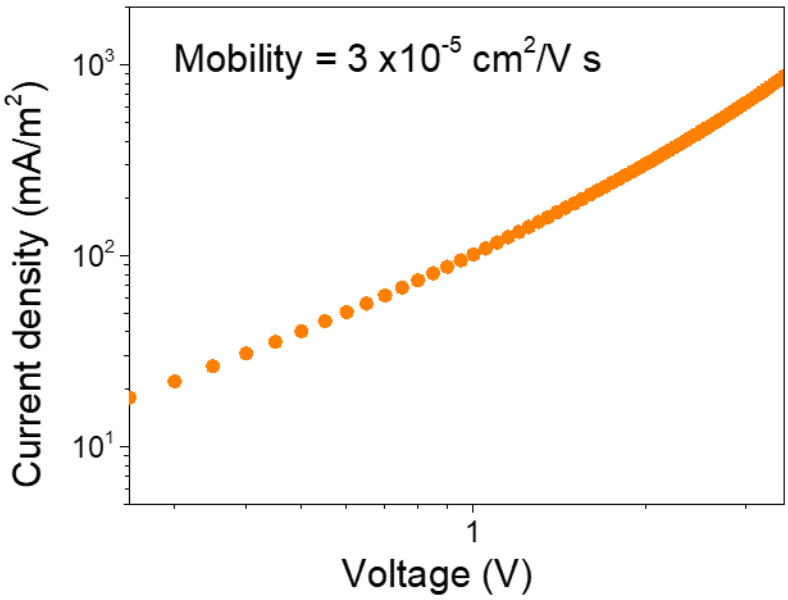

Figure S 6.5: *J-V* curves of single "hole-only" devices. Device architecture: ITO)/MoO_x/EDOT-MPH/MoO_x/Au. The mobility was obtained by fitting the equation for space-charge limited current.

Photovoltaic Performance

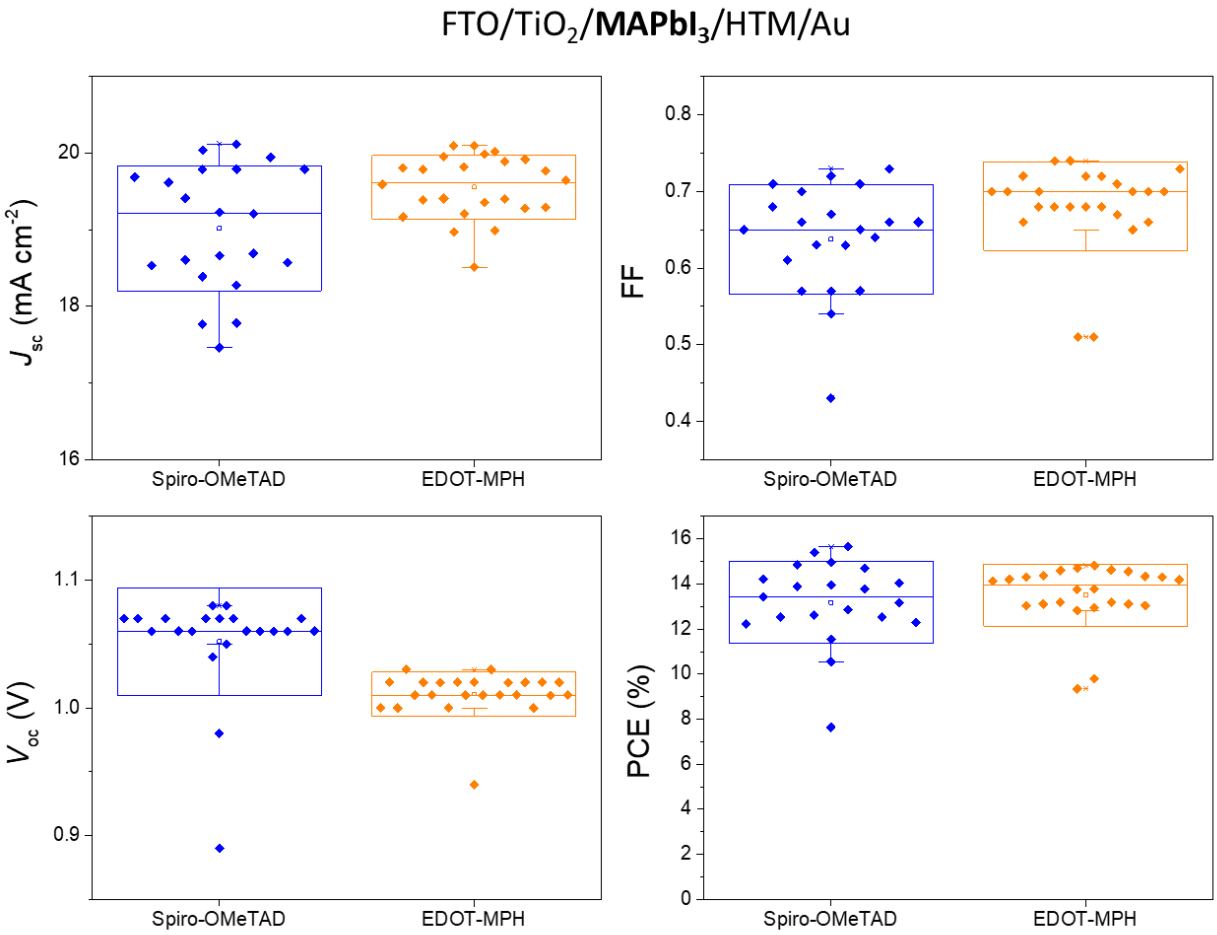

Figure S 6.6: Photovoltaic performance $MAPbI_3$ devices. Box-plot of 45 individual devices prepared showing the comparison of the photovoltaic parameters of devices comprising either EDOT-MPH or Spiro-OMeTAD as HTM. Device architecture: FTO/TiO_x/$MAPbI_3$/HTM/Au.

Table S 6.2: Overview statistical analysis of 45 individual $MAPbI_3$ devices

	dF	T stat	P (T<=t) two-tail	T critical two tail
J_{SC}	29	2.74	0.010	2.05
V_{OC}	26	-4.14	0.0003	2.06
FF	39	2.21	0.033	2.02
PCE	37	0.68	0.501	2.03

Null hypothesis: the photovoltaic parameters for devices comprising EDOT-MPH and Spiro-OMeTAD are the same. If T stat > T critical we can conclude that, with a certainty of 95%, the null-hypothesis for the given parameter is not true (meaning the improvement is significant). dF is the degrees of freedom (number closely

related to the sample size). The P-value determines the statistical significance (should not be confused with the error rate).

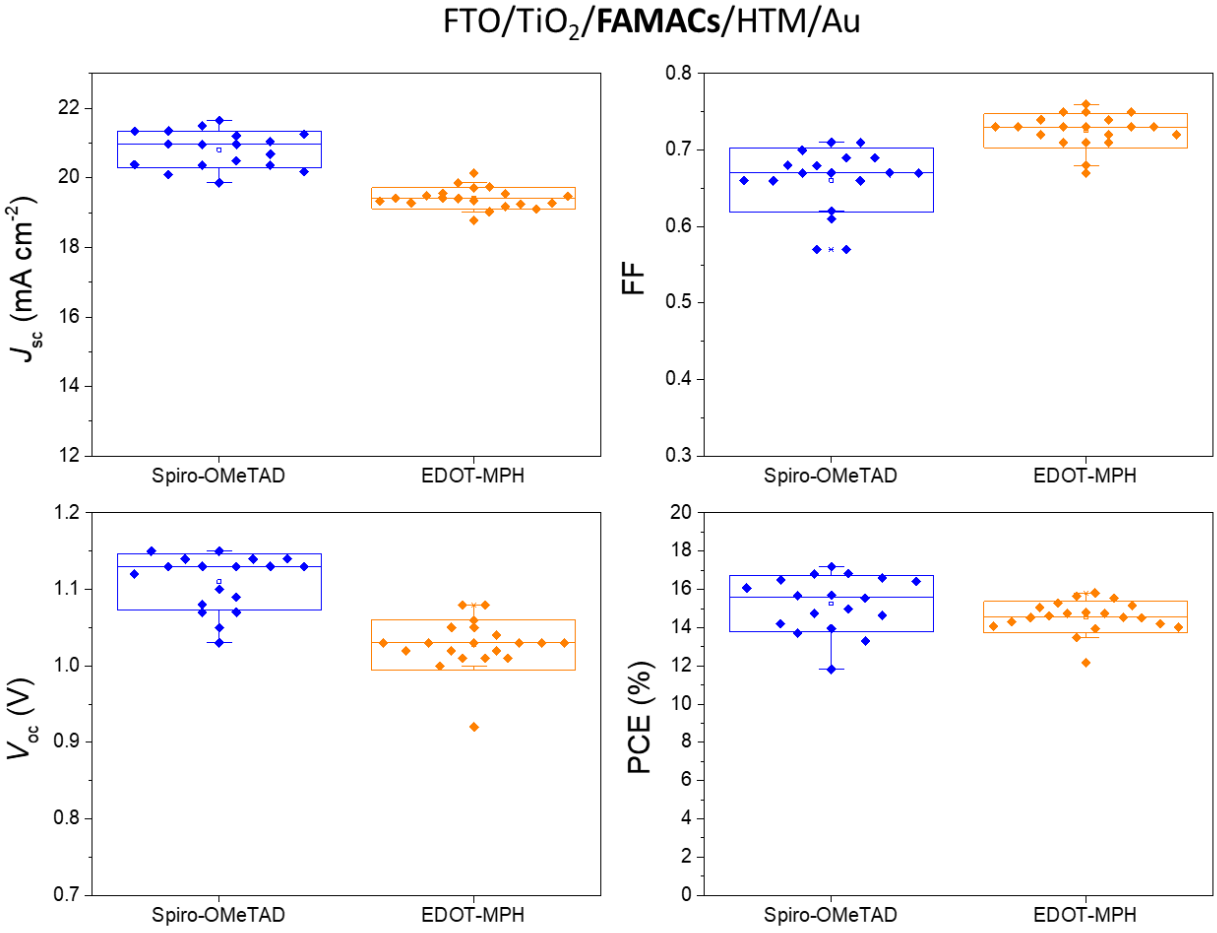

Figure S 6.7: Photovoltaic performance FAMACs devices. Box-plot of 38 individual devices prepared showing the comparison of the photovoltaic parameters of devices comprising either EDOT-MPH or Spiro-OMeTAD as HTM. Device architecture: FTO/TiO_x/FAMACs/HTM/Au.

Table S 6.3: Overview statistical analysis of 38 individual FAMACs devices

	dF	T stat	P (T<=t) two-tail	T critical two tail
J_{SC}	27	-9.88	1.8×10^{-10}	2.05
V_{OC}	35	-7.25	1.8×10^{-8}	2.03
FF	25	5.86	4.1×10^{-6}	2.06
PCE	26	-1.79	0.086	2.06

Null hypothesis: the photovoltaic parameters for devices comprising EDOT-MPH and Spiro-OMeTAD are the same. If T stat > T critical we can conclude that, with a certainty of 95%, the null-hypothesis for the given parameter is not true (meaning the improvement is significant). dF is the degrees of freedom (number closely related to the sample size). The P-value determines the statistical significance (should not be confused with the error rate).

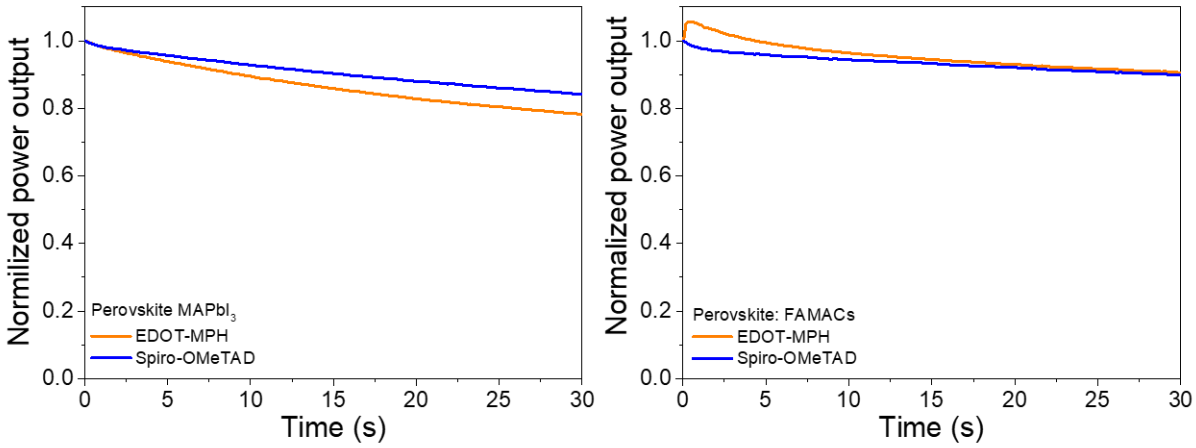

Figure S 6.8: Stabilized power output curves of the photovoltaic devices comprising the different HTMs in combination with the different perovskite absorber.

Charge Carrier Lifetime

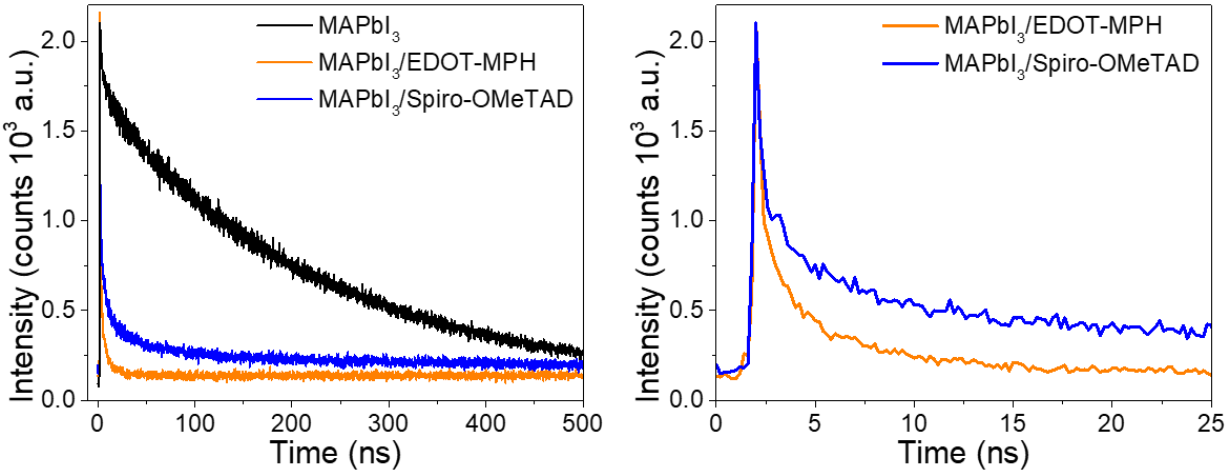

Figure S 6.9: Time resolved photoluminescence decay of $MAPbI_3$ films and bilayers consisting of $MAPbI_3$/HTM, obtained for the same amount of counts.

6.7 References

[1] M. L. Petrus, J. Schlipf, C. Li, T. P. Gujar, N. Giesbrecht, P. Müller-Buschbaum, M. Thelakkat, T. Bein, S. Hüttner, P. Docampo, *Advanced Energy Materials* **2017**, *7*, 1700264.

[2] Z. H. Bakr, Q. Wali, A. Fakharuddin, L. Schmidt-Mende, T. M. Brown, R. Jose, *Nano Energy* **2017**, *34*, 271.

[3] K. Rakstys, S. Paek, P. Gao, P. Gratia, T. Marszalek, G. Grancini, K. T. Cho, K. Genevicius, V. Jankauskas, W. Pisula, *Journal of Materials Chemistry A* **2017**, *5*, 7811.

[4] D. Bi, B. Xu, P. Gao, L. Sun, M. Grätzel, A. Hagfeldt, *Nano Energy* **2016**, *23*, 138.

[5] G.-W. Kim, J. Lee, G. Kang, T. Kim, T. Park, *Advanced Energy Materials* **2018**, *8*, 1701935.

[6] J. Zhang, B. Xu, L. Yang, C. Ruan, L. Wang, P. Liu, W. Zhang, N. Vlachopoulos, L. Kloo, G. Boschloo, *Advanced Energy Materials* **2018**, *8*, 1701209.

[7] T. P. Osedach, T. L. Andrew, V. Bulović, *Energy & Environmental Science* **2013**, *6*, 711.

[8] M. L. Petrus, T. Bein, T. J. Dingemans, P. Docampo, *Journal of Materials Chemistry A* **2015**, *3*, 12159.

[9] M. L. Petrus, A. Music, A. C. Closs, J. C. Bijleveld, M. T. Sirtl, Y. Hu, T. J. Dingemans, T. Bein, P. Docampo, *Journal of Materials Chemistry A* **2017**, *5*, 25200.

[10] W.-Y. Chen, L.-L. Deng, S.-M. Dai, X. Wang, C.-B. Tian, X.-X. Zhan, S.-Y. Xie, R.-B. Huang, L.-S. Zheng, *Journal of Materials Chemistry A* **2015**, *3*, 19353.

[11] P. Gratia, A. Magomedov, T. Malinauskas, M. Daskeviciene, A. Abate, S. Ahmad, M. Grätzel, V. Getautis, M. K. Nazeeruddin, *Angewandte Chemie International Edition* **2015**, *54*, 11409.

[12] A. Magomedov, S. Paek, P. Gratia, E. Kasparavicius, M. Daskeviciene, E. Kamarauskas, A. Gruodis, V. Jankauskas, K. Kantminiene, K. T. Cho, *Advanced Functional Materials* **2018**, *28*, 1704351.

[13] A. Binek, M. L. Petrus, N. Huber, H. Bristow, Y. Hu, T. Bein, P. Docampo, *ACS applied materials & interfaces* **2016**, *8*, 12881.

[14] M. L. Petrus, R. K. Bouwer, U. Lafont, S. Athanasopoulos, N. C. Greenham, T. J. Dingemans, *Journal of Materials Chemistry A* **2014**, *2*, 9474.

[15] M. E. Mulholland, D. Navarathne, M. L. Petrus, T. J. Dingemans, W. G. Skene, *Journal of Materials Chemistry C* **2014**, *2*, 9099.

[16] M. Daskeviciene, S. Paek, Z. Wang, T. Malinauskas, G. Jokubauskaite, K. Rakstys, K. T. Cho, A. Magomedov, V. Jankauskas, S. Ahmad, *Nano Energy* **2017**, *32*, 551.

[17] D. Demeter, S. Mohamed, A. Diac, I. Grosu, J. Roncali, *ChemSusChem* **2014**, *7*, 1046.

[18] S. Urnikaite, T. Malinauskas, I. Bruder, R. Send, V. Gaidelis, R. Sens, V. Getautis, *The Journal of Physical Chemistry C* **2014**, *118*, 7832.

[19] S. Urnikaite, T. Malinauskas, V. Gaidelis, I. Bruder, R. Send, R. Sens, V. Getautis, *Chemistry–An Asian Journal* **2013**, *8*, 538.

[20] V. Getautis, J. V. Grazulevicius, T. Malinauskas, V. Jankauskas, Z. Tokarski, N. Jubran, *Chemistry letters* **2004**, *33*, 1336.

[21] R. Lygaitis, V. Getautis, J. V. Grazulevicius, *Chemical Society Reviews* **2008**, *37*, 770.

[22] I. A. Tonks, A. C. Durrell, H. B. Gray, J. E. Bercaw, *Journal of the American Chemical Society* **2012**, *134*, 7301.

[23] A. K. Mohanakrishnan, A. Hucke, M. A. Lyon, M. V. Lakshmikantham, M. P. Cava, *Tetrahedron* **1999**, *55*, 11745.

[24] D. Ma, Q. Cai, H. Zhang, *Organic letters* **2003**, *5*, 2453.

[25] E. Greul, M. L. Petrus, A. Binek, P. Docampo, T. Bein, *Journal of Materials Chemistry A* **2017**, *5*, 19972.

[26] F. Hao, C. C. Stoumpos, D. H. Cao, R. P. H. Chang, M. G. Kanatzidis, *Nature photonics* **2014**, *8*, 489.

[27] R. A. Sheldon, *Chemical Communications* **2008**.

[28] W.-J. Chi, Q.-S. Li, Z.-S. Li, *Nanoscale* **2016**, *8*, 6146.

[29] A. Abate, T. Leijtens, S. Pathak, J. Teuscher, R. Avolio, M. E. Errico, J. Kirkpatrik, J. M. Ball, P. Docampo, I. McPherson, *Physical Chemistry Chemical Physics* **2013**, *15*, 2572.

[30] M. L. Petrus, F. S. F. Morgenstern, A. Sadhanala, R. H. Friend, N. C. Greenham, T. J. Dingemans, *Chemistry of Materials* **2015**, *27*, 2990.

[31] D. D. Medina, M. L. Petrus, A. N. Jumabekov, J. T. Margraf, S. Weinberger, J. M. Rotter, T. Clark, T. Bein, *ACS nano* **2017**, *11*, 2706.

[32] T. Leijtens, I.-K. Ding, T. Giovenzana, J. T. Bloking, M. D. McGehee, A. Sellinger, *ACS nano* **2012**, *6*, 1455.

[33] M. L. Petrus, R. K. M. Bouwer, U. Lafont, D. H. Murthy, R. J. P. Kist, M. L. Böhm, Y. Olivier, T. J. Savenije, L. D. A. Siebbeles, N. C. Greenham, *Polymer Chemistry* **2013**, *4*, 4182.

[34] M. Koole, R. Frisenda, M. L. Petrus, M. L. Perrin, H. S. J. van der Zant, T. J. Dingemans, *Organic Electronics* **2016**, *34*, 38.

[35] Y. Hu, E. M. Hutter, P. Rieder, I. Grill, J. Hanisch, M. F. Aygüler, A. G. Hufnagel, M. Handloser, T. Bein, A. Hartschuh, *Advanced Energy Materials* **2018**, *8*, 1703057.

[36] Y. Hu, M. F. Aygüler, M. L. Petrus, T. Bein, P. Docampo, *ACS Energy Letters* **2017**, *2*, 2212.

[37] M. F. Aygüler, A. G. Hufnagel, P. Rieder, M. Wussler, W. Jaegermann, T. Bein, V. Dyakonov, M. L. Petrus, A. Baumann, P. Docampo, *ACS applied materials & interfaces* **2018**, *10*, 11414.

[38] M. Saliba, S. Orlandi, T. Matsui, S. Aghazada, M. Cavazzini, J.-P. Correa-Baena, P. Gao, R. Scopelliti, E. Mosconi, K.-H. Dahmen, *Nature Energy* **2016**, *1*, 1.

[39] E. M. Hutter, J.-J. Hofman, M. L. Petrus, M. Moes, R. D. Abellón, P. Docampo, T. J. Savenije, *Advanced Energy Materials* **2017**, *7*, 1602349.

[40] J. Jiménez-López, W. Cambarau, L. Cabau, E. Palomares, *Scientific reports* **2017**, *7*, 1.

[41] C. M. Cardona, W. Li, A. E. Kaifer, D. Stockdale, G. C. Bazan, *Advanced materials (Deerfield Beach, Fla.)* **2011**, *23*, 2367.

7 Conclusions and Outlook

This thesis focused on the exploration of the lead-free double perovskite $Cs_2AgBiBr_6$ in order to investigate and shed light onto the intrinsic bottlenecks limiting this material from exceeding efficiencies above 3 % when employed as absorber material in solar cells.

In the first part of this work, the bottlenecks of the complete solar cells are investigated. The experiments show that the material is dominated by rather large ionic conductivity, showing that the current of the cells is dependent on the scan rate. This shows that documentation of the solar cells' scan speed is vital for every publication in order to determine the reliability of the reported efficiencies. Moreover, we found that for these solar cells, a field inversion happens at rather low applied external voltage. This led to the conclusion that the solar cells suffer from a rather low selectivity at the contacts, as well as a rather small built-in potential. Lastly, we determined the radiative V_{OC} losses within the solar cells by measuring the electroluminescence of the devices and calculating a radiative V_{OC} limit of 1.6 V for the investigated solar cells, using the determined electroluminescence quantum yield. Altogether, this project provided insights into the intrinsic limiting factors, opening up several pathways to improve the overall efficiency of $Cs_2AgBiBr_6$ based solar cells.

The second part of this thesis investigates the influence of the precursor stoichiometry of the $Cs_2AgBiBr_6$ double perovskite. Here, we changed the stoichiometric ratios of AgBr and $BiBr_3$ in a large variety of combinations and investigated the influence of these combinations on the optoelectronic properties of the resulting double perovskite thin films. We found that changing the stoichiometry towards a $BiBr_3$ deficient system combined with the same amount of AgBr excess leads to a pronounced change of the orientation of the investigated thin films. Following up, we found that the optoelectronic properties of the thin films were influenced as well, expressing a rather large increase in the charge carrier lifetime, as well as mobility. This observation was consistent with the structural changes. Employing the stochiometrically altered $Cs_2AgBiBr_6$ thin films as absorber material in solar cells showed an enhancement of the resulting photovoltaic performance, boosted by an increase of the short-circuit current. This is in good agreement with the observed optoelectronic improvements and provides a convenient toolset to improve the structural, optoelectronic and solar cell properties in a simple way.

In the third part of this work, we addressed the above-mentioned bottleneck of the low selectivity of $Cs_2AgBiBr_6$ thin film solar cells. Here, we applied a thin layer of a

phenethylammonium-based 2D perovskite directly on top of the 3D compound $Cs_2AgBiBr_6$. The investigation of the resulting solar cells revealed a significant increase of the efficiency which was related to a boost of the open circuit voltage. While the optoelectronic investigation of the pristine thin films did not reveal changes that could explain the improvement of the V_{OC}, examination of full solar cells revealed a change of the recombination regime. This led to the conclusion that the application of the 2D layer only influences the full devices and hence the interface between the hole-transport material (HTM) and the active layer. Further measurements showed a larger built-in potential for the 2D/3D hybrid double perovskite solar cells, as well as no change in the field direction of said built-in field, pointing towards an enhanced contact selectivity. Hence, the energy levels of the materials were investigated and indeed showed a better energy level alignment of the valence band maximum of the perovskite towards the HTM site, as well as a better electron blocking behavior towards the same direction. Thus, our work shows how to overcome the rather serious bottleneck of a poor contact-selectivity by improving the electron blocking behavior as well as the hole-extraction towards the HTM site by applying a thin 2D perovskite layer.

In the last part of the work, we introduced a new hydrazone-based hole-transporting material for lead-based perovskite solar cells. Here, we synthesized a material *via* condensation chemistry to improve the environmental impact of the HTM synthesis in general and to find low-cost alternatives to the established materials, all of which are synthesized *via* complex cross-coupling reactions using palladium-based catalysts and a large amount of halogenated solvents. Not only do the established materials have a large environmental impact, the often used Spiro-OMeTAD incurs synthesis costs ten times higher compared to the EDOT-MPH introduced here. When employed in solar cells, both Spiro-OMeTAD and EDOT-MPH show comparable efficiencies, with EDOT-MPH showing small V_{OC} losses due to increased interfacial recombination. Altogether, this work extends our efforts towards developing low-cost HTMs synthesized *via* simple and low-cost condensation chemistry. This leads to a smaller environmental impact at only a fraction of the synthesis cost.

Although $Cs_2AgBiBr_6$ based solar cells so far did not exceed efficiencies above 3 %, this thesis shows promising ways to reach the theoretical limits of this material. Even though these limits are relatively low due to the large bandgap of this material, $Cs_2AgBiBr_6$ and its substitutional relatives remain highly interesting subjects for further research. Increasing the effort in exploring these will not only lead to an improvement of $Cs_2AgBiBr_6$ solar cells, but also helps

establishing, developing and improving other double perovskites with large potential but still missing solar cell applications. This thesis demonstrates opportunities towards tuning the optoelectronic properties of both pristine thin films of double perovskites as well as complete solar cells and provides ideas on how to improve solar cells as a whole, which are expected to be applicable for other double perovskite systems.

8 Publications and Presentations

List of Publications

1) Maximilian T. Sirtl, Firouzeh Ebadi, Bas T. van Gorkom, Patrick Ganswindt, René A. Janssen, Thomas Bein* and Wolfgang Tress*, *Adv. Opt. Mater.* **2021**, 2100202

2) Melina Armer, Julian Höcker, Carsten Büchner, Sophie Häfele, Patrick Dörflinger, Maximilian T. Sirtl, Kristofer Tvingstedt, Thomas Bein and Vladimir Dyakonov, *Cryst. Eng. Comm*, **2021**,

3) Maximilian T. Sirtl‡, Melina Armer‡, Lennart K. Reb, Rik Hooijer, Patrick Dörflinger, Manuel A. Scheel, Kristofer Tvingstedt, Phillipp Rieder, Nadja Glück, Pallavi Pandit, Stephan Roth, Peter Müller-Buschbaum, Vladimir Dyakonov and Thomas Bein*, *ACS Appl. Energy Mater.* **2020**, 3, 11597-11609

4) Michiel L. Petrus,‡ Maximilian T. Sirtl,‡ Anna C. Closs, Thomas Bein, Pablo Docampo, *Mol. Syst. Des. Eng.*, **2018**, 3, 734-740.

5) Michiel L. Petrus, Kelly Schutt, Maximilian T. Sirtl, Eline M. Hutter, Anna C. Closs, James M. Ball, Johan C. Bijleveld, Annamaria Petrozza, Thomas Bein, Theo J. Dingemans, Tom J. Savenije, Henry Snaith, and Pablo Docampo, *Adv. Energy Mater.* **2018**, 8 (38), 1801605

6) Michiel L. Petrus, Arif Music, Anna C. Closs, Johan Bijleveld, Maximilian T. Sirtl, Yinghong Hu, Theo J. Dingemans, Thomas Bein, Pablo Docampo, *J. Mater. Chem. A* **2017**, 5 (48), 25200 – 25210

‡ These authors equally contributed to the work.

Oral Presentations

1) Maximilian T. Sirtl, Melina Armer, Rik Hooijer, Firouzeh Ebadi, Bas van Gorkom, Mahdi Mohammadi, Andreas Weis, Sebastian Häringer, Patrick Ganswindt, Clément Maheu, Thomas Mayer, René Janssen, Vladimir Dyakonov, Wolfgang Tress and Thomas Bein "Thin Films Based on $Cs_2AgBiBr_6$ as Absorber Materials in Lead-Free Perovskite Solar Cells" *Solar Technologies go Hybrid Conference*, **2021**, Munich, Germany

2) Maximilian T. Sirtl, Melina Armer, Elizabetta Landini, Karsten Reute, Vladimir Dyakonov and Thomas Bein "Lead-Free Double Perovskites for Photovoltaic Applications" *SPP online Meeting*, **2021**, Online Conference

3) Maximilian T. Sirtl, Melina Armer, Lennart K. Reb, Rik Hooijer, Patrick Dörflinger, Manuel A. Scheel, Kristofer Tvingstedt, Phillipp Rieder, Nadja Glück, Pallavi Pandit, Stephan Roth, Peter Müller-Buschbaum, Vladimir Dyakonov and Thomas Bein "Optoelectronic Properties of $Cs_2AgBiBr_6$ Thin Films: The Influence of Precursor Stoichiometry" *Solar Technologies go Hybrid Conference,* **2020,** Online Conference

4) Maximilian T. Sirtl, Michiel L. Petrus, Kelly Schutt, Eline M. Hutter, Anna C. Closs, James M. Ball, Johan C. Bijleveld, Annamaria Petrozza, Thomas Bein, Theo J. Dingemans, Tom J. Savenije, Henry Snaith, and Pablo Docampo "New Generation Hole Transporting Materials for Perovskite Solar Cells: Amide-based Small-Molecule with a Non-Conjugated Backbone" *E-MRS Fall Meeting* **2018**, Warsaw, Poland

Poster Presentations

1) Maximilian T. Sirtl, Melina Armer, Lennart K. Reb, Rik Hooijer, Patrick Dörflinger, Manuel A. Scheel, Kristofer Tvingstedt, Phillipp Rieder, Nadja Glück, Pallavi Pandit, Stephan Roth, Peter Müller-Buschbaum, Vladimir Dyakonov and Thomas Bein "Optoelectronic Properties of $Cs_2AgBiBr_6$ Thin Films: The Influence of Precursor Stoichiometry" *NIPHO*, **2020,** Seville, Spain.

2) Maximilian T. Sirtl, Melina Armer, Lennart K. Reb, Rik Hooijer, Patrick Dörflinger, Manuel A. Scheel, Kristofer Tvingstedt, Phillipp Rieder, Nadja Glück, Pallavi Pandit, Stephan Roth, Peter Müller-Buschbaum, Vladimir Dyakonov and Thomas Bein "Optoelectronic Properties of $Cs_2AgBiBr_6$ Thin Films: The Influence of Precursor Stoichiometry" *NIM Summer Retrat,* **2019,** Klosterseeon, Germany

3) Maximilian T. Sirtl, Melina Armer, Lennart K. Reb, Rik Hooijer, Patrick Dörflinger, Manuel A. Scheel, Kristofer Tvingstedt, Phillipp Rieder, Nadja Glück, Pallavi Pandit, Stephan Roth, Peter Müller-Buschbaum, Vladimir Dyakonov and Thomas Bein "Optoelectronic Properties of $Cs_2AgBiBr_6$ Thin Films: The Influence of Precursor Stoichiometry" *Solar Technologies go Hybrid Conference,* **2019,** Nuremburg, Germany.

4) Maximilian T. Sirtl, Melina Armer, Lennart K. Reb, Rik Hooijer, Patrick Dörflinger, Manuel A. Scheel, Kristofer Tvingstedt, Phillipp Rieder, Nadja Glück, Pallavi Pandit, Stephan Roth, Peter Müller-Buschbaum, Vladimir Dyakonov and Thomas Bein "Optoelectronic Properties of $Cs_2AgBiBr_6$ Thin Films: The Influence of Precursor Stoichiometry" *Solar Technologies go Hybrid Conference,* **2018,** Würzburg, Germany

5) Maximilian T. Sirtl, Melina Armer, Lennart K. Reb, Rik Hooijer, Patrick Dörflinger, Manuel A. Scheel, Kristofer Tvingstedt, Phillipp Rieder, Nadja Glück, Pallavi Pandit, Stephan Roth, Peter Müller-Buschbaum, Vladimir Dyakonov and Thomas Bein "Optoelectronic Properties of $Cs_2AgBiBr_6$ Thin Films: The Influence of Precursor Stoichiometry" *CeNS Conference,* **2018,** Venice, Italy